

**The Catalytic Decarbonylation of Unstrained
Ketones mediated by Platinum(II)
Complexes**

Julia Paula Sarju

Doctor of Philosophy

**University of York
Chemistry**

September 2016

Abstract

Cyclohexanone, an unstrained ketone, was found to undergo decarbonylation in the presence of soluble platinum(II) complexes of the general formula [Pt(tolpy)Cl(L)] (where tolpy is 2-(4-tolyl)pyridine and L is a neutral ligand) to afford the platinum carbonyl complex [Pt(tolpy)Cl(CO)] as well as carbon monoxide, methane and butane. As such, the activation of the cyclohexanone must proceed *via* the cleavage of three carbon–carbon bonds. However, the stoichiometric balance of the reaction required additional hydrogen, which implied a coupled transfer hydrogenation step.

As part of a mechanistic investigation, a number of novel cycloplatinated complexes were prepared and characterised and their ability to catalyse the decarbonylation reactions was investigated. Many of them were identified as active catalyst precursors and, in particular, this was found to be true for [Pt(tolpy)Cl(CO)], suggesting that the reaction is catalytic. It was commonplace for reactions to be accompanied by decomposition to what was assumed to be colloidal platinum.

In addition to cyclohexanone, a range of other carbonyl-containing substrates were investigated and examples of cyclic and acyclic ketones as well as aldehydes were found undergo decarbonylation under the conditions employed. A mechanistic investigation was undertaken involving *in situ* spectroscopic studies, dynamic light scattering, deuterium labelling and mercury poisoning experiments. A mechanism for the decarbonylation of cyclohexanone is proposed whereby fragmentation and transfer hydrogenation take place to afford acetaldehyde, which then undergoes decarbonylation to afford methane.

For the family of complexes of formula [Pt(tolpy)Cl(L)] prepared to study the mechanism, a combination of spectroscopic and computational techniques were employed to study the structural and bonding properties of the complexes and the relative *trans*-influence of the ligands. An ordered series for the *trans*-influence of the ligands was identified using bond lengths obtained from analyses of single crystal X-ray data and this trend was also consistent with quantum chemical calculations. The trend was also analysed for possible correlations with chemical shifts and coupling constants obtained from ^1H , $^{13}\text{C}\{^1\text{H}\}$, ^{15}N and $^{195}\text{Pt}\{^1\text{H}\}$ NMR spectroscopy.

List of Contents

Abstract	2
List of Contents	3
List of Tables	11
List of Figures	16
Acknowledgements	29
Author's Declaration	30
Chapter One: Introduction to Decarbonylation Reactions	31
1.1.0 Decarbonylation	31
1.2.0 Cleavage of C–C Single Bonds	31
1.3.0 Strategies for Promoting Decarbonylation Reactions	33
1.3.1 Ring Strain	33
1.3.2 Chelation/Coordination	35
1.4.0 Active Substrates for Decarbonylation Reactions.....	36
1.4.1 Ketones.....	36
1.4.2 Aldehydes	39
1.4.3 Esters.....	40
1.5.0 Applications of Decarbonylation Reactions	41
1.5.1 Synthesis of Natural Products.....	41
1.5.2 Sustainable Chemistry Applications of Decarbonylation	44
1.6 Reaction Mechanisms Reported for Decarbonylation Reactions.....	46
1.7 Conclusion.....	50
Chapter Two: Transition Metal Mediated Decarbonylation	51

2.1	Previous Work	51
2.1.1	Initial Study into the Decarbonylation Reactions	53
2.2	Aims	55
2.3	The Decarbonylation of Cyclohexanone	56
2.3.1	Head-space Analysis Methodology	56
2.3.2	Identification of the Hydrocarbon Products.....	58
2.3.3	Quantification of Methane and Butane Produced by the Decarbonylation of Cyclohexanone	59
2.4	Identification of Solvent System for the Decarbonylation of Cyclohexanone Mediated by [Pt(tolpy)Cl(S-dms)] (3)	60
2.4.1	Results of the Control Reactions	61
2.4.2	Decarbonylation of Cyclohexanone in Different Solvents.....	63
2.5	Substrate Scope	67
2.5.1	Cyclic Ketones	67
2.5.2	Linear Ketones.....	70
2.5.3	Ketones Substituted in the α -Position	71
2.5.4	Non-ketone Containing Substrates: Ethers, Ester, Aldehydes, Carboxylic Acids and Alcohols.....	74
2.5.5	Summary of the Results from the Substrate Scope Experiments	76
2.6	The Activity of Different Metal Catalysts	79
2.6.1	Variation of Ligand, L, for the Family of Platinum Complexes, [Pt(tolpy)Cl(L)].....	79
2.6.2	Pt ^{II} Complexes with other Chelating Ligands	82
2.6.3	Rhodium Complexes.....	83
2.6.4	Heterogeneous Catalysis	84

2.6.5 Comparison of Active Systems	84
2.7 Summary and Outlook.....	86
Chapter Three: Mechanistic Investigation	87
3.1 Introduction.....	87
3.1.1 Main Aims	87
3.1.2 Photochemical Decarbonylation Reactions.....	88
3.1.3 Transfer Hydrogenation	90
3.1.4 Transition Metal Nanoparticle Catalysis.....	93
3.2 Determination of the Source of Energy Required to Drive the Decarbonylation Reactions.....	98
3.2.1 Is the Decarbonylation of Cyclohexanone a Thermal or Photochemical Process?.....	98
3.2.2 Determination of the Onset Temperature.....	98
3.3 Radical Process	99
3.4 Transfer Hydrogenation.....	100
3.4.1 Addition of Transfer Hydrogenation Donors.....	100
3.4.2 UV-Vis Spectroscopic Analysis.....	102
3.4.3 Ketone Substrates Revisited.....	103
3.5 Deuterium Labelling Studies.....	106
3.5.1 Cyclohexanone	106
3.5.2 Cycloheptanone.....	111
3.5.3 Cyclooctanone	112
3.6 Observation of New Platinum Species Formed During the Decarbonylation Reactions	113

3.6.1 Formation and Decarbonylation Activity of [Pt(tolpy)(μ -Cl)] (1)	113
3.6.2 Formation and Decarbonylation Activity of [Pt(tolpy)Cl(H-tolpy)] (2)	114
3.6.3 Formation of [Pt ^{IV} (tolpy) ₂ Cl ₂] (11)	114
3.7 <i>In Situ</i> Infra-red (IR) Spectroscopy	116
3.7.1 <i>In Situ</i> IR Spectroscopy of the Decarbonylation of Cyclohexanone	116
3.7.2 Varying the Ketone Substrate	118
3.7.3 Varying the Metal Complex used to Catalyse Decarbonylation Reactions.....	123
3.8 Distinguishing Between Molecular and Nanoparticle Catalysis	125
3.8.1 Dynamic Light Scattering (DLS)	125
3.8.2 Mercury Drop Test	127
3.8.3 Use of Polyvinylpyrrolidone (PVP)	128
3.8.4 Synergistic Hetero- and Homogeneous Catalysis.....	129
3.9 Introduction of Substrate to Metal Centre	129
3.9.1 Loss of the Neutral Ligand in [Pt(tolpy)Cl(L)]	131
3.9.2 Oxidative Addition	131
3.10 C–C Bond Scission to Afford an Aldehyde	132
3.11 Proposed Mechanistic Route for the Decarbonylation of Cyclohexanone	133
3.12 Summary	136
Chapter Four: Investigating the <i>trans</i>-Influence using a Combined Spectroscopic and Computational Approach	138
4.1.0 Introduction.....	138
4.1.1 <i>Trans</i> -Influence.....	139

4.1.2 Experimental Techniques to Probe the <i>trans</i> -Influence	140
4.1.3 Computational Techniques to Probe the <i>trans</i> -Influence	143
4.1.4 Research Objectives	145
2.0 Summary of the Spectroscopic Properties of the [Pt(tolpy)CL(L)] Complexes	145
2.1 [Pt(tolpy)(μ -Cl)] ₂ (1)	145
2.2 Nitrogen Donor Ligands	154
2.3 Sulfur Donor Ligands	164
2.4 Carbon Donor Ligands	172
2.5 Phosphorus Donor Ligands	178
3.0 Probing the <i>trans</i> -Influence of Different Ligands using Spectroscopic Techniques	187
3.1 X-ray Diffraction	187
3.2 Far-infrared Spectroscopy	191
3.3 NMR spectroscopy	193
4.0 Probing the <i>trans</i> -Influence of Different Ligands using Natural Bond Order Analysis	206
5.0 Summary	209
Experimental Section	211
1.0 Analytical Techniques	211
NMR Spectroscopy	211
IR Spectroscopy	212
Single Crystal X-ray Diffraction	212
UV-Vis Spectroscopy	212

Dynamic Light Scattering	213
High Resolution Mass Spectrometry	213
CHN Elemental Analysis	213
Peroxide Test.....	213
Gas Chromatography (GC).....	213
2.0 Materials.....	220
3.0 Purification of Solvents and Reagents.....	220
Acetone.....	220
Acetophenone.....	220
Cyclic Ketones	221
Cyclopentylmethylether.....	221
Dioxane.....	221
4.0 Synthesis.....	222
4.1 Synthesis of Platinum(II) Complexes.....	222
Synthesis of $[\text{Pt}(\text{tolpy})(\mu\text{-Cl})_2]$ (1)	222
Synthesis of $[\text{Pt}(\text{tolpy})\text{Cl}(\text{H-tolpy})]$ (2)	224
Synthesis of $[\text{Pt}(\text{tolpy})\text{Cl}(\text{S-dms})]$ (3) from $[\text{Pt}(\text{tolpy})\text{Cl}]_2$ (1)	228
Synthesis of $[\text{Pt}(\text{tolpy})\text{Cl}(\text{S-dms})]$ (3) from $[\text{Pt}(\text{tolpy})\text{Cl}(\text{H-tolpy})]$ (2)	229
Synthesis of $[\text{Pt}(\text{tolpy})\text{Cl}(\text{S-dms})]$ (3) from $\text{K}_2[\text{PtCl}_4]$	230
Synthesis of $[\text{Pt}(\text{tolpy})\text{Cl}(\text{CO})]$ (4) <i>via</i> Carbonylation of $[\text{Pt}(\text{tolpy})(\mu\text{-Cl})_2]$ (1)	234
Synthesis of $[\text{Pt}(\text{tolpy})\text{Cl}(\text{py})]$ (5)	237
Synthesis of $[\text{Pt}(\text{tolpy})\text{Cl}(\text{CH}_3\text{CN})]$ (6)	240

Synthesis of [Pt(tolpy)Cl(dms)] (7)	241
Synthesis of [Pt(tolpy)Cl(tht)] (8)	244
Synthesis of [Pt(tolpy)Cl(PPh ₃)] (9)	247
Synthesis of [Pt(tolpy)Cl(P(OPh) ₃)] (10)	249
Synthesis of [Pt(IV)(tolpy) ₂ Cl ₂] (11)	252
Synthesis of [Pt(tolpy)Cl(PhCN)] (12)	254
Synthesis of [Pt(tolpy)Cl(PCy ₃)] (13)	255
4.2 Decarbonylation Reactions	257
General Procedure for Decarbonylation of Neat Substrates	257
Effect of Air and Light on the Decarbonylation of Cyclohexanone	259
Irradiation of [Pt(tolpy)Cl(S-dms)] and Cyclohexanone	260
The Effect of Additives to the Decarbonylation of Cyclohexanone	260
Substrate Scope	261
Variation of the Metal Catalyst	267
Rhodium Complexes	268
Heterogeneous Catalysis	270
<i>In situ</i> IR Monitoring of Decarbonylation Reactions	271
Determination of the Onset Temperature for Decarbonylation of Cyclohexanone Mediated by [Pt(tolpy)Cl(S-dms)] (3)	271
General Procedure for Control Solvent Reactions	272
General Procedure for Decarbonylation of Cyclohexanone in Solvent	274
General Procedure for Decarbonylation of Substrates in Solvent with a Transfer Hydrogenation Donor (THD)	275
UV-Vis Spectroscopic Analysis	277

4.3 Deuteration of Ketones at the α -Position.....	277
2,2,6,6-Tetradeuterio-cyclohexanone	277
2,2,7,7-Tetradeuterio-cycloheptanone	278
2,2,8,8-Tetradeuterio-cyclooctanone	278
4.4 Deuterium Labelling experiments	278
Acetone-d ₆	278
2,2',6,6'-Tetradeuterated cyclohexanone.....	279
Cyclohexanone with IPA-d ₈	280
Decarbonylation of 2,2',6,6'-Tetradeuterated and <i>Per</i> -deuterated Cyclohexanone in the presence of 1,3-Cyclohexadiene	280
2,2',7,7'-Tetradeuterated Cycloheptanone.....	281
2,2',8,8'-Tetradeuterated Cyclooctanone	282
5.0 Computational Methods.....	283
Geometry Optimisations	283
NBO Analysis.....	286
Appendices	287
Appendix I: Details of Crystal Data and Structure Refinement	287
Appendix II: Introduction to DFT and explanation of Relevant Terms	294
Appendix III: List of Transition Metal Compounds	296
Abbreviations	300
References	304

List of Tables

Table 1:	Summary of the results of the solvent control experiments using [Pt(tolpy)Cl(S-dmsO)] (3).....	62
Table 2:	Summary of the solvent trials for decarbonylation of cyclohexanone	63
Table 3:	Summary of the experimental conditions and results for the solvents in which decarbonylation occurred.....	64
Table 4:	The effect of varying the number of equivalents of cyclohexanone w.r.t. complex 3 on the decarbonylation of cyclohexanone in acetonitrile, toluene or 1,2-dichlorobenzene.	66
Table 5:	Data for the percentage of the enol form present in the pure liquid of a selection of ketones.	73
Table 6:	Summary of the activity of different substrates	77
Table 7:	Summary of the hydrocarbon products formed and comparison of the conversion to [Pt(tolpy)Cl(CO)] (4) when the substrates were heated with [Pt(tolpy)Cl(S-dmsO)] (3) under standard decarbonylation conditions	79
Table 8:	Comparison of the experimental data collected for the decarbonylation of cyclohexanone mediated by [Pt(tolpy)(μ -Cl)] ₂ and [Pt(tolpy)Cl(L)].....	85
Table 9:	Results of the decarbonylation of cyclohexanone mediated by [Pt(tolpy)Cl(S-dmsO)] (3) in the presence of 1,3-cyclohexadiene or IPA in acetonitrile	101
Table 10:	The effect of varying the number of molar equivalents of 1,3-cyclohexadiene (HD = hydrogen donor) on the relative amounts of the platinum complexes observed by ¹ H NMR spectroscopy after the decarbonylation of acetophenone mediated by [Pt(tolpy)Cl(S-dmsO)] (3).....	105
Table 11:	Isotopic distribution of methane formed by decarbonylation of 2,2',6,6'-tetradeuterated cyclohexanone	108

Table 12:	Distribution of isotopomers observed by GC-MS analysis of the reaction headspace after the decarbonylation of 2,2',6,6'-tetradeuterated and per-deuterated cyclohexanone in the presence of 1,3-cyclohexadiene	110
Table 13:	Summary of the peak areas corresponding to butane measured after mercury was added to the solution of cyclohexanone and [Pt(tolpy)Cl(S-dmsu)] (3) and heated under standard decarbonylation conditions	128
Table 14:	Values for the vibrational frequencies for Pt–Cl stretches reported in the literature.....	141
Table 15:	Summary of the geometry optimisation for 1a and b	147
Table 16:	Comparison of the bond lengths reported for [Pt(tolpy)Cl(H-tolpy)] (3) here and by Rodriguez-Castro <i>et al.</i> with [Pt(ppy)Cl(H-ppy)].....	155
Table 17:	Comparison of the bond lengths reported for [Pt(tolpy)Cl(S-dmsu)] (3) reported here and [Pt(ppy)Cl(S-dmsu)] reported by Kobayashi and co-workers.....	167
Table 18:	Comparison of the calculated and experimental vibrational frequencies and the relative energies of the isomers 4a and 4b	172
Table 19:	Comparison of the bond lengths measure by X-ray crystallography for isomers 4a and 4b	177
Table 20:	Comparison of bond lengths measured using single crystal X-ray diffraction	188
Table 21:	Comparison of the $\bar{\nu}$ (Pt–Cl) and the Pt–Cl bond length	192
Table 22:	NMR spectral data for the platinum complexes synthesised recorded in CDCl ₃	194
Table 23:	Summary of bond strength parameters and bond lengths for the Pt–N bond in [Pt(tolpy)Cl(L)] and [Pt(tolpy)(μ -Cl)] ₂	207
Table 24:	Summary of GC retention times including study of C ₄₋₇ hydrocarbons using GC method described above for GC-B.....	216

Table 25:	Summary of the data collected using the selective 1D NOE Spectra recorded for 1a	223
Table 26:	Summary of the coupling observed in the ^1H - ^1H COSY experiment for 1a	223
Table 27:	Summary of the data collected using the selective 1D NOE Spectra for 2	225
Table 28:	Summary of the coupling observed in the ^1H - ^1H COSY experiment for 2	225
Table 29:	Summary of the coupling was observed in the HMQC spectra for 2	226
Table 30:	Summary of the coupling was observed in the HMBC spectra for 2	227
Table 31:	Summary of the coupling observed in the ^1H - ^1H COSY experiment for 3	230
Table 32:	Summary of the coupling was observed in the HMQC spectra for 3	232
Table 33:	Summary of the coupling was observed in the HMBC spectra for 3 232	
Table 34:	Summary of the coupling was observed in the HMQC spectra for 7	238
Table 35:	Summary of the coupling was observed in the HMBC spectra for 5	239
Table 36:	Summary of the coupling was observed in the HMQC spectra for 7	241
Table 37:	Summary of the coupling was observed in the HMBC spectra for 5	243
Table 38:	Summary of the coupling observed in the ^1H - ^1H COSY experiment for 8	244

Table 39:	Summary of the coupling was observed in the HMQC spectra of 8	245
Table 40:	Summary of the coupling was observed in the HMQC spectra for 10	250
Table 41:	Summary of the coupling was observed in the HMQC spectra for 13	256
Table 42:	Head space analysis after decarbonylation of cyclohexanone mediated by complex (3), (GC-A)	258
Table 43:	Head space analysis after decarbonylation of cyclohexanone mediated by complex (3), (GC-B)	258
Table 44:	Initial studies of the decarbonylation of cyclohexanone mediated by [Pt(tolpy)Cl(S-dms)] (3) under different conditions.....	259
Table 45:	Summary of the peak areas corresponding to butane measured after mercury was added to the solution of cyclohexanone and [Pt(tolpy)Cl(S-dms)] (3) and heated under standard decarbonylation conditions	260
Table 46:	Summary of the effect of additives on the decarbonylation of cyclohexanone mediated by [Pt(tolpy)Cl(S-dms)] (3).....	261
Table 47:	Decarbonylation of the different substrates mediated by [Pt(tolpy)Cl(S-dms)] (3).....	262
Table 48:	The decarbonylation of cyclohexanone mediated by different metal complexes.....	267
Table 49:	Relative peak areas of hydrocarbon products observed using GC-B	268
Table 50:	Summary of the results of the solvent control experiments using [Pt(tolpy)Cl(S-dms)] (3).....	273
Table 51:	Summary of the experimental conditions and results for the solvent optimisation study	274

Table 52:	The effect of varying the equivalents of cyclohexanone in the decarbonylation reactions mediated by [Pt(tolpy)Cl(S-dmsO)] (3) and performed in acetonitrile275
Table 53:	The effect of adding a transfer hydrogenation donor on the decarbonylation reactions mediated by [Pt(tolpy)Cl(S-dmsO)] (3)276
Table 54:	Isotopic distribution of methane formed by decarbonylation of acetone-d ₈279
Table 55:	Isotopic distribution of methane formed by decarbonylation of 2,2',6,6'-tetradeuterated cyclohexanone279
Table 56:	Distribution of isotopomers observed by GC-MS analysis of the reaction headspace after the decarbonylation of 2,2',6,6'-tetradeuterated and per-deuterated cyclohexanone in the presence of 1,3-cyclohexadiene281
Table 57:	Summary of the results of the quantum mechanical calculations performed on the <i>cis</i> and <i>trans</i> isomers of [Pt(tolpy)(μ-Cl)] ₂ (1a and 1b)284
Table 58:	Crystal data and structure refinement for compounds 1 - 3287
Table 59:	Crystal data and structure refinement for compounds 4 - 5289
Table 60:	Crystal data and structure refinement for compounds 7 - 9290
Table 61:	Crystal data and structure refinement for compounds 10, 11, 13 and 18292
Table 62:	Description of the functionals and methods discussed in this thesis294
Table 63:	Description of the basis sets discussed in this thesis295

List of Figures

Figure 1:	First example of the decarbonylation of cyclohexanone reported by Rusina and Vlček.....	31
Figure 2:	Comparison of the transition metal bonding to C–H and C–C bonds	32
Figure 3:	Platinacyclobutane complex formed <i>via</i> oxidative addition of cyclopropane	32
Figure 4:	Graphs showing the number of publications and citations covering the topic C–C activation.....	32
Figure 5:	Comparison of the orbitals in cyclopropane and cyclohexane and their potential overlap with transition metal <i>d</i> -orbitals	33
Figure 6:	Decarbonylation of cyclobutanone and cyclopentanone functional groups by Murakami <i>et al.</i>	34
Figure 7:	Catalytic C–C bond activation reported by Murakami <i>et al.</i>	34
Figure 8:	Room-temperature decarbonylation reported by Murakami <i>et al.</i>	34
Figure 9:	Decarbonylation of phenyl ketones reported by Chen <i>et al.</i>	35
Figure 10:	Catalytic decarbonylation of conjugated diyne reported by Dong <i>et al.</i>	35
Figure 11:	The cleavage of C–C bonds of ketones mediated by [(1,2,4-tri- <i>tert</i> -butylcyclopentadienyl)rhodium(<i>bis</i> -ethylene)] reported by Brookhart and Daugulis	36
Figure 12:	Oxidative cleavage of the C _(CO) –C α bond of aryl methyl ketones reported by Zhang <i>et al.</i>	37
Figure 13:	Selective mono- and double-decarbonylation of alkynyl α -diones reported by Whittaker and Dong	38
Figure 14:	The first example of the catalytic C–C activation of α -keto esters reported by Whittaker and Dong	38

Figure 15:	Synthesis of 2-quinolinone derivatives <i>via</i> decarbonylation of isosatins reported by Zeng and Dong	39
Figure 16:	Palladium-catalysed synthesis of apopinene from mertynal.....	39
Figure 17:	Oxidative, decarbonylative arylation of aromatic aldehydes reported by Shuai <i>et al.</i>	39
Figure 18:	Synthesis of vinyl arenes <i>via</i> decarbonylative coupling of aryl esters and alkenes	40
Figure 19:	Synthesis of fused rings and spirocycles <i>via</i> coupling of alkenes and benzocyclobutanones.	42
Figure 20:	Proposed mechanism for the formation of fused rings or spirocycles	43
Figure 21:	Synthesis of fused β -naphthols or indenenes <i>via</i> direct or decarbonylative alkyne-benzocyclobutanone coupling	43
Figure 22:	Chemical structure of DTBM-SEGPHOS.....	44
Figure 23:	Chemical structures of 5-(hydroxymethyl)furfural and furfuryl alcohol	44
Figure 24:	Selective decarbonylation of 5-hydroxymethylfufuryl alcohol to afford fufuryl alcohol reported by Geilen <i>et al.</i>	45
Figure 25:	Biomass-derived furfural substrates for decarbonylation	46
Figure 26:	Iron catalysed C–C bond cleavage reported by Xing <i>et al.</i>	47
Figure 27:	Reaction mechanism proposed by Xing <i>et al.</i> for the C–C bond activation of carbonyl compounds.....	47
Figure 28:	Mechanism for the decarbonylation of diynones proposed by Dong <i>et al.</i>	48
Figure 29:	Decarbonylation of conjugated ynones reported by Dermenci <i>et al.</i>	49
Figure 30:	Tentative catalytic cycle proposed by Fristrup <i>et al.</i> for the rhodium-catalysed decarbonylation of aldehydes	50

Figure 31:	Formation of dinuclear μ -acetato complex <i>via</i> oxidation of <i>cis</i> -[PtCl ₂ (S-dmsO) ₂].....	51
Figure 32:	Reduction of platinum-bound dmsO to dms when <i>cis</i> -[PtCl ₂ (S-dmsO) ₂] was heated to reflux with 2-(4-tolyl)pyridine in 2-ethoxy ethanol.	52
Figure 33:	Unexpected decarbonylation of cyclohexanone observed when <i>cis</i> -[PtCl ₂ (S-dmsO) ₂] was heated with 2-(4-tolyl)pyridine in cyclohexanone.....	52
Figure 34:	Metal systems investigated for their activity with regards to the decarbonylation of ketones	53
Figure 35:	Active substrates for decarbonylation mediated by [Pt(tolpy)Cl(S-dmsO)] (3) studied by Torroba	54
Figure 36:	Non-active substrates for decarbonylation mediated by [Pt(tolpy)Cl(S-dmsO)] (3) studied by Torroba	54
Figure 37:	Attempted decarbonylation of cyclohex-2-en-1-one studied by Torroba	54
Figure 38:	Photograph of a 10 ml gas-tight Fisher-Porter vessel equipped with a pressure gauge and a Luer lock adapter.	57
Figure 39:	The formation of cycloundecane from the stoichiometric decarbonylation of cyclododecanone reported by Murakami <i>et al.</i>	58
Figure 40:	Platinum-catalysed decarbonylation of cyclohexanone to afford methane, carbon monoxide, butane and [Pt(tolpy)Cl(CO)] (4) involving the cleavage of three C–C bonds.....	59
Figure 41:	Single crystal X-ray crystal structure for [Pt ^{IV} (tolpy) ₂ Cl ₂].CHCl ₃ (11), with ellipsoids at 50% probability	68
Figure 42:	Mass spectrum of cyclohexene which eluted at 11.4 minutes	68
Figure 43:	Study of the decarbonylation of cyclohex-2-en-1-one mediated by [Pt(tolpy)Cl(S-dmsO)] (3).....	70

Figure 44:	Decarbonylation of acetone reported by Celenligil <i>et al.</i>	71
Figure 45:	Chemical structures of α - and β -tetralone	72
Figure 46:	Chemical structures of the platinum complexes studied as alternative to the [Pt(tolpy)Cl(L)] family of complexes for decarbonylation reactions.	82
Figure 47:	Decarbonylation of cyclohexanone showing the imbalance in hydrogen.....	87
Figure 48:	Photochemical cleavage of the C $_{\alpha}$ -C $_{\beta}$ bond of 2,6-dimethyl cyclohexanone as reported by Lee <i>et al.</i>	89
Figure 49:	The formation of [Co ^{III} (ttp)COCHMe(CH ₂) ₃ COMe] observed by Lee <i>et al.</i>	89
Figure 50:	Reaction mechanism proposed by Lee <i>et al.</i> for the cleavage of the C $_{\alpha}$ -C $_{\beta}$ bond of 2,6-dimethyl cyclohexanone.....	90
Figure 51:	Palladium-catalysed conversion of cyclohexanones to phenols using molecular oxygen as terminal oxidant reported by Izawa <i>et al.</i>	91
Figure 52:	Homogeneous catalysis of the transfer hydrogenation of ketones by direct hydrogen transfer and by metal hydride or di-hydride routes	93
Figure 53:	Heterogeneous/nanoparticle surface catalysis of the transfer hydrogenation of ketones.....	93
Figure 54:	Palladium nanoparticle-catalysed asymmetric Suzuki–Miyaura coupling reaction reported by Fujihara <i>et al.</i>	95
Figure 55:	Mechanism for the Suzuki reaction including both nanoparticle catalysis (heterogeneous) and mononuclear catalysis (homogeneous) proposed by Perez-Lorenzo.....	96
Figure 56:	A plot of the normalised intensity of the vibration at 2098 cm ⁻¹ versus temperature for the decarbonylation of mediated by [Pt(tolpy)Cl(S-dmsu)] (3).....	99

- Figure 57: UV-Visible spectra recorded on samples taken at the beginning ($t = 0$ h) and end ($t = 16$ h) of the decarbonylation of cyclohexanone mediated by [Pt(tolpy)Cl(S-dmsu)] (**3**) in the presence of the hydrogen donor 1,3-cyclohexadiene in acetonitrile..... 102
- Figure 58: Comparison between the fitted curve and the difference spectrum obtained by subtracting the UV-Vis spectra recorded. 103
- Figure 59: Decarbonylation of deuterated acetone mediated by [Pt(tolpy)Cl(S-dmsu)] (**3**) in the presence of 1,3-cyclohexadiene. 106
- Figure 60: Anticipated hydrocarbon products for the decarbonylation of deuterated cyclohexanone..... 107
- Figure 61: EI mass spectrum for the peak corresponding to tri-deuterated butane..... 108
- Figure 62: Proposed donation of hydrogen and deuterium atoms from 2,2',6,6'-tetradeuterated cyclohexanone to afford 2-mono deuterated cyclohex-2-en-1one. 108
- Figure 63: Possible transfer hydrogenation of d_7 -butene and d_7 -butadiene intermediates. 111
- Figure 64: Mass spectrum of d_2 -cyclohexene observed as the major product of decarbonylation of d_4 -cycloheptanone using GC-MS analysis of the reaction headspace 112
- Figure 65: Mass spectrum of d_2 -cycloheptene observed using GC-MS 113
- Figure 66: X-ray crystal structure of [Pt(tolpy)Cl(H-tolpy)] (**2**) showing the tolpy ligand blocking the top face of the complex. 114
- Figure 67: Possible routes to [Pt(*p*-fluorophenylpyridine)₂Cl₂]. proposed by Newman and co-workers 115
- Figure 68: Decarbonylation of cyclohexanone mediated by [Pt(tolpy)Cl(S-dmsu)] (**3**)..... 116

- Figure 69: Plot of peak height as a function of time as recorded during *in situ* IR monitoring of the reaction between cyclohexanone and [Pt(tolpy)Cl(S-dmsO)] (3)..... 117
- Figure 70: Plot of intensity of the peak corresponding to $\bar{\nu}(\text{CO})$ of [Pt(tolpy)Cl(CO)] (4) as a function of time recorded during *in situ* IR monitoring of the reaction between different ketones and [Pt(tolpy)Cl(S-dmsO)] (3)..... 118
- Figure 71: Hydrocarbon products of the decarbonylation of cyclopentanone by [Pt(tolpy)Cl(S-dmsO)] (3)..... 119
- Figure 72: Plot of intensity for the peaks at 2064 cm^{-1} and 2100 cm^{-1} as a function of time (min^{-1}) measured using an *in situ* IR spectroscopy for the decarbonylation of cyclopentanone. 120
- Figure 73: Decarbonylation of cycloheptanone mediated by [Pt(tolpy)Cl(S-dmsO)] (3)..... 120
- Figure 74: Plot of intensity for the peaks at 2033 cm^{-1} and 2099 cm^{-1} as a function of time (min^{-1}) during the decarbonylation of cycloheptanone..... 121
- Figure 75: Decarbonylation of cyclooctanone mediated by [Pt(tolpy)Cl(S-dmsO)] (3)..... 121
- Figure 76: Plot of intensity for the peaks at 2053 cm^{-1} and 2098 cm^{-1} as a function of time (min^{-1}) measured during the decarbonylation of cyclooctanone..... 122
- Figure 77: Plot of intensity for the peaks at 2034 cm^{-1} and 2098 cm^{-1} as a function of time (min^{-1}) measured during the decarbonylation of β -tetralone..... 123
- Figure 78: Comparison of the change in peak intensity at 2098 cm^{-1} and $2063\text{-}2071\text{ cm}^{-1}$ during the decarbonylation of cyclohexanone mediated by [Pt(tolpy)(μ -Cl)]₂/([Pt(tolpy)Cl(L)]) and monitored by *in situ* IR spectroscopy..... 124

Figure 79:	Photograph taken of the reaction solutions of two reactions, at the beginning and end of the decarbonylation of cyclohexanone mediated by [Pt(tolpy)Cl(S-dmsO)] (3).....	125
Figure 80:	Plot of average hydrodynamic diameter <i>versus</i> intensity obtained <i>via</i> dynamic light scattering from the reaction solution after decarbonylation of cyclohexanone mediated by [Pt(tolpy)Cl(CO)] (4).	126
Figure 81:	Coordination modes and resonance forms for metal complexes of ketones	131
Figure 82:	X-ray crystal structure of [PtCl{CH ₂ C(O)CH ₃ }(1,10-phenanthroline)] and the packing of the molecules reported by Barone <i>et al.</i> with the hydrogen atoms and solvent molecules removed for clarity	132
Figure 83:	Proposed C–C bond activation of cyclohexanone	133
Figure 84:	Proposed mechanism for the decarbonylation of acetaldehyde fragment by [Pt(tolpy)Cl(L)].....	134
Figure 85:	Preliminary mechanism proposed for the decarbonylation of cyclooctanone.....	135
Figure 86:	Spectrochemical and <i>trans</i> -effect series	139
Figure 87:	Schematic of Grinberg's polarisation theory	140
Figure 88:	General structure of the platinum complexes for which the $\bar{\nu}(\text{Pt}-\text{Cl})$ vibrational frequencies were collected by Appleton <i>et al.</i>	141
Figure 89:	Chemical structure of <i>trans</i> -[Pt(H)(L)(PMe ₃) ₂]......	143
Figure 90:	Deshielding and shielding of the hydride ligand caused by electron donation between the orbitals of the Pt–H bond and the orbitals centred on platinum.	143
Figure 91:	General structure of the PCP pincer complexes studied by Jia <i>et al.</i>	144
Figure 92:	General structures for the cyclometallated platinum complexes studied in this chapter	145

Figure 93:	Geometry optimisation of the <i>cis</i> -isomer 1a using the DFT functional BP86 and the basis sets 6-311+G(d,p) and LANL2DZ (for Pt), which includes ECP and the D3-BJ correction.....	148
Figure 94:	Geometry optimisation of the <i>trans</i> -isomer 1b using the DFT functional BP86 and the basis sets 6-311+G(d,p) and LANL2DZ (for Pt), which includes ECP and the D3-BJ correction	148
Figure 95:	Calculated far-infrared spectra for the <i>cis</i> - and <i>trans</i> -isomers of [Pt(tolpy)(μ -Cl)] ₂ (1), overlaid with the measured spectrum.	149
Figure 96:	Single crystal X-ray structure of [Pt(tolpy)(μ -Cl)] ₂ .2CHCl ₃ (1), with ellipsoids at 50% probability.....	150
Figure 97:	Packing in the crystal for [Pt(tolpy)(μ -Cl)] ₂ .2CHCl ₃ (1) in the unit cell, with ellipsoids at 50% probability and the H atoms removed for clarity and a view of one of the π - π stacked pairs	151
Figure 98:	Partly solved crystal of 1b by X-ray crystallography.	152
Figure 99:	Annotated ¹ H NMR spectrum of [Pt(tolpy)(μ -Cl)] ₂ (1)	153
Figure 100:	¹ H- ¹ H DQF-COSY NMR spectra of [Pt(tolpy)(μ -Cl)] ₂ (1)	153
Figure 101:	General chemical structure of the complexes reported by Fuentes <i>et al.</i> to exhibit a T-shaped C _{Ar} -H \cdots π _{py} interaction	155
Figure 102:	Single crystal X-ray structure for [Pt(tolpy)Cl(H-tolpy)].CH ₂ Cl ₂ (2), with ellipsoids at 50% probability..	155
Figure 103:	Single crystal X-ray crystal structure showing the packing of [Pt(tolpy)Cl(H-tolpy)].CH ₂ Cl ₂	155
Figure 104:	Annotated ¹ H NMR spectrum of [Pt(tolpy)Cl(H-tolpy)] (2)	157
Figure 105:	¹ H- ¹ H DQF-COSY NMR spectra of [Pt(tolpy)Cl(H-tolpy)] (2).....	158
Figure 106:	Structure of [Pt(tolpy)Cl(H-tolpy)] (2) with the carbon atoms labelled from 1 to 22 and the assignment of the signals observed in the ¹ H NMR spectrum.....	159
Figure 107:	¹ H- ¹³ C HMQC spectra for [Pt(tolpy)Cl(H-tolpy)] (2)	160

Figure 108: ^1H - ^{15}N HMBC spectra for $[\text{Pt}(\text{tolpy})\text{Cl}(\text{Htolpy})]$ (2)..	161
Figure 109: Single crystal X-ray structure of $[\text{Pt}(\text{tolpy})\text{Cl}(\text{py})]$ (5)	163
Figure 110: Packing of $[\text{Pt}(\text{tolpy})\text{Cl}(\text{py})]$ determined by single crystal X-ray crystallography.....	163
Figure 111: Resonance forms of the ligand dmsO	165
Figure 112: Single crystal X-ray crystal structure for $[\text{Pt}(\text{tolpy})\text{Cl}(\text{S-dmsO})]$ (3)..	165
Figure 113: Packing of $[\text{Pt}(\text{tolpy})\text{Cl}(\text{S-dmsO})]$ (3) in the unit cell determined by X-ray crystallography	166
Figure 114: Packing of $[\text{Pt}(\text{ppy})\text{Cl}(\text{S-dmsO})]$ determined by single crystal X-ray diffraction reported by Kobayashi and co-workers	166
Figure 115: Single crystal X-ray crystal structure of $[\text{Pt}(\text{tolpy})\text{Cl}(\text{dms})]$ (7)....	168
Figure 116: Packing of $[\text{Pt}(\text{tolpy})\text{Cl}(\text{dms})]$ (7) in the unit cell determined by X-ray crystallography and image showing π - π stacking of tolpy ligands	169
Figure 117: Front on and side on views of the single crystal X-ray crystal structure of $[\text{Pt}(\text{tolpy})\text{Cl}(\text{tht})]$ (8)	170
Figure 118: Packing of $[\text{Pt}(\text{tolpy})\text{Cl}(\text{tht})]$ (8) in the unit cell determined by X-ray crystallography.....	170
Figure 119: View of the packing in the crystal structure of 8 highlighting the short contact between the chloride ligand and a hydrogen atom of the tht ligand	171
Figure 120: Geometry and proton assignment of the coordinated tht ligand.	171
Figure 121: The calculated HOMO for complex 4a using BP86/6-31G(d)/LANL2DZ for Pt for the geometry optimisation and the utility Cubegen within Gaussian09	174
Figure 122: The calculated LUMO for complex 4a using BP86/6-31G(d)/LANL2DZ for Pt for the geometry optimisation and the utility Cubegen within Gaussian09	174

Figure 123: Single crystal X-ray structure for [Pt(tolpy)Cl(CO)] (4a).....	175
Figure 124: Packing of [Pt(tolpy)Cl(CO)] (4) in the unit cell of the single crystal X-ray crystal structure, and top view of two molecules arranged on top of each other	176
Figure 125: Molecular structure of [Pt(tolpy)Cl(CO)] (4b).....	177
Figure 126: Packing of [Pt(tolpy)Cl(CO)] (4b) in the unit cell of the single crystal X-ray crystal structure, and top view of two molecules arranged on top of each other.....	177
Figure 127: Front on and side on views of the single crystal X-ray crystal structure of [Pt(tolpy)Cl(PPh ₃)] (9)	179
Figure 128: Packing of [Pt(tolpy)Cl(PPh ₃)] (9) determined by X-ray crystallography.....	179
Figure 129: Close contact observed between the chloride ligand and a hydrogen atom of the PPh ₃ ligand by X-ray diffraction	180
Figure 130: ¹ H (left) and ¹ H{ ³¹ P} (right) NMR spectra of [Pt(tolpy)Cl(PPh ₃)] (9) in region of H ¹	181
Figure 131: ³¹ P NMR spectrum of [Pt(tolpy)Cl(PPh ₃)] (9)	181
Figure 132: Front on and side on views of the single crystal X-ray crystal structure of [Pt(tolpy)Cl(P(OPh) ₃)] (10).	182
Figure 133: Packing of [Pt(tolpy)Cl(P(OPh) ₃)] (10) determined by X-ray crystallography.....	182
Figure 134: Short contact between the chloride ligand and a hydrogen atom of the tolyl ring observed in the packing of 10 in the X-ray crystal structure.....	183
Figure 135: Short contact between the oxygen atoms and hydrogen atoms of the phenyl rings observed in the packing of 10 in the X-ray crystal structure.....	183
Figure 136: ¹ H NMR and ¹ H{ ³¹ P} spectra of [Pt(tolpy)Cl(P(OPh) ₃)] (10) in region of H ¹	184

Figure 137: ^{31}P NMR spectrum of $[\text{Pt}(\text{tolpy})\text{Cl}(\text{P}(\text{OPh})_3)]$ (10).....	184
Figure 138: Front on and side on views of the single crystal X-ray crystal structure of $[\text{Pt}(\text{tolpy})\text{Cl}(\text{PCy}_3)]\cdot\text{CH}_2\text{Cl}_2$ (13).	185
Figure 139: Packing of $[\text{Pt}(\text{tolpy})\text{Cl}(\text{PCy}_3)]\cdot\text{CH}_2\text{Cl}_2$ (13) determined by X-ray crystallography.....	185
Figure 140: Short contacts observed between the chloride ligand and hydrogen atoms of the CH_2Cl_2 solvent molecule and the pyridyl ring of the tolpy ligand.....	186
Figure 141: ^1H and $^1\text{H}\{^{31}\text{P}\}$ NMR spectrum of $[\text{Pt}(\text{tolpy})\text{Cl}(\text{PCy}_3)]$ (13).....	186
Figure 142: The Pt–C and Pt–N bond lengths measured using single crystal X-ray diffraction for the series of complexes, $[\text{Pt}(\text{tolpy})\text{Cl}(\text{L})]$	189
Figure 143: The Pt–Cl bond lengths measured using single crystal X-ray diffraction for the series of complexes, $[\text{Pt}(\text{tolpy})\text{Cl}(\text{L})]$	190
Figure 144: The difference from 180° of the angle between <i>trans</i> -ligands was compared to the Pt-bidentate ligand bond lengths.....	191
Figure 145: Comparison of the vibrational frequency of the Pt–Cl stretching mode with the experimentally measured Pt–N bond length for $[\text{Pt}(\text{tolpy})\text{Cl}(\text{L})]$, where L = CO, tht, dms, tolpy, S-dms, py.	193
Figure 146: Proton and carbon assignments for dinuclear and mononuclear platinum complexes.....	193
Figure 147: Comparison of the chemical shift data for H^1 and the Pt–N bond length showing no correlation..	195
Figure 148: Comparison of the $^3J_{\text{HPt}}$ for H^1 and the Pt–N bond length for $[\text{Pt}(\text{tolpy})\text{Cl}(\text{L})]$	196
Figure 149: Comparison of the chemical shift data for H^8 and the Pt–C bond length showing no correlation	196
Figure 150: Comparison of the $^3J_{\text{HPt}}$ for H^8 and the Pt–C bond length for $[\text{Pt}(\text{tolpy})\text{Cl}(\text{L})]$	197

Figure 151: Stacked $^{13}\text{C}\{^1\text{H}\}$ NMR spectra of $[\text{Pt}(\text{tolpy})\text{Cl}(\text{dms})]$ (7) recorded using a 400 MHz and 300 MHz instruments.	198
Figure 152: $^{13}\text{C}\{^1\text{H}\}$ NMR spectra of $[\text{Pt}(\text{tolpy})\text{Cl}(\text{dms})]$ recorded using a 300 MHz zoomed in of the carbanion signal	199
Figure 153: The relationship between $^1J_{\text{C}_{\text{Pt}}}$ coupling constant and the experimentally determined Pt–N bond lengths	199
Figure 154: The relationship between $^1J_{\text{C}_{\text{Pt}}}$ coupling constant and the experimentally determined Pt–C bond lengths	200
Figure 155: Comparison of the ^{15}N chemical shift and the Pt–N bond length for $[\text{Pt}(\text{tolpy})\text{Cl}(\text{L})]$	201
Figure 156: Comparison of the ^{195}Pt chemical shift and the Pt–N bond length for $[\text{Pt}(\text{tolpy})\text{Cl}(\text{L})]$	202
Figure 157: Variation in ^{195}Pt chemical shift among the family of $[\text{Pt}(\text{tolpy})\text{Cl}(\text{L})]$ complexes.....	203
Figure 158: The correlation between $^3J_{\text{H}_{\text{Pt}}}$ for H^1 and ^{195}Pt chemical shift.....	204
Figure 159: The correlation between $^1J_{\text{C}_{\text{Pt}}}$ for C^{12} and ^{195}Pt chemical shift...	205
Figure 160: The correlation between ^{15}N and ^{195}Pt chemical shifts	205
Figure 161: Comparison between experimental and calculated Pt–N bond lengths.	207
Figure 162: Comparison of bond strength parameters calculated using population analysis <i>versus</i> Pt–N bond length calculated using DFT and determined from X-ray crystallography.	208
Figure 163: Variation in ^{195}Pt chemical shift experimentally recorded with the calculated Wiberg bond order	209
Figure 164: Calibration curve for methane analysed using a mass spectral detector, GC-E.....	219
Figure 165: Plot of average hydrodynamic diameter <i>versus</i> intensity obtained <i>via</i> dynamic light scattering from the reaction solution after	

decarbonylation of cyclohexanone mediated by [Pt(tolpy)Cl(CO)] (4).....	268
Figure 166: Gas Chromatogram of the reaction headspace after attempted decarbonylation of cyclohexanone mediated by Pt/C	270
Figure 167: Gas Chromatogram of the reaction headspace after attempted decarbonylation of cyclohexanone mediated by Pd/C	271
Figure 168: A plot of the normalised intensity of the vibration at 2098 cm ⁻¹ versus temperature for the decarbonylation of mediated by [Pt(tolpy)Cl(S-dmsO)] (3).....	272

Acknowledgements

During my time at York I have been very lucky to meet so many kind and funny people, too many to list here. Firstly, I would like to thank my supervisor, Duncan Bruce, for his time, support and ideas. I am very grateful for the financial support from the Department of Chemistry, through the teaching scholarship. I would also like to thank David Pugh for being a fantastic mentor and role model for undergraduate teaching.

I would also like to thank Jason Lynam for stepping in and taking Imelda and I under his wing for part of our second year. Thanks also go to Alice Mcellin, for her hard work and enthusiasm during her vacation placement within the group and Adrian, Sam, Rachel, Natalie and Jess for solving the X-ray crystal structures of the complexes discussed in this thesis. I would like to thank all of the technical staff at York especially Heather Fish, for all the time she spent teaching me how to use the NMR spectrometers and Karl Heaton for huge amounts of support and time developing and troubleshooting the gas injection GC-MS methods and for making the process so much fun. I would also like to thank the National Service for Computational Chemistry Software, especially Alexandra Simperler, for their wonderful training in computational chemistry.

I am so lucky to have been part of such a fun and friendly group and I would all the members of the materials group past and present and I would also like to single out Richard and Rachel for huge amounts of help and support during the thesis writing process. Finally and most importantly, I would like to thank all my family and friends who have been so supportive and reminded me daily to “just keep swimming”, with special thanks for my parents, Julien and Mary, to my fiancé Richard, to my sister, Maria, my cousin, Siobhan and to my chemistry bffs Rachael, Lyndsay and Imelda.

Author's Declaration

I declare that the work presented in this thesis is my own work unless otherwise stated or indicated by references. This work has not been presented for an award at this, or any other, university. The synthesis of some of the platinum complexes presented in this thesis carried out by the vacation student, Alice Mcellin, under my supervision and the natural bond order analysis (NBO) was carried out by Marsel Shafikov.

Chapter One: Introduction to Decarbonylation Reactions

1.1.0 Decarbonylation

Thermal transition-metal-mediated decarbonylation can be defined as the extrusion of a carbonyl fragment from an organic compound upon heating with a transition metal complex, resulting in the formation of organic products and either a metal-carbonyl bond or liberated carbon monoxide. In addition to being of academic interest, extrusion of a carbonyl group has the potential to be a useful synthetic transformation in organic synthesis. Catalytic decarbonylation reactions offer an atom-economical way of using a commonly found functional group to prepare new compounds that may be difficult to access by traditional routes.

Decarbonylation of carbonyl containing molecules was first reported in 1965, by Rusina and Vlček. They observed the activation of DMF, THF, cyclohexanone, dioxane and acetophenone when each was heated with RhCl_3 and triphenylphosphine to afford $[\text{RhCl}(\text{CO})(\text{PPh}_3)_2]$ and unknown hydrocarbon products (Figure 1).¹ A mechanism for this transformation was not proposed, and experimental details, conversions or isolated yields were not reported.

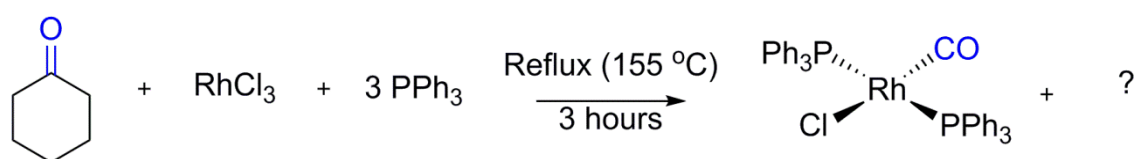


Figure 1: First example of the decarbonylation of cyclohexanone reported by Rusina and Vlček.¹

1.2.0 Cleavage of C–C Single Bonds

Transition-metal-mediated decarbonylation of organic compounds is an example of C–C bond activation.²⁻⁵ The cleavage of these bonds is normally difficult and generally, C–C single bonds are considered unreactive.⁶ The bonds are stable thermodynamically with average bond dissociation energies of around 380 kJ mol^{-1} ,⁷ and the metal–carbon bonds formed by oxidative addition are usually weaker ($80 - 125 \text{ kJ mol}^{-1}$ per bond).^{2, 8} The bonds are also protected sterically by the surrounding atoms bound to the carbon and the orbitals in a C–C bond have less favourable directionality for interaction with transition metals than the adjacent C–H bonds (Figure 2). Although the σ -orbital of the C–H bond lies along the plane of the bond, the s-orbital on the hydrogen atom is spherical; this atom has no other substituents and so end on approach of the metal is

possible. Crabtree proposed that oxidative addition of C–H bonds is initiated by an end on interactive before the side on coordination.⁹

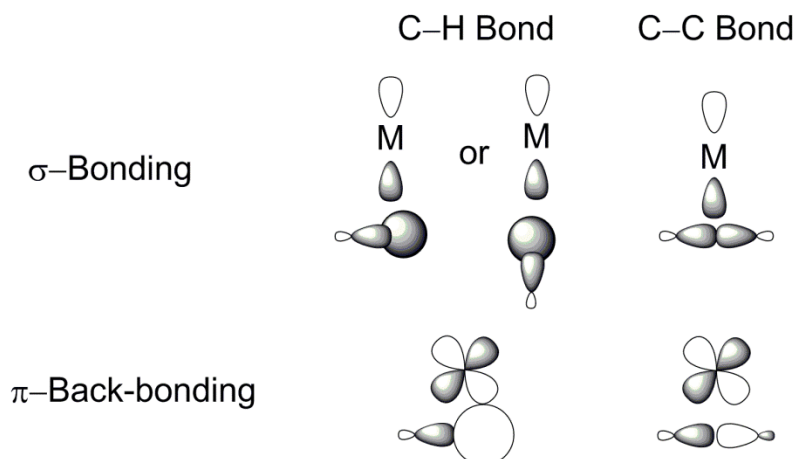


Figure 2: Comparison of the transition metal bonding to C–H and C–C bonds

The first reported transition metal insertion into a C–C single bond was reported in 1955 and involved the oxidative addition of cyclopropane to chloroplatinic acid, yielding a platinacyclobutane complex (Figure 3).¹⁰ This result was then confirmed by Adams *et al.* using ¹H NMR and IR spectroscopy and by Keeton *et al.* using X-ray crystallography.^{11, 12} Since then, this area of research has grown significantly, motivated by applications in synthetic and sustainable chemistry (Figure 4).¹³

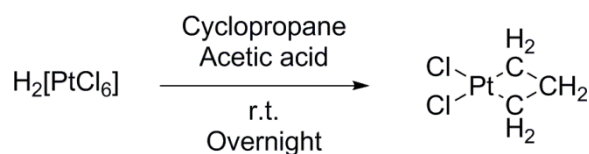


Figure 3: Platinacyclobutane complex formed *via* oxidative addition of cyclopropane¹⁰

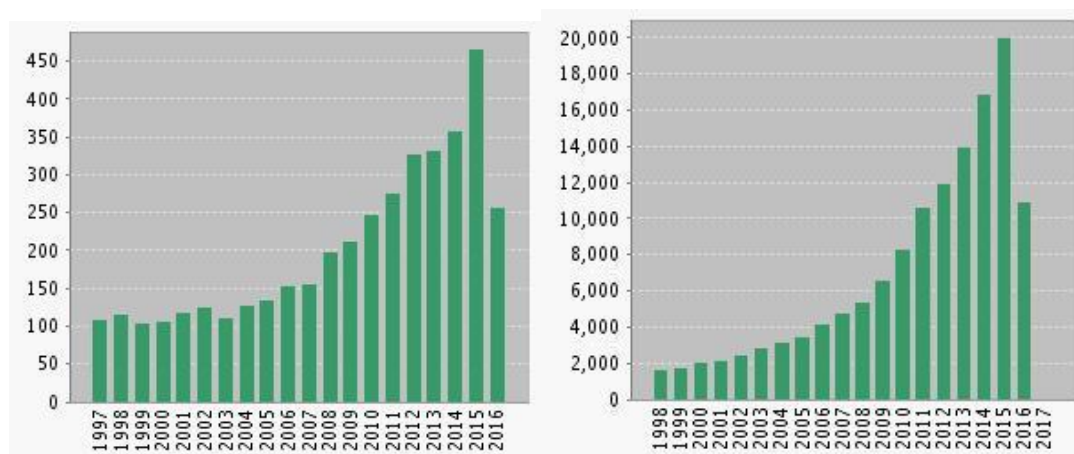


Figure 4: Graphs showing the number of publications (left) and citations (right) covering the topic C–C activation generated by Web of Science, Thompson Reuters™. The data for 2016 have been collected up to June.

1.3.0 Strategies for Promoting Decarbonylation Reactions

Due to the unreactive nature of the C–C bond, most decarbonylation reactions of ketones utilise ring strain or coordinating groups to promote the reaction; examples of these strategies are described below.

1.3.1 Ring Strain

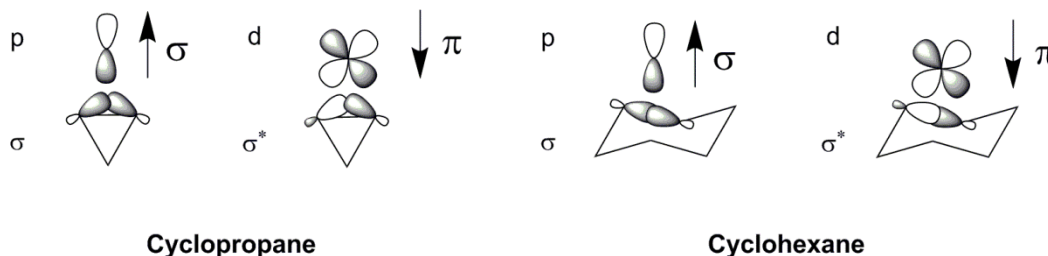


Figure 5: Comparison of the orbitals in cyclopropane and cyclohexane and their potential overlap with transition metal *d*-orbitals

As shown in the comparison between cyclopropane and cyclohexane in Figure 5, the C–C bonding molecular orbitals in strained systems are more available to the metal, which lowers the kinetic barrier to C–C cleavage.³ Utilising the greater reactivity of strained systems, Murakami *et al.* published the thermal decarbonylation of fused cyclobutanones mediated by Wilkinson's catalyst, $[\text{RhCl}(\text{PPh}_3)_3]$ (Figure 6).^{14, 15} They postulated that the ring strain is relieved by the initial C–C activation to form a five-membered rhodacycle, promoting the reaction. The efficiency of this system was reduced greatly when extended to the analogous and less strained fused cyclopentanone where reaction times increased from 41 hours to 8 days and the yield decreased from 99% to 57%. When combined with hydrogenolysis, catalytic C–C activation was achieved (Figure 7). However, the reaction is no longer an example of thermal decarbonylation as extrusion of the carbonyl does not occur and only one C–C single bond is cleaved to afford the alcohol product. The active catalytic species was prepared *in situ* by mixing $[\text{Rh}_2\text{Cl}_2(\text{cod})_2]$ with the bidentate diphosphine $\text{Ph}_2\text{P}(\text{CH}_2)_2\text{PPh}_2$ (dppe).

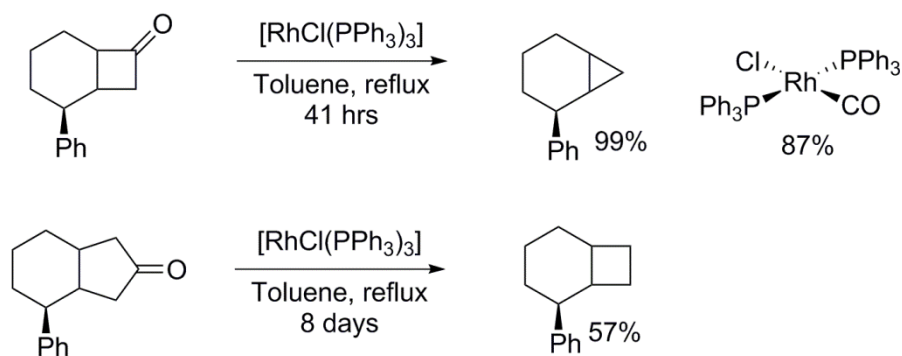


Figure 6: Decarbonylation of cyclobutanone and cyclopentanone functional groups by Murakami *et al.* (isolated yields are given shown)^{14, 15}

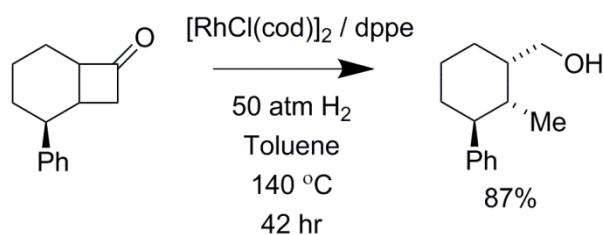


Figure 7: Catalytic C–C bond activation reported by Murakami *et al.*^{14, 15}

Most reported decarbonylation reactions require forcing conditions with high temperatures and the reactions described above all required temperatures between 120 and 140 °C. However, recently Murakami *et al.* published the decarbonylation of cyclobutanones at room temperature.¹⁶ Their procedure requires a polymeric rhodium complex containing the PBP pincer ligand (Figure 8), prepared by treatment of $[\text{Rh}(\text{H})(\text{PBP})]\text{OTf}$ with $\text{Me}_3\text{SiCH}_2\text{Li}$ *in situ*. They suggest that the electron-rich rhodium centre facilitates cleavage of the C–C single bond. Although this is a unique example of decarbonylation of ketones at room temperature, its synthetic utility is reduced by its stoichiometric nature.

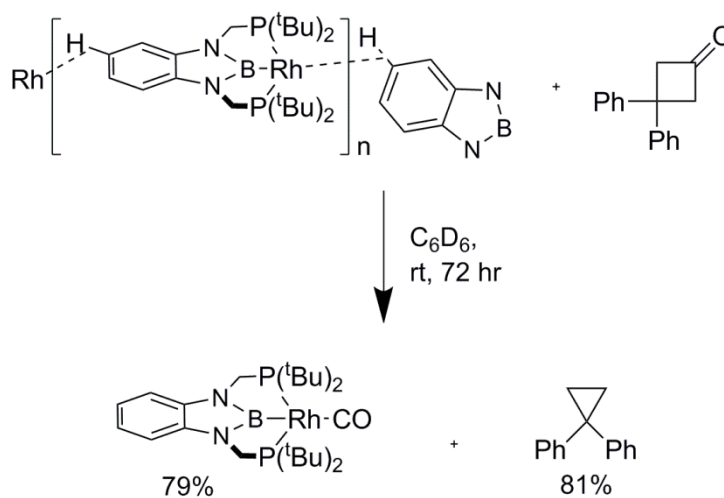


Figure 8: Room-temperature decarbonylation reported by Murakami *et al.*¹⁶

1.3.2 Chelation/Coordination

Functional groups that are able to coordinate to metal centres can be employed to bring the carbonyl group into close proximity with the metal, promoting bond activation. Unless a fortuitous coordinating group is already part of the substrate close to the carbonyl group, this strategy requires the use of auxiliary coordinating groups. Chen *et al.* reported rhodium-mediated decarbonylation of non-strained phenyl ketones bearing a coordinating pyridine group (Figure 9).¹⁷ This is a rare example of catalytic decarbonylation and, although the requirement for coordinating groups limits the substrate scope, Chen *et al.* demonstrated that this reaction could tolerate many different R groups, including alkyl, aryl and heteroaromatic substituents.

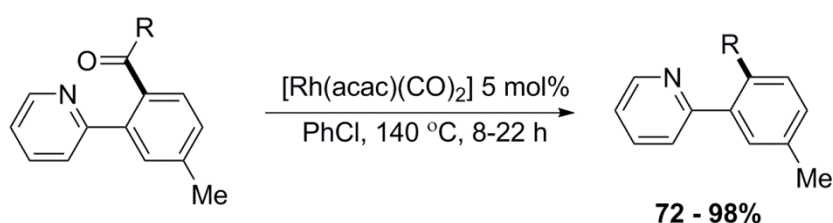


Figure 9: Decarbonylation of phenyl ketones reported by Chen *et al.*¹⁷

The stoichiometric decarbonylation of diynones was first reported by Müller and Segnitz in 1973 using $[\text{RhCl}(\text{PPh}_3)_3]$ in xylene under reflux to yield 1,3-diynes and the carbonyl complex, $[\text{RhCl}(\text{CO})(\text{PPh}_3)_2]$.¹⁸ 1,3-Diynes are a structural motif present in some natural products and they are usually prepared by copper-catalysed coupling reactions, however, these methods often lead to the formation of homo-coupled undesired side products.¹⁹⁻²¹ In 2013, Dong *et al.* published the high-yield synthesis of conjugated diynes *via* Rh^I-catalysed decarbonylation of diynones (Figure 10).²²

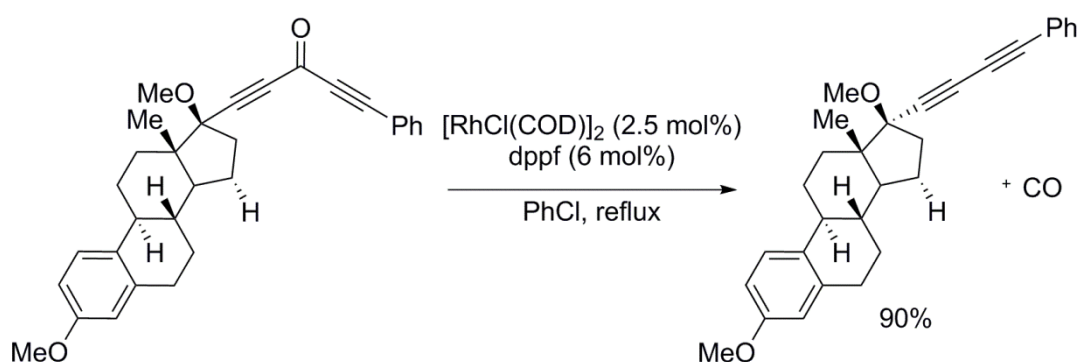


Figure 10: Catalytic decarbonylation of conjugated diynone reported by Dong *et al.*²²

1.4.0 Active Substrates for Decarbonylation Reactions

1.4.1 Ketones

Most examples for decarbonylation of ketones require activated or strained substrates, such as diketones or strained cyclic ketones. The active metal systems reported are mostly late transition metals, usually rhodium, as part of coordinatively unsaturated 16-electron complexes such as Wilkinson's catalyst $[\text{RhCl}(\text{PPh}_3)_3]$.¹⁵ Forcing conditions with high temperatures and long reaction times (16 - 48 hours) are often required, and many examples require stoichiometric amounts of the transition metal complex.⁶

The decarbonylation of benzophenones and acetophenones was reported by Brookhart and Daugulis using bulky rhodium complexes at 120 - 150 °C.²³ The products of the decarbonylation were reported to be a rhodium carbonyl dimer with a metal-metal double bond, $[\text{Cp}'\text{Rh}(\mu\text{-CO})_2]$, a rhodium carbonyl species ($\text{Cp}' = 1,2,4\text{-tri-}t\text{-butyl cyclopentadienyl}$), $[\text{Cp}'\text{Rh}(\text{CO})_2]$, a carbonyl ethylene complex, and biphenyls from benzophenones or toluenes from acetophenones (Figure 11). The carbonyl dimer is believed to be formed from the carbonyl ethylene complex upon CO loss. Scrambling of the ketone starting material was also reported as a major by-product. This is the first and only published example of the catalytic decarbonylation of unstrained ketones. During their study they monitored the formation of the rhodium carbonyl complexes by NMR spectroscopy but not the formation of the organic product. In order to isolate the organic product, they conducted a larger-scale decarbonylation of 4,4'-dimethyl benzophenone and 4,4'-dimethyl biphenyl was identified as the organic product (82% isolated yield, TON = 2-3).

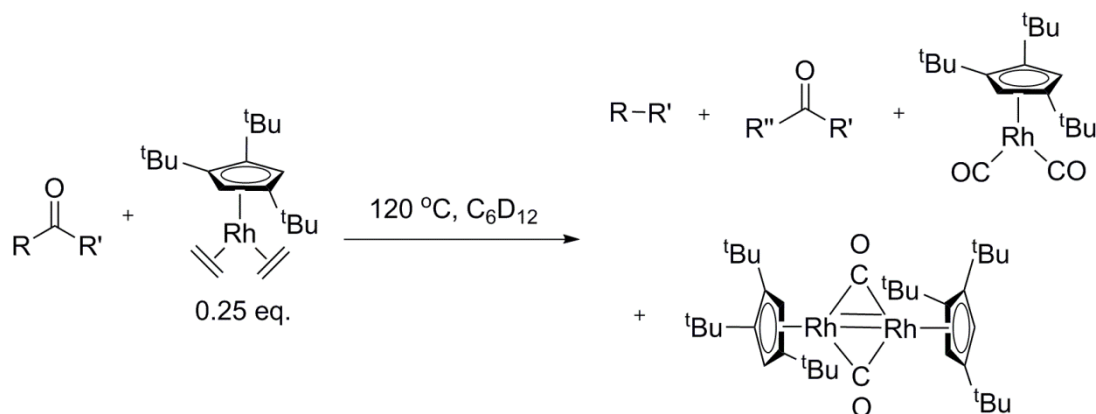


Figure 11: The cleavage of C–C bonds of ketones mediated by [(1,2,4-tri-*tert*-butylcyclopentadienyl)rhodium(*bis*-ethylene)] reported by Brookhart and Daugulis²³

The oxidative cleavage of the C_(CO)–C_α bond of acetophenone was reported by Zhang *et al.*²⁴ In their study, arylmethyl ketones were converted to the corresponding aryl aldehyde by copper iodide and molecular oxygen (Figure 12). They found that arylethylketones such as propiophenone were unreactive, and suggested that was due to oxidation of the methyl substituent being more favourable than methylene. After conducting deuterium labelling studies, they identified the C_(methyl)–H bond cleavage as the rate-determining step. The studies also showed that the proton corresponding to the aldehyde originates from the methyl group.

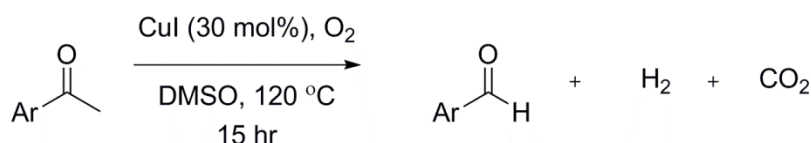


Figure 12: Oxidative cleavage of the C_(CO)–C_α bond of aryl methyl ketones reported by Zhang *et al.*²⁴

Diketones are inherently more reactive than the analogous mono-ketones and there is the possibility for the decarbonylation of either or both ketone groups in the molecule. The first example of the decarbonylation of 1,2- and 1,3-diketones was reported by Kaneda *et al.* using rhodium catalysis.²⁵ In this study only single decarbonylation was observed and the [RhCl(CO)(PPh₃)₂] formed during the reaction was also found to mediate decarbonylation reactions on these substrates.

Double decarbonylation was achieved 40 years later by Whittaker and Dong, who, by taking advantage of the ability of rhodium to coordinate to an alkyne group, obtained conjugated ynones or alkynes selectively from alkynyl α -diones (Figure 13).²⁶ Interestingly, selective control over the formation of the singly or doubly decarbonylated product was observed by changing the phosphine ligand and solvent combination. Single decarbonylation was observed when 1,2-bis(diphenylphosphine)ethane (dppe) was used in toluene, whereas double decarbonylation was observed when 4,5-bis-(diphenylphosphino)-9,9-dimethylxanthene (xantphos) was used in combination with ethyl benzene. They successfully extended their methodology to include the first example of the catalytic C–C activation of α -keto esters (Figure 14).

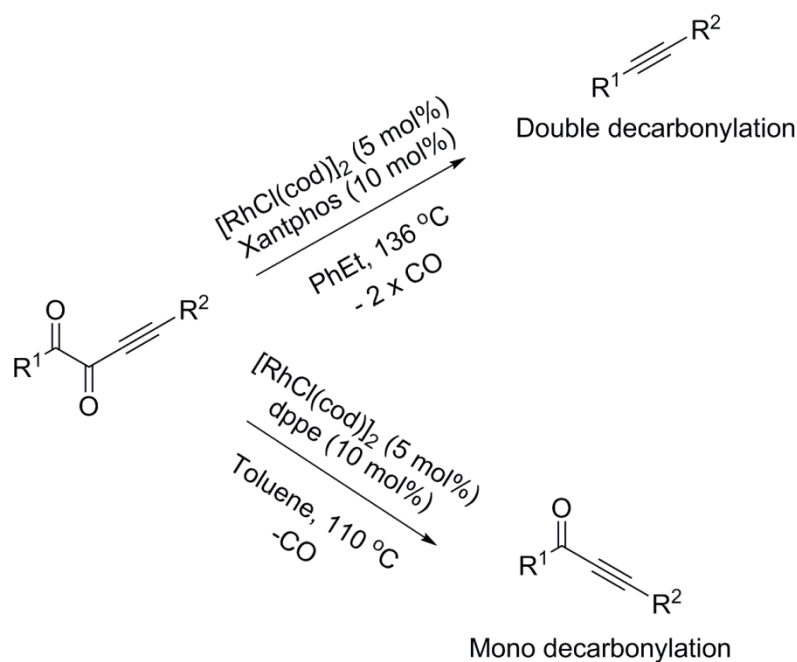


Figure 13: Selective mono- and double-decarbonylation of alkynyl α -diones reported by Whittaker and Dong²⁶

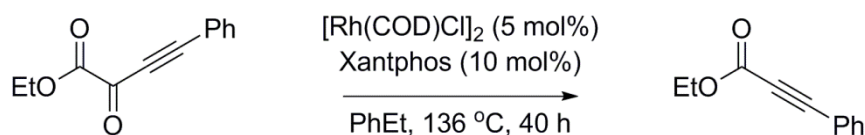


Figure 14: The first example of the catalytic C–C activation of α -keto esters reported by Whittaker and Dong²⁶

Zeng and Dong reported the catalytic synthesis of 2-quinolinone derivatives by the decarbonylation of isatins combined with coupling to alkynes at room temperature (Figure 15).²⁷ The reaction is catalysed using $[RhCl(cod)]_2$ (5 mol%) and proceeds *via* initial C–C bond activation of the isatin, followed by decarbonylation and finally alkyne insertion. They used control of the orientation of the directing group to suppress a potentially competitive C–H activation reaction, and found that 3-methyl-2-pyridyl was the ideal directing group. When the substrate scope was investigated they found that both aryl and alkyl substituted internal alkynes with various electronic properties worked very well, affording high yields of the corresponding 2-quinolinones. The reaction conditions are pH and redox neutral, which allows the tolerance of various functional groups and heterocycles.



Figure 15: Synthesis of 2-quinolinone derivatives *via* decarbonylation of isotatins reported by Zeng and Dong²⁷

1.4.2 Aldehydes

Compared with ketones, decarbonylation of aldehydes, acyl halides, and anhydrides is more straightforward and there are many examples in the literature.⁴ Most examples use transition metal catalysis including ruthenium,²⁸ rhodium,²⁹⁻³¹ iridium,³² and platinum.³³ The earliest examples of decarbonylation of aldehydes were reported by Eschinazi in 1959 for the palladium-catalysed synthesis of apopinene from mertynal (Figure 16).³⁴ In 1965 and 1966, Tsuji and Ohno reported the use of Wilkinson's complex, palladium on carbon (Pd/C) and PdCl₂ for the decarbonylation of aldehydes and acyl halides.^{35, 36}

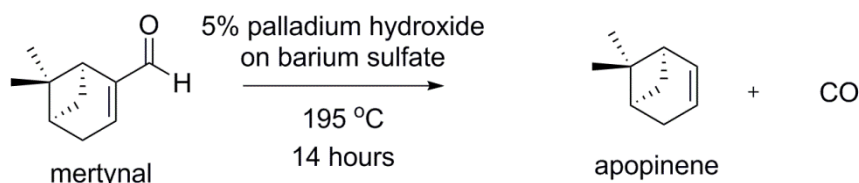


Figure 16: Palladium-catalysed synthesis of apopinene from mertynal³⁴

More recently decarbonylation of aldehydes has been used to synthesise coupled products from aromatic aldehydes and aryl-pyridines (Figure 17).³⁷ They used a rhodium catalyst and the oxidant, tertiary butyl peroxide (TBP) under neat conditions. They suggest that the mechanism goes *via* initial oxidation addition of the aromatic aldehyde, followed by extrusion of the carbonyl group. They suggest concurrent ligand substitution of the carbon monoxide and hydride ligands for the aryl pyridine, with the TBP facilitating the loss of the hydride. Finally, reductive elimination of the coupled product from the cyclometallated rhodium intermediate occurs.

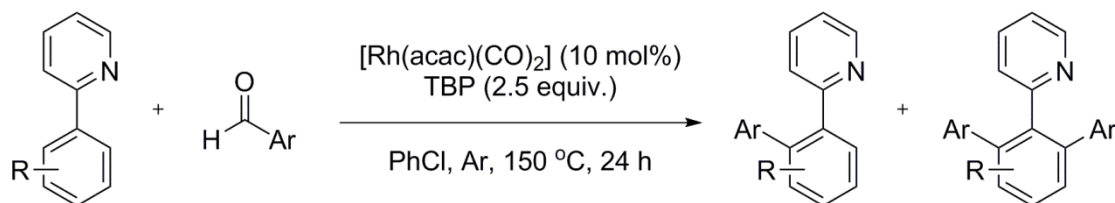


Figure 17: Oxidative, decarbonylative arylation of aromatic aldehydes reported by Shuai *et al.*³⁷

Zhao and co-workers conducted a theoretical investigation into Co^I mediated decarbonylation of acetaldehyde and concluded that the C–C bond is activated first in preference to the C–H bond.³⁸ They believe that cobalt can be used as a model system for other transition metal catalysed decarbonylation reactions of acetaldehyde. They suggest that the reaction proceeds *via* four steps: coordination, C–C activation, aldehyde proton shift (rds) and dissociation. However, their later work suggests that for iron and nickel, either C–C or C–H bond activation could lead to decarbonylation of acetaldehyde.³⁹

Crabtree and co-workers sought to design a catalyst for the decarbonylation of aldehydes with improved activity and selectivity.³⁰ They wanted to facilitate C–H activation, to disfavour β -H elimination (and the formation of unwanted alkene side products) and to promote the release CO from the coordination sphere (to prevent catalyst poisoning). To satisfy these criteria they investigated cationic Rh^I complexes of *bis*-(diphenylphosphinoethyl)phenylphosphine (triphos) and found that [Rh(CO)(triphos)]⁺ catalysed decarbonylation of aldehydes at 100 °C with little formation of side-product alkenes.

1.4.3 Esters

In contrast to the examples given above, there are fewer reports of decarbonylation of esters compared with aldehydes and acyl halides. However, in 2002 Gooßen *et al.* reported the synthesis of vinyl arenes by catalytic decarbonylative alkenylation of aryl esters using PdCl₂ (3 mol%) as the pre-catalyst, combined with LiCl (9 mol%) and isoquinoline (30 mol%) (Figure 18).⁴⁰ They observed that while the reaction would proceed initially with a fast turnover in the absence of isoquinoline as a stabilising ligand, extensive decomposition of the catalyst and that loss of catalytic activity occurred before complete conversion of the substrate. The addition of isoquinoline reduced the rate of reaction, but greatly enhanced the stability of the catalyst, increasing the overall yield.

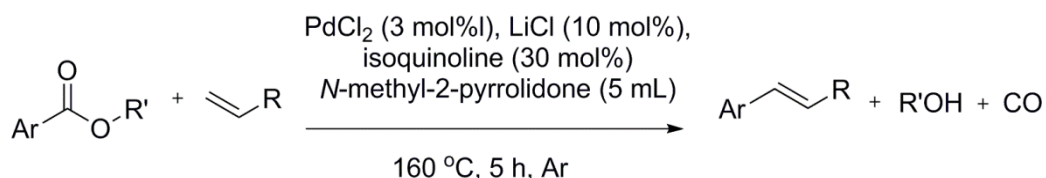


Figure 18: Synthesis of vinyl arenes *via* decarbonylative coupling of aryl esters and alkenes⁴⁰

They proposed that the reaction proceeds *via* oxidative addition of the ester's C–C single bond to the palladium centre, followed by extrusion of the carbonyl to

afford an aryl-palladium species. The alkene inserts into the palladium–carbon bond, followed by β -hydride elimination and reductive elimination to give the vinyl arene product and the alcohol by-product. Vinyl arenes can be synthesised by using a Wittig^{41, 42} or Heck reaction.⁴³ The Heck reaction is the palladium-catalysed regioselective addition of unsaturated halides or triflates to alkenes and requires stoichiometric quantities of base, which introduces a significant amount of waste. Gooßen *et al.* proposed that their decarbonylative route offers a less environmentally costly route because the addition of stoichiometric quantities of base is not required and the alcohol by-product can be recycled back into the starting ester by esterification.

1.5.0 Applications of Decarbonylation Reactions

In addition to the synthesis of cyclopropanes and 1,3-diynes described above, the number of examples of decarbonylation in organic synthesis has been growing.⁴ These examples demonstrate the advantages of decarbonylation where substrates do not need to be pre-functionalised with a reactive leaving group. Where more than one C–C bond can be activated under different conditions, a small library of compounds can be prepared by common starting materials, simplifying synthetic pathways and reducing the time and cost of synthesis.

1.5.1 Synthesis of Natural Products

Dong and co-workers have published many examples where they demonstrate the use of transition metal catalysed C–C activation as a tool in organic synthesis.^{26, 27, 44-51} Their work uses benzocyclobutanones substrates to synthesis a range of products including the synthesis of fused-ring systems⁵⁰ and spirocycles,⁵² (Figure 19) and both motifs are found in bio-active natural products. These transformations are highly chemoselective and it is reported that a variety of functional groups were tolerated including dienes, ketones, enamides, esters, benzyl and vinyl ethers and unprotected tertiary alcohols.

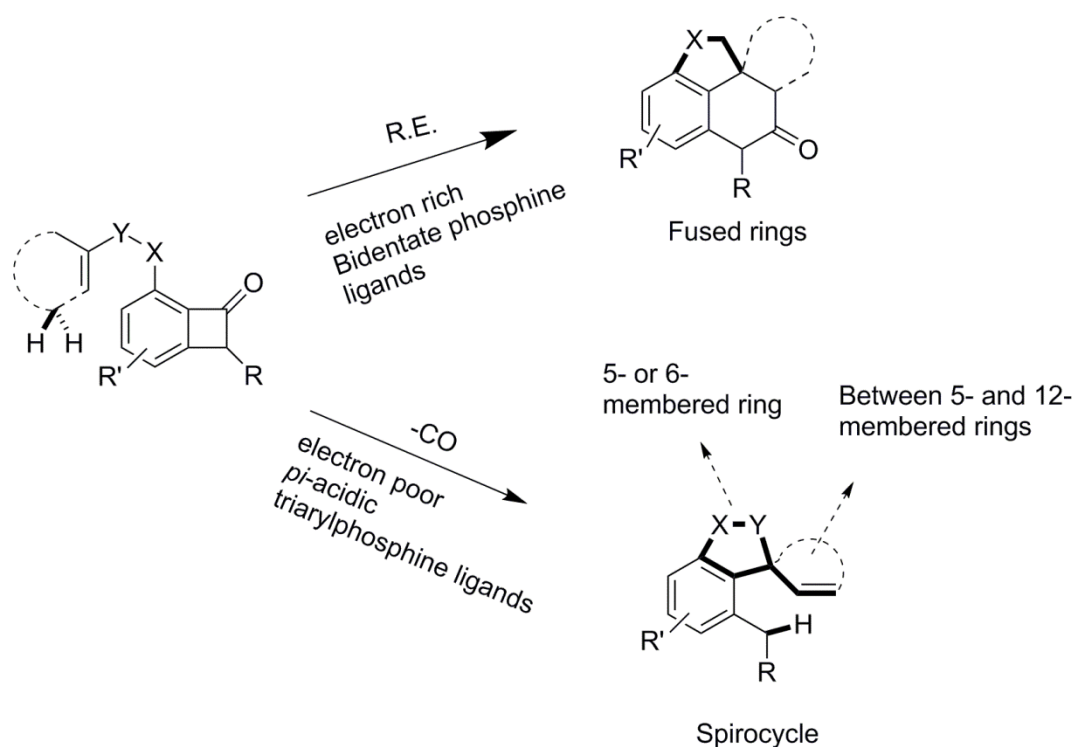


Figure 19: Synthesis of fused rings and spirocycles *via* coupling of alkenes and benzocyclobutanones^{50, 52} The abbreviation, R.E., in the figure above refers to reductive elimination.

For a given starting material the product can be controlled selectively *via* the ligand employed. Dong *et al.* proposed a mechanism (Figure 20), where Rh^I adds oxidatively into the $C_{CO}-C_{\alpha}$ bond, followed by migratory insertion into the alkene to afford a seven-membered rhodacycle. When reductive elimination occurs, a fused-ring system is formed. However, when β -H elimination occurs, followed by decarbonylation, the spirocyclic product is formed. They report that by using bidentate phosphine ligands with a large bite angle the direct reductive elimination route is promoted; addition of a Lewis acid to increase the electrophilicity of the alkene is also required. The decarbonylative route is promoted when monodentate, π -acidic ligands are used, because the ligand exchange is quicker, facilitating the formation of open coordination sites on rhodium which will promote β -H elimination.⁵³ In addition the electron-poor catalyst would coordinate more strongly with the alkene promoting the migratory insertion.

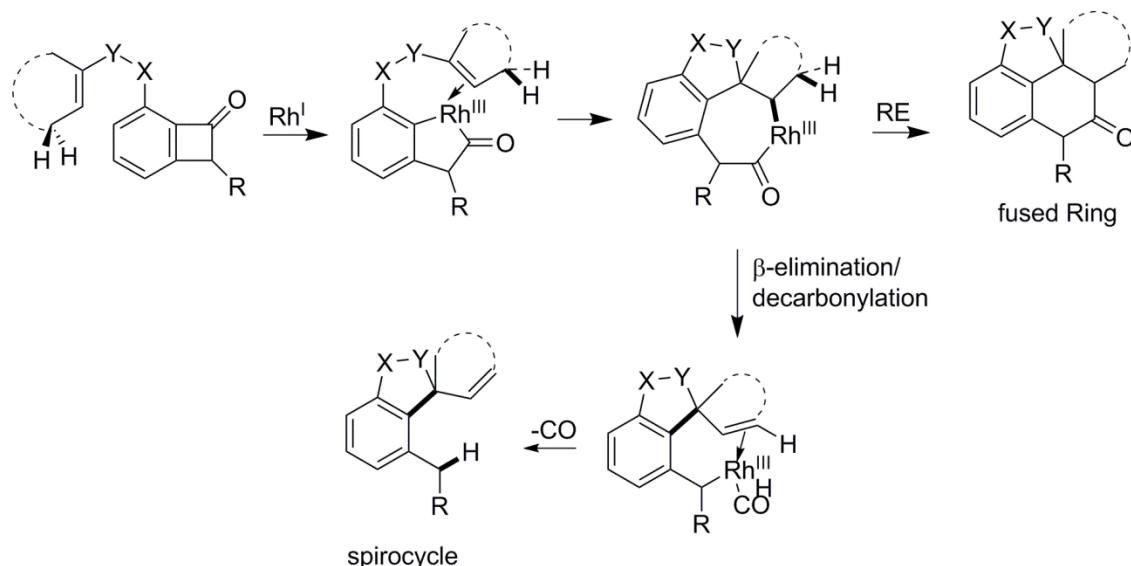


Figure 20: Proposed mechanism for the formation of fused rings or spirocycles⁴⁶

In another example, Dong *et al.* reported the selective synthesis of fused β -naphthols or indenenes *via* direct or decarbonylative alkyne-benzocyclobutanone coupling respectively (Figure 21).⁴⁷ Formation of either the direct or decarbonylative insertion product can be controlled selectively. Thus, when $[\text{RhCl}(\text{COD})]_2$ is combined with 1,3-bis(diphenylphosphino)propane (dppp) and ZnCl_2 in 1,4-dioxane, the direct insertion occurs to afford the β -naphthol product. However, when $[\text{RhCl}(\text{COD})]_2$ is combined with DTBM-SEGPHOS (Figure 22) in xylene, the decarbonylative indene product is formed.⁴⁷

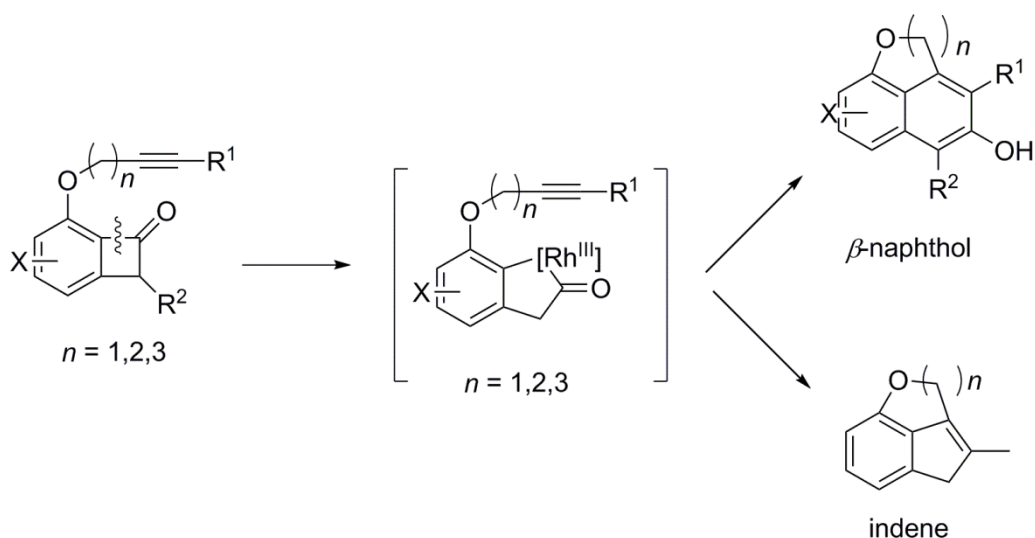


Figure 21: Synthesis of fused β -naphthols or indenenes *via* direct or decarbonylative alkyne-benzocyclobutanone coupling respectively⁴⁷

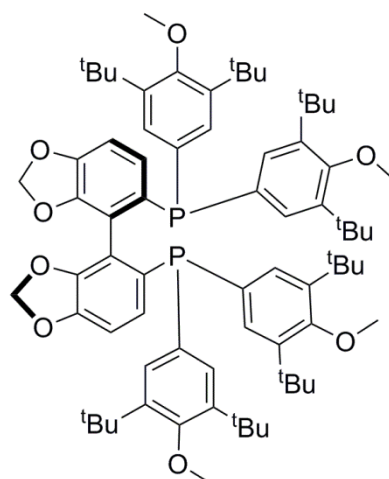


Figure 22: Chemical structure of DTBM-SEGPHOS

1.5.2 Sustainable Chemistry Applications of Decarbonylation

The conversion of inedible biomass to fuels and high-value chemical feedstocks is a very active area of research.⁵⁴⁻⁵⁹ One of the limitations of biofuels is their high oxygen content and so methods to deoxygenate by dehydration, decarboxylation or decarbonylation are attractive targets.^{60,61, 62} An example of this is the decarbonylation and decarboxylation of fatty acid esters using the heterogeneous catalyst, Pt/Al₂O₃.⁶³ It was found that while under an atmosphere of helium, oxygenated products were observed, while when the reactions were carried out under H₂, mostly unsaturated hydrocarbons were obtained.

The reactivity of 5-(hydroxymethyl)furfural (HMF, Figure 23) has been studied as many of the routes from sugars to liquid fuels include furanic intermediates. Furfural is produced from pentose sugars on an industrial scale,^{64 54, 55} and 5-(hydroxymethyl)furfural (HMF) can be obtained from hexoses and cellulose.⁶⁵⁻⁶⁷ The decarbonylation of furfural can be used to produce furan, an intermediate in the production of the widely used solvent, tetrahydrofuran (THF).⁶²

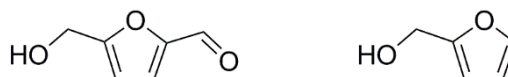


Figure 23: Chemical structure of 5-(hydroxymethyl)furfural (HMF, left) and furfuryl alcohol (FFA, right)

The selective decarbonylation of 5-(hydroxymethyl)furfural to furfuryl alcohol was achieved using an iridium/phosphine catalyst system in the presence of compressed carbon dioxide, 50 bar (Figure 24).⁶⁸ The carbon dioxide had a beneficial effect on both reactivity and selectivity and to investigate this effect, high-pressure NMR experiments were conducted. However, an interaction between the substrate and CO₂ was not observed, and hence the authors excluded the possibility of an *in situ* protection of HMF. In order to improve the green credentials of the process, the petrochemical solvent 1,4-dioxane was replaced with the bio-derived solvents, 2-methyltetrahydrofuran (2-MTHF) and tetrahydrofurfuryl alcohol (THFA); similar activity and selectivity was observed when either of these solvents were used.

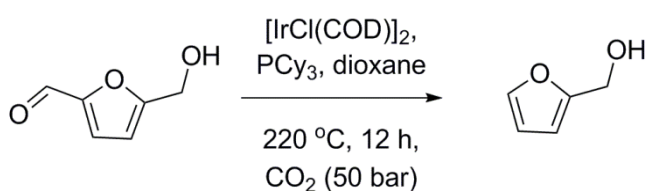


Figure 24: Selective decarbonylation of 5-hydroxymethylfurfuryl alcohol to afford furfuryl alcohol reported by Geilen *et al.*⁶⁸

Mitra *et al.* investigated the decarbonylation, hydrogenation and hydrogenolysis reactions of HMF and reported that the decarbonylation mediated by the heterogeneous catalyst, Pd/C (5 wt% loading) in dioxane afforded furfuryl alcohol (FFA) in 95% conversion within 20 hours.⁶⁹ An extension of this study to a number of biomass-derived furfurals (Figure 25) was successful; and with the exception of the 5-chloromethylfurfural, all the other substrates underwent decarbonylation with conversions in excess of 83%. The authors suggest that the lack of activity of 5-(chloromethyl)furfural may be due to catalyst deactivation by the alkyl chloride. Interestingly, the decarbonylation of 2-(methylformate)furfural proceeded *via* decarbonylation of the aldehyde group rather than the formate with 95% selectivity.

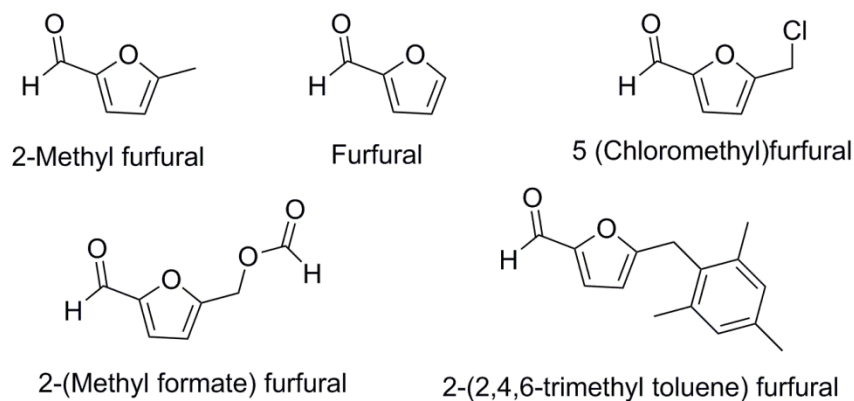


Figure 25: Biomass-derived furfural substrates for decarbonylation⁶⁹

1.6 Reaction Mechanisms Reported for Decarbonylation Reactions

A mechanism was not proposed for the stoichiometric decarbonylation of cyclohexanone reported by Rusina and Vlček and for most reported examples of decarbonylation only speculative mechanisms are proposed.¹ In this section, some of the mechanistic investigations into decarbonylation reactions are summarised.

Most procedures reported are conducted under nitrogen or argon. Xing *et al.* reported the activation of $C_{CO}-C_{\alpha}$ bonds in carbonyl-containing molecules, catalysed by $FeCl_3$ and using molecular oxygen in air as an oxidant.⁷⁰ They report that their methodology can be used chemoselectively on aldehydes, ketones and 1,2-dicarbonyl compounds without over-oxidation (Figure 26). The reactions are conducted in dmsO at 110 °C for 20 hours at atmospheric pressure. While optimising the reaction conditions they found that other iron compounds such as $[FeCl_2]$ and $[Fe(OTf)_3]$ could also catalyse the reaction but with lower efficiency, whereas $[Cu]$ gave similar results to $[FeCl_3]$. Interestingly, one equivalent of water is required for the reaction to proceed and they propose that it plays an essential role in the C–C bond activation as a nucleophile (Figure 27). A radical process seems unlikely as the reactions proceeded well in the presence of the radical scavengers, BHT, TEMPO and 1,1-diphenylethylene. Lee *et al.*⁷¹ reported C–C cleavage reactions of dimethylcyclohexanone using $[Rh^{III}(ttp)(OH)(PPh_3)]$ (ttp = tetratolylporphyrinato dianion) which are promoted by the presence of water. Both of these examples demonstrate C–C bond activation of ketones rather than decarbonylation, but they may provide mechanistic insight to decarbonylation reactions requiring oxygen or water.

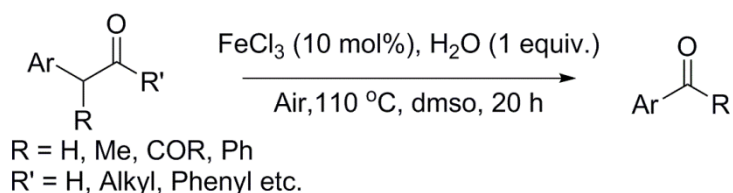


Figure 26: Iron catalysed C–C bond cleavage reported by Xing *et al.*⁷⁰

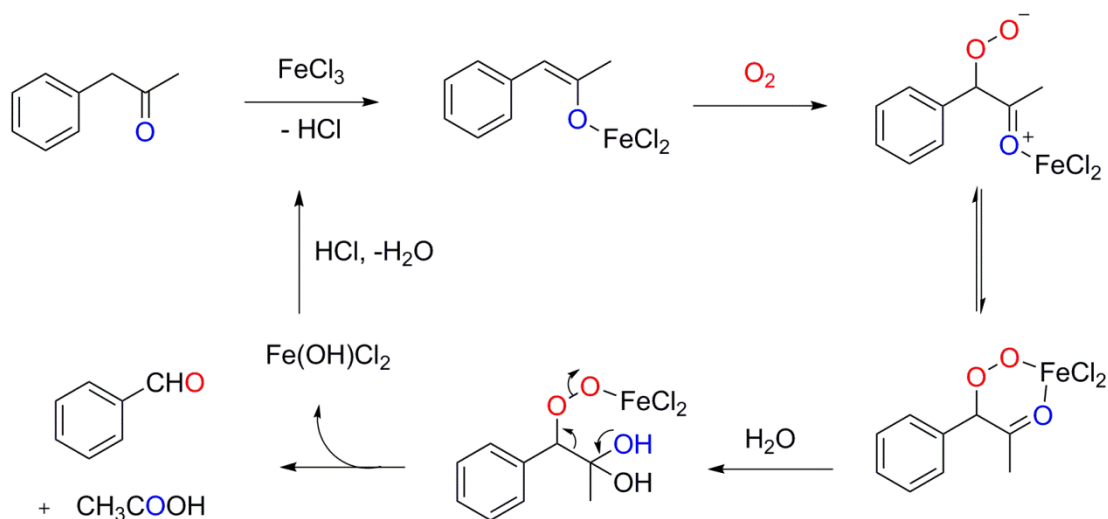


Figure 27: Reaction mechanism proposed by Xing *et al.* for the C–C bond activation of carbonyl compounds.⁷⁰

A mechanism for the decarbonylation of diynones by $[\text{RhCl}(\text{dppf})]_2$ (dppf = 1,1'-bis(diphenylphosphino)ferrocene) was proposed by Dong *et al.* (Figure 28).²² In the first step there is dissociation of a carbon monoxide ligand and coordination of the diynone through both alkyne functional groups. This is followed by oxidative addition of $\text{C}_\alpha\text{--C}_{\text{CO}}$ bond to the rhodium centre and the extrusion of the carbonyl group to form the rhodium carbonyl species. The final step is reductive elimination which affords the coupled 1,3-diyne product.

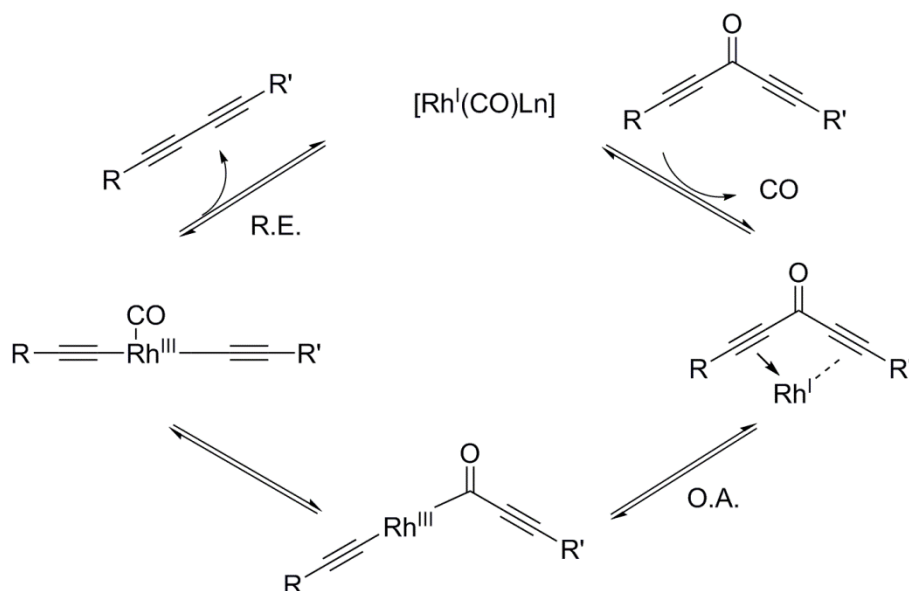


Figure 28: Mechanism for the decarbonylation of diyones proposed by Dong *et al.*²² The abbreviations, O.A. and R.E. which appear in the figure refer to oxidative addition and reductive elimination

Dermenci and co-workers expanded upon the decarbonylation of diyones to include conjugated ynones, and investigated the mechanism of this transformation using density functional theory (DFT) calculations (Figure 29).⁴⁵ They used the functional B3LYP and the basis set LANL2TZ(f) for rhodium and 6-311+G(d,p) for all other elements. Solvation energies in ethylbenzene were determined using a self-consistent reaction field using the universal solvation model (SMD) with radii and non-electrostatic terms.

They propose a mechanism whereby the initial step is substrate coordination to the Rh^I through the alkynyl group, followed by oxidative addition of a C–C bond, extrusion of the carbonyl group and finally reductive elimination to afford the alkyne product. Their DFT calculations indicated that the alkyne-coordinated complex was more stable than the carbonyl-coordinated complex by 30 kJ mol^{-1} . One of the aims of the study was to identify which C–C bond is broken first, $C_{CO}-C_{Ar}$ or $C_{CO}-C_{alkyne}$ and the results suggest that activation of the latter is more energetically favourable. The rate-determining step of the catalytic cycle was identified as the reductive elimination step and the overall activation free energy of the catalytic cycle is 120 kJ mol^{-1} in gas phase, which the authors believe explains the need for high reaction temperatures.

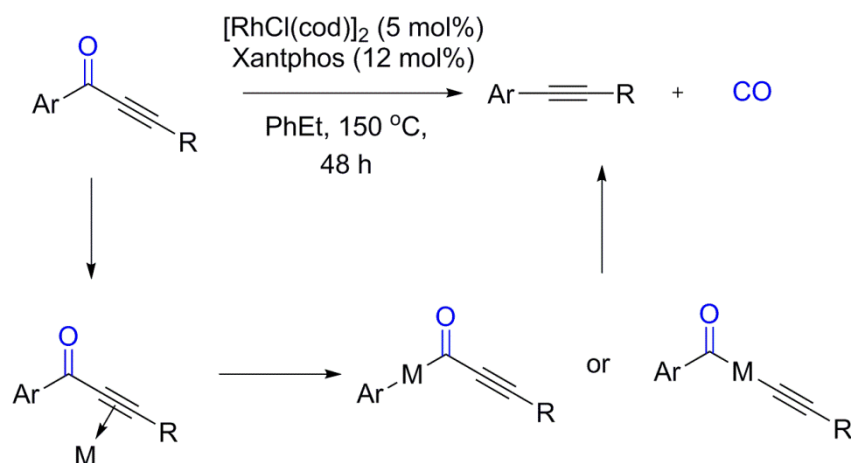


Figure 29: Decarbonylation of conjugated ynones reported by Dermenci *et al.*⁴⁵

The mechanism for the rhodium-catalysed decarbonylation of aldehydes was investigated using Hammett studies and kinetic isotope effects which was complemented by a computational study using DFT calculations.⁷² For both benzaldehyde and phenyl acetaldehyde derivatives, the Hammett plots indicated a build-up of negative charge in the selectivity determining step. The DFT studies suggested that oxidative addition of the C_{CO}-H of the aldehyde occurs quickly and that CO extrusion and reductive elimination are rate limiting. The theoretical kinetic isotope effects based on this mechanism were in agreement with the experimental values for both substrates when extrusion of CO was selected as the rate-determining step. From these combined studies they suggested that the mechanism of decarbonylation proceeds as follows: initially there is concerted coordination of the aldehyde through the oxygen and dissociation of the carbonyl ligand, this is followed by oxidative addition of the C-H bond, carbonyl extrusion and finally reductive elimination (Figure 30).

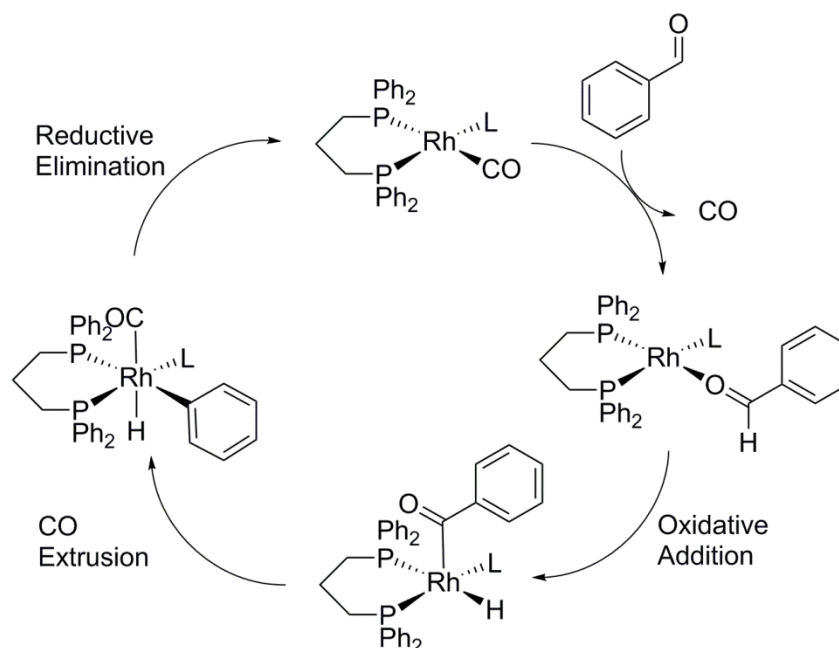


Figure 30: Tentative catalytic cycle proposed by Frisrup *et al.* for the rhodium-catalysed decarbonylation of aldehydes⁷²

1.7 Conclusion

A range of functional groups, including ketones, diketones, aldehydes, carboxylic acids and esters, can undergo decarbonylation reactions. Examples of the decarbonylation of esters are limited and the reactions of ketones are mostly restricted to strained ketones or those with a second functional group capable of coordinating to the metal catalyst. The majority of the procedures reported for the decarbonylation of ketones require high temperature and long reaction times. Homogeneous rhodium complexes are used for the majority of catalytic methods. Both fragmented organic and C–C bond formation products are reported. The mechanisms of the decarbonylation reactions of ketones are poorly understood but the study of the related decarbonylation of aldehydes have suggested that reductive elimination of the organic products is rate limiting. This chapter demonstrates that the chemistry of decarbonylation is an active area of research; current challenges include elucidation of reaction mechanisms, reducing reaction temperatures and expanding upon the current substrate scope.

Chapter Two: Transition Metal Mediated Decarbonylation

2.1 Previous Work

While studying emissive, liquid-crystalline Pt^{II} complexes, Santoro *et al.* observed a surprising oxidation; heating 2,5-bis(4-alkoxyphenyl)pyridine with *cis*-[PtCl₂(S-dmso)₂] under reflux in acetic acid, afforded the dinuclear, acetate-bridged Pt^{III} complex (Figure 31), the structure of which was confirmed by single crystal X-ray diffraction.¹⁰⁸ The reaction proceeded in the absence of oxygen and the oxidant was identified as dmso in the presence of H⁺, following precedent from earlier work by Kukushkin *et al.*⁷³ and Alexandrova *et al.*⁷⁴

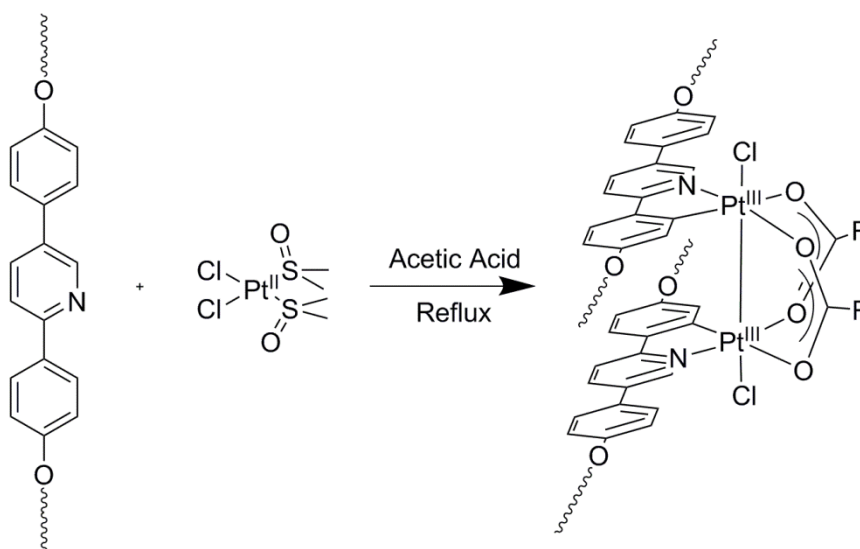


Figure 31: Formation of dinuclear μ -acetato complex *via* oxidation of *cis*-[PtCl₂(S-dmso)₂]

As part of the investigation to confirm the role of acetic acid in the oxidation reaction, the experiment was repeated in 2-ethoxy ethanol. A simpler, model cyclometallating ligand (2-(4-tolyl)pyridine (tolpy)) was used and this time, in the absence of acid, the formation of the dinuclear complex was not observed, instead reduction of coordinated dmso to dms occurred (Figure 32).⁷⁵ It was suspected that the 2-ethoxy ethanol was oxidised by dmso, most likely to 2-ethoxyethanal or 2-ethoxyethanoic acid. However, it was not possible to detect such a product as 2-ethoxyethanol was also used as the solvent and so was in large excess.

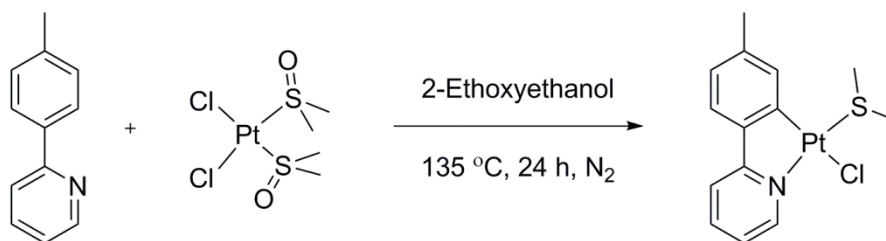


Figure 32: Reduction of platinum-bound dms to dms when *cis*-[PtCl₂(S-dms)₂] was heated to reflux with 2-(4-tolyl)pyridine in 2-ethoxy ethanol.

Cyclohexanone was identified as a potentially 'innocent' solvent in which the stoichiometric reaction of the Pt^{II} complex with 2-ethoxy ethanol could be studied, because it is also polar and has a high boiling point (155.6 °C compared to 135.6 °C for 2-ethoxyethanol). However, in a control reaction when cyclohexanone was heated with 2-(4-tolyl)pyridine and *cis*-[PtCl₂(S-dms)₂], Dey observed the formation of [Pt(tolpy)Cl(CO)] (**4**), which appeared to arise from thermal decarbonylation of the cyclohexanone (Figure 33). As discussed in Chapter One, there are few examples of decarbonylation of unstrained and non-coordinating ketones such as cyclohexanone. Further investigation into this reaction could illuminate new synthetic pathways where the C–C single bond could be considered a reactive functional group. C–C cleavage has been used by other groups to target the synthesis of natural products and pharmaceuticals. Furthermore, Milstein highlighted the importance of transition metal catalysed C–C bond cleavage in the refinement of petroleum.⁷⁶ The cleavage of the C_{CO}–C_α bonds of carbonyl containing molecules may have potential for the processing of oxygen rich bio-derived fuel alternatives.

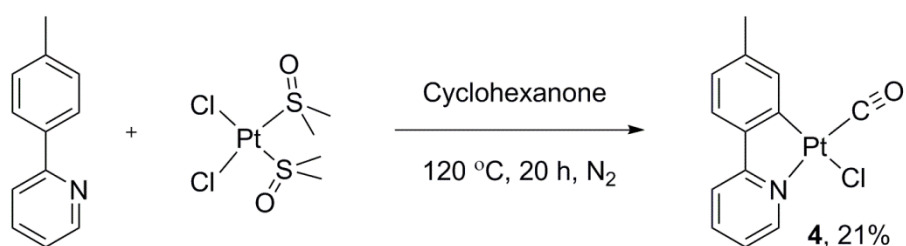


Figure 33: Unexpected decarbonylation of cyclohexanone observed when *cis*-[PtCl₂(S-dms)₂] was heated with 2-(4-tolyl)pyridine in cyclohexanone.

2.1.1 Initial Study into the Decarbonylation Reactions

The initial observation of decarbonylation was investigated further by Torroba,⁷⁷ who evaluated a range of metal complexes for their activity as well as a range of substrates. Of the metal complexes investigated, (Figure 34), cycloplatinated complexes were found to mediate thermal decarbonylation reactions and [Pt(tolpy)Cl(S-dms)] (**3**) was chosen as the most suitable because of its activity and good solubility. Similar results were found using the analogous dimethylsulfide (dms) complex, which suggests that an oxidative pathway involving dms is not involved. Minor decomposition to Pt⁰ was suspected, due to darkening of the solution and the formation of a precipitate, when the dichlorobridged dimer [Pt(tolpy)(μ -Cl)]₂ (**1**) and the platinum phosphine complex, [Pt(tolpy)Cl(PPh₃)] (**9**) were studied. The formation of a carbonyl species when the non-cyclometallated complexes, **14** and **15**, were investigated was not observed. The cyclopalladated complexes, **16** and **17**, suffered extensive decomposition and no evidence of the formation of a palladium carbonyl complex was obtained.

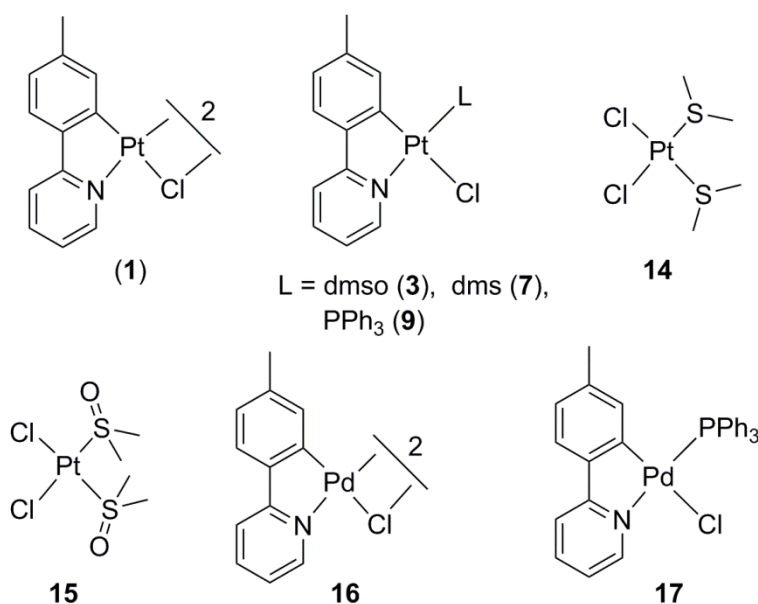


Figure 34: Metal systems investigated for their activity with regards to the decarbonylation of ketones

The range of substrates investigated is shown in figures 35 and 36, and significantly, quantitative conversion to [Pt(tolpy)Cl(CO)] (**4**) was achieved using cyclohexanone, which is non-strained and without a second functional group capable of coordinating to a metal centre. Both cyclic and acyclic substrates were active, with decarbonylation being observed also with 5-methyl hexan-2-one, pentan-2-one and cyclopentanone.

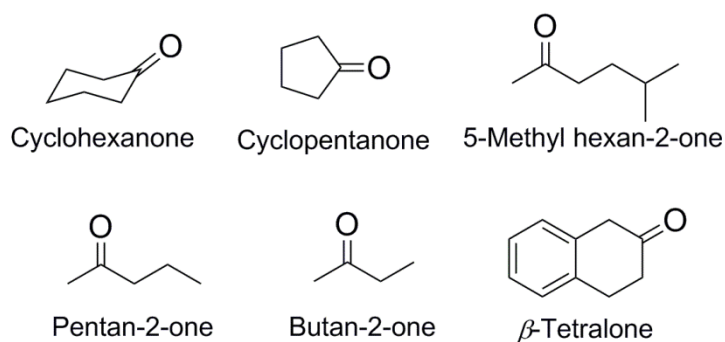


Figure 35: Active substrates for decarbonylation mediated by [Pt(tolpy)Cl(S-dmsO)] (**3**) studied by Torroba⁷⁷

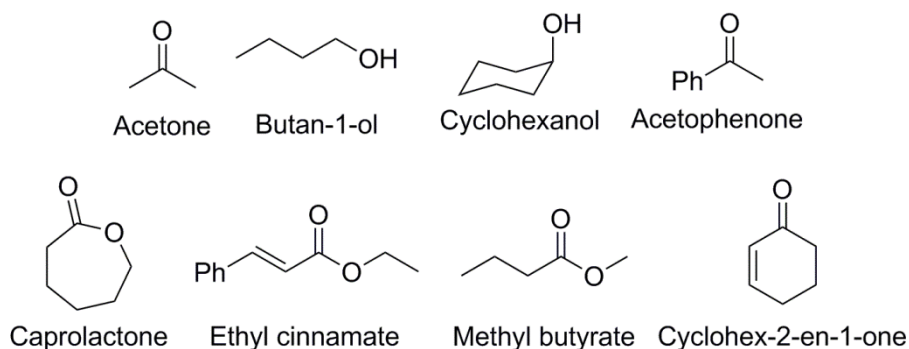


Figure 36: Non-active substrates for decarbonylation mediated by [Pt(tolpy)Cl(S-dmsO)] (**3**) studied by Torroba⁷⁷

A reduced conversion of 60% was observed for butan-2-one, which may be due to the lower reaction temperature of 79 °C (boiling point, 79.6 °C). Lower conversion (50%) was also observed for β -tetralone and no evidence for decarbonylation was observed when acetone or acetophenone were investigated. When cyclohex-2-en-1-one was tested by Torroba, only a small signal for [Pt(tolpy)Cl(CO)] (**4**) was observed by ¹H NMR spectroscopy in a mixture with three other cyclometallated complexes (Figure 37). Extensive decomposition of the platinum complexes was also indicated by the formation of a dark precipitate. The alcohols 1-butanol, cyclohexanol and the esters, methyl butyrate, caprolactone and ethyl cinnamate were also found to be inactive.

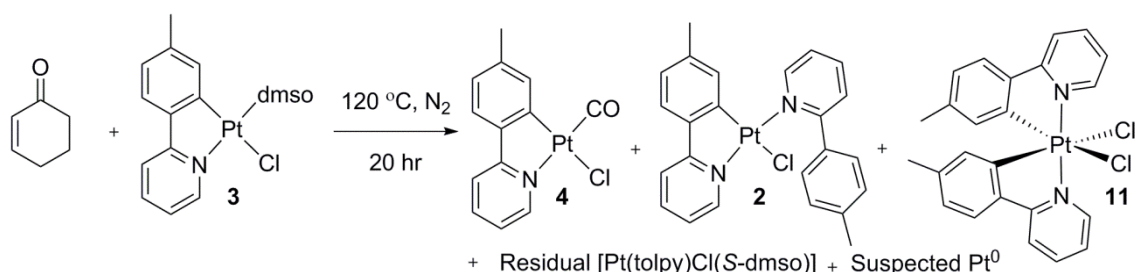


Figure 37: Attempted decarbonylation of cyclohex-2-en-1-one studied by Torroba⁷⁷

2.2 Aims

The first objective of the project is to study systematically and optimise the platinum-mediated decarbonylation of cyclohexanone observed initially by Dey.⁷⁵ *In situ* infrared (IR) and nuclear magnetic resonance (NMR) spectroscopic methods will be used to monitor the progress of the reaction. Identification of the organic products of the decarbonylation of cyclohexanone will be achieved a combination of gas chromatography (GC) and gas chromatography mass spectrometry (GC-MS) analysis.

The next step will be to establish the generality of the reaction by investigating the substrate scope; focusing on ketone-containing compounds. *In situ* IR monitoring can be used to compare the reactivity of different substrates. A family of cyclometallated complexes will be synthesised and their ability to mediate thermal decarbonylation reactions of ketones will be evaluated in order to establish rules on catalyst design. The role of the labile ligand, L in the complexes [Pt(tolpy)Cl(L)] will be investigated. This will include evaluating the possibility for dmsol to act as an oxidant, as described above.

The mechanism of the decarbonylation of cyclohexanone will be investigated; this will be informed by the results of the study described above and will also involve deuterium labelling experiments and *in situ* IR monitoring during the reactions. Identification of the position of deuterium in the hydrocarbon products using ²H NMR spectroscopy and mass spectrometry after selective deuteration at the α -carbons of the substrate ketones should indicate which C–C bonds have been activated. By elucidating the mechanism we hope to gain insight which will lead to the development of decarbonylation reactions which are preparative, predictable and general.

Finally, efforts will be focused towards identifying whether the current reaction is catalytic. Published examples of the decarbonylation of non-strained and non-activated ketones are limited to stoichiometric reactions with the exception of the decarbonylation of aryl ketones such as acetophenone catalysed by bulky cyclopentadienylbis(ethylene)rhodium(I) complexes reported by Daugulis and Brookhart (Chapter One).²³ Should a catalytic system be identified, insights into the reactions will be used to optimise the catalyst design and the reaction conditions.

This chapter will concentrate on the results of the decarbonylation reactions and Chapter Three will be concerned with the discussion of the mechanism.

2.3 The Decarbonylation of Cyclohexanone

The decarbonylation of cyclohexanone mediated by [Pt(tolpy)Cl(S-dmsO)] (**3**) was the focus of the initial study, whose aims were to identify the hydrocarbon reaction products, to isolate and characterise the [Pt(tolpy)Cl(CO)] (**4**) product formed and to establish whether the reaction was a thermal or photochemical process. Formation of complex **4** was confirmed using ^1H and $^{195}\text{Pt}\{^1\text{H}\}$ NMR and IR spectroscopy ($\bar{\nu}(\text{CO}) = 2098 \text{ cm}^{-1}$, $\delta_{\text{H}} \text{CDCl}_3$: 9.46 ppm, dd, $^3J_{\text{HH}} = 6$, $^3J_{\text{HPt}} = 32 \text{ Hz}$, $\delta_{\text{Pt}} -3947 \text{ ppm}$). Initial attempts to reproduce the work of Torroba, summarised in Section 2.1, were unsuccessful and it was found that the decarbonylation reactions required the presence of air to proceed. Although the reactions in the previous work were conducted under an atmosphere of nitrogen, this was not with the rigorous exclusion of oxygen. Thus, when the decarbonylation reaction was attempted under the strict exclusion of oxygen, no conversion to [Pt(tolpy)Cl(CO)] (**4**) was observed but when the reaction was repeated in air quantitative conversion to [Pt(tolpy)Cl(CO)] (**4**) was observed. Partial decomposition of the platinum complexes was also suspected due to the darkening of the reaction solution, formation of precipitates and the observation of the free tolpy ligand by ^1H NMR spectroscopy. For the subsequent studies, standard decarbonylation conditions were defined as follows: a solution of [Pt(tolpy)Cl(S-dmsO)] (**3**) (10 mg, 0.021 mmol) cyclohexanone (1 ml, 9.7 mmol) was heated to 120 °C for 16 hours under an atmosphere of air.

2.3.1 Head-space Analysis Methodology

In order to identify gaseous reaction products, the reaction headspace was analysed by GC and GC-MS; requiring a gas-tight reaction vessels, capable of withstanding a modest increase in pressure. Decarbonylation reactions which were performed for head-space analysis were conducted in a gas-tight Fisher-Porter vessel (Figure 38). Samples were taken at 25 °C using a gas-tight syringe with a Luer lock, which could be directly connected to the pressure vessel and the inlet to the gas sampling valve of the GC instrument.



Figure 38: Photograph of a 10 ml gas-tight Fisher-Porter vessel equipped with a pressure gauge and a Luer lock adapter.

During the course of this research project, five GC instruments were used to analyse the reaction head-space (see Experimental). GC-A was used initially to identify hydrocarbons present in the reaction headspace by comparison to known standards. This instrument was fitted with a hydrocarbon trap for pre-concentration and parallel columns for separating out low molecular weight hydrocarbons and oxygenated species. GC-B was used for routine reaction headspace analysis; it was equipped with two detectors, TCD and FID in series. GC-C, GC-D and GC-E were GC-MS instruments used to confirm the identity of the analytes and determine the isotopic distribution. GC-D was used for the quantitative analysis of butane and GC-E was used to identify methane and carbon monoxide present in the reaction headspace.

2.3.2 Identification of the Hydrocarbon Products

So far the only product of the decarbonylation of cyclohexanone detected was carbon monoxide in the form of $[\text{Pt}(\text{tolpy})\text{Cl}(\text{CO})]$ (**4**), leaving the equivalent of C_5H_{10} unaccounted for. It was suspected therefore, that the other product of decarbonylation would be a C_5 hydrocarbon, either pentene or cyclopentane. Reports from other authors normally report activation of the C–C bonds α to the carbonyl group often followed by the formation of a C–C bond between the β -carbon atoms.^{3,78} In particular, the decarbonylation reactions of fused cyclobutanones and cyclododecanone reported by Murakami led to the formation of ring closed cyclopropane products and cycloundecane respectively (Figure 39).¹⁵

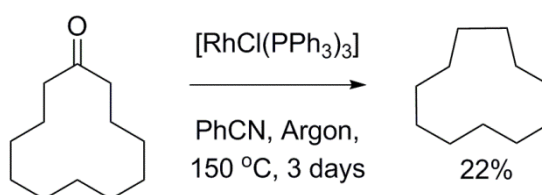


Figure 39: The formation of cycloundecane from the stoichiometric decarbonylation of cyclododecanone reported by Murakami *et al.*¹⁵

In the first instance, the reaction headspace was analysed using the GC analysis (see Experimental). Peak identification was achieved by referencing to a number of certified gas standard mixtures combined with injection of single hydrocarbons (C_2 - C_8). Butane (95%) was found to be the major product of the decarbonylation of cyclohexanone mediated by $[\text{Pt}(\text{tolpy})\text{Cl}(\text{S-dmsO})]$ (**3**). Very small amounts of ethane (0.40% by integration of chromatogram), ethene (0.70%), propane (4.0%), propene (0.02%) and isobutene (0.03%) were also observed. In order to analyse low concentrations of hydrocarbons, the gas samples were passed through a pre-concentration trap prior to GC analysis. Due to inefficient trapping of methane, the peak area recorded was not reliable and underestimated the true concentration of methane. However, methane was estimated to be present in at least similar quantities to butane by comparison to samples of ambient air which contain methane (1900 ppb). The formation of butane as the major hydrocarbon product for the decarbonylation of cyclohexanone was further confirmed by GC-MS analysis of the reaction.

The results described above therefore identified the products of the decarbonylation of cyclohexanone mediated by $[\text{Pt}(\text{tolpy})\text{Cl}(\text{S-dmsO})]$ (**3**) to be butane and methane. Catalytic decarbonylation reactions should also evolve carbon monoxide; however, it was not possible to separate carbon monoxide

from nitrogen and oxygen in air using the GC systems described above. A porous layer open tubular (PLOT) designed to separate permanent gases was used to separate carbon monoxide from oxygen and nitrogen in air, and this was coupled with a mass detector. Using this method, carbon monoxide and methane were observed successfully in the reaction headspace.

The products observed, namely CO, methane and butane require that three C–C bonds, (two C_{CO}–C_α and one C_α–C_β bond) are broken at some stage during the reaction as indicated in (Figure 40). Currently, there are no examples of decarbonylation reactions involving the cleavage of three C–C bonds or cleavage of the C_α–C_β bond reported. The cleavage of the C_α–C_β bond has been reported for Norrish type II photochemical radical reactions for ketones where the γ-hydrogen can be abstracted.⁷⁹ Additionally, when the stoichiometry of the reaction was considered, it was clear that there was an imbalance in hydrogen on the two sides of the reaction. The source of the additional hydrogen atoms and the significance of this to the reaction mechanism is discussed in Chapter Three.



Figure 40: Platinum-catalysed decarbonylation of cyclohexanone to afford methane, carbon monoxide, butane and [Pt(tolpy)Cl(CO)] (**4**) involving the cleavage of three C–C bonds

2.3.3 Analysis of Methane, Carbon Monoxide and Butane Produced by the Decarbonylation of Cyclohexanone

Once the products of the decarbonylation of cyclohexanone were identified as methane, carbon monoxide and butane, the next step was to quantify the amounts formed. The headspace was sampled at 25 °C and the samples taken were analysed using selected ion mode mass-spectrometry in order to improve sensitivity. A calibration curve was used to determine the relative response factors for methane and carbon monoxide by analyses of different concentrations of equimolar amounts of the gases in air. Air was chosen for diluting the gases instead of helium so that the calibrant gas mixtures were as similar as possible to the reaction headspace (for details of the calibration see the Experimental Section). Using this method, carbon monoxide and methane were observed with

retention times of nine and twelve minutes, respectively, demonstrating good resolution of the two permanent gases. A much larger peak for carbon monoxide than methane was observed using the mass spectrometry detector (relative response of CO:Me = 52:1); because carbon monoxide is more readily ionised.

The decarbonylation of cyclohexanone mediated by [Pt(tolpy)Cl(CO)] (**4**) was studied by the method described above. Complex **4** was chosen because the major products would be carbon monoxide, methane and butane, and because for all the other active platinum complexes, the formation of complex **4** was also observed. By comparison to calibration curves, the number of moles of product in the reaction headspace could be quantified and the turnover number calculated.

The quantities of gases calculated by this method are an underestimate as only the components of the reaction headspace are taken into account. Some of the gases produced by decarbonylation of cyclohexanone will have dissolved in the liquid phase to varying extents as the different gases produced will also have different solubilities in cyclohexanone. Furthermore, the calibration of the gases is not absolute, the composition of the headspace will vary with pressure and there will also be variation in ionisation and hence response.

2.4 Identification of Solvent System for the Decarbonylation of Cyclohexanone Mediated by [Pt(tolpy)Cl(S-dmsO)] (3**)**

One drawback when attempting to investigate the mechanism of this reaction using standard decarbonylation conditions is that the substrate, cyclohexanone, also acts as the solvent. This means that currently only ketones that are liquid at the reaction temperature are suitable substrates and makes identification of non-volatile hydrocarbon products more difficult, as their signals will be swamped by those of the ketone starting material when using spectroscopic techniques. Separating and identifying the products from the reactants can be extremely challenging, and therefore, there is a need to identify an 'innocent' solvent that allows the reaction to proceed and in which the substrate can be used in lower concentrations. A suitable solvent system would also allow screening of ketones not available in bulk quantity as might be required if the method were able to be applied synthetically.

There were then three initial criteria for choosing an appropriate solvent. Firstly, the platinum reagent, [Pt(tolpy)Cl(S-dmsO)] (**3**) must be soluble in the chosen solvent. The solvents hexane and xylene were ruled out of the study due to poor solubility of complex **3**. Secondly the solvent must possess a high boiling point in order to avoid increasing the pressure inside the Fisher-Porter vessel (which is required for headspace sampling) close to its safety limit of 10 bar. Finally, the solvent must be inert under the decarbonylation reaction conditions. Ten different solvents were chosen initially, with the list including polar aprotic, polar protic, apolar and coordinating solvents.

2.4.1 Results of the Control Reactions

Control reactions were conducted to establish whether a reaction between the platinum reagent, [Pt(tolpy)Cl(S-dmsO)], and the chosen solvent would occur. The conditions for the control reactions were: [Pt(tolpy)Cl(S-dmsO)] (**3**) was heated to 120 °C for 16 hours in the chosen solvent under an atmosphere of air, without cyclohexanone (observations are summarised in Table 1). Decomposition of [Pt(tolpy)Cl(S-dmsO)] (**3**), to varying extents, was observed when CPME, dichlorobenzene, DCE, dioxane, nitromethane and TCE were used. Darkening of the reaction solutions, deposits of dark grey precipitate, presumably Pt⁰ on the glassware, and the presence of signals corresponding to the free tolpy ligand in the ¹H NMR spectrum were observed.

Table 1: Summary of the results of the solvent control experiments using [Pt(tolpy)Cl(S-dmsO)] (3)

Solvent	Decomposition observed	Reaction with solvent observed	Details
Acetonitrile	No	Yes	Formation of [Pt(tolpy)Cl(NCMe)] (6)
Cyclopentyl methyl ether (CPME)	Yes	Yes	Formation of [Pt(tolpy)Cl(CO)] (4)
Dichlorobenzene	Yes	No	Free tolpy observed in the ¹ H NMR spectrum and small amounts of Pt ⁰ observed.
Dichloroethane (DCE)	Yes	No	Small amounts of Pt ⁰ observed.
1,4-Dioxane	Yes	Yes	Large amounts of Pt ⁰ observed and formation of [Pt(tolpy)Cl(CO)] (4)
Ethyl acetate	No	No	Inert solvent
Nitromethane	Yes	No	Free tolpy observed in the ¹ H NMR spectrum
Tetrachloroethene (TCE)	Yes	No	Small amounts of Pt ⁰ observed.
Tetrahydrofuran (THF)	No	No	Inert solvent.
Toluene	No	No	[Pt(tolpy)Cl(S-dmsO)] not fully soluble

For three of the controls, a reaction between the solvent and the platinum complex was observed. Two of the ether solvents, 1,4-dioxane and CPME, underwent activation and the formation of [Pt(tolpy)Cl(CO)] (**4**) was observed (up to 89% and 15% conversion, respectively, determined by integration of the ^1H NMR spectrum). This suggests that extrusion of the C–O ether group mediated by [Pt(tolpy)Cl(S-dmsO)] (**3**) has occurred. At this point both 1,4-dioxane and CPME were eliminated as potential solvents for decarbonylation, but their reactivity will be discussed in more detail in Section 2.5.4. Interestingly the third ether in the trial, THF, did not undergo such activation. When complex **3** was heated in acetonitrile, ligand exchange between acetonitrile and dmsO was observed to afford [Pt(tolpy)Cl(CH₃CN)] (**6**) (12% by integration of the ^1H NMR spectrum). As acetonitrile is a very labile ligand, it is suspected that complex **6** may also mediate decarbonylation reactions.

2.4.2 Decarbonylation of Cyclohexanone in Different Solvents

The remaining eight solvents were screened for the decarbonylation of cyclohexanone (results summarised in Table 2). The conditions for the solvent trials were: 10 molar equivalents of cyclohexanone w.r.t. [Pt(tolpy)Cl(S-dmsO)] (**3**), heated to 120 °C under an atmosphere of air for 16 hours in a constant volume Fisher-Porter vessel.

Table 2: Summary of the solvent trials for decarbonylation of cyclohexanone

No Conversion	Suitable
Toluene	Acetonitrile
Tetrahydrofuran (THF)	Ethyl acetate
1,2-Dichlorethane (DCE)	Nitromethane
Tetrachloroethylene (TCE)	1,2-Dichlorobenzene

As the hydrocarbon products of the decarbonylation reaction are gases under ambient conditions, the different solvents were compared using the values of conversion from [Pt(tolpy)Cl(S-dmsO)] (**3**) to [Pt(tolpy)Cl(CO)] (**4**). No such was observed when DCE, TCE, toluene or THF were used. Although no reaction took place between complex **3** and DCE or TCE in the solvent control reactions, when decarbonylation of cyclohexanone was attempted in these solvents only the

formation of [Pt(tolpy)Cl(H-tolpy)] (**2**) (4% and 14% conversion for DCE and TCE, respectively) was observed by comparison to the separately synthesised and characterised compound using ^1H and ^{195}Pt NMR spectroscopy (δ_{H} in CDCl_3 H^1 , *ortho* to tolpy nitrogen 9.59 ppm, d, $^3J_{\text{HH}} = 6$ Hz, $^3J_{\text{HPt}} = 36$ Hz, H^9 *ortho* to H-tolpy nitrogen at 9.24 ppm, d, $^3J_{\text{HH}} = 6$ Hz, $^3J_{\text{HPt}} = 40$ Hz, H^8 , *ortho* to tolpy carbanion at 6.01 ppm, s, $^3J_{\text{HPt}} = 48$ Hz, δ_{Pt} in CDCl_3 -3195 ppm). It is suspected that [Pt(tolpy)Cl(Htolpy)] (**2**) is formed *via* reaction with free tolpy released during decomposition of [Pt(tolpy)Cl(S-dmsO)] (**3**). This suggests that although [Pt(tolpy)Cl(S-dmsO)] (**3**) does not readily dissociate in these chlorinated solvents, when cyclohexanone is present the complex is activated and forms [Pt(tolpy)Cl(H-tolpy)] (**2**).

Table 3: Summary of the experimental conditions and results for the solvents in which decarbonylation occurred.

Solvent	Boiling point, °C	No. equiv. cyclohexanone w.r.t [Pt]	T, °C	Residual 3 , % ^a	Conversion to 4 , % ^a
1,2-Dichlorobenzene	180	10	120	86	4
Nitromethane	100	10	120	85	12
Ethyl acetate	77	10	120	90	10
Toluene	110	5	120	97	3
Acetonitrile	82	10	120	36	0

^a Estimated using the integration of H^1 in the ^1H NMR spectrum

The decarbonylation of cyclohexanone was observed when acetonitrile, 1,2-dichlorobenzene, ethyl acetate, toluene or nitromethane were used as the solvent (Table 3). This demonstrates that the decarbonylation reaction can proceed in a range of polar and apolar aprotic solvents. The highest conversion was observed for 1,2-dichlorobenzene and the lowest for ethyl acetate and nitromethane. When acetonitrile was used, greater conversion to complex [Pt(tolpy)Cl(NCMe)] (**6**) was observed. Although the formation of complex **4** was not observed it is suspected that **4** forms by decarbonylation of cyclohexanone and then undergoes conversion to **6**.

Due to the formation of $[\text{Pt}(\text{tolpy})\text{Cl}(\text{NCMe})]$ (**6**), observed when acetonitrile was used as the reaction solvent, the lability of the carbonyl ligand of $[\text{Pt}(\text{tolpy})\text{Cl}(\text{CO})]$ (**4**) was investigated under similar conditions. When heated to 120 °C under an atmosphere of nitrogen for 16 hours, partial ligand substitution was observed to afford the acetonitrile complex with 18% conversion (estimated from integration of the ^1H NMR spectrum). This shows that the $[\text{Pt}(\text{tolpy})\text{Cl}(\text{CH}_3\text{CN})]$ (**6**) formed during the decarbonylation reactions in acetonitrile could be by substitution of either the dmsu or carbon monoxide ligand. The complex formed, $[\text{Pt}(\text{tolpy})\text{Cl}(\text{NCCH}_3)]$ (**6**), is structurally similar to the active decarbonylation agents, **3** and **4**, and may also mediate decarbonylation reactions itself. Evaluating the activity of **6** with regards to mediating decarbonylation reactions has not been possible; this is because of difficulty purifying the complex when synthesised separately from $[\text{Pt}(\text{tolpy})(\mu\text{-Cl})]$ (**1**) due to poor stability of complex **6**.

Results from initial trials showed low conversions to complex **4** when using ten molar equivalents of cyclohexanone. In order to investigate the effect of the stoichiometry of the substrate, cyclohexanone, a selection of the solvents were investigated again using different numbers of equivalents (Table 4). Comparison of these the solvents, 1,2-dichlorobenzene or toluene with acetonitrile is complicated by coordination of acetonitrile. Although, formation of complex **4** is usually the evidence required for decarbonylation, as the number of molar equivalents used increased, so did the conversion to complex **6** observed for the reactions conducted in acetonitrile; this is due to an increase in conversion to complex **4** which undergoes conversion to **6**. Hence, whether acetonitrile, toluene or 1,2-dichlorobenzene was used, the formation of complex **4**, by decarbonylation of cyclohexanone, increased with increasing number of molar equivalents of cyclohexanone used.

Table 4: The effect of varying the number of equivalents of cyclohexanone w.r.t. complex **3** on the decarbonylation of cyclohexanone in acetonitrile, toluene or 1,2-dichlorobenzene.

Solvent	No. Equiv. cyclohexanone	Atmos.	Conversion to 4, or 6, % ^a
CH ₃ CN	10	air	0, 64
CH ₃ CN	5	air	0, 67
CH ₃ CN	3	air	0, 44
CH ₃ CN	2	air	0, 41
CH ₃ CN	1	air	0, 33
CH ₃ CN	1	N ₂	0, 52
Toluene	60	air	29, 0
1,2-Dichlorobenzene	1	air	0, 0
1,2-Dichlorobenzene	10	air	4, 0
1,2-Dichlorobenzene	100	air	81, 0
1,2-Dichlorobenzene	10	N ₂	0, 0

Five solvents have been identified for the decarbonylation of cyclohexanone; 1,2-dichlorobenzene, nitromethane, ethyl acetate, toluene and acetonitrile. However, conversion to [Pt(tolpy)Cl(CO)] by decarbonylation of cyclohexanone in these solvents is low, with conversion between 3 and 29% reported when ten equivalents of cyclohexanone was used. Higher conversion can be achieved when greater excess of cyclohexanone is used but the reactions were very sensitive to the number of molar equivalents of cyclohexanone, with no decarbonylation observed when reactions with only one molar equivalent of cyclohexanone were attempted. These data suggest cyclohexanone may have another role in this reaction, rather than just acting as a substrate and this will be studied further in Chapter Three.

2.5 Substrate Scope

The initial substrate screen conducted by Torroba identified a range of cyclic and acyclic ketones as active substrates for decarbonylation. Reactions within this screen had been conducted under an atmosphere of nitrogen, although not with the complete exclusion of oxygen and water. The previous study also relied on the observation of formation of [Pt(tolpy)Cl(CO)] (**4**) by IR or NMR spectroscopy. This initial study was repeated under optimised conditions in air and conducted in gas-tight Fisher Porter vessels so that the hydrocarbon products could be identified by GC and GC-MS analysis. Additional ketones were screened and successful candidates were identified by observation of [Pt(tolpy)Cl(CO)] (**4**); in most cases the hydrocarbon products were also identified. The substrate screen described below includes cyclic and linear ketones, some with aromatic or electron-withdrawing functional groups as well as other carbonyl-containing molecules such as ethers, esters, aldehydes and diketones.

2.5.1 Cyclic Ketones

In the first instance, three cyclic ketones were studied; cyclopentanone, cycloheptanone and cyclooctanone. When cyclopentanone was investigated, all of [Pt(tolpy)Cl(*S*-dmsO)] (**3**) was consumed and the formation of [Pt(tolpy)Cl(CO)] (**4**) (89% by integration of the ^1H NMR spectrum) and another cyclometallated species, [Pt^{IV}(tolpy)₂Cl₂] (**11**) was observed (11% by integration of the ^1H NMR spectrum). The formation of [Pt^{IV}(tolpy)₂Cl₂] (**11**) had not been observed previously and its identity was confirmed when the complex was synthesised separately and characterised by ^1H NMR spectroscopy (δ_{H} recorded in CDCl₃, H¹ *ortho* to tolpy nitrogen at 10.00 ppm, d, $^3J_{\text{HH}} = 6.0$ Hz, $^3J_{\text{HPt}} = 29$ Hz, H⁸ *ortho* to tolpy carbanion at 5.83 ppm, s, $^3J_{\text{HPt}} = 33$ Hz) and single crystal X-ray diffraction (Figure 41). The role, if any, of this Pt^{IV} species is as yet unknown, and the formation and role of this complex is discussed in more detail in Chapter Three. The headspace of the reaction was analysed by GC, and the major component was found to be propane.

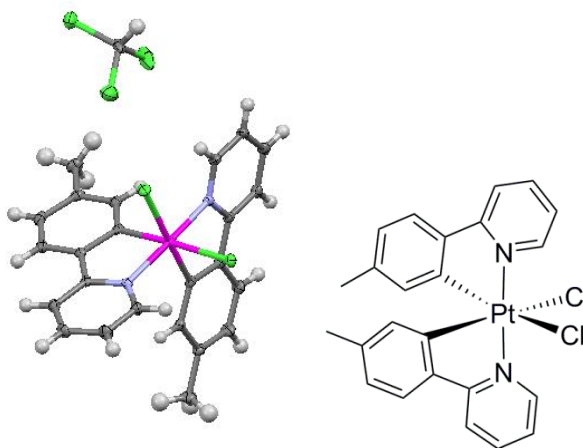


Figure 41: Single crystal X-ray crystal structure for $[\text{Pt}^{\text{IV}}(\text{tolpy})_2\text{Cl}_2]\cdot\text{CHCl}_3$ (**11**), with ellipsoids at 50% probability (left) and the structural formula (right).

When the decarbonylation of cycloheptanone was studied, and in two out of three repeats, quantitative conversion to $[\text{Pt}(\text{tolpy})\text{Cl}(\text{CO})]$ (**4**) was observed by integration of the ^1H NMR spectrum. When non-quantitative conversion was observed, the formation of $[\text{Pt}^{\text{IV}}(\text{tolpy})_2\text{Cl}_2]$ (**11**) was also observed. Initial GC studies of the reaction headspace after the decarbonylation of cycloheptanone by $[\text{Pt}(\text{tolpy})\text{Cl}(\text{S-dms})]$ (**3**) suggested a $\text{C}_5\text{-C}_6$ carbon fragment which elutes between pentane and hexane. When the headspace was analysed by GC-MS, the product was successfully identified cyclohexene (Figure 42).

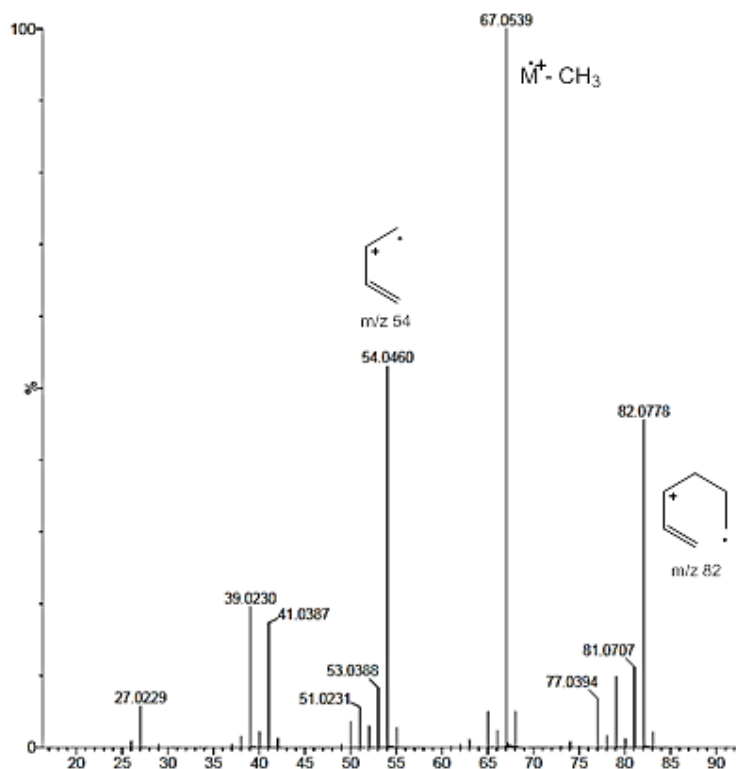


Figure 42: Mass spectrum of cyclohexene which eluted at 11.4 minutes

The equation for the reaction between cycloheptanone and [Pt(tolpy)Cl(S-dmsO)] (**3**) to form cyclohexene and [Pt(tolpy)Cl(CO)] (**4**) is not mass balanced which suggests that one equivalent of dihydrogen is formed and a transfer hydrogenation step is not required for this reaction.

Quantitative conversion to [Pt(tolpy)Cl(CO)] (**4**) was observed when [Pt(tolpy)Cl(S-dmsO)] (**3**) was heated in cyclooctanone. GC-MS analysis of the reaction headspace after the decarbonylation identified cycloheptene as the product of decarbonylation. Just as with cycloheptanone, the equation for the reaction between cyclooctanone and [Pt(tolpy)Cl(S-dmsO)] (**3**) to form cycloheptene and [Pt(tolpy)Cl(CO)] (**4**) is not mass balanced. Decarbonylation could be a useful way to prepare functionalised cycloheptanes which are structural motifs found in bio-active natural products.⁸⁰

Subsequently, molecules based on cyclohexanone but with additional functionality were investigated. Cyclohex-2-en-1-one was studied to see whether the decarbonylation reaction would be promoted by the presence of an alkene group to coordinate to the platinum centre. When cyclohex-2-en-1-one was heated with [Pt(tolpy)Cl(S-dmsO)] (**3**) under standard decarbonylation conditions, the reaction solution remained yellow and there were no visual signs of decomposition of the platinum complexes. Analysis of the headspace showed a very small amount of butane was formed (barely above the baseline and only 5% conversion from [Pt(tolpy)Cl(S-dmsO)] (**3**) to [Pt(tolpy)Cl(CO)] (**4**) was estimated from analysis of the ¹H NMR spectrum (Figure 43). The much lower reactivity of cyclohex-2-en-1-one compared to cyclohexanone suggests that the presence of an alkene functional group inhibits decarbonylation. Interestingly, under these conditions the formation of [Pt^{IV}(tolpy)₂Cl₂] (**11**) or [Pt(tolpy)Cl(H-tolpy)] (**2**) was not observed but the formation of the dimer, complex 1, was observed (8%, δ_{H} recorded in CDCl₃, H¹ *ortho* to pyridyl nitrogen at 8.88 ppm, ³J_{HH} = 5.6 Hz, ³J_{HPt} = 45 Hz).

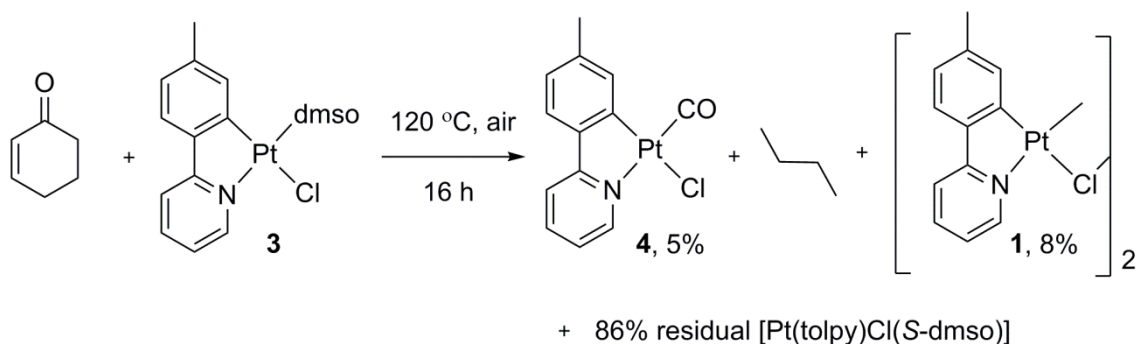


Figure 43: Study of the decarbonylation of cyclohex-2-en-1-one mediated by [Pt(tolpy)Cl(S-dms)] (**3**)

1,2-Cyclohexadione was also investigated; the second carbonyl group should withdraw electron density from the $C_{CO}-C_{CO}$ bond, weakening it and increasing its reactivity. It is also possible that both carbonyl groups may undergo decarbonylation. Complete conversion to [Pt(tolpy)Cl(CO)] (**4**) was observed when 1,2-cyclohexadione was heated with [Pt(tolpy)Cl(S-dms)] (**3**) to 120 °C for 16 hours. After the reaction the headspace was analysed by GC, where the four major components observed were hexane, cyclohexene, dimethylsulfide (dms) and benzene after comparison to reference gas samples. The formation of these hydrocarbons was surprising as they could not be accounted for simply by extrusion of the carbonyl group to afford complex **4**. The formation of dms can be explained by reduction of the free ligand after decomposition of the platinum complexes and it is known that dms can undergo thermal decomposition to afford dms.⁸¹ The formation of hexane, cyclohexene and benzene suggests a competing reduction of the carbonyl group, followed by dehydrogenation, has occurred. A relatively small amount of butane was also observed which is likely to be the product of decarbonylation of 1,2-cyclohexadione. To act as a control, neat 1,2-cyclohexadione was heated in a sealed Fisher-Porter vessel on its own and the headspace analysed by GC; again, butane, cyclohexadiene and benzene were observed but in much smaller amounts. This result demonstrates that 1,2-cyclohexadione can undergo decarbonylation thermally in the absence of a transition metal catalyst.

2.5.2 Linear Ketones

The linear ketones, 2-pentanone, 2-hexanone and 2-heptanone, were analysed for their activity as substrates for decarbonylation. When the decarbonylation of 2-pentanone was conducted under a constant volume in air, 87% conversion to complex **4** (by integration of the 1H NMR spectrum) was achieved after 16 hours. No obvious signs of decomposition of the platinum complexes were observed between 0-10 hours, but after heating for 16 hours a dark precipitate, suspected

to be Pt^0 , could be seen visibly, and free tolpy ligand were observed by ^1H NMR spectroscopy. Less than 1% conversion to complex **4** was observed when 2-hexanone was studied and 2-heptanone was found not to undergo decarbonylation under these conditions. In both cases the formation of a small amount of $[\text{Pt}(\text{tolpy})(\mu\text{-Cl})]_2$ (**1**) was observed (for 2-hexanone 0.5% and for 2-heptanone 24% by integration of the ^1H NMR spectrum).

Acetone is a non-activated linear ketone without the stabilisation of the enol tautomer. Although there are examples of metal activation of acetone to afford transition metal keto complexes by C–H activation,⁸²⁻⁸⁴ Celenligil-Cetin *et al.* alone have reported decarbonylation of acetone (Figure 44).⁸⁵ They use the ruthenium complex, $[\text{RuH}(\text{H}_2)(\text{PNP})]$, ligated by a pincer bis(*o*-phosphinoaryl)amine (PNP) ligand and the reaction is driven thermodynamically by the formation of methane. Hartwig *et al.* previously reported cleavage of one C–C bond in acetone at 45 °C by a ruthenium benzyne complex to yield a cyclometallated enolate complex.⁸⁶

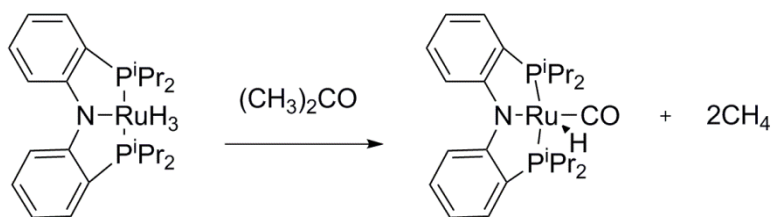


Figure 44: Decarbonylation of acetone reported by Celenligil *et al.*⁸⁵

The first attempts to decarbonylate acetone, at reflux under an atmosphere of air, were not encouraging and after one week, only 1% conversion to complex **4** was observed by ^1H NMR spectroscopy. The reaction was then repeated in a sealed reaction vessel for 16 hours, in order to promote the reaction by heating to 120 °C, beyond the boiling point of acetone, generating 4 bar pressure. Again, only low conversions, between 1 and 4%, to complex **4** were observed.

2.5.3 Ketones Substituted in the α -Position

The effect of substitution at the α -position relative to the carbonyl was investigated using a range of ketones with and without protons in the α -position. First α - and β -tetralone were investigated; these are both comprised of a cyclohexanone group fused to an aromatic ring (Figure 45). These substrates also allowed for investigation into whether substitution at the α -position, as for α -tetralone, affected a substrate's ability to undergo decarbonylation.

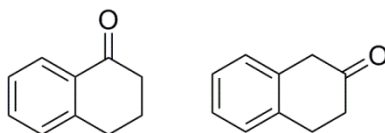


Figure 45: Chemical structures of α - (left) and β -tetralone (right)

Compared to cyclohexanone, lower conversion of [Pt(tolpy)Cl(S-dmsO)] (**3**) into [Pt(tolpy)Cl(CO)] (**4**) was observed when either α - (29%) or β -tetralone (50%) were investigated. The observation of dark precipitates suggested that decomposition of the platinum complexes occurred for both substrates. When α -tetralone was heated with [Pt(tolpy)Cl(S-dmsO)] (**3**) for 16 hours the formation of three cyclometallated species were observed by ^1H NMR spectroscopy; the relative composition of the mixture was made up of [Pt(tolpy)Cl(S-dmsO)] (**3**) (56%), [Pt(tolpy)Cl(CO)] (**4**) (29%) and [Pt^{IV}(tolpy)₂Cl₂] (**11**) (15%). When the reaction time was extended to 20 hours, greater conversion to complex **4** was observed and the amount of **11** unchanged within error; [Pt(tolpy)Cl(S-dmsO)] (**3**) (16%), [Pt(tolpy)Cl(CO)] (**4**) (71%) and [Pt^{IV}(tolpy)₂Cl₂] (**11**) (13%). The lower conversion observed for α -tetralone may be due to the increased difficulty of metal insertion into the C_{CO}-C_{Ar} bond. In the mechanistic study conducted by Dermenci *et al.* they reported that rhodium insertion into the C_{CO}-C_{Ar} bond is very energetically unfavourable.⁴⁵

2-Fluorocyclohexanone, which has a strongly electron-withdrawing group adjacent to the carbonyl, was studied, and cyclohexene was observed as the major component of the reaction headspace by GC-MS. However, the entire vessel contents had been transformed from a pale yellow liquid to a black solid. The reduction of 2-fluorocyclohexanone to 2-fluorocyclohexanol has been reported upon heating over cinchonidine- or methoxycinchonidine-modified Pt/Al₂O₃.⁸⁷ The 2-fluorocyclohexanol formed could then eliminate hypofluorous acid (OHF) to afford cyclohexene, which was observed by mass spectrometry. The gas-phase photolysis of 2-fluorocyclohexanone has also been reported and causes the formation of pentenes and cyclopentane.⁸⁸ The identity of the black solid obtained is unknown but it was soluble in chloroform. The fluorine signal for 2-fluorocyclohexanone (-188.14 ppm, d, $^2J_{\text{HF}} = 51$ Hz) has been replaced with a new signal (-152.65 ppm, d, $J_{\text{HF}} = 19$ Hz). The smaller coupling observed between the fluorine and the proton would suggest that this is a three bond coupling rather than a two bond coupling, suggesting that the α -proton has been removed. This indicates that all of the 2-fluorocyclohexanone has been consumed. The black solid was also studied by elemental analysis, which indicated that the solid is a substituted hydrocarbon or a mixture of substituted hydrocarbons.

Acetophenone and propiophenone both have a phenyl substituent on the α -carbon to the carbonyl group. When these substrates were investigated under standard decarbonylation conditions they were found to be inactive and no evidence for decarbonylation was observed with either. It was thought that the lack of reactivity of acetophenone and propiophenone may be due to the inability to form a stable enol tautomer or the close proximity of the aromatic ring to the carbonyl group (Table 5). However, the identification of α -tetralone as an active substrate demonstrates that ketones with adjacent aromatic substituents can still undergo decarbonylation. Buteriphenone was investigated under the same conditions and, again, no evidence was found for the formation of [Pt(tolpy)Cl(CO)] (**4**) by ^1H NMR spectroscopy, however, the formation of [Pt^{IV}(tolpy)₂Cl₂] (**11**) (9.99 ppm, dd, $^3J_{\text{HPt}} = 29$ Hz) was observed.

Table 5: Data for the percentage of the enol form present in the pure liquid of a selection of ketones.⁸⁹

Carbonyl	% Enol in Neat Liquid
Acetone	0.00025
2-Butanone	0.012
2-Pentanone	0.0086
3-Pentanone	0.067
Acetophenone	0.035
Buteriphenone	0.010

When dicyclohexylketone was investigated under standard decarbonylation conditions, 58% conversion to **4** was observed, as well as the formation of 20% [Pt(tolpy)(μ -Cl)]₂ (**1**). Finally, benzophenone which has no α -hydrogen atoms was investigated; this time five cycloplatinated species were observed by ^1H NMR spectroscopy; [Pt^{IV}(tolpy)₂Cl₂] (**11**, 18%), [Pt(tolpy)Cl(S-dmso)] (**3**, 12%), [Pt(tolpy)Cl(CO)] (**4**, 9%), [Pt(tolpy)Cl(H-tolpy)] (**2**, 41%) and [Pt(tolpy)(μ -Cl)]₂ (**1**, 20%). The formation of a small amount of [Pt(tolpy)Cl(CO)] (**4**) suggests that some decarbonylation did take place. This demonstrates that decarbonylation can occur in the absence of protons on the α -carbon atoms but it appears to be inhibited, at least for these substrates.

2.5.4 Non-ketone Containing Substrates: Ethers, Ester, Aldehydes, Carboxylic Acids and Alcohols

Other substrates were investigated in order to determine whether other carbonyl groups, namely aldehydes, carboxylic acids and esters, could undergo decarbonylation under these conditions. Ethers were also investigated after a reaction between [Pt(tolpy)Cl(S-dmsO)] (**3**) and either 1,4-dioxane or cyclopentylmethylether (CPME) was observed during the solvent study (Section 2.4).

Aldehydes

Both of the aldehydes studied, pentanal and hexanal, were found to undergo decarbonylation. Using the normal decarbonylation conditions, specifically the reaction temperature of 120 °C, it was not possible to calculate the conversion from [Pt(tolpy)Cl(S-dmsO)] (**3**) to [Pt(tolpy)Cl(CO)] (**4**) for the decarbonylation of pentanal because of extensive decomposition of the platinum complexes, but the formation of butane was observed by GC analysis of the reaction headspace. The decarbonylation of pentanal was repeated at room temperature and the formation of butane by decarbonylation and partial decomposition of the platinum complexes was observed. Conversion to [Pt(tolpy)Cl(CO)] (**4**) was estimated to be 28%. Most of the reported decarbonylation procedures require high temperatures in excess of 100 °C. Previously, room temperature decarbonylation of primary aldehydes was achieved using [Rh(PPh₃)₃Cl] (2.5 mol%), with stoichiometric amounts of diphenylphosphoryl azide.⁹⁰

When hexanal was studied, quantitative conversion from [Pt(tolpy)Cl(S-dmsO)] (**3**) to [Pt(tolpy)Cl(CO)] (**4**) was observed under standard decarbonylation conditions and the hydrocarbon product was identified as cyclopentane by GC analysis. The decarbonylation of aldehydes mediated by transition metal complexes is reasonably well established.^{36, 91-94} However, there are no previous examples of the formation of cyclopentane *via* decarbonylation of hexanal. The formation of this product suggests that a C_{CO}-C_α bond cleavage, a C_{CO}-H bond cleavage and one C-C bond formation have taken place.

Esters

The cyclic C₆ ester caprolactone was chosen as it has a ring size similar to cyclohexanone. Caprolactone was studied previously by Torroba and found to be inactive when heated to reflux with [Pt(tolpy)Cl(S-dmsO)] (**3**) in toluene under an

atmosphere of nitrogen. When the reactivity of this substrate was reinvestigated under an atmosphere of air using the neat substrate, formation of a small amount of [Pt(tolpy)Cl(CO)] (**4**, 4%) was observed. Although the conversion is very small, it demonstrates that it is possible for this substrate to undergo decarbonylation. Residual **3** made up the majority of the cyclometallated complexes observed by ^1H NMR spectroscopy (19% [Pt(tolpy)($\mu\text{-Cl}$)]₂ (**1**), 7% [Pt(tolpy)Cl(H-tolpy)] (**2**), 63% [Pt(tolpy)Cl(S-dmsO)] (**3**), 7% [Pt^{IV}(tolpy)₂Cl₂] (**11**)).

Ethers

Activation of ethers is attractive for both sustainable chemistry, with regards to the deoxygenation of biomass-derived ethers, and synthetic applications such as the synthesis of allylic ether products which are important structural motifs in some bioactive molecules.⁹⁵⁻⁹⁷ Acyclic ethers can undergo deoxygenation by C–O cleavage,⁹⁸ but cyclic ethers require both C–O and C–C bond cleavages to occur. There are currently no reported examples of (CO) extrusion from cyclic ethers as was observed when 1,4-dioxane was heated with [Pt(tolpy)Cl(S-dmsO)]. There are examples of C–O activation,^{97, 99-101} but very few describing C–C bond activation.^{102, 103} Gao *et al.* reported the chemo- and regioselective hydrogenolysis of the C–O bonds in diaryl ethers using heterogeneous nickel particles supported on activated carbon.¹⁰⁴ The catalyst is very stable thermally and can catalyse bond cleavage in highly substituted ethers similar to those found in lignin. The cleavage of C–O, C–C and C \equiv C bonds in acyclic alkynyl ethers has been achieved using gold catalysis and molecular oxygen.¹⁰²

Formation of complex **4** was observed by ^1H and ^{195}Pt NMR and IR spectroscopy ($\bar{\nu}(\text{CO}) = 2093\text{ cm}^{-1}$, $\delta_{\text{H}} 9.41\text{ ppm}$, dd, $^3J_{\text{HH}} = 6$, $^4J_{\text{HH}} = 0.8\text{ Hz}$, $^3J_{\text{HPt}} = 32\text{ Hz}$, $\delta_{\text{Pt}} -3947\text{ ppm}$) when complex **3** was heated under standard decarbonylation conditions in 1,4-dioxane. As no other species was present in the reaction it was suspected that 1,4-dioxane was the source of the carbon and oxygen atoms; the loss of CO would involve at least one C–C and one C–O bond activation. To the best of our knowledge this is the first example of C–C bond activation of a cyclic ether. Due to the significant increase in pressure during the reaction it was not possible to use gas-tight Fisher-Porter vessels to trap the hydrocarbon products. Instead a round-bottom flask fitted with an empty balloon was used to conduct the reaction; when the headspace was analysed using GC-MS both carbon monoxide and methane were observed. Taking the relative responses of methane and carbon monoxide into account the ratio between the products was

3:1 in favour of carbon monoxide. Further analysis is required to investigate whether higher molecular weight hydrocarbons are also formed. The formation of a C₂ fragment, ethane or ethene could also occur but it is not possible to observe such a species using the GC systems described here.

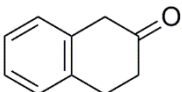
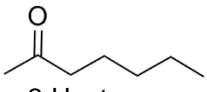
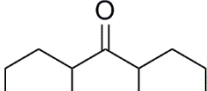
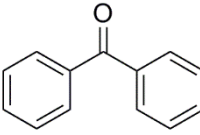
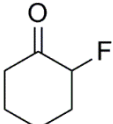
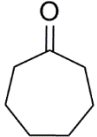
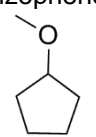
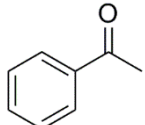
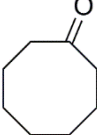
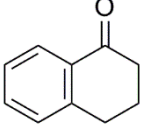
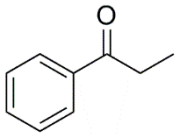
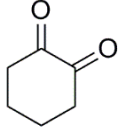
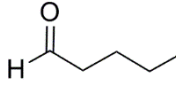
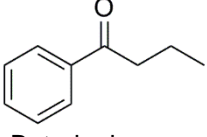
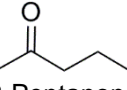
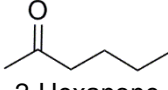
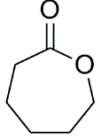
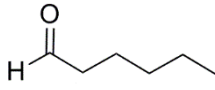
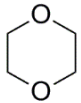
It is well known that ethers can undergo auto-oxidation in the presence of light, air or a metal to form peroxides.¹⁰⁵ Experiments were conducted where 1,4-dioxane and a solution of [Pt(tolpy)Cl(*S*-dmsO)] (**3**) in 1,4-dioxane were heated in separate pressure tubes to 120 °C for 16 hours. The peroxide content at the start and end of both experiments was found to be below 1 ppm, indicating that a long lived peroxide intermediate is not involved.

When CPME was investigated, extensive decomposition to Pt(0) was observed and a sharp band in the IR spectrum at 2091 cm⁻¹ consistent with complex **4** was also found. This reaction was repeated and samples were taken after 1, 2 and 3 hours, the solvent removed and the residue dissolved in chloroform and analysed by ¹H NMR. Formation of the platinum carbonyl complex **4** was observed, with 15% conversion after 3 hours estimated by ¹H NMR spectroscopy (1 hour: 2% **4**, 2 hours: 9% **4**)

2.5.5 Summary of the Results from the Substrate Scope Experiments

Different ketones have been investigated, and from the results some tentative insights about the substrate scope have been gained (Table 6). In this context, high activity denotes a conversion to complex **4** above 80%, medium activity is between 40 and 80% conversion and low activity is below 40%. Poorer conversion was observed where the carbonyl is proximal (or adjacent) to an unsaturated system compared to structurally similar substrates without. This may be due to a competing interaction between the unsaturated functional group, be it alkenyl or aryl, and the platinum complex or due to increased difficulty in breaking a C–C_{Ar} bond. The ketones with the carbonyl group in the 2-position of the alkyl backbone were either found not to be active, or had very low activity towards decarbonylation. This may be due to less stabilisation of the enol tautomer in 2-ketones as shown in Table 5.

Table 6: Summary of the activity of different substrates

Highly Active Substrates ^a	Medium Activity Substrates ^b	Low Activity Substrates ^c	Inactive Substrates
 Cyclopentanone	 β -Tetralone	 Cyclohex-2-ene-1-one	 2-Heptanone
 Cyclohexanone	 Di-cyclohexyl ketone	 Benzophenone	 2-Fluoro cyclohexanone
 Cycloheptanone		 CPME	 Acetophenone
 Cyclooctanone		 α -Tetralone	 Propiophenone
 1,2-Cyclohexadione		 Pentanal ^d	 Buteriophenone
 2-Pentanone		 2-Hexanone	 Caprolactone
 Hexanal		 Acetone	
 1,4-Dioxane			

^a >80% conversion to [Pt(tolpy)Cl(CO)] (**4**) estimated from integration of the ¹H NMR spectra

^b Between 40 and 80% conversion to [Pt(tolpy)Cl(CO)] (**4**) estimated from integration of the ¹H NMR spectra

^c <40% conversion to [Pt(tolpy)Cl(CO)] (**4**) estimated from integration of the ¹H NMR spectra

^d Conversion recorded for the reaction conducted at 20 °C, extensive decomposition observed under normal decarbonylation conditions *ie.* 120 °C, suspected highly active substrate.

Decarbonylation mediated by [Pt(tolpy)Cl(S-dmsO)] (**3**) has been observed for cyclic and acyclic ketones and the hydrocarbon products have been identified for the majority of the examples (Table 7). Different patterns of hydrocarbon products were observed for different substrates. Cyclopentanone underwent decarbonylation in a similar way to cyclohexanone to afford propane and methane. For these two ketones the hydrocarbon products indicate that three C–C cleavages have taken place. The additional cleavage of a C_β–C_{alkyl} bond is more common among the radical C–C cleavage reactions such as photochemical Norrish type I reactions.¹⁰⁶ The products observed for cycloheptanone and cyclooctanone differed from the expected acyclic products of pentane and hexane respectively; here the cyclised, C–C bond formation products cyclohexene and cycloheptene respectively were observed. This may suggest nature of the products formed depends on the size of the substrate.

The aldehydes observed both readily underwent decarbonylation with the reaction of pentanal even proceeding at room temperature. These substrates should be more reactive than their keto counterparts due to the acidity of the aldehyde proton. The decarbonylation of hexanal leads to the ring closed product, cyclopentane. Cyclopentanes are ubiquitous in nature and they were listed in the top 20 most frequently used ring systems for small molecule drugs listed in the Food and Drug Administration (FDA) orange book.¹⁰⁷

Table 7: Summary of the hydrocarbon products formed and comparison of the conversion to [Pt(tolpy)Cl(CO)] (**4**) when the substrates were heated with [Pt(tolpy)Cl(S-dmso)] (**3**) under standard decarbonylation conditions

Substrate	HC Product Identified	% Conversion to 4 ^a
Cyclopentanone	Propane	89
Cyclohexanone	Butane (88%) and methane (12%) ^b	100
Cycloheptanone	Cyclohexene	100
Cyclooctanone	Cycloheptene	100
Cyclohex-2-ene-1-one	Butane	5
1,2-Cyclohexadione	Butane	100
Pentanal	Butane	Extensive decomposition
Hexanal	Cyclopentane	100
1,4-Dioxane	Methane	89

^a Estimated using the relative integration of H¹ (*ortho* to tolpy nitrogen) in the ¹H NMR spectra.

^b Determined using GC-MS (GC-D and GC-E) analysis and comparison to standard samples.

2.6 The Activity of Different Metal Catalysts

2.6.1 Variation of Ligand, L, for the Family of Platinum Complexes, [Pt(tolpy)Cl(L)]

Following the initial work by Torroba described in Section 2.1, a range of metal complexes was investigated under aerobic conditions in order to optimise the reaction and gain insight into the mechanism. Specifically, the conversion to [Pt(tolpy)Cl(CO)] (**4**) was recorded using ¹H NMR spectroscopic analysis and the hydrocarbon products were determined and quantified by GC and GC-MS analysis of the reaction headspace.

Investigating the Role of the dmsO Ligand

Quantitative conversion to $[\text{Pt}(\text{tolpy})\text{Cl}(\text{CO})]$ (**4**) by decarbonylation of cyclohexanone has been observed when $[\text{Pt}(\text{tolpy})\text{Cl}(\text{S-dmsO})]$ (**3**) was used to mediate the reaction. It is known that in the presence of both an acid and a platinum(II) complex, it is possible for dmsO to act as an oxidant.^{73, 74, 108} There are many examples of the use of sulfoxides to promote C–H activation,^{109, 110} either as an internal directing group facilitating coordination to the catalyst,¹¹¹⁻¹¹⁴ or as a ligand of the catalyst.¹¹⁵⁻¹¹⁸

Additionally, $[\text{Pd}(\text{dmsO})_2(\text{TFA})_2]$ (where TFA = trifluoroacetic acid) has been reported as an effective catalyst system for oxidation reactions using molecular O_2 as the oxidant, including the dehydrogenation of cyclohexanone to cyclohex-2-en-1-one.¹¹⁹ Therefore the activity of the related complex, $[\text{Pt}(\text{tolpy})\text{Cl}(\text{dms})]$ (**7**), was investigated in order to evaluate whether the coordinated dmsO ligand has an additional role, such as taking part in a redox process, in addition to being a leaving group.

When this reaction was carried out with $[\text{Pt}(\text{tolpy})\text{Cl}(\text{dms})]$ (**7**) under standard decarbonylation conditions, quantitative conversion to $[\text{Pt}(\text{tolpy})\text{Cl}(\text{CO})]$ (**4**) was observed. The major products observed by GC and GC-MS analysis of the reaction headspace (method described in Section 2.3.1) were *n*-butane, methane and carbon monoxide. This confirms that $[\text{Pt}(\text{tolpy})\text{Cl}(\text{dms})]$ (**7**) mediates the decarbonylation of cyclohexanone and affords the same hydrocarbon products as when complex **3** was used. From these results, a redox pathway involving dmsO can be ruled out of the decarbonylation mechanism.

Investigating the Activity of $[\text{Pt}(\text{tolpy})\text{Cl}(\text{py})]$ (**5**), $[\text{Pt}(\text{tolpy})\text{Cl}(\text{PPh}_3)]$ (**9**) and $[\text{Pt}(\text{tolpy})(\mu\text{-Cl})_2]$ (**1**)

In order to investigate the role of the neutral ligand, L, which is presumed to dissociate during the reaction, the range of ligands investigated was extended further to include pyridine and triphenylphosphine. Both $[\text{Pt}(\text{tolpy})\text{Cl}(\text{py})]$ (**5**) and $[\text{Pt}(\text{tolpy})\text{Cl}(\text{PPh}_3)]$ (**9**) were found to be active in the decarbonylation of cyclohexanone and again the major products of the decarbonylation of cyclohexanone were found to be CO, methane and butane. These results demonstrate that the neutral ligand is not restricted to sulfur donors and that changing the neutral ligand, L, does not change the major products of the decarbonylation. This suggests that the decarbonylation reactions proceed by the same mechanism independent of L, supporting the view that L dissociates.

As with complexes where L = S-dmso (**3**) or dms (**7**), quantitative conversion to [Pt(tolpy)Cl(CO)] (**4**) was observed when the triphenylphosphine complex (**11**) was used. Lower conversion to **4** (78% and 22% residual **5** estimated by integration of the ^1H NMR spectra) was observed when [Pt(tolpy)Cl(py)] (**5**) was employed. This may indicate that the pyridyl ligand is less labile under these conditions, leading to lower activity. The triphenylphosphine ligand is sterically bulky which may promote ligand dissociation and coordination of the substrate.

The platinum complexes described above were synthesised from [Pt(tolpy)(μ -Cl)] (**1**), and so this complex was investigated in order to determine whether the precursor could also mediate decarbonylation reactions. Quantitative conversion to complex **4** and the formation of butane was observed when complex **1** was used, under standard decarbonylation conditions.

Potential for Catalysis: Investigating the Activity of [Pt(tolpy)Cl(CO)] (**4**)

Given the activity towards decarbonylation of complexes with bidentate 2-(4-tolyl)pyridine ligand and a labile neutral ligand *trans* to the nitrogen, it is possible that the platinum product of decarbonylation, complex **4** may also mediate decarbonylation reactions. Complex **4** was synthesised *via* the method published by Ford *et al.* (with an extended reaction time of six hours) and crystallised from CH_2Cl_2 and hexane.¹²⁰ When **4** was heated in cyclohexanone under standard decarbonylation conditions, CO, methane and butane were observed by analysis of the reaction headspace. This provides strong evidence for the decarbonylation of cyclohexanone mediated by complexes [Pt(tolpy)Cl(μ -Cl)]₂ and [Pt(tolpy)Cl(L)] (where L = S-dmso, dms, PPh₃ and py) being catalytic processes and to our knowledge the first reported platinum catalysed decarbonylation of unstrained ketones.

2.6.2 Pt^{II} Complexes with other Chelating Ligands

So far the active metal systems for decarbonylation have all included a bidentate tolypy ligand, and so to probe further possible active catalysts, complexes with other chelating ligands were prepared and evaluated (Figure 46).

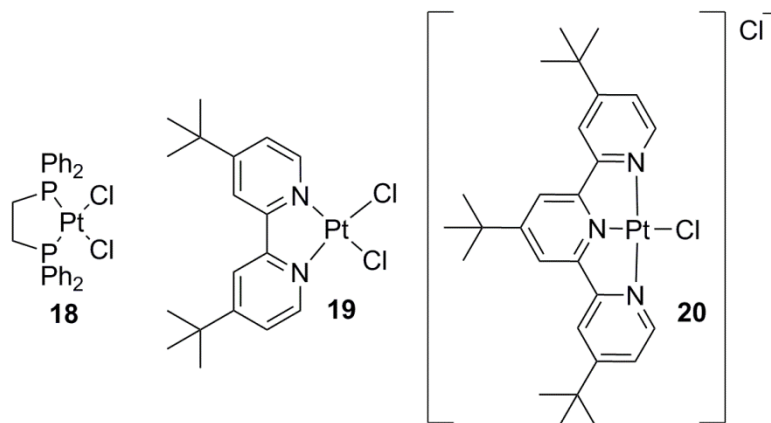


Figure 46: Chemical structures of the platinum complexes studied as alternative to the [Pt(tolpy)Cl(L)] family of complexes for decarbonylation reactions.

Attempting decarbonylation using either the terpyridine complex **20** or the dppe complex **18** did not lead to the formation of butane by decarbonylation of cyclohexanone. Partial decomposition of **20** during the experiment was suspected as darkening of the reaction solution was observed. However, use of the bipyridine complex **19** did lead to formation of butane, which was found to be the major product of the decarbonylation of cyclohexanone. Indeed, even though its solubility in cyclohexanone was much lower than for the [Pt(tolpy)Cl(L)] family of complexes, comparable and even greater peak areas for the product butane were observed by GC analysis of the reaction headspace. The ¹H NMR spectrum confirmed the presence of two platinum complexes after the reaction, of which the major component was assigned to **19** (85% by integration), with the second species showing significantly deshielded resonances for the bipy ligand (15%); the identity of this species is not yet known. When **19** was used in the decarbonylation of cycloheptanone, again the same major product, cyclohexene, was observed just as when [Pt(tolpy)Cl(S-dmsO)] (**3**) was used. This suggests the reaction proceeds *via* a very similar mechanism to that of the [Pt(tolpy)Cl(L)] family of complexes.

2.6.3 Rhodium Complexes

The first decarbonylation of cyclohexanone was reported by Rusina and Vlcek and their example used RhCl_3 and PPh_3 which were heated to reflux for three hours in cyclohexanone.¹ The hydrocarbon products of the reaction were not reported and so the reaction was repeated in order to analyse the reaction headspace. In their paper they report that they observed partial decomposition of the rhodium complex to rhodium metal and we have observed extensive decomposition when conducted under an atmosphere of air. When this reaction has been repeated, formation of butane was observed by GC analysis, which may suggest that the reaction proceeds *via* a similar mechanism as the decarbonylation of cyclohexanone mediated by $[\text{Pt}(\text{tolpy})\text{Cl}(\text{L})]$ and the bipyridine complex, **19**. However, cyclohexane, cyclohexene and benzene were also observed (butane: cyclohexane: cyclohexene: benzene ratio was 1.1: 0.7: 1: 2.9). The distribution of products suggests that one or more competing reaction mechanism(s) leading to the formation of C_4 and C_6 hydrocarbons.

The formation of cyclohexane, cyclohexene and benzene mediated by rhodium may be due to reduction of cyclohexanone followed by dehydrogenation and disproportionation. Williams and co-workers¹²¹ have reported the disproportionation of cyclohexene to afford benzene and cyclohexane in the presence of palladium and platinum dimers, $[\text{M}^{\text{II}}(\text{diimine})(\mu\text{-OH})_2]^{2+}$. They state although disproportionation has previously been proposed to involve heterogeneous catalysis,^{122, 123} their example is homogeneous. When the precipitated solids from the reaction were isolated and reused, they were not found to have any activity towards disproportionation. They also found that the reaction continued in the presence of an excess of mercury.

The reaction was repeated under standard decarbonylation conditions (i.e. 120 °C, under an atmosphere of air for 16 hours) in order to enable direct comparison with the other platinum complexes in this study. After 16 hours, the reaction headspace was sampled and the main components of the headspace were identified as butane, cyclohexane, cyclohexene and benzene using GC analysis and comparison to the references reported in the Experimental Section. However, under these conditions there was significant decomposition and so it was repeated under an atmosphere of nitrogen. This time there was less visible signs of decomposition and the same peaks were observed by GC but with higher peak areas. For example, the peak area for butane increased six-fold upon moving from an atmosphere of air to one of nitrogen; this indicates lower peak

areas observed for the reactions conducted under air were due to deactivation and decomposition of the active catalyst.

Wilkinson's catalyst, $[\text{RhCl}(\text{PPh}_3)_3]$, was found by Murakami *et al.* to mediate the stoichiometric decarbonylation reactions of cyclic ketones.^{14, 15} When trialled under the standard decarbonylation conditions, the formation of butane was not observed. Benzene and additional peaks with retention times similar to butene ionomers were observed in the headspace. This suggests that unlike, $[\text{RhCl}_3(\text{PPh}_3)]$, the Rh^{I} species cannot mediate decarbonylation reactions to afford butane under these conditions, which in addition to the different product distribution, suggests that the decarbonylation of cyclohexanone reported here does not proceed *via* the same mechanism as the examples using Wilkinson's catalyst.

2.6.4 Heterogeneous Catalysis

The majority of examples of decarbonylation report the use of homogeneous catalysts. Although homogeneous catalysts are generally thought to offer better selectivity the separation from the reaction mixture can be difficult. Heterogeneous catalysts in comparison are more readily isolated and can be used at high temperatures. However, carbon monoxide, which is produced by decarbonylation may poison heterogeneous catalysts by coordinating to and blocking active sites.¹²⁴

The activities of platinum on charcoal (Pt/C, 10 wt%) and platinum on charcoal (Pd/C, 5 wt%) towards decarbonylation reactions were investigated. At least 15 organic components were observed by GC analysis of the headspace, all with small peak areas when Pt/C was used. This evidence suggests that both activity and selectivity are very low for Pt/C. When Pd/C was investigated better selectivity was observed but the peak areas were still low (<400 pA).

2.6.5 Comparison of Active Systems

The experimental data collected for the decarbonylation of cyclohexanone mediated by $[\text{Pt}(\text{tolpy})(\mu\text{-Cl})_2]$ and $[\text{Pt}(\text{tolpy})\text{Cl}(\text{L})]$ complexes is summarised in Table 8 (the relative peak areas are given for each gas which have been treated individually). Decarbonylation of cyclohexanone to afford $[\text{Pt}(\text{tolpy})\text{Cl}(\text{CO})]$ (**4**) with good conversions (in excess of 78%) was observed for all of the active complexes. The relative peaks areas observed gives a complicated picture where the value obtained varies with the products analysed and the catalyst employed.

In all cases partial decomposition of the platinum complexes was suspected. The presence of platinum particles could provide a site for carbon monoxide to bind to, reducing its concentration in the headspace. The decomposition observed also suggests that the catalysts are being deactivated. No carbon monoxide was observed in the headspace when $[\text{Pt}(\text{tolpy})(\mu\text{-Cl})]_2$ was studied even though quantitative conversion to $[\text{Pt}(\text{tolpy})\text{Cl}(\text{CO})]$ (**4**) was observed, this may suggest that for this complex the process is not catalytic. However there were signs of extensive decomposition when this complex was used, so the absence of carbon monoxide in the headspace may be due to chemisorption onto platinum particles. Interestingly, even though CO and butane were observed for $[\text{PtCl}_2(\text{{}^t\text{Bu}}_2\text{-bipy})]$, the absence of a peak for methane may suggest that this reaction proceeds *via* a different mechanism than for the other platinum complexes studied.

Table 8: Comparison of the experimental data collected for the decarbonylation of cyclohexanone mediated by $[\text{Pt}(\text{tolpy})(\mu\text{-Cl})]_2$ and $[\text{Pt}(\text{tolpy})\text{Cl}(\text{L})]$

Complex	Conversion to [4], ^a %	Relative Peak Area Methane	Relative Peak area CO	Relative Peak area butane
$[\text{Pt}(\text{tolpy})(\mu\text{-Cl})]_2$	100	1	0	23
$[\text{Pt}(\text{tolpy})\text{Cl}(\text{S-dms})]$	100	6	4	1
$[\text{Pt}(\text{tolpy})\text{Cl}(\text{dms})]$	100	2	1	9
$[\text{Pt}(\text{tolpy})\text{Cl}(\text{py})]$	78	-	-	-
$[\text{Pt}(\text{tolpy})\text{Cl}(\text{PPh}_3)]$	100	12	1	23
$[\text{Pt}(\text{tolpy})\text{Cl}(\text{CO})]$	Na	13	1	69
$[\text{PtCl}_2(\text{{}^t\text{Bu}}_2\text{-bipy})]$	Na	0	2	40

^a Estimated using the integration of the proton *ortho* to the nitrogen of the coordinated tolpy ligand in the ¹H NMR spectrum

2.7 Summary and Outlook

Cyclic and acyclic ketones were found to undergo decarbonylation mediated by a family of platinum(II) complexes of the general formula $[\text{Pt}(\text{tolpy})\text{Cl}(\text{L})]$, with $[\text{Pt}(\text{tolpy})\text{Cl}(\text{CO})]$ as the major Pt-containing product. Ketones with aryl functionality were also tolerated but lower conversions to $[\text{Pt}(\text{tolpy})\text{Cl}(\text{CO})]$ (**4**) were observed. When other functional groups were studied, the ethers 1,4-dioxane and cyclopentylmethyl ether, and the aldehydes, pentanal and hexanal, were also found to undergo decarbonylation but the ester, caprolactone, was inactive. Decarbonylation of cyclopentanone and cyclohexanone led to the formation of methane, CO and propane or butane, respectively, and the mechanism requires the breaking of three carbon-carbon bonds. Furthermore, the balanced equation (ketone \rightarrow products) requires the incorporation of four additional hydrogen atoms, the origin of which is suspected to be the ketone substrate. This suggests a transfer hydrogenation mechanism which will be investigated in the next chapter.

Not only was $[\text{Pt}(\text{tolpy})\text{Cl}(\text{CO})]$ identified as a product of the decarbonylation, but it was also identified as an active system to mediate the reaction, hence demonstrating that the process is in principle catalytic. However, there was also evidence for formation of particulate platinum (darkening of post-reaction solutions), which could mean that the reaction is at least partly heterogeneous in nature and requires further investigation. A range of $[\text{Pt}(\text{tolpy})(\mu\text{-Cl})_2]$ and $[\text{Pt}(\text{tolpy})\text{Cl}(\text{L})]$ complexes were identified to mediate decarbonylation reactions. Several solvents were found to be suitable for these reactions, but the conversion to $[\text{Pt}(\text{tolpy})\text{Cl}(\text{CO})]$ (**4**) was sensitive to the stoichiometry of the substrate, cyclohexanone. Having defined the basic characteristics of the reactions here, a mechanistic discussion will follow in the next chapter.

Chapter Three: Mechanistic Investigation

3.1 Introduction

This chapter is concerned with a mechanistic investigation into the decarbonylation reactions of ketones. The focus will be on the unstrained, non-activated ketone cyclohexanone, but other substrates such as cyclic ketones (cyclopentanone, cycloheptanone and cyclooctanone) and acetone will also be discussed. Observations made whilst screening reaction solvents, substrates and metals catalysts reported in Chapter Two have provided mechanistic insight into platinum-mediated decarbonylation which will be investigated further here. The relevant recent literature concerning photochemical decarbonylation reactions, transfer hydrogenation and nanoparticles in catalysis will be discussed in this Introduction Section.

3.1.1 Main Aims

1. The formation of the products of the decarbonylation of cyclopentanone and cyclohexanone, namely methane, carbon monoxide and either propane or butane for cyclopentanone and cyclohexanone, respectively, require the cleavage of three C–C bonds. The additional cleavage of an alkyl C_α–C_β bond has not been reported previously for decarbonylation reactions of ketones, and attempts will be made in this chapter to identify how this occurs. The source of energy, be it thermal or photochemical, required to overcome the large energy barrier for C–C cleavage will also be investigated further.

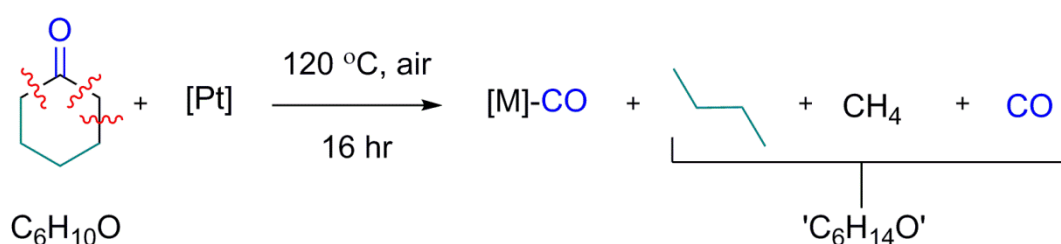


Figure 47: Decarbonylation of cyclohexanone showing the imbalance in hydrogen

2. The formation of these hydrocarbon products, discussed in Chapter Two, is not mass balanced and requires a source of hydrogen. For example cyclohexanone, shown in Figure 47, where an additional four hydrogen atoms are required. This work will consider possible sources of hydrogen, evaluate additional hydrogen sources and conduct deuterium labelling experiments to derive mechanistically useful information.
3. During the decarbonylation reactions, darkening of the reaction solution has been observed, suggesting decomposition of the platinum complexes. This may have led to the formation of platinum nanoparticles *in situ* and therefore raises the question of their possible involvement in the reaction. The identity and role of these nanoparticles will be investigated using dynamic light scattering and mercury poisoning experiments.
4. It is anticipated that the combination of the work described above will lead to mechanistic insight which will allow a mechanism to be proposed.

3.1.2 Photochemical Decarbonylation Reactions

There are two main types of photochemical reactions observed in aldehydes and ketones, namely Norrish Type I reactions, where $C_{CO}-C_{\alpha}$ bond cleavage occurs, and Norrish Type II reactions, where γ -H-atom transfer to the carbonyl group occurs.¹²⁵ The homolytic cleavage of the $C_{CO}-C_{\alpha}$ bond follows from either the S_1 or T_1 state and the radical products formed can undergo further secondary reactions.

Blacet *et al.* studied the photochemical decomposition of cyclic ketones, including cyclohexanone, and identified the products using mass spectrometry.¹²⁶ When irradiated with UV-light, cyclohexanone undergoes photo-dissociation in the gas phase to afford the major reaction products CO, cyclopentane and 1-pentene, and the minor products ethene and propene. Photoexcitation of cyclic ketones has been reported to begin with a cleavage of one of the two $C_{CO}-C_{\alpha}$ bonds, forming a diradical.

Selective photochemical cleavage of the $C_{\alpha}-C_{\beta}$ bond of *iso*-propyl ketones has been reported by Lee *et al.* using visible light and a cobalt porphyrin catalyst (Figure 48).¹²⁷ They reported the photocatalytic C–C oxidation of neat 2,6-dimethylcyclohexanone, which affords 2-heptanone with a TON of up to 24. The reaction requires *iso*-propyl alcohol (IPA) as the H atom donor and water as the oxidant. They have also applied their method to other ketones; 2-methyl

cyclohexanone (TON = 9), 2,4-dimethyl-3-pentanone (TON = 11) and *iso*-butyrophenone (TON = 2). Not only is this an example of catalytic low temperature C–C bond activation, it also utilises a less expensive and more abundant metal than the more common rhodium and iridium catalysts.

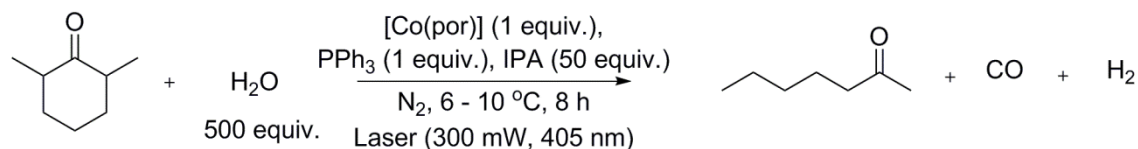


Figure 48: Photochemical cleavage of the C $_{\alpha}$ –C $_{\beta}$ bond of 2,6-dimethyl cyclohexanone as reported by Lee *et al.*¹²⁷

When the reaction was conducted in the absence of light or a hydrogen donor, C–C activation was still observed, but this time the insertion product, [Co^{III}(ttp)COCHMe(CH₂)₃COMe] (where ttp = 5,10,15,20-tetratolylporphyrinato dianion), was observed (Figure 49). This demonstrates that the initial C–C activation is not a photochemical process but the Co_{por}–C_{acyl} bond could be cleaved photolytically to afford 2-heptanone and heptan-6-en-2-one. Selectivity for 2-heptanone was achieved by the addition of the hydrogen donor, *iso*-propyl alcohol, and they found the addition of triphenylphosphine increased the TON.

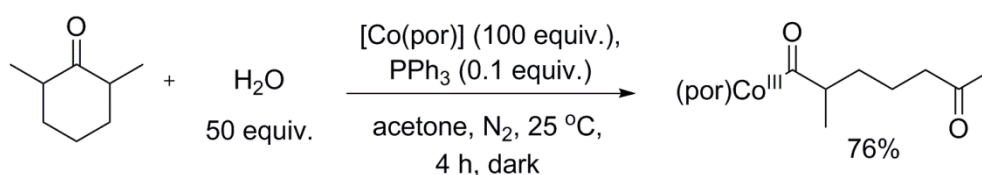


Figure 49: The formation of [Co^{III}(ttp)COCHMe(CH₂)₃COMe] observed by Lee *et al.*¹²⁷

In order to identify the source of the additional oxygen in the products, a H₂¹⁸O labelling experiment was conducted, and they found that the photocatalytic bond oxidation of 2,6-dimethylcyclohexanone yielded 2-heptanone and ¹⁸O-labeled 2-heptanone in a 1:1 ratio, with the minor side product, heptan-6-ene-2-one, also observed. The mechanism proposed by Lee *et al.* is shown in Figure 50, initially, the Co^{II} porphyrin (por = tetrakis(4-anisyl)porphyrin or 5,10,15,20-tetratolylporphyrinato) reacts with H₂O and coordinates triphenylphosphine to form [Co^{III}(por)(OH)(PPh₃)] and [Co^{III}(por)(H)(PPh₃)]. The active species for C_{CO}–C $_{\alpha}$ cleavage is [Co^{III}(por)(OH)(PPh₃)], which is followed by catalytic dehydrogenation to afford [Co^{III}(por)COCHCH₃(CH₂)₃COCH₃]. [Co^{III}(por)COCHCH₃(CH₂)₃COCH₃] can then undergo photolytic homolysis to afford the acyl radical, which in turn undergoes decarbonylation to form the more

stable secondary radical. 2-Heptanone is formed after hydrogen transfer from *iso*-propyl alcohol or the C α -H bond of the substrate.

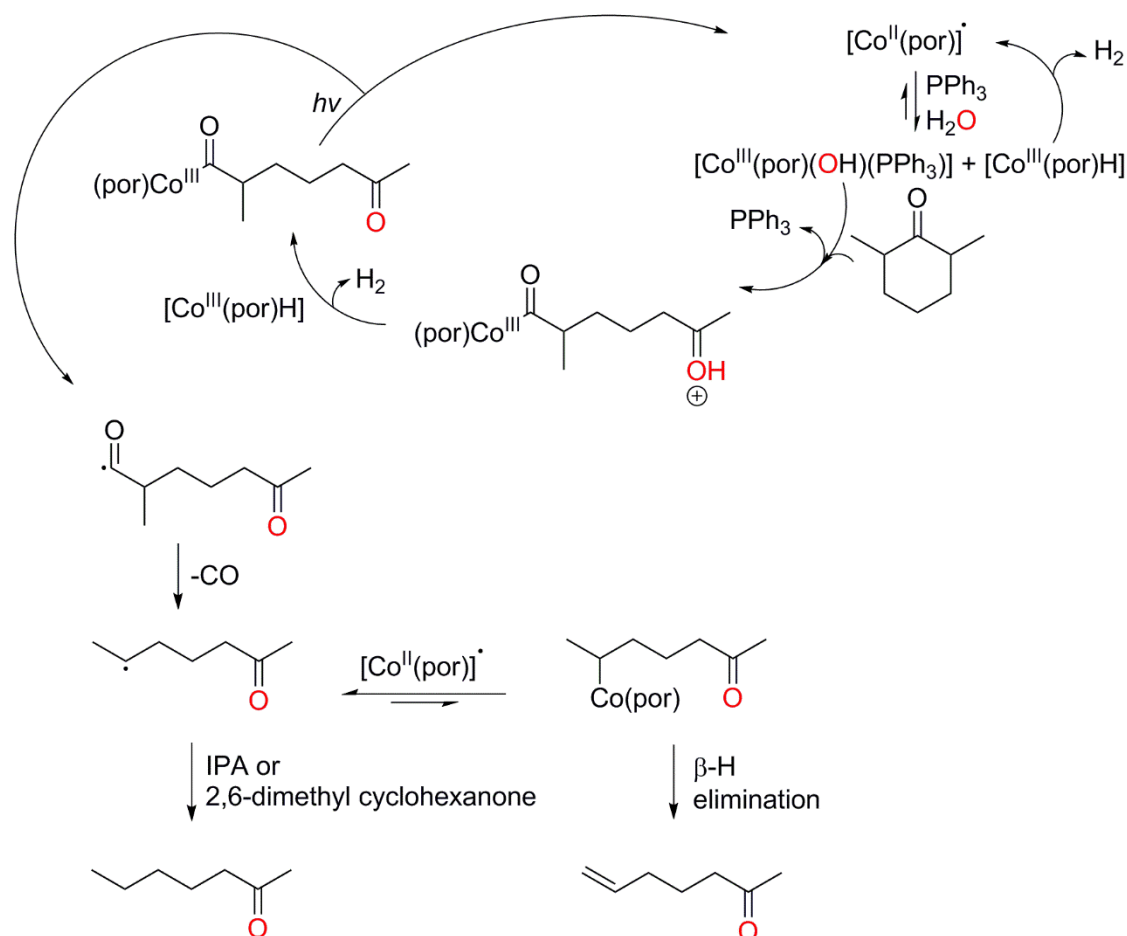


Figure 50: Reaction mechanism proposed by Lee *et al.* for the cleavage of the C α -C β bond of 2,6-dimethyl cyclohexanone¹²⁷

3.1.3 Transfer Hydrogenation

Transfer hydrogenation involves the hydrogenation of a substrate where the hydrogen atoms are abstracted from a donor source rather than directly from molecular hydrogen.¹²⁸ Braude and Linstead published a review of hydrogenation reactions (hydrogen migration, hydrogen disproportionation and transfer hydrogenation) in 1954,¹²⁸ in which they state that any organic compound which has an oxidation potential sufficiently low enough to allow hydrogen transfer to occur under mild conditions can be a hydrogen donor compound (DHx). The use of molecular oxygen as terminal oxidant and hydrogen acceptor in the palladium-catalysed conversion of cyclohexanones to phenols was reported by Izawa *et al.* (Figure 51).¹¹⁹ Their study shows that it is possible for cyclohexanone to act as a hydrogen donor and take part in transfer hydrogenation in the

presence of air. They reported that the dehydrogenation of cyclohexanone goes *via* successive C_{α} -H activations and β -hydride elimination steps to afford the dienone which tautomerises to phenol. The $[Pd^0Ln]$ species formed can be oxidised by molecular oxygen to regenerate the active Pd^{II} species.

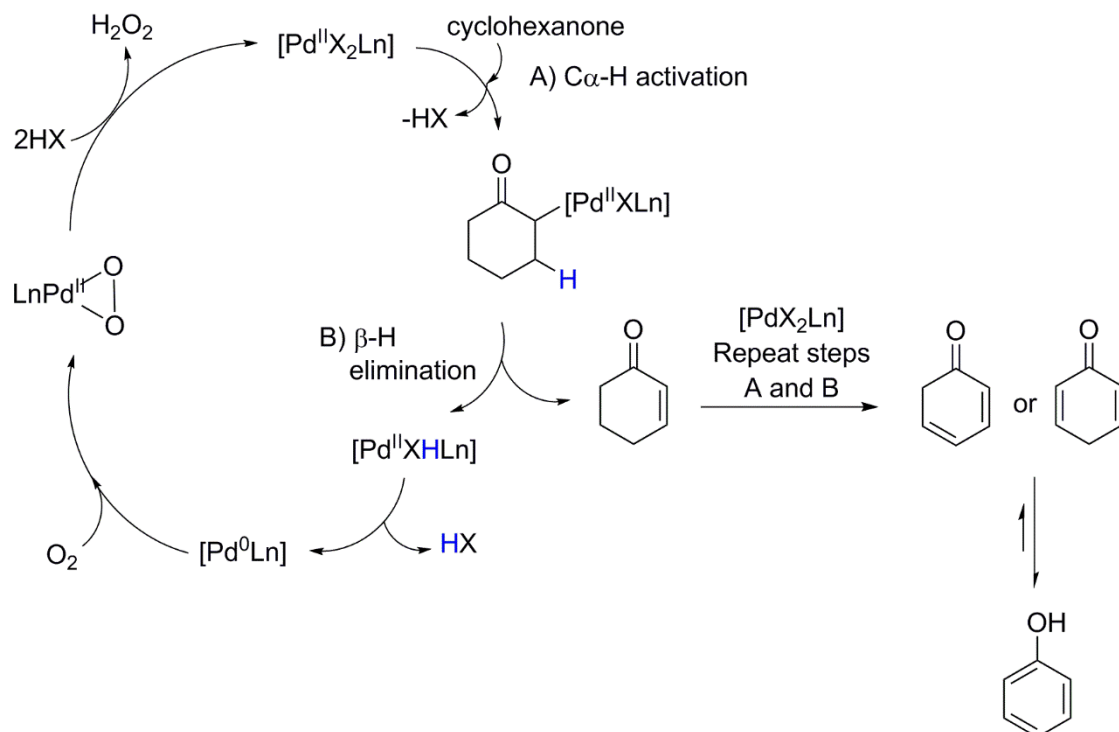


Figure 51: Palladium-catalysed conversion of cyclohexanones to phenols using molecular oxygen as terminal oxidant reported by Izawa *et al.*¹¹⁹

Transfer hydrogenation reactions can be catalysed by late transition metals, organic catalysts, enzymes or bases,¹²⁹ with homogeneous late transition metal catalysts in particular being used extensively, the most popular being ruthenium.¹²⁹⁻¹³⁴ Recently efforts have been directed to identifying less expensive and more abundant metal catalysts such as cobalt,^{135, 136} nickel,¹³⁷⁻¹³⁹ and iron.¹⁴⁰⁻¹⁴³ Gold¹⁴⁴ and iron¹⁴⁵ nanoparticles have also been employed and palladium nanoparticles formed *in situ* were identified as the active catalyst for the transfer hydrogenation of ketones using $[Pd(acac)_2]$ and *iso*-propyl alcohol.¹⁴⁶

Haddad *et al.* demonstrated that a combination of chloroiridic acid with either trimethyl phosphite or dmsO could catalyse the hydrogenation of cyclohexanone to cyclohexanol using isopropanol as the hydrogen donor.¹⁴⁷ Whereas more recently, Castellanos-Blanco *et al.* reported the nickel-catalysed transfer hydrogenation of cyclohexanone using ethanol as both the solvent and hydrogen donor (98% yield using [Ni(dcype)(cod)], 2 mol%).¹³⁹ The results of their control experiments and of the mercury drop test (see below) supported a homogeneous catalytic system.

In many examples where an alcoholic hydrogen donor is used, a base is also included amongst the reagents. Chowdhury and Bäckvall found that the transfer hydrogenation of ketones, including cyclohexanone and acetophenone catalysed by [RuCl₂(PPh₃)₃], using the donor *iso*-propyl alcohol, only proceeded with addition of catalytic quantities of sodium hydroxide.¹⁴⁸ A mechanism for the formation of hydrogen from alcohols was proposed by Morton and Cole-Hamilton whereby the negatively charged, deprotonated alcohol substrate coordinates to the metal, in this case ruthenium, and then undergoes β -hydride elimination to afford a metal carbonyl and a ruthenium hydride species.¹⁴⁹ The complex then abstracts a proton from another molecule of alcohol, forming a dihydride, which can then eliminate hydrogen, reductively regenerating the ruthenium catalyst. Chowdhury and Bäckvall applied this approach to their system but in the final step they suggest that the ruthenium dihydride reduces the ketone rather than eliminating hydrogen reductively.¹⁴⁸

Two routes have been proposed for the transfer hydrogenation of ketones or aldehydes; either direct hydrogen transfer from the donor molecule or the transfer *via* a metal hydride.¹⁵⁰ In a review of transfer hydrogenation reactions by Gilkey and Xu, they describe both of these mechanisms by both homogeneous and heterogeneous/surface catalysis (Figures 52 and 53).¹⁵¹ Direct hydrogen transfer using an alcoholic hydrogen donor proceeds *via* a six-membered-ring intermediate, whereby the alcohol's C_{OH}-H is transferred to the carbonyl carbon without forming a metal hydride. The surface catalysis mechanism involves an intermediate where hydrogen atoms are adsorbed or coordinated to the surface, which is similar to the homogeneous dihydride route. It is possible to distinguish between the mono-hydride and di-hydride routes by selective deuterium labelling of the alcoholic proton as for a di-hydride route a 50:50 distribution of the deuterium bound either to the oxygen of the alcohol group or to the α -carbon atom is observed.

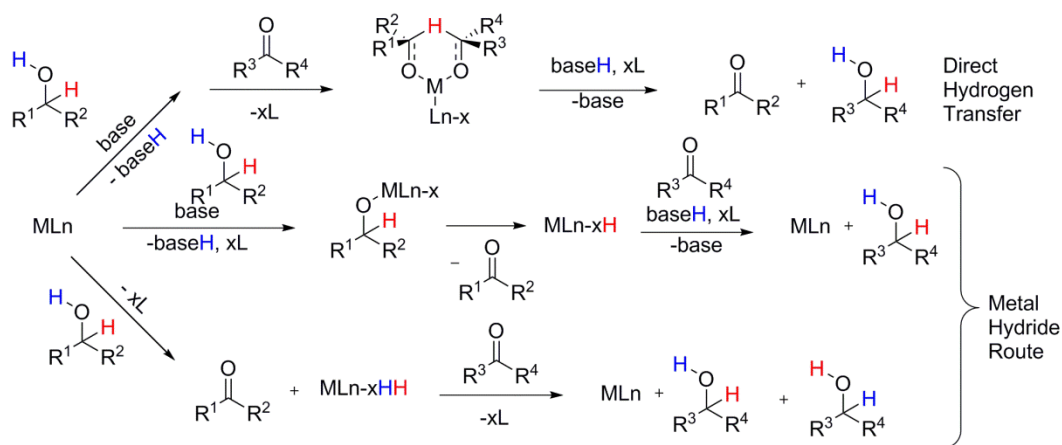


Figure 52: Homogeneous catalysis of the transfer hydrogenation of ketones by direct hydrogen transfer and by metal hydride or di-hydride routes

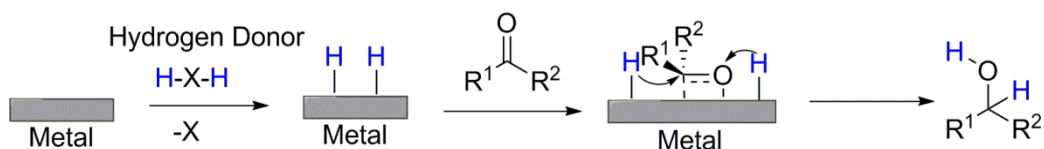


Figure 53: Heterogeneous/ nanoparticle surface catalysis of the transfer hydrogenation of ketones

3.1.4 Transition Metal Nanoparticle Catalysis

Given the observation of darkening of the reaction solutions during decarbonylation reactions, which may suggest the presence of platinum nanoparticles, a brief introduction to nanoparticles in catalysis and methods of identifying them is presented.

Nanoparticles in Catalysis

The terms homogeneous and heterogeneous can be ambiguous and have been reported to mean different things by different authors. Homogeneous catalysts can refer to those which are in the same phase as the reactants, which would include soluble nanoparticles. However, the terms homogeneous catalyst and heterogeneous catalyst have also been used to distinguish between mononuclear complexes with one active site and particles/clusters which have multiple active sites; when applied this way, homogeneous catalysts would not include soluble nanoparticles. Here, the first definition will be used.

Nanoparticles (metal particles between 10 -1000 Å in size) have catalytic activity due to their high surface-to-volume ratio which maximises catalyst exposure to the substrate. Metal nanoparticles usually have a broad size and shape distribution, a non-uniform surface and the activity is dependent on the availability of surface sites. The type and number of active sites on a metal-particle can change with particle size, synthetic procedure, and catalytic conditions. The coordination of ligands to the nanoparticle surface can also be used to tune the catalytic behaviour and increase particle stability by reducing particle aggregation. The presence of multiple, different active sites means that metal particles may have very different, often poorer, selectivity compared to homogeneous catalysts. Smaller particles are usually more active than larger particles, due to their larger surface-area-to-volume ratio; this means that aggregation of particles should be inhibited in order to increase the catalytic lifetime. However, small particles may be more susceptible to surface poisoning by strongly adsorbing substrates.

Heterogeneous catalysts are often more thermally robust than homogeneous catalysts and they can offer easier separation from the products. However, only the surface atoms can take part in the reactions, which are often also less selective. The activity and selectivity of homogeneous catalysts can be tuned by changing the ligands. However, good selectivity does not necessarily mean that a reaction is mediated by a homogeneous catalyst and examples have been reported of highly regio- and enantio-selective reactions mediated by heterogeneous catalysts. Fujihara *et al.* reported a palladium nanoparticle-catalysed asymmetric Suzuki–Miyaura coupling reaction,¹⁵² in which the palladium nanoparticles were stabilised by the phosphine ligand, (S)-BINAP (Figure 54). Under these conditions, greater enantioselectivity was achieved than when [PdCl₂] and (S)-BINAP were used. Another example by Chaudret *et al.* utilised palladium nanoparticles stabilised by the chiral xylofuranoside diphosphate to catalyse the allylic alkylation of rac-3-acetoxy-1,3-diphenyl-1-propene with dimethyl malonate with good enantioselectivity (90% e.e.).¹⁵³

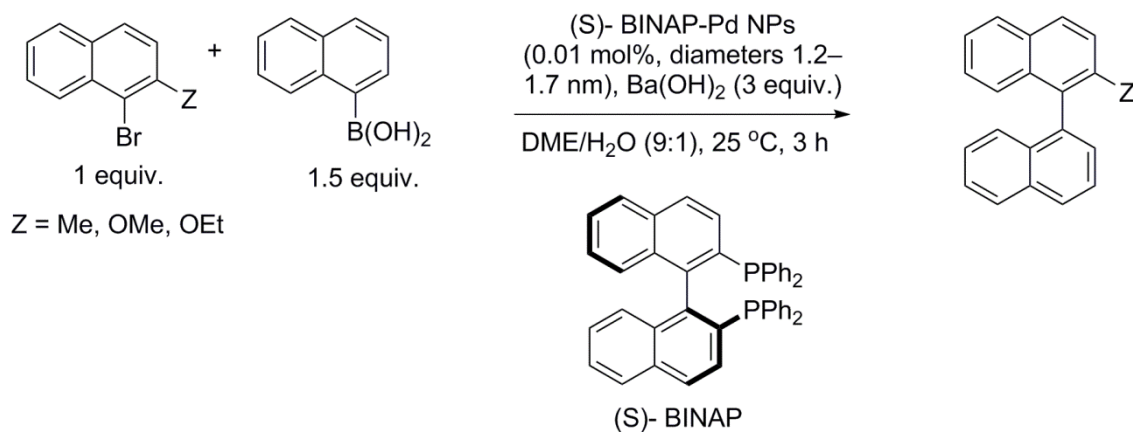


Figure 54: Palladium nanoparticle-catalysed asymmetric Suzuki–Miyaura coupling reaction reported by Fujihara *et al.*¹⁵²

Homogeneous catalysts can decompose to give nanoparticles, and transition metal nanoparticles have been linked to the activity of a range of catalytic processes including hydrosilylation and palladium cross-coupling reactions.^{154–156} Nanoparticles generated *in situ* have been identified as active for many reactions that were originally thought to be homogeneous in nature, for example, the Heck coupling of phenyl halides with styrene starting from palladium P[∧]C[∧]P pincer complexes.¹⁵⁷ In addition to these, there are also examples where the nanoparticles only act as a source of the transition metal, which, when leached from the particle, catalyse a homogeneous reaction. It was reported by de Vries that regardless of the nature of the palladium complex used, high-temperature Heck reactions are catalysed by monomeric or dimeric palladium species formed by attack of the arylating agent on the surface palladium atoms of the nanoparticles.¹⁵⁸

As well as activity of the nanoparticle surface, nanoparticles can be a source of active mononuclear species leached from the surface. Perez-Lorenzo has proposed a mechanism for Suzuki cross-coupling reactions that includes both active nanoparticles and active mononuclear species leached from the particles (Figure 55).¹⁵⁹

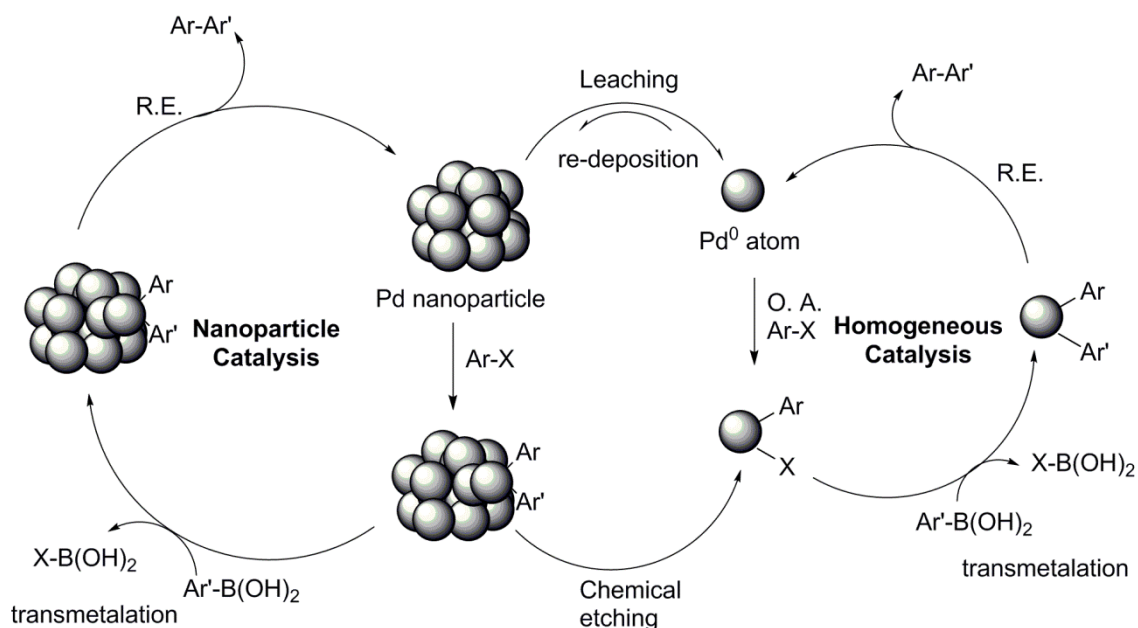


Figure 55: Mechanism for the Suzuki reaction including both nanoparticle catalysis (heterogeneous) and mononuclear catalysis (homogeneous) proposed by Perez-Lorenzo¹⁵⁹

The mechanism of formation of transition metal nanoparticles has been described to occur *via* LaMer burst nucleation,^{160, 161} followed by Ostwald ripening.¹⁶² LaMer burst nucleation is the increase of free monomers in solution, followed by “burst nucleation” where the concentration of free monomers is greatly reduced, then as the concentration increases the nucleation growth is controlled by diffusion of the monomers. Ostwald ripening occurs because larger nanoparticles are more energetically favourable than smaller nanoparticles due to their greater surface-to-volume ratio. Atoms on the surface are higher in energy than those packed in the interior, and therefore, they aggregate to attain a lower energy state, diffusing to form larger nanoparticles. This theory was expanded upon by Watzky and Finke,¹⁶³ who proposed a two-step mechanism with both steps occurring simultaneously. One step is a diffusion controlled, slow and continuous nucleation, and the other is an autocatalytic surface growth. Peng *et al.* suggested that diffusion of the monomers on the surface of the nanoparticles causes the change in shape of particles over time.^{164, 165}

The formation of transition metal nanoparticles *in situ* is more likely when pre-catalysts are used that are prone to reduction. The formation of these particles is also promoted by the use of forcing reaction conditions or the presence of nanoparticle stabilisers.¹⁶⁶ Nanoparticles can be stabilised electrostatically, such as by anionic ligands on the surface, which cause repulsion between particles, or sterically, using bulky ligands that hinder agglomeration.

Methods for Identifying the Nature of the True Catalyst

Methods for identifying the true nature of a catalyst have been reviewed extensively by Finke *et al.* who state that there is no single experiment for making this distinction.^{166, 167} Although the darkening of reaction solutions and the formation of metal precipitates may indicate the formation of nanoparticles, soluble nanoparticles may mimic the appearance of a mononuclear system. Other indicators of heterogeneous and nanoparticle catalysis include irreproducible reaction kinetics with sigmoidal curves and the observation of induction periods.¹⁶⁶ However, there are examples of highly reproducible catalytic systems involving nanoclusters.^{168, 169}

Mercury poisoning is a commonly used technique for distinguishing between homogeneous and heterogeneous metal-particle catalysts. Mercury deactivates heterogeneous catalysts, by amalgamation or by adsorption onto the surface, but normally leaves homogeneous catalysts unaffected.¹⁷⁰ The mercury should remain in the reaction solution until the reaction is complete, and ideally only be added once the reaction has started. A large excess of mercury combined with good stirring are necessary for complete poisoning. The results of the mercury drop test can be ambiguous and it is not universally applicable, for example, it does not form amalgams with iridium, rhodium or ruthenium. Mercury has also been reported to react with some transition metal complexes, for example when added to the high-temperature thermal decomposition of *cis*-[Pt^{II}(Me)₂(PMe₂Cp)] (Cp = cyclopentyl).¹⁷¹

Ligands such as CS₂ or thiophene that strongly bind to the late transition metals can also be used to poison active metal particles.¹⁷²⁻¹⁷⁵ As only a fraction of the metal particles are on the surface, only a very small amount (1-3 mol%.) of ligand will be required for complete poisoning.¹⁷² A limitation of this method is that the reactions studied must take place below 50 °C in order to avoid ligand dissociation at the metal surface.

Chemisorption can be used to identify the number of active sites using a model substrate, such as H₂, O₂ or CO. The size and morphology of the particles can be studied using light scattering techniques such as Small Angle X-ray Scattering (SAXS) and Dynamic Light Scattering (DLS) which detect particles in solution. Transmission and Scanning Electron Microscopy (TEM and SEM) can be combined with Energy Dispersive X-ray (EDX) detection to obtain elemental analysis. Both of these techniques are limited to dry, *ex situ* analysis.

Furthermore, although transmission electron microscopy (TEM) can be used to detect particles in a reaction medium, it cannot be used to probe whether the particles are involved in the decarbonylation reactions.

3.2 Determination of the Source of Energy Required to Drive the Decarbonylation Reactions

3.2.1 Is the Decarbonylation of Cyclohexanone a Thermal or Photochemical Process?

Given the photochemical reactivity of cyclic ketones shown in Section 3.1.2, it was important to determine the extent of any photochemical influence on the decarbonylation reaction. In order to evaluate whether the decarbonylation of cyclohexanone involved a photochemical process, control reactions were performed in the absence of light. When the decarbonylation of cyclohexanone mediated by [Pt(tolpy)Cl(S-dmsO)] (**3**) was conducted in amber glassware to exclude natural light, just as with the reactions which take place in light, quantitative conversion to [Pt(tolpy)Cl(CO)] (**4**) was observed by integration of the ^1H NMR spectrum. Butane was observed as one of the reaction products when the headspace was analysed by GC. These observations suggest that light is not required for decarbonylation to occur.

In order to investigate whether decarbonylation could be achieved non-thermally, a solution of [Pt(tolpy)Cl(S-dmsO)], (**3**) in cyclohexanone was irradiated using a medium pressure mercury vapour lamp (125 W, $\lambda > 250$ nm) at room temperature under an atmosphere of air. After 16 hours, CDCl_3 was added, and the reaction was analysed by ^1H NMR spectroscopy. Only one platinum species, [Pt(tolpy)Cl(S-dmsO)], (**3**) was observed by ^1H NMR and ^1H - ^{195}Pt HMQC spectroscopy. These results, together with the results of the decarbonylation in amber glassware suggest that the decarbonylation is purely a thermal process.

3.2.2 Determination of the Onset Temperature

The decarbonylation reactions reported in Chapter Two were conducted at high temperatures in excess of 100 °C and decomposition of the platinum complexes was observed. In order to optimise the reaction conditions the minimum temperature required for decarbonylation was investigated using *in situ* infrared spectroscopy (IR) using the procedure described in the Experimental Section. The onset temperature for the decarbonylation of cyclohexanone mediated by [Pt(tolpy)Cl(S-dmsO)] (**3**) was estimated by slowly increasing the temperature (10

°C every 15 min) while monitoring the IR spectra *in situ*. The internal temperature was measured using a thermocouple placed in the solution during the reaction. It was not possible to observe the $\bar{\nu}(\text{S}=\text{O})$ vibration responding to complex **3**, but a very small vibration at 2098 cm^{-1} ($\bar{\nu}(\text{CO})$) of $[\text{Pt}(\text{tolpy})\text{Cl}(\text{CO})]$ (**4**) was observed at an internal temperature of $64.5\text{ }^{\circ}\text{C}$, the intensity of which began to increase significantly at $83.5\text{ }^{\circ}\text{C}$ (Figure 56). The total study duration was three hours; however, the reaction was only at or above $83.5\text{ }^{\circ}\text{C}$ for 50 minutes. During this time 50% conversion from $[\text{Pt}(\text{tolpy})\text{Cl}(\text{S-dms})]$ (**3**) to $[\text{Pt}(\text{tolpy})\text{Cl}(\text{CO})]$ (**4**) was observed, as estimated by integration of the ^1H NMR spectrum. This study demonstrates that the decarbonylation of cyclohexanone can proceed at lower temperatures, which if employed may lead to a reduction in the decomposition of the platinum complexes observed.

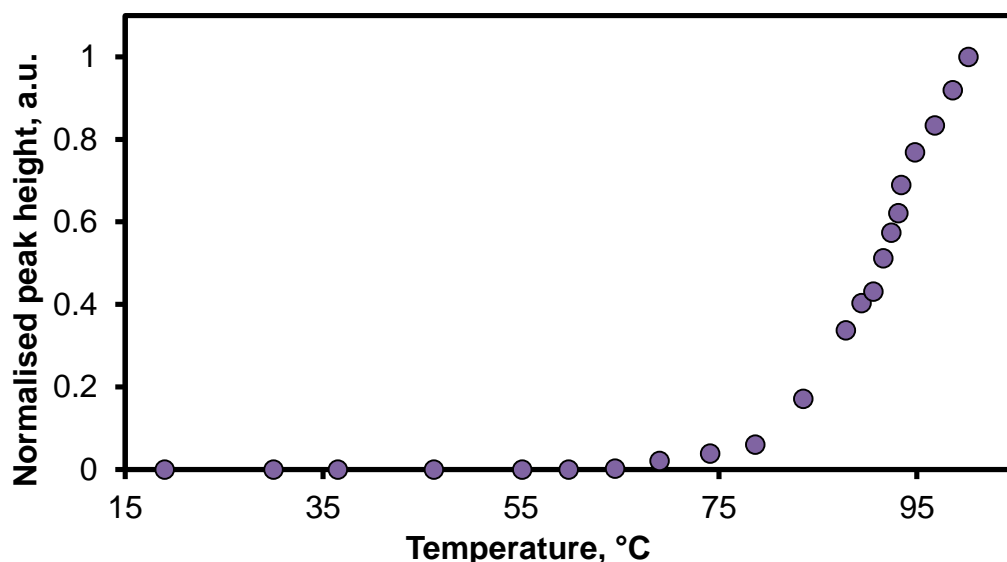


Figure 56: A plot of the normalised intensity of the vibration at 2098 cm^{-1} versus temperature for the decarbonylation of mediated by $[\text{Pt}(\text{tolpy})\text{Cl}(\text{S-dms})]$ (**3**)

3.3 Radical Process

While the multiple C–C cleavages required for formation of the observed decarbonylation products, and the deuterium scrambling of the deuterium in cross labelling experiments (described later in Section 3.5), could be explained in terms of known homogeneous and heterogeneous chemistry, a decision was made to eliminate (or otherwise) a radical process. Therefore, the effect of adding an inhibitor was investigated and phenothiazine was chosen as it works under both aerobic and anaerobic conditions, and does not contain any carbonyl functional groups. The effect of the presence of phenothiazine was then investigated on the decarbonylation of cyclohexanone, catalysed by

[Pt(tolpy)Cl(S-dmsO)] (**3**). When the headspace was analysed by GC, the formation of butane was observed and the ^1H NMR spectrum showed 100% conversion from [Pt(tolpy)Cl(S-dmsO)] (**3**) to [Pt(tolpy)Cl(CO)] (**4**), suggesting that the addition of the radical inhibitor had no effect on the decarbonylation.

3.4 Transfer Hydrogenation

As noted above, when considering the decarbonylation of cyclohexanone, it is evident that there is a mass imbalance between reactant and observed products that amounts to four hydrogen atoms. With no other source of hydrogen present, this could suggest a transfer hydrogenation mechanism, and in the cases where the reaction is carried out in neat cyclohexanone, the substrate may also act as a transfer hydrogenation donor. As also noted above, the ability of cyclohexanone to act as a hydrogen donor was demonstrated by Izawa *et al.*, who reported palladium-catalysed conversion of cyclohexanones to phenols using molecular oxygen as terminal oxidant (Figure 51).¹¹⁹ While cyclohexanone can then act as a source of hydrogen in transfer hydrogenation reactions, it would not be the substrate of choice and using a different hydrogen source would allow for labelling experiments. Thus, a series of experiments was conducted with well-defined transfer hydrogenation donors.

3.4.1 Addition of Transfer Hydrogenation Donors

Low conversions were observed when the decarbonylation of cyclohexanone was conducted in a solvent, rather than in neat cyclohexanone, unless the cyclohexanone was present in very significant excess and with only one molar equivalent with respect to the catalyst, no conversion was observed. Therefore, decarbonylation of one molar equivalent of cyclohexanone was repeated in acetonitrile in the presence of the well-known transfer hydrogenation donors 1,3-cyclohexadiene and *iso*-propyl alcohol (IPA),^{151, 176-181} which on loss of hydrogen give rise to benzene and acetone respectively. The reaction conditions were; one equivalent each of cyclohexanone and **3** and two equivalents of the hydrogen donor (*iso*-propyl alcohol or 1,3-cyclohexadiene) heated to 120 °C in a gas-tight Fisher-Porter vessel for 16 hours.

The results when IPA or 1,3-cyclohexadiene were used as a hydrogen donor were very similar (Table 9). Although [Pt(tolpy)Cl(CO)] (**4**) was present in quantities less than 1% in both cases, the amount of [Pt(tolpy)Cl(NCCH₃)] (**6**) was much higher when the hydrogen donor was present. GC analysis of the reaction

headspace confirmed that butane was present; showing that decarbonylation had taken place (GC-B).

Table 9: Results of the decarbonylation of cyclohexanone mediated by [Pt(tolpy)Cl(S-dmsO)] (**3**) in the presence of 1,3-cyclohexadiene or IPA in acetonitrile

No. Equiv. Cyclohexanone	[Pt(tolpy)Cl(S-dmsO)] (3), %	[Pt(tolpy)Cl(NCMe)] (6), %
1	67	33
1 (+ 2 equiv. 1,3 - cyclohexadiene)	27	73
1 (+ 2 equiv. IPA)	26	74
5	31	67

The results suggest that the low conversions observed in solution may be due to low availability of a substrate to act as a hydrogen donor. If this is the case, the conversions observed may be improved if a solvent is chosen which can also act as a transfer hydrogenation donor. To this end, the decarbonylation of one equivalent of cyclohexanone by [Pt(tolpy)Cl(S-dmsO)] (**3**) was attempted in IPA. When IPA was used as a solvent for the decarbonylation reaction, it proceeded with only one molar equivalent of cyclohexanone with respect to the [Pt(tolpy)Cl(S-dmsO)] (**3**), giving 27% conversion to [Pt(tolpy)Cl(CO)] (**4**) without visible signs of decomposition; small amounts of [Pt^{IV}(tolpy)₂Cl₂] (**11**, <0.01%) and [Pt(tolpy)(μ-Cl)]₂ (**1**, 8%) were also observed. When acetonitrile or 1,2-dichlorobenzene were employed as the solvent under the same conditions, no evidence for any decarbonylation taking place was observed. These results are strongly supportive of a transfer hydrogenation mechanism, but further evidence is required for confirmation.

3.4.2 UV-Vis Spectroscopic Analysis

In order to support the hypothesis that a transfer hydrogenation step is part of the decarbonylation mechanism, the post-reaction solution was analysed by UV-Vis spectroscopy to try to identify the benzene which is suspected to form when 1,3-cyclohexadiene donates two hydrogen atoms. For this study, two molar equivalents of 1,3-cyclohexadiene and one molar equivalent of cyclohexanone were used with one molar equivalent of [Pt(tolpy)Cl(S-dmsO)] (**3**).

The electronic spectrum of the reaction mixture was recorded before and after the reaction and the deconvoluted difference spectrum is shown in Figure 57. Peaks at 255 and 282 nm relating to benzene and cyclohexanone, respectively, were observed suggesting that 1,3-cyclohexadiene has reacted to form benzene and supporting a transfer hydrogenation step. The typical UV-vis spectrum of benzene also includes a strong absorption at 180 nm (out of the range of the instrument used), a weaker absorption at 200 nm (observed in the difference spectrum but complicated by the CH₃CN). There is good agreement between the difference spectrum and the fitted curve shown in Figure 58 in the region 200-300 nm where the peaks of interest appear.

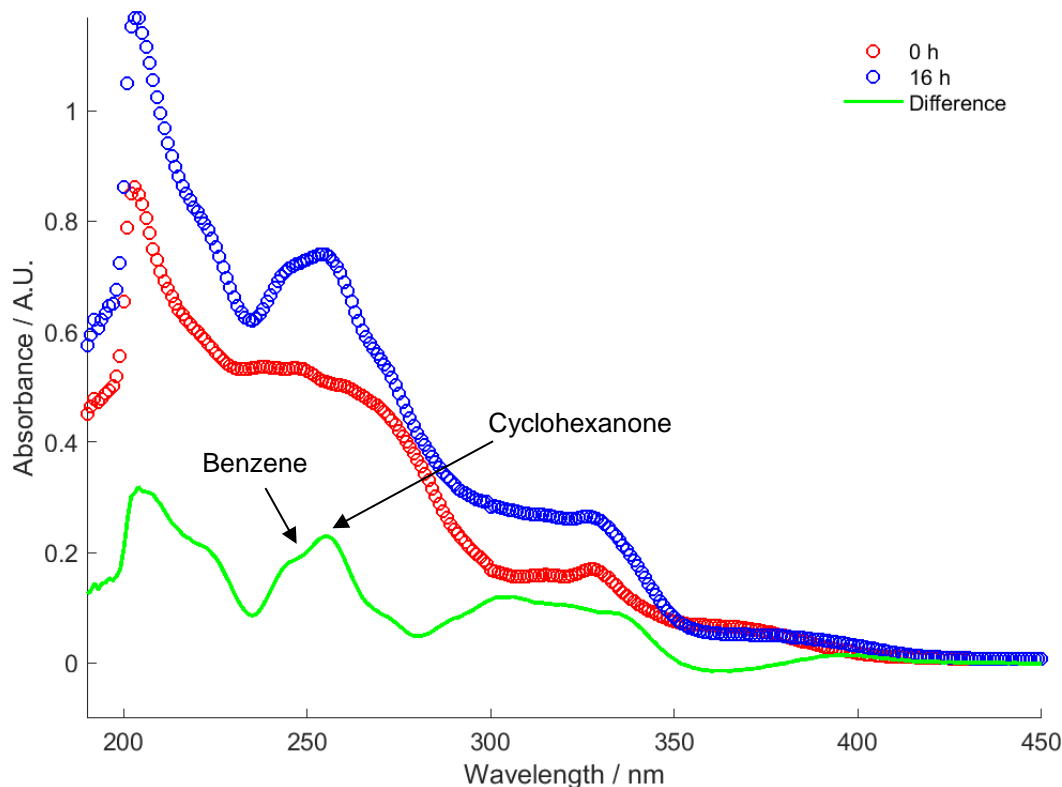


Figure 57: UV-Visible spectra recorded on samples taken at the beginning ($t = 0$ h, in red) and end ($t = 16$ h, in blue) of the decarbonylation of cyclohexanone mediated by [Pt(tolpy)Cl(S-dmsO)] (**3**) in the presence of the hydrogen donor

1,3-cyclohexadiene in acetonitrile. The difference between the two spectra is shown in green.

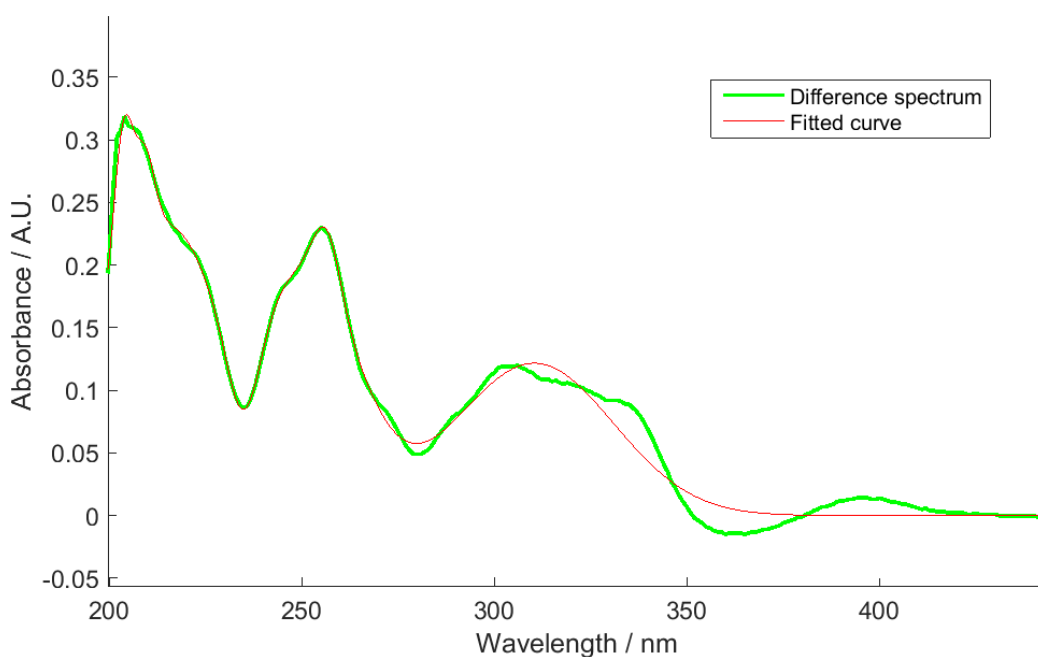


Figure 58: Comparison between the fitted curve and the difference spectrum obtained by subtracted the UV-Vis spectra recorded at $t = 0$ and 16 hr.

3.4.3 Ketone Substrates Revisited

Some of the substrates which demonstrated low activity or no activity at all in the substrate screen described in Chapter Two were then reinvestigated with the addition of a transfer hydrogenation donor, both *iso*-propyl alcohol or 1,3-cyclohexadiene were used. The inactivity observed previously may have been due to the inability of substrates such as acetone and acetophenone to donate hydrogen atoms as part a potential transfer hydrogen step.

Bicyclohexylketone

When decarbonylation of the active substrate, bicyclohexylketone, was repeated in the presence of 1,3-cyclohexadiene, the conversion to $[\text{Pt}(\text{tolpy})\text{Cl}(\text{CO})]$ (**4**) by decarbonylation improved from 58 to 100%. Darkening of the reaction solution and the formation of precipitates were also observed. The observation that the decarbonylation of bicyclohexylketone was promoted in the presence of 1,3-cyclohexadiene further suggests that the reaction proceeds by a transfer hydrogenation step.

Cyclohex-2-en-2-one

Very low conversion to [Pt(tolpy)Cl(CO)] (**4**) was previously observed, but when the experiment was repeated using two molar equivalents of 1,3-cyclohexadiene a relatively small peak for butane was observed but the conversion to [Pt(tolpy)Cl(CO)] (**4**) increased from 5% to 39%. Visual signs of extensive decomposition were also observed. When the number of molar equivalents of 1,3-cyclohexadiene added was increased to ten, a further increase in the conversion to [Pt(tolpy)Cl(CO)] (**4**) was observed (70%). As well as butane, the hydrocarbons, cyclohexene, 1,3-cyclohexadiene and benzene were also observed in the reaction headspace by GC-MS analysis. The cyclohexene observed could be due to disproportionation of 1,3-cyclohexadiene or by reduction of cyclohex-2-en-2-one. Reduction of ketones to alkanes is well known but requires hydrazine and a strong base in the case of the Wolff-Kishner reduction,^{182, 183} or a zinc and mercury amalgam and an acid for the Clemmensen reduction.¹⁸⁴ However the disproportionation of 1,3-cyclohexadiene to benzene and cyclohexene has been reported, with examples of catalyst systems including both homogeneous including iridium,¹⁸⁵ rhodium complexes,¹⁸⁶ platinum and palladium,¹²¹ and heterogeneous systems such as palladium on carbon and nickel nanoparticles.^{187, 188}

Acetophenone

Previously, when acetophenone was heated with [Pt(tolpy)Cl(S-dmsO)] (**3**), there was no evidence for decarbonylation. However, in the presence of 1,3-cyclohexadiene (two molar equivalents of 1,3-cyclohexadiene and one molar equivalent of [Pt(tolpy)Cl(S-dmsO)] (**3**)), the formation of [Pt(tolpy)Cl(CO)] (**4**) was observed by ¹H NMR spectroscopy, demonstrating that decarbonylation of acetophenone had taken place. This reaction was repeated using different numbers of equivalents of 1,3-cyclohexadiene (Table 10); even when only one equivalent of 1,3-cyclohexadiene was used the formation of [Pt(tolpy)Cl(CO)] (**4**) was observed.

When the number of equivalents of transfer hydrogenation donor was increased to four, an increase in the conversion to [Pt(tolpy)Cl(CO)] (**4**) was not observed. This may suggest that the reaction is complete at 20% conversion, or that once [Pt(tolpy)Cl(CO)] (**4**) is formed, it mediates the decarbonylation reactions preferentially to [Pt(tolpy)Cl(S-dmsO)] (**3**). 1,3-cyclohexadiene forms benzene when it donates two hydrogen atoms, this could interfere with identification of the

hydrocarbon products of the decarbonylation of acetophenone. Using the alternative hydrogen donor, *iso*-propyl alcohol, the reaction was repeated to analyse the hydrocarbon products in the reaction headspace. Benzene, carbon monoxide and methane were identified using GC-MS analysis of the reaction headspace.

Table 10: The effect of varying the number of molar equivalents of 1,3-cyclohexadiene (HD = hydrogen donor) on the relative amounts of the platinum complexes observed by ^1H NMR spectroscopy after the decarbonylation of acetophenone mediated by $[\text{Pt}(\text{tolpy})\text{Cl}(\text{S-dms})]$ (**3**)

No. equiv. HD	$[\text{Pt}^{\text{IV}}(\text{tolpy})_2\text{Cl}_2]$ (11), %	$[\text{Pt}(\text{tolpy})\text{Cl}(\text{S-dms})]$ (3), %	$[\text{Pt}(\text{tolpy})\text{Cl}(\text{CO})]$ (4), %	$[\text{Pt}(\text{tolpy})\text{Cl}(\text{H-tolpy})]$ (2), %	$[\text{Pt}(\text{tolpy})(\mu\text{-Cl})_2]$ (1), %
0	5	68	0	19	8
1	<1	68	3	12	16
2	11	58	23	8	0
4	8	53	20	7	12

Propiophenone

Propiophenone, which was previously found to be inactive, underwent decarbonylation in the presence of 1,3-cyclohexadiene. Using two equivalents of 1,3-cyclohexadiene and standard decarbonylation conditions, 65% conversion from $[\text{Pt}(\text{tolpy})\text{Cl}(\text{S-dms})]$ (**3**) to $[\text{Pt}(\text{tolpy})\text{Cl}(\text{CO})]$ (**4**) was observed. Residual starting material, $[\text{Pt}(\text{tolpy})\text{Cl}(\text{S-dms})]$ (**3**, 27%) and the formation of $[\text{Pt}^{\text{IV}}(\text{tolpy})_2\text{Cl}_2]$ (**11**, 7%) were also observed in the ^1H NMR spectrum. IPA was used as the hydrogen donor when the reaction was repeated in order to analyse the hydrocarbon products in the reaction headspace. Benzene was identified as one of the products, but C_2H_4 could not be detected using the available GC instruments.

Acetone

Previously, acetone has been found to be an inactive substrate for decarbonylation. When decarbonylation was repeated in the presence of two equivalents of 1,3-cyclohexadiene, evidence for decarbonylation was observed (13% conversion to $[\text{Pt}(\text{tolpy})\text{Cl}(\text{CO})]$ (**4**)). In order to investigate the products the

decarbonylation reaction, it was repeated using fifty equivalents of 1,3-cyclohexadiene, and carbon monoxide and methane were observed by GC-MS analysis. In order to confirm the additional hydrogen atoms required to form methane originate from the transfer hydrogen donor, the reaction was repeated using perdeuterated acetone (Figure 59). The major isotopomer observed had a mass of 19, corresponding to CHD_3 , confirming that 1,3-cyclohexadiene is the source of the hydrogen atoms incorporated in the product.

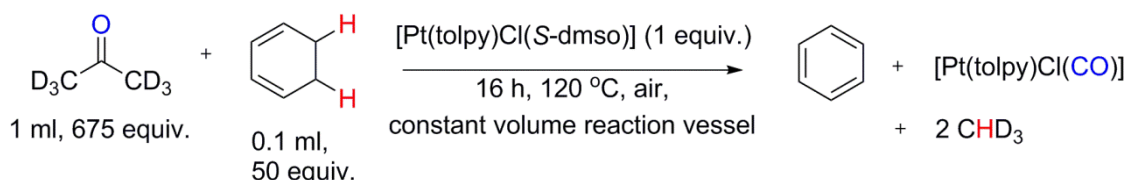


Figure 59: Decarbonylation of deuterated acetone mediated by $[\text{Pt}(\text{tolpy})\text{Cl}(\text{S-dmsO})]$ (**3**) in the presence of 1,3-cyclohexadiene.

3.5 Deuterium Labelling Studies

In order to probe the transfer hydrogenation further, the possibilities offered by selective deuteration of various substrates of the reactions were investigated. Some deuterated substrates were available commercially, whereas d_4 -cyclohexanone, d_4 -cycloheptanone and d_4 -cyclooctanone were prepared as described in the Experimental Section. The general method employed was to heat the substrate to reflux in deuterium oxide with potassium carbonate for three days under nitrogen and then isolate the product and repeat the reaction to improve the deuterium incorporation until values above 90% were achieved.

3.5.1 Cyclohexanone

2,2',6,6'-Tetradeuterated cyclohexanone

The α -positions of cyclohexanone were deuterated selectively using the method described above; according to integration, by ^1H NMR spectroscopy, the percentage deuteration was 92%. Decarbonylation of this cyclohexanone- d_4 using $[\text{Pt}(\text{tolpy})\text{Cl}(\text{S-dmsO})]$ (**3**) would then afford deuterated hydrocarbon products that could be analysed by GC-MS. The anticipated products were di-deuterated methane and terminally di-deuterated butane (Figure 60). If cyclohexanone is also a hydrogen source, through transfer hydrogenation, then depending on the regiochemistry of the dehydrogenation, there may be further deuterium incorporation.

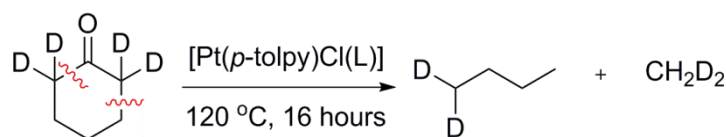


Figure 60: Anticipated hydrocarbon products for the decarbonylation of deuterated cyclohexanone

The decarbonylation of 2,2',6,6'-tetradeuterated cyclohexanone affords both di- and tri-deuterated butane (m/z 60 and 61, respectively, which correspond to $M^{+\bullet}$) with a terminal CD_2 group as the major isotopomer in each case (Figure 61). Peaks corresponding to mono-, di- and tetra-deuterated butane were also observed. This confirms that the butane observed originates from cyclohexanone and the incorporation of a third deuterium supports the view that cyclohexanone can also act as a transfer hydrogenation donor (Figure 62). Cyclohexanone may donate 2H to form cyclohexene or 4H to form cyclohexadiene which can tautomerise to phenol with either route leading to the formation of butane- d_3 .

In the first fragment there are roughly equal signals at m/z values 43, 44, and 45. The fragment observed at 43 is due to a loss of the terminal CHD_2 group from butane- d_2 to afford C_3H_7 . The fragment observed at m/z 44 is due to a loss of the terminal CHD_2 group from butane- d_3 to afford C_3H_6D . Finally, the fragment observed at m/z 45 could be due to either or both of the loss of CH_3 from butane- d_2 and the loss of CDH_2 from butane- d_3 (if the third deuterium is bonded to the second terminal carbon) to afford $C_3H_2D_2$. Furthermore, the loss of CH_3 from butane- d_2 provides further evidence that the deuterium atoms are bonded to a terminal carbon atom. The EI-MS data then suggest that the butane products are terminally di-deuterated which would support the theory that a C–C cleavage has occurred between the carbonyl and the α -carbon atom with is consistent with Figure 60.

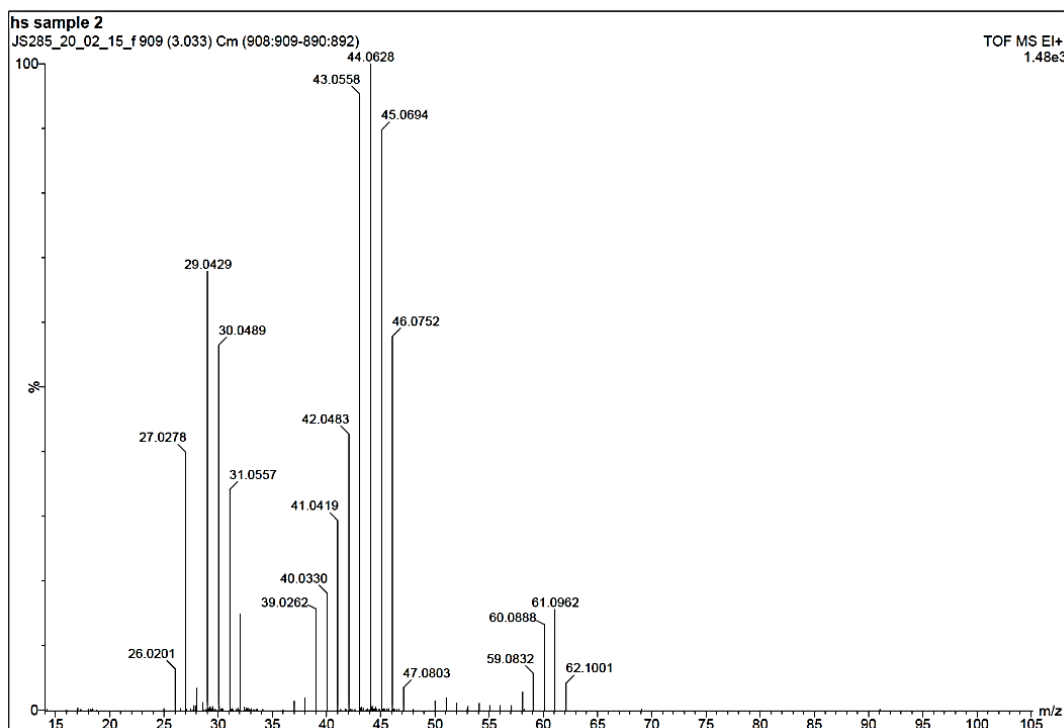


Figure 61: EI mass spectrum for the peak corresponding to tri-deuterated butane

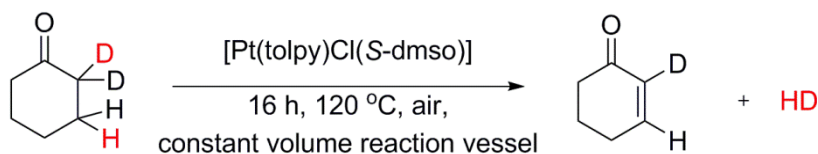


Figure 62: Proposed donation of hydrogen and deuterium atoms from 2,2',6,6'-tetradeuterated cyclohexanone to afford 2-mono-deuterated cyclohex-2-en-1-one.

Further analysis of the headspace, showed the presence of both carbon monoxide and methane and it was also possible to evaluate the distribution of the isotopomers of methane (Table 11). The major isotopomer observed was the expected product, CD_2H_2 which implies strongly that this product originates from an α -carbon atom.

Table 11: Isotopic distribution of methane (R_T 8.8 min) formed by decarbonylation of 2,2',6,6'-tetradeuterated cyclohexanone

$M^{+\bullet}$	$\text{CH}_4^{+\bullet}$	$\text{CH}_3\text{D}^{+\bullet}$	$\text{CH}_2\text{D}_2^{+\bullet}$	$\text{CHD}_3^{+\bullet}$	$\text{CD}_4^{+\bullet}$
Mass	16	17	18	19	20
Ratio	22	30	119	7	1

Deuterium Cross Labelling Studies

The reaction headspace was then analysed by GC-MS after carrying out the decarbonylation of cyclohexanone mediated by [Pt(tolpy)Cl(*S*-dmsu)] (**3**) using 200 molar equivalents of IPA-d₈ as a deuterium source. Curiously, incorporation of deuterium was not observed, and non-deuterated butane was the major product determined by GC-MS. Integration of the ¹H NMR spectrum showed 90% conversion from [Pt(tolpy)Cl(*S*-dmsu)] (**3**) to [Pt(tolpy)Cl(CO)] (**4**). The formation of [Pt(tolpy)Cl(CO)] (**4**) confirms that decarbonylation took place but the absence of deuterium incorporation into the products may suggest that cyclohexanone itself still dominated the hydrogen donation which was thought to be due to its large excess. When a 50:50 solution of cyclohexanone and IPA-d₈ (50 mol%) and heated under the same conditions, still only non-deuterated butane was observed by GC-MS analysis. This suggests that under these conditions cyclohexanone is a better hydrogen donor than d₆-IPA. As discussed above (in Section 3.1.3), IPA and other alcoholic hydrogen sources are often used in combination with a base but there is no base present under the conditions employed here as it is anticipated that its presence would cause scrambling of the acidic C_α-H hydrogen atoms. As such, IPA appears not to be useful in the study of this reaction.

Using 1,3-cyclohexadiene as the hydrogen donor, the decarbonylation of 2,2',6,6'-tetradeuterated and per-deuterated cyclohexanone were investigated. Assuming 1,3-cyclohexadiene is the major hydrogen donor, decarbonylation of 2,2',6,6'-tetradeuterated cyclohexanone should afford di-deuterated methane and terminally di-deuterated butane and the decarbonylation of perdeuterated cyclohexanone should afford 1,1',2,2',3,3',4,4'-octadeuterated butane and di-deuterated methane.

The major isotopomer for methane observed when 2,2',6,6'-tetradeuterated cyclohexanone was studied was indeed di-deuterated methane. However, for butane, non-deuterated butane was the major isomer observed, suggesting further hydrogen incorporation from the 1,3-cyclohexadiene. Smaller peaks corresponding to mono-, di- and tri-deuterated butane were also observed (each isotopomer makes up less than 5% of the total ion count for butane).

Table 12: Distribution of isotopomers observed by GC-MS analysis of the reaction headspace after the decarbonylation of 2,2',6,6'-tetradeuterated and per-deuterated cyclohexanone in the presence of 1,3-cyclohexadiene

2,2',6,6'-Tetradeuterated cyclohexanone	Methane at R_T 8.8 min									
	Mass	16	17	18	19	20				
	Ratio	15	19	100	3	1				
	Butane									
	Mass	58	59	60	61					
	Ratio	41	2	1	2					
Per-deuterated cyclohexanone	Methane at R_T 8.8 min									
	Mass	16	17	18	19	20				
	Ratio	4	6	23	2	1				
	Butane at R_T 15 min									
	Mass	58	59	61	62	63	64	65	66	67
	Ratio	2	2	10	35	218	218	190	7	1

When perdeuterated cyclohexanone was studied, again the major isotopomer of methane observed was di-deuterated methane. However, instead of the expected d₈-butane, this time a broad distribution of isotopomers were observed the most abundant of which corresponded to penta-, hexa- and hepta-deuterated butane. The difference in deuterium incorporation observed for the two hydrocarbon products observed hints at a process where the methane and butane are formed in two separate steps. In both cases the expected isotopomer, di-deuterated methane was observed for methane but a range of isotopomers were observed for butane. This may suggest that the formation of each product proceeds by separate processes. The distribution of butane isotopomers observed may be due to scrambling but may also suggest an alkene or dialkene intermediate (Figure 63).

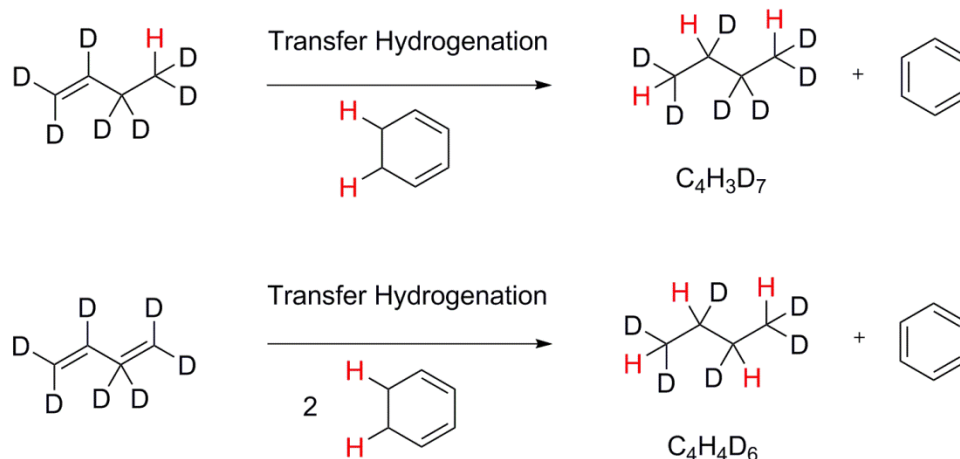


Figure 63: Possible transfer hydrogenation of d₇-butene and d₇-butadiene intermediates.

3.5.2 Cycloheptanone

Using GC-MS analysis of the reaction headspace, d₂-cyclohexene (Figure 64) was observed as the major product of decarbonylation of 2,2',7,7'-tetradeuterated cycloheptanone. Although, both cyclohexane and d₂-cyclohexene would have the same molecular ion, $m/z = 84$, the fragmentation pattern for each compound is slightly different. Fragmentation of cycloalkanes is characterised by the loss of ethylene ($m/z 28$) from the parent molecule or intermediate radical-ion and the other major fragments observe for cyclohexane would be 69, 56 and 41. A major fragment ion for d₂-cyclohexene would also appear at $m/z 56$ formed *via* a retro-Diels-Alder fragmentation and additional fragments at m/z values 69, 68, 41 and 39 would also be expected and all of these fragment ions were observed in the mass spectrum.

The formation of the di-deuterated product suggests that the alkene double bond in the product forms between the two α -carbon atoms. There is also a significant peak at $m/z 82$ for non-deuterated cyclohexene, indicating that deuterium scrambling has occurred. Smaller peaks for butane and benzene were also observed in the total ion chromatogram. The formation of benzene is proposed to go *via* platinum mediated dehydrogenation of cyclohexene.

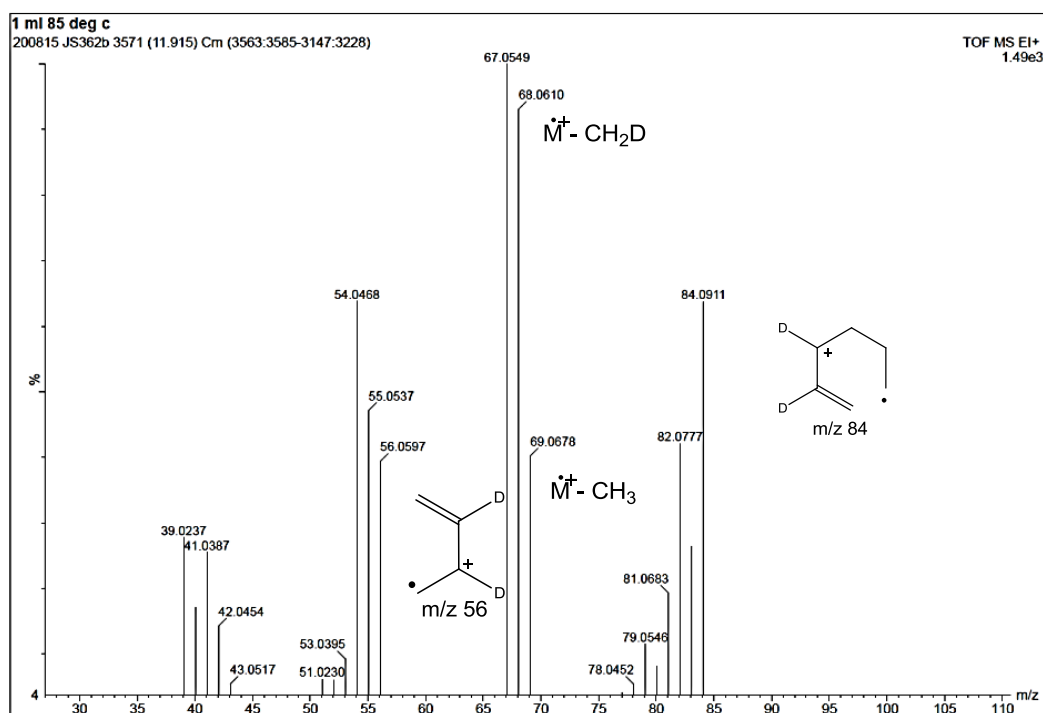


Figure 64: Mass spectrum of d_2 -cyclohexene observed as the major product of decarbonylation of d_4 -cycloheptanone using GC-MS of the reaction headspace

3.5.3 Cyclooctanone

Previously the GC-MS analysis of the reaction headspace identified cycloheptene as the product of decarbonylation of cyclooctanone. The major product of the decarbonylation of d_4 -cyclooctanone was d_2 -cycloheptene (Figure 65) and a small amount of dms was also observed. The mass spectra for cycloheptane and d_2 -cycloheptene are very similar, however, the spectrum for cycloheptane should include a major fragment at $m/z = 29$ assigned to an ethyl ion, $[\text{CH}_3\text{CH}_2]^+$. As observed for cycloheptanone, the formation of the di-deuterated isotopomer suggests that the alkene double bond in the product forms between the two α -carbon atoms in the starting material.

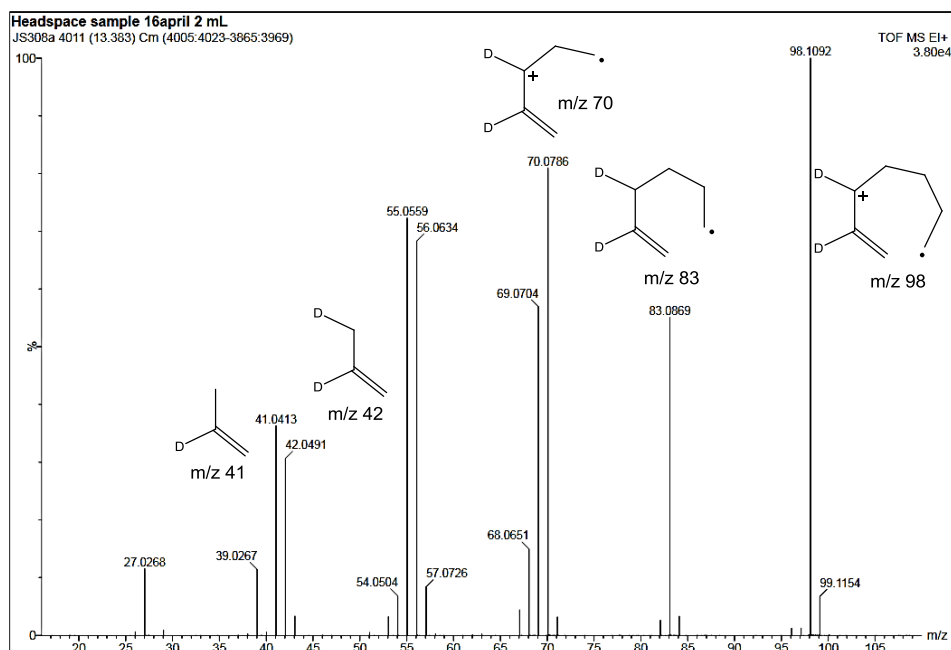


Figure 65: Mass spectrum of d_2 -cycloheptene observed using GC-MS at 13.4 minutes

3.6 Observation of New Platinum Species Formed During the Decarbonylation Reactions

The formation of $[\text{Pt}(\text{tolpy})\text{Cl}(\text{CO})]$ (**4**) by decarbonylation was not always clean and the formation of other cycloplatinated species, namely $[\text{Pt}(\text{tolpy})(\mu\text{-Cl})]$ (**1**), $[\text{Pt}(\text{tolpy})\text{Cl}(\text{H-tolpy})]$ (**2**) and $[\text{Pt}^{\text{IV}}(\text{tolpy})_2\text{Cl}_2]$ (**11**) were also observed. They may be formed as intermediates, decomposition products or by competitive reactions. Whether the formation of these products is important to the decarbonylation reaction is discussed here.

3.6.1 Formation and Decarbonylation Activity of $[\text{Pt}(\text{tolpy})(\mu\text{-Cl})]$ (**1**)

The formation of the dimeric complex **1** was observed when attempting decarbonylation of the less active substrates acetophenone, benzophenone, dicyclohexylketone, caprolactone and 2-hexanone with $[\text{Pt}(\text{tolpy})\text{Cl}(\text{S-dms})]$ (**3**). This suggests that complex **1** is not involved directly in the decarbonylation process, rather that it results from the loss of coordinated dms from **3** leading to a 14-electron species, and then dimerisation to **1** competes with the decarbonylation chemistry. In Chapter Two the decarbonylation activity of this complex was demonstrated and it was found to undergo quantitative conversion to $[\text{Pt}(\text{tolpy})\text{Cl}(\text{CO})]$ (**4**) upon decarbonylation of cyclohexanone.

3.6.2 Formation and Decarbonylation Activity of [Pt(tolpy)Cl(H-tolpy)] (2)

The formation of [Pt(tolpy)Cl(H-tolpy)] (2) was observed during decarbonylation of acetophenone, benzophenone, dicyclohexylketone and caprolactone. This complex is similar to the platinum complexes found to decarbonylate cyclohexanone. Complex 2 has two tolpy ligands which indicated that decomposition of a platinum complex, starting material or [Pt(tolpy)Cl(CO)] (4), must have taken place to provide the additional free tolpy ligand.

The complex was synthesised in order to evaluate the activity of the complex towards catalysing decarbonylation reactions. When investigated it was found that it is not an active decarbonylating agent, but instead underwent extensive decomposition. Analysis of the reaction headspace by GC showed no evidence for the formation of butane by decarbonylation of cyclohexanone. Due to extensive decomposition of the platinum species, the ^1H NMR spectrum was very messy but it does show the presence of [Pt^{IV}(tolpy)₂Cl₂] (11) presumably formed by the oxidation of [Pt(tolpy)Cl(H-tolpy)] (2). The lack of activity observed may be due the additional steric hindrance provided by the phenyl substituent compared to the active complex, [Pt(tolpy)Cl(py)] (5), hindering attack of the ketone and preventing the first stage of the reaction. However, the bottom face of the square planar complex is unhindered, providing space for ligand coordination (Figure 66).

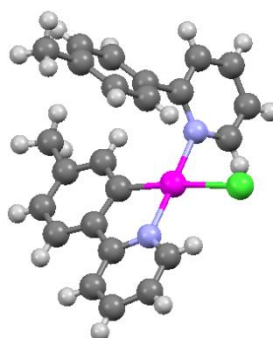


Figure 66: X-ray crystal structure of [Pt(tolpy)Cl(H-tolpy)] (2) showing the tolpy ligand blocking the upper face of the complex.

3.6.3 Formation of [Pt^{IV}(tolpy)₂Cl₂] (11)

The presence of [Pt^{IV}(tolpy)₂Cl₂] (11) was observed after the decarbonylation of cyclopentanone, cycloheptanone, α -tetralone, acetophenone, propiophenone, benzophenone, dicyclohexylketone and caprolactone. Although it was not observed during the decarbonylation of neat cyclohexanone, it was observed

after some of the reactions that took place in acetonitrile. It was also observed after the unsuccessful decarbonylation of buteriophenone and when $[\text{Pt}(\text{tolpy})\text{Cl}(\text{H-tolpy})]$ (**2**) was evaluated for the decarbonylation of cyclohexanone, even though no reaction took place. The formation of this complex in the absence of decarbonylation suggests that its formation is due to oxidation of the decomposition product $[\text{Pt}(\text{tolpy})\text{Cl}(\text{H-tolpy})]$ (**2**), under the relatively harsh reaction conditions rather than as part of the decarbonylation process. The formation of $[\text{Pt}(\text{tolpy})\text{Cl}(\text{H-tolpy})]$ (**2**) was observed in all cases where $[\text{Pt}^{\text{IV}}(\text{tolpy})_2\text{Cl}_2]$ (**11**) was observed, except for when propiophenone or buteriophenone were studied. The oxidation of cyclometallated platinum(II) complexes to platinum(IV) has been reported previously by Newman and co-workers;¹⁸⁹ oxidation of $[\text{Pt}(p\text{-fluoro-ppy})\text{Cl}(\text{H}p\text{-fluoro-ppy})]$ leads to the $[\text{Pt}(p\text{-fluoro-ppy})_2\text{Cl}_2]$ (Figure 67). Both of these pathways require oxidative addition either by Cl_2 or ClX , a source of which is not present during the decarbonylation reactions. It is suspected that the formation of $[\text{Pt}^{\text{IV}}(\text{tolpy})_2\text{Cl}_2]$ (**11**) proceeds *via* oxidative addition of the C–H bond of the tolpy ligand of complex **2**, followed by coordination of a chloride ligand, present in solution after the decomposition of a $[\text{Pt}(\text{tolpy})\text{Cl}(\text{L})]$ species.

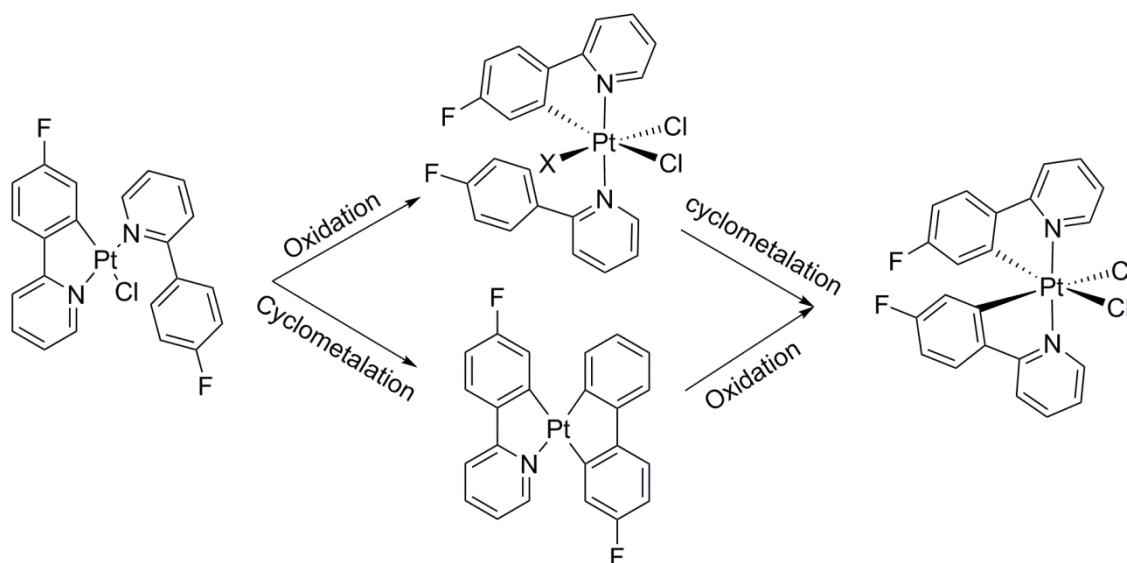


Figure 67: Possible routes to $[\text{Pt}(p\text{-fluorophenylpyridine})_2\text{Cl}_2]$. proposed by Newman and co-workers¹⁸⁹

3.7 *In Situ* Infra-red (IR) Spectroscopy

In situ IR spectroscopy was used to monitor the formation of [Pt(tolpy)Cl(CO)] (**4**) ($\bar{\nu}(\text{CO}) \approx 2098 \text{ cm}^{-1}$ dependent on the solvent ketone) during the decarbonylation reactions and to ascertain the time required for its quantitative formation. It should also be possible to identify whether there is an induction period or sigmoidal kinetics, which would be characteristic of nanoparticle-catalysed reactions. Finally, it should allow for comparison between different substrates and different platinum catalysts. The decarbonylation of different ketone substrates mediated by [Pt(tolpy)Cl(L)] (L = S-dmsso, CO, py) and [Pt(tolpy)(μ -Cl)] were monitored using *in situ* IR spectroscopy (method is described in the Experimental section). The silicon IR probe was introduced into the reaction vessel and spectra were recorded every two minutes using a thermocouple to record the internal reaction temperature.

3.7.1 *In Situ* IR Spectroscopy of the Decarbonylation of Cyclohexanone

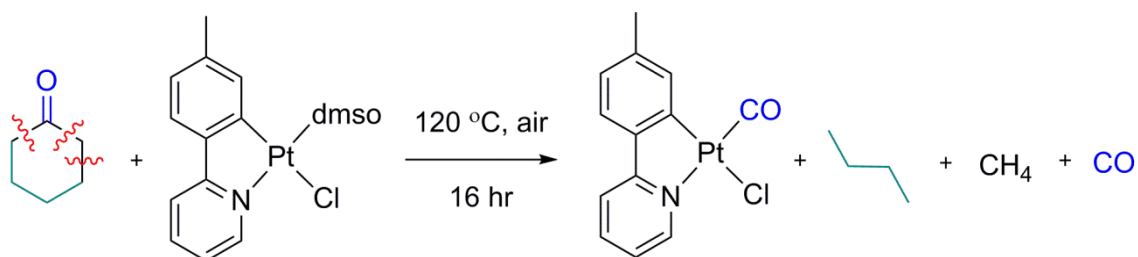


Figure 68: Decarbonylation of cyclohexanone mediated by [Pt(tolpy)Cl(S-dmsso)] (**3**)

Although the oil bath was heated to 120 °C the internal temperature of the solution was measured to be 108 °C using a thermocouple inside the reaction vessel (Figure 68). No induction period was observed and the formation of [Pt(tolpy)Cl(CO)] (**4**) was seen within the first two minutes (1st scan) with $\bar{\nu}(\text{CO})$ measured at 2098 cm^{-1} in cyclohexanone. The initial results showed that complete conversion from [Pt(tolpy)Cl(S-dmsso)] (**3**) to [Pt(tolpy)Cl(CO)] (**4**) occurred within 1.5 hours (Figure 69). The peak at 2098 cm^{-1} increased in intensity until 90 minutes had elapsed, where it started to decrease with concomitant growth of two, new carbonyl stretches at 2059 cm^{-1} and 2071 cm^{-1} . During the course of the reaction, the peak corresponding to [Pt(tolpy)Cl(CO)] (**4**) decreases to a third of its maximum intensity; although quantitative conversion to **4** was observed in all cases, difficulty in reproducibility of isolated yields was encountered (between 0 – 60%) which could be explained by decomposition of the complex. The vibrational frequencies of these new peaks are lower than reported for free carbon monoxide, suggesting the presence of a coordinated

carbonyl species. The peak at 2059 cm^{-1} reaches its maxima before the peak at 2071 cm^{-1} and then begins to gradually decrease.

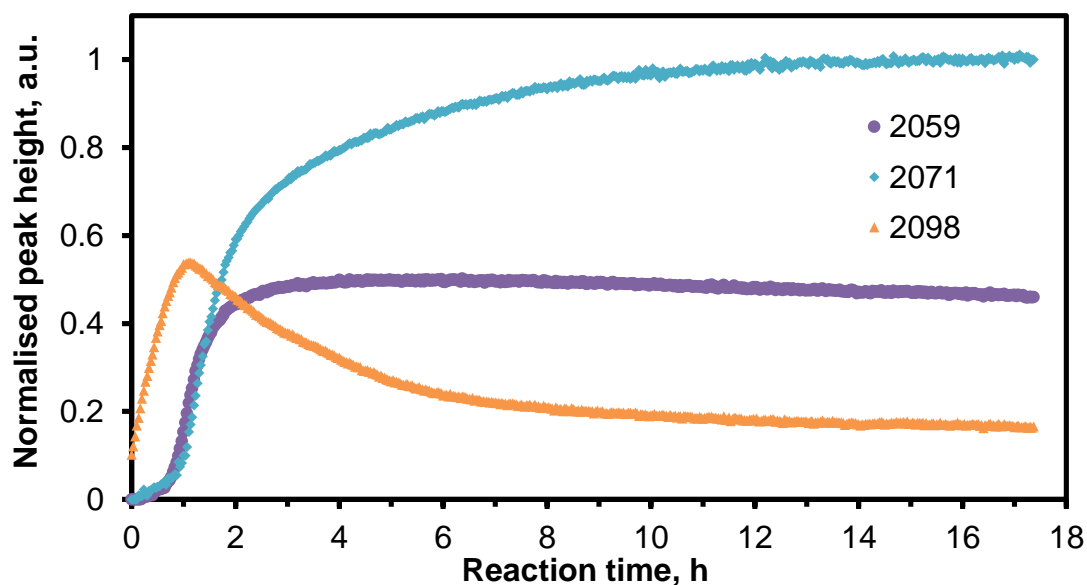


Figure 69: Plot of peak height as a function of time as recorded during *in situ* IR monitoring of the reaction between cyclohexanone and $[\text{Pt}(\text{tolpy})\text{Cl}(\text{S-dms})]$ (**3**). The formation of $\bar{\nu}(\text{CO})$ at 2098 cm^{-1} corresponding to complex **4** is shown in orange and the formation of two other $\bar{\nu}(\text{CO})$ peaks at 2059 cm^{-1} and 2071 cm^{-1} are shown in purple and teal respectively. Data were collected every two minutes and normalised to the maximum intensity of the peak at 2071 cm^{-1} .

Two possible origins of these peaks are carbon monoxide interacting with the silicon probe used for *in situ* IR spectroscopy and platinum nanoparticles with carbon monoxide adsorbed on the surface. Guczi *et al.* have reported that the vibrational frequency for the stretch relating to carbon monoxide adsorbed on 50 nm palladium nanoparticles stabilised by polyvinylpyrrolidone (PVP) appears at 2047 cm^{-1} in 2-ethoxyethanol.¹⁹⁰ Published *in situ* IR data for carbon monoxide ligands bound to surface of $\text{Pt}/\text{Al}_2\text{O}_3$ have vibrational frequencies between $2093 - 2064\text{ cm}^{-1}$ which are very similar to those observed in this study.¹⁹¹ Zecchina *et al.* studied the IR spectra of silicas in the presence of carbon monoxide;¹⁹² the vibrational frequency of carbon monoxide physisorbed in channels was reported to be 2138 cm^{-1} . This suggests that the peaks observed at 2071 cm^{-1} and 2059 cm^{-1} are due to platinum nanoparticles with carbon monoxide adsorbed on the surface. The presence of two different vibrational frequencies suggests that they are due to different environments at the coordination site; both values are consistent with terminal coordination of CO.

3.7.2 Varying the Ketone Substrate

The use of cyclohexanone, cyclopentanone, β -tetralone, cycloheptanone and cyclooctanone as substrates was also studied using this method (Figure 70). The results for cyclopentanone and cyclohexanone are very similar to one another, but, it seems like an induction period is present during the decarbonylation of cyclooctanone and β -tetralone. While for cycloheptanone, the reaction begins more slowly for the cyclopentanone or cyclohexanone Unlike the other cyclic ketones, decay in the peak at 2098 cm^{-1} corresponding to $[\text{Pt}(\text{tolpy})\text{Cl}(\text{CO})]$ (**4**) is not observed for cyclooctanone or β -tetralone. Each substrate will now be considered in more detail.

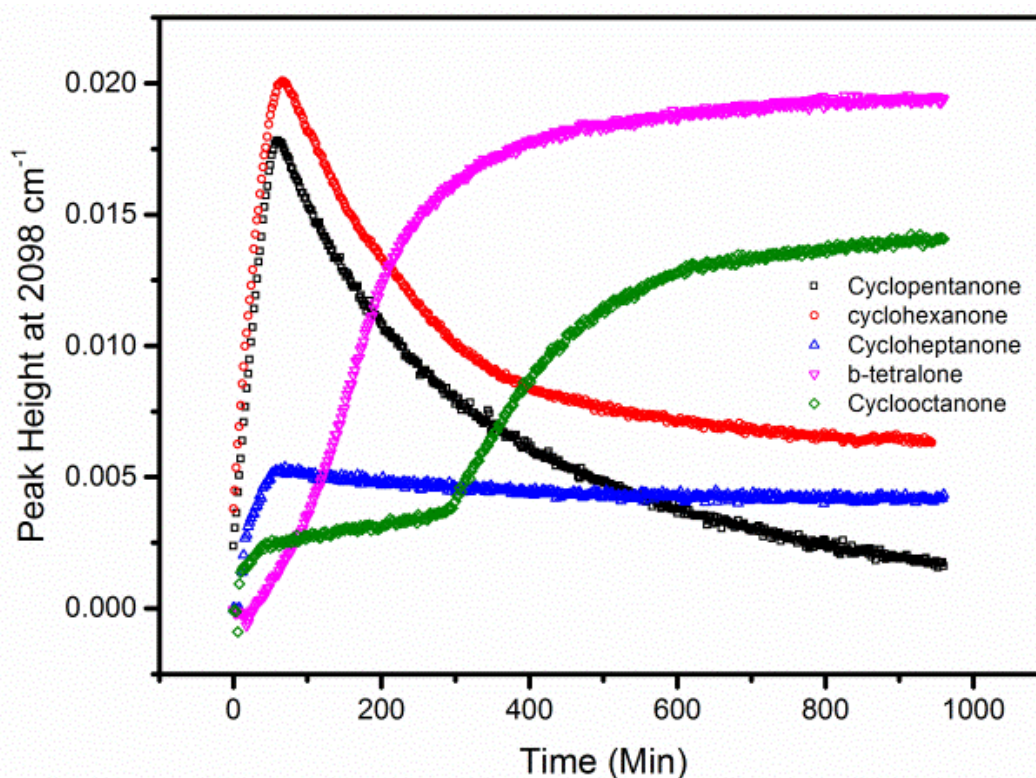


Figure 70: Plot of intensity of the peak corresponding to $\bar{\nu}(\text{CO})$ of $[\text{Pt}(\text{tolpy})\text{Cl}(\text{CO})]$ (**4**) as a function of time as recorded during *in situ* IR monitoring of the reaction between different ketones and $[\text{Pt}(\text{tolpy})\text{Cl}(\text{S-dmsol})]$ (**3**). The peak height is given in arbitrary units.

Cyclopentanone

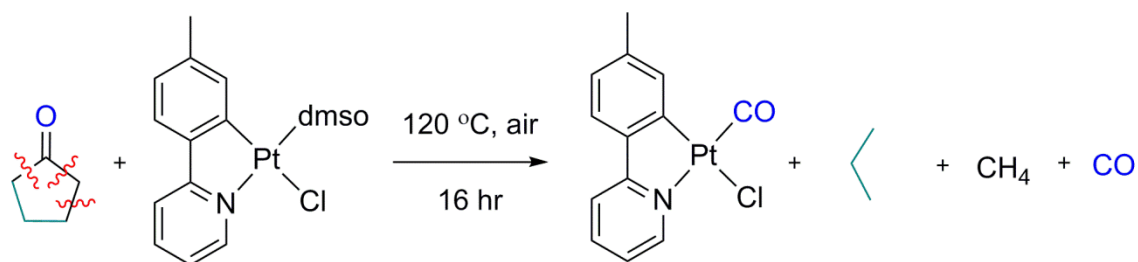


Figure 71: Hydrocarbon products of the decarbonylation of cyclopentanone by [Pt(tolpy)Cl(S-dmsso)] (3)

The decarbonylation was carried out at an internal temperature of 112 °C (Figure 71). Formation of the [Pt(tolpy)Cl(CO)] (4) was observed within the first two minutes (1st scan) with $\bar{\nu}(\text{CO})$ measured at 2100 cm^{-1} (Figure 72). This peak increased in intensity for 60 minutes, after which its intensity started to fall and a new signal was observed at 2064 cm^{-1} . This second peak grew to a maximum absorbance after six hours, and extensive decomposition of platinum complex was observed visibly (for an example of this see Figure 79). These results were similar to those observed during the decarbonylation of cyclohexanone mediated by [Pt(tolpy)Cl(S-dmsso)] (3) and, in addition to the similar pattern of products for both substrates, further supports the proposition that both substrates undergo decarbonylation by similar mechanisms.

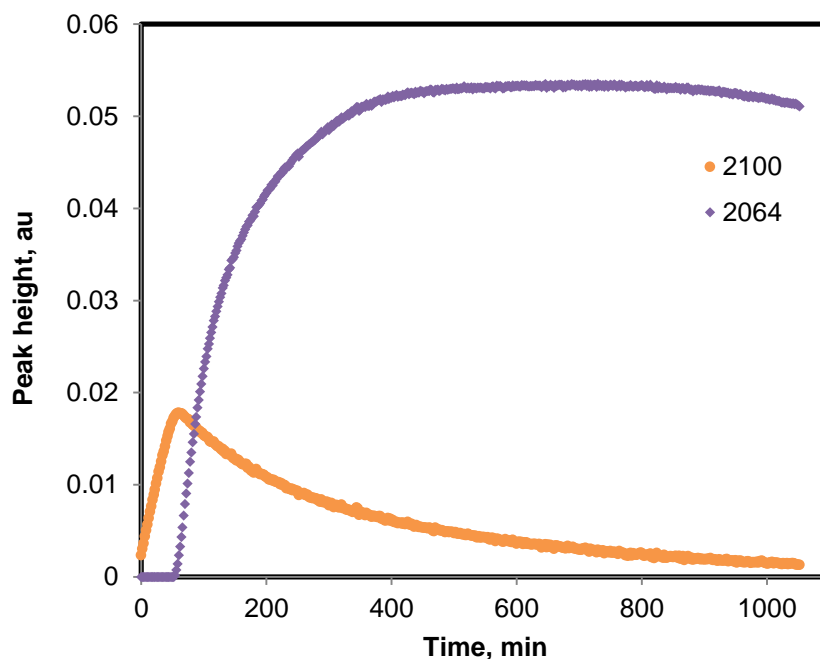


Figure 72: Plot of intensity for the peaks at 2064 cm^{-1} (purple) and 2100 cm^{-1} (orange) as a function of time (min^{-1}) measured using an *in situ* IR spectroscopy for the decarbonylation of cyclopentanone.

Cycloheptanone

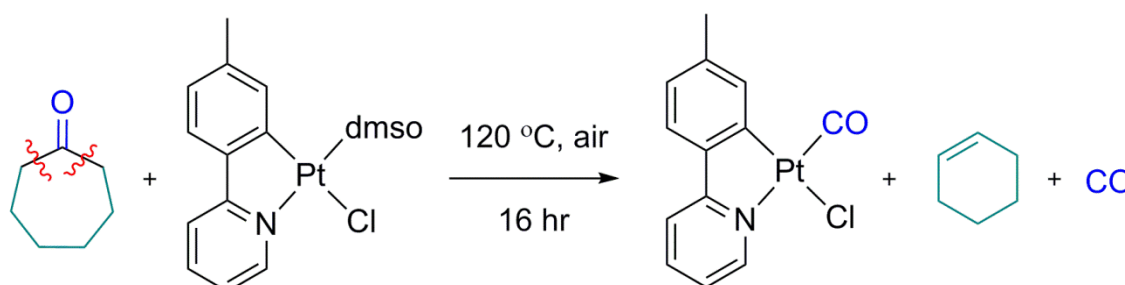


Figure 73: Decarbonylation of cycloheptanone mediated by $[\text{Pt}(\text{tolpy})\text{Cl}(\text{S-dms})]$ (**3**)

The decarbonylation was monitored at an internal temperature of $110.5\text{ }^{\circ}\text{C}$ (Figure 73) and the formation of $[\text{Pt}(\text{tolpy})\text{Cl}(\text{CO})]$ (**4**) was observed within the first two minutes (1st scan) with $\bar{\nu}(\text{CO})$ measured at 2099 cm^{-1} (Figure 74). The formation of a new metal carbonyl species with a vibrational frequency around 2060 cm^{-1} observed in the decarbonylation of cyclopentanone and cyclohexanone was not however observed here. However, instead a peak appeared at 2033 cm^{-1} appeared within two minutes and grew for an hour before gradually decaying. Signs of extensive decomposition of the platinum species (**4**) were observed

visibly during the reaction, which suggests that platinum nanoparticles are present in the reaction solution.

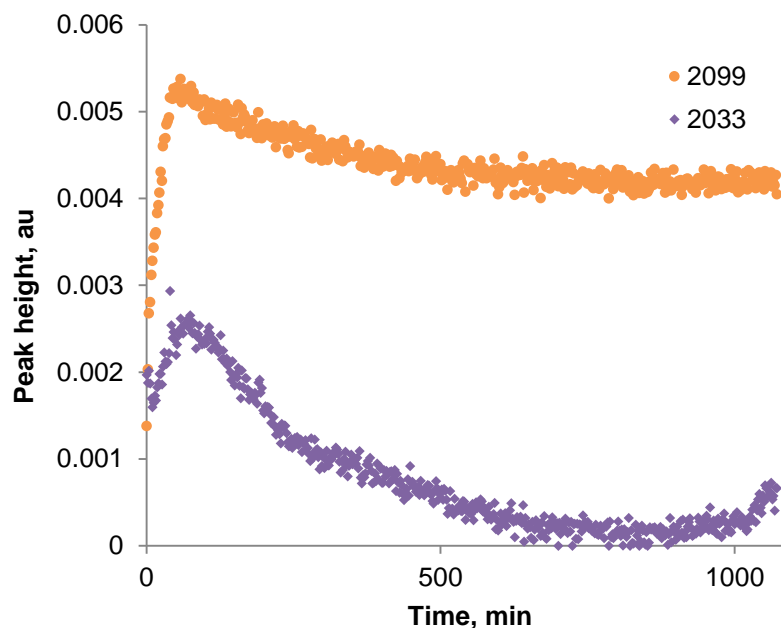


Figure 74: Plot of intensity for the peaks at 2033 cm^{-1} (purple) and 2099 cm^{-1} (orange) as a function of time (min^{-1}) during the decarbonylation of cycloheptanone.

Cyclooctanone

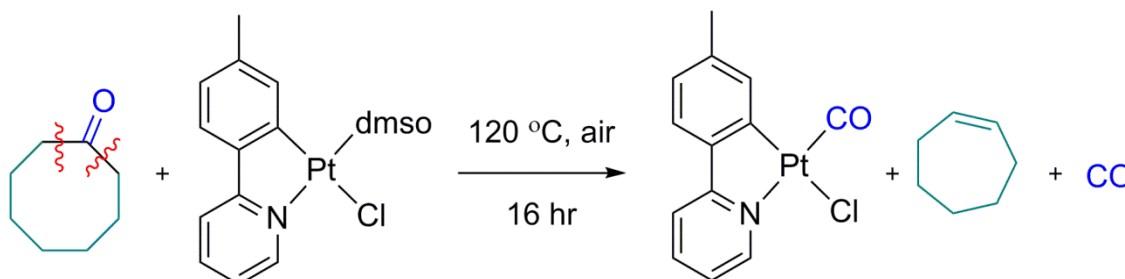


Figure 75: Decarbonylation of cyclooctanone mediated by $[\text{Pt}(\text{tolpy})\text{Cl}(\text{S-dms})]$ (**3**)

The decarbonylation of cyclooctanone was monitored at an internal temperature 109 °C (Figure 75), and the formation of $[\text{Pt}(\text{tolpy})\text{Cl}(\text{CO})]$ (**4**) was again observed within the first two minutes (1st scan) with $\bar{\nu}(\text{CO})$ measured at 2098 cm^{-1} (Figure 76). An additional peak at 2053 cm^{-1} , which is thought to be due to adsorption of carbon monoxide formed in the reaction onto platinum particles, was also observed and gradually increased over the course of the study. Interestingly the peak at 2098 cm^{-1} , assigned to $[\text{Pt}(\text{tolpy})\text{Cl}(\text{CO})]$ (**4**), very gradually increased in intensity for the first five hours after which its intensity increased more rapidly.

This has not been observed previously for the other cyclic ketones studied and is indicative of an induction period for formation of this species. In general, induction periods can be indicative of an increase in temperature due to an exothermic process, transformation of a pre-catalyst to the active catalyst or transformation of the substrate to a more reactive species. Here, complex **4**, which is formed by decarbonylation, is the species studied, rather than the organic products of the reaction, so an induction period caused by formation of an alternate, true catalyst would not be observed.

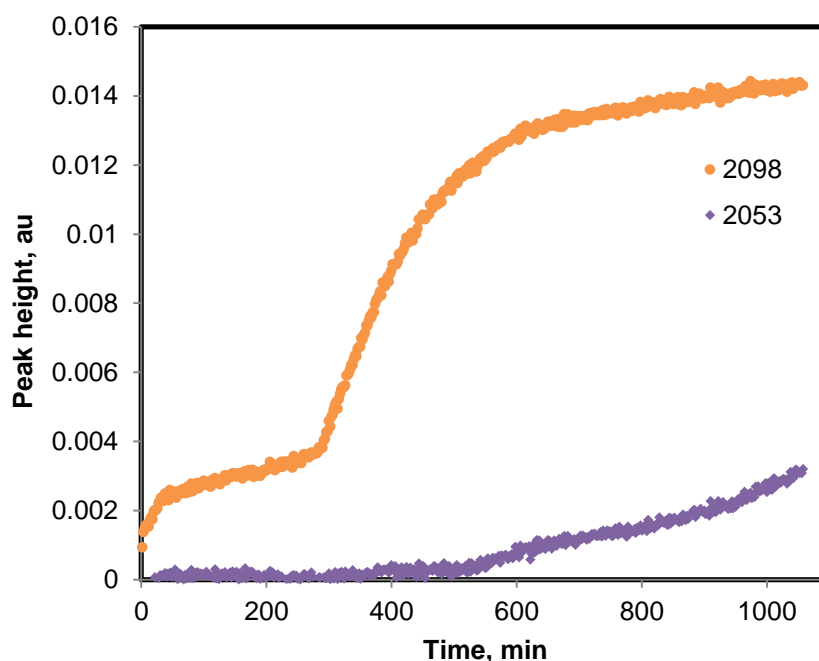


Figure 76: Plot of intensity for the peaks at 2053 cm^{-1} and 2098 cm^{-1} as a function of time (min^{-1}) measured during the decarbonylation of cyclooctanone.

β -Tetralone

When the decarbonylation of β -tetralone was monitored at an internal temperature of 108 °C (Figure 77), the $\bar{\nu}(\text{CO})$ stretch of $[\text{Pt}(\text{tolpy})\text{Cl}(\text{CO})]$ **4** was not observed for 15 minutes, after which it began to grow in intensity concomitant with the formation of another carbonyl species with a $\bar{\nu}(\text{CO})$ observed at 2034 cm^{-1} . Overall, these IR data are similar to that collected for cycloheptanone, which may suggest that they undergo decarbonylation *via* a similar mechanism. The peaks observed at 2033 and 2034 cm^{-1} for cycloheptanone and β -tetralone, respectively, were observed during the decarbonylation of the other substrates.

These values are still consistent with carbon monoxide coordinated to platinum particles. Bazin *et al.* reported IR absorptions at 2033 cm^{-1} which they assigned to adsorption of carbon monoxide onto low coordinated sites on small platinum particles.¹⁹³

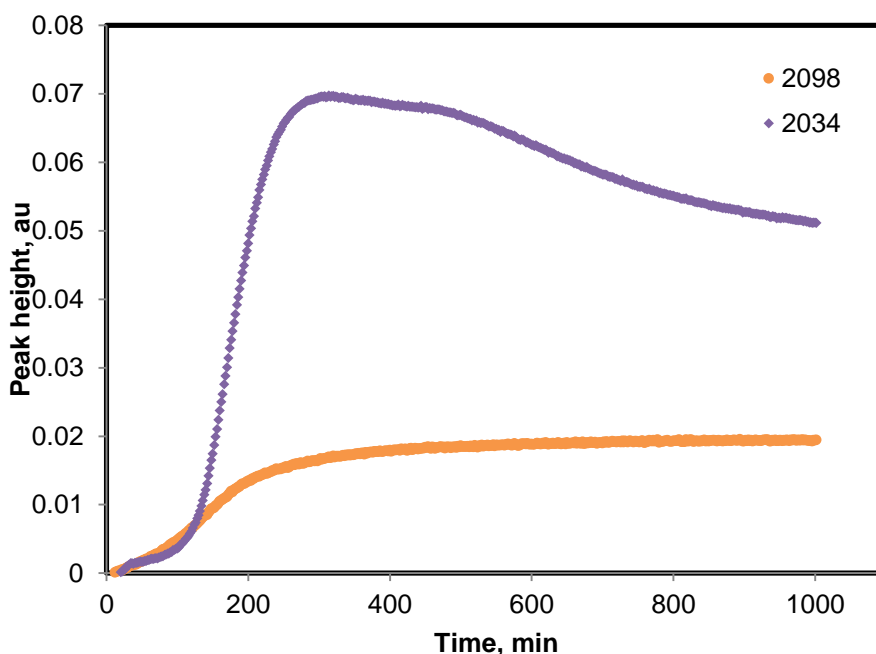


Figure 77: Plot of intensity for the peaks at 2034 cm^{-1} (purple) and 2098 cm^{-1} (orange) as a function of time (min^{-1}) measured during the decarbonylation of β -tetralone.

3.7.3 Varying the Metal Complex used to Catalyse Decarbonylation Reactions

The decarbonylation reactions of cyclohexanone mediated by $[\text{Pt}(\text{tolpy})(\mu\text{-Cl})_2]$ (**1**), $[\text{Pt}(\text{tolpy})\text{Cl}(\text{S-dms})]$ (**3**), $[\text{Pt}(\text{tolpy})\text{Cl}(\text{CO})]$ (**4**) and $[\text{Pt}(\text{tolpy})\text{Cl}(\text{py})]$ (**5**) were also monitored *in situ* using IR spectroscopy at internal temperatures in the range $107 - 110\text{ }^\circ\text{C}$. For all complexes studied, a small absorption at 2098 cm^{-1} corresponding to $\bar{\nu}(\text{CO})$ of $[\text{Pt}(\text{tolpy})\text{Cl}(\text{CO})]$ (**4**) was observed within the first two minutes (one scan) and then an unidentified $\bar{\nu}(\text{CO})$ stretch in the region $2063 - 2066\text{ cm}^{-1}$ was observed after around 90 minutes for all complexes except $[\text{Pt}(\text{tolpy})\text{Cl}(\text{py})]$ (**5**) (Figure 78). The peak height of the new absorption is greater than the maximum peak height for the peak at 2098 cm^{-1} (by at least a factor of ten for $[\text{Pt}(\text{tolpy})\text{Cl}(\text{CO})]$ (**4**) and $[\text{Pt}(\text{tolpy})(\mu\text{-Cl})_2]$ (**1**)). The formation of the peaks in the region $2063\text{-}2066\text{ cm}^{-1}$ was very similar for $[\text{Pt}(\text{tolpy})(\mu\text{-Cl})_2]$ (**1**) and $[\text{Pt}(\text{tolpy})\text{Cl}(\text{CO})]$ (**4**). However, the maximum peak height was much lower for $[\text{Pt}(\text{tolpy})\text{Cl}(\text{S-dms})]$ (**3**). This suggests that free or coordinated dms inhibits the

formation of the species which gives rise to the absorption at 2066 cm^{-1} , suspected to be carbon monoxide coordinated to platinum particles, this may be due to competitive coordination to the metal surface. As mentioned above, sulfur containing ligands, such as CS_2 are well known poisons for platinum nanoparticle catalysts.¹⁷² These results may also suggest that the presence of free pyridine in solution prevents coordination/adsorption of carbon monoxide onto such particles or that there is simply less free CO generated to adsorb onto the surface of platinum particles.

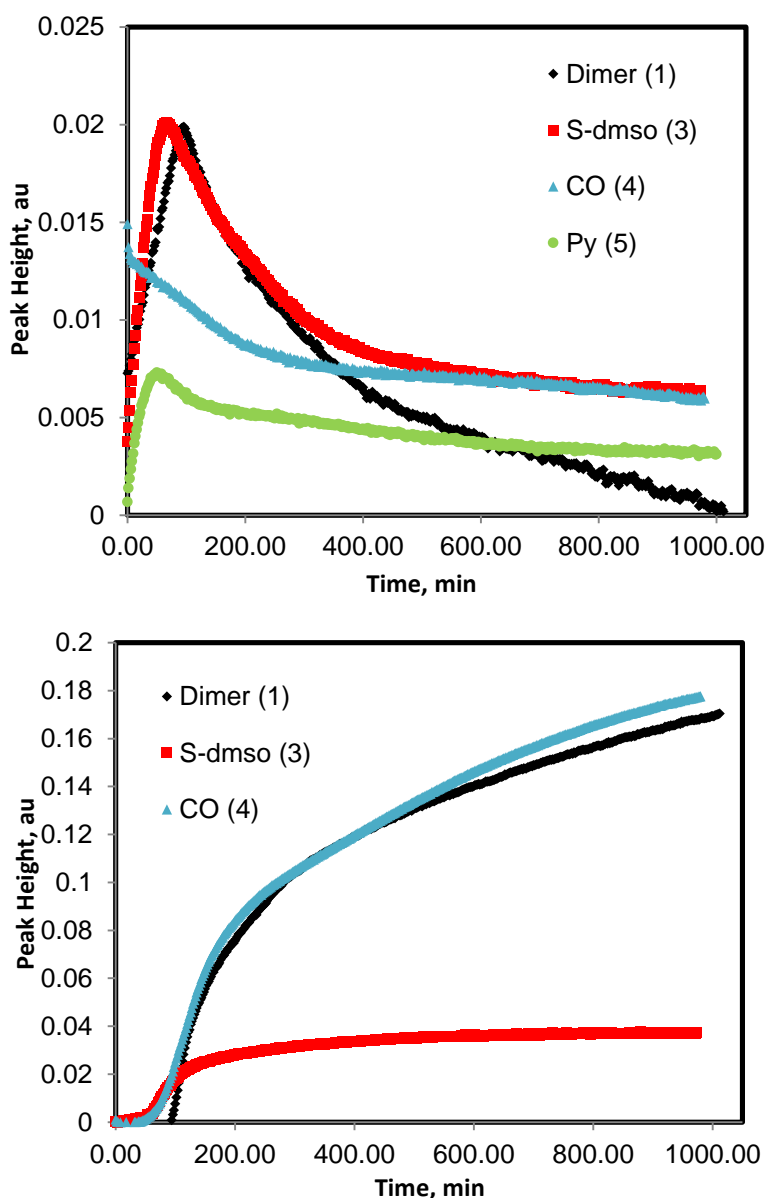


Figure 78: Comparison of the change in peak intensity at 2098 cm^{-1} (upper) and $2063\text{-}2071\text{ cm}^{-1}$ (lower) as a function of time during the decarbonylation of cyclohexanone mediated by $[\text{Pt}(\text{tolpy})(\mu\text{-Cl})_2]/[\text{Pt}(\text{tolpy})\text{Cl}(\text{L})]$ and monitored by *in situ* IR spectroscopy

3.8 Distinguishing Between Molecular and Nanoparticle Catalysis

In all reactions where decarbonylation took place, partial decomposition of the platinum complex was also suspected (Figure 79) and in the *in situ* IR spectroscopic data discussed above, the formation of new peaks consistent with carbon monoxide bound to transition metal particles was observed. Palladium nanoparticles have been reported to be active for C–H activation,^{154, 194-196} it is possible that during the decomposition of the platinum(II) species, reactive platinum(0) nanoparticles are formed which may somehow play a role in the overall decarbonylation reaction.

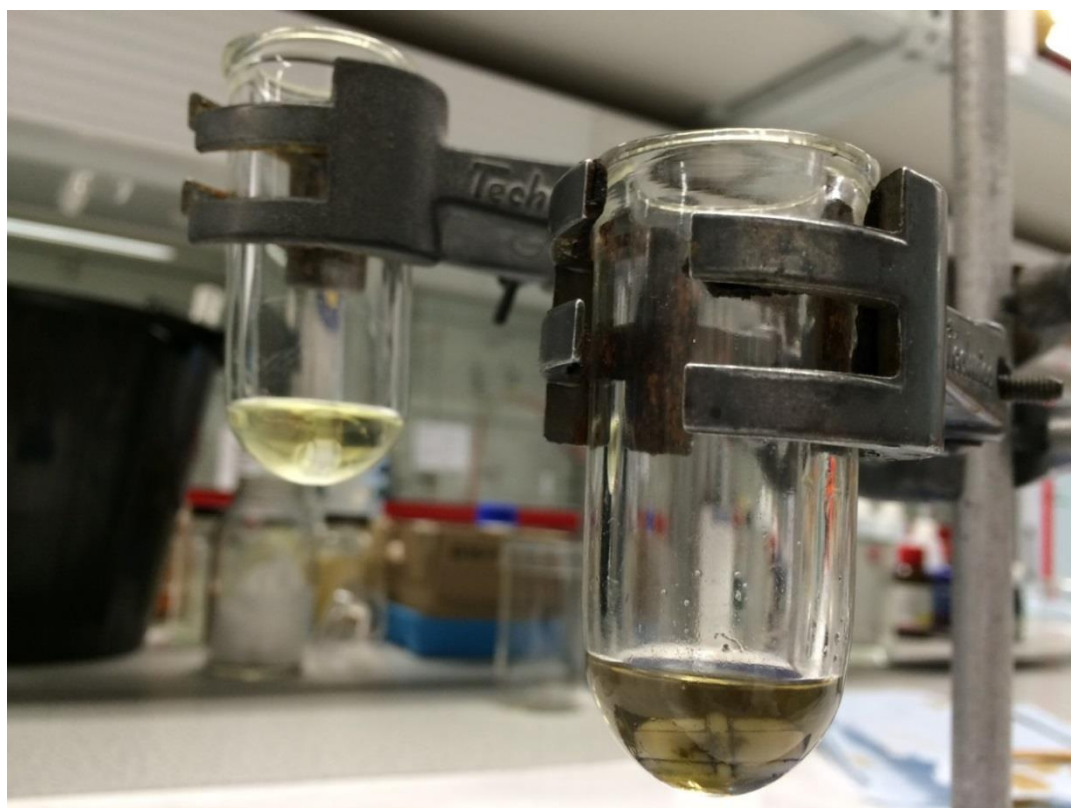


Figure 79: Photograph taken of the reaction solutions of two reactions, at the beginning (left) and end (right) of the decarbonylation of cyclohexanone mediated by [Pt(tolpy)Cl(*S*-dms)].

3.8.1 Dynamic Light Scattering (DLS)

One of the methods used for detecting the presence of nanoparticles is dynamic light scattering, and an advantage of this technique is that it is conducted in solution (*i.e. in situ*). The hydrodynamic diameter, which can be determined by measuring the changes in the intensity of light scattered from a suspension or solution, and will depend on the size of the particle and any surface structure.

The instrument used can measure sizes in the range 10^{-7} - 10^{-10} m and the calculations involved assume that the particles are spherical in shape.

When the post-reaction solution (Figure 79), after the decarbonylation of cyclohexanone catalysed by $[\text{Pt}(\text{tolpy})\text{Cl}(\text{S-dms})]$ (**3**), was analysed by dynamic light scattering (DLS), particles with an average hydrodynamic diameter of 47 nm were observed by dynamic light scattering (polydispersity index = 0.34), these particles accounted for 88% of those observed. The second peak relates to larger particles with diameters between 480 – 860 nm, and may arise from the presence of larger aggregates of platinum(0) or dust particles.

When the post-reaction solution was analysed where $[\text{Pt}(\text{tolpy})\text{Cl}(\text{CO})]$ (**4**) was used as the catalyst, nanoparticles with average diameters of 11 and 180 nm were observed (Figure 80). However, the quality of the data collected was low due to high polydispersity and the presence of large aggregates or dust.

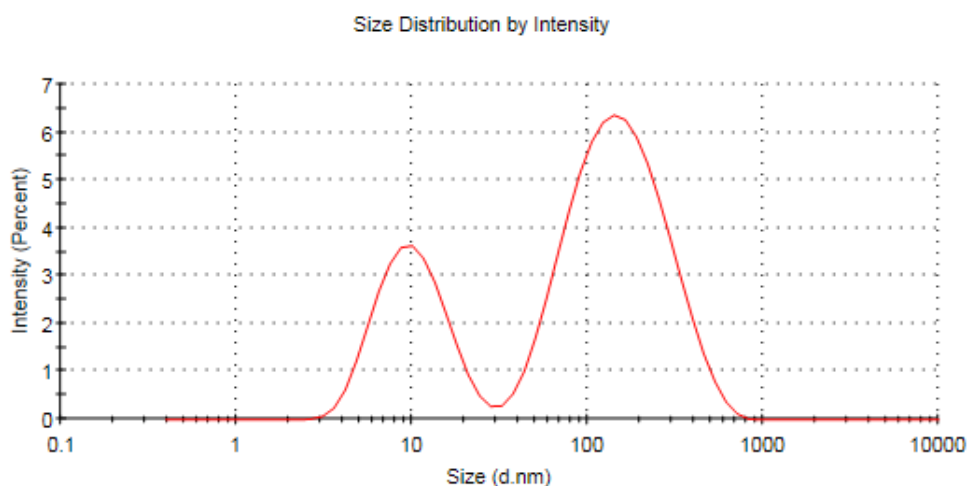


Figure 80: Plot of average hydrodynamic diameter *versus* intensity obtained *via* dynamic light scattering from the reaction solution after decarbonylation of cyclohexanone mediated by $[\text{Pt}(\text{tolpy})\text{Cl}(\text{CO})]$ (**4**).

Earlier, $[\text{Pt}(\text{tolpy})\text{Cl}(\text{H-tolpy})]$ (**2**) was identified as an inactive complex for the decarbonylation of cyclohexanone, although, decomposition of the complex was observed which suggested that platinum nanoparticles may be present. When the reaction was repeated, again no decarbonylation took place, but analysis of the solution showed particles with an average hydrodynamic particle diameter of 250 nm. During the five DLS experiments (of 56 scans of ten seconds) the average particle size increased from 160 nm to 310 nm, which shows that the particles are not effectively stabilised and were aggregating during the experiment. This suggests that cyclohexanone alone is not sufficient to stabilise

the platinum nanoparticles. The observation of nanoparticles in solution when using a metal complex which does not lead to the observation of a decarbonylation reaction suggests that nanoparticles are not the active catalytic species in the first step of the reaction.

The post-reaction solution after the decarbonylation of cyclohexanone (ten molar equivalents) by [Pt(tolpy)Cl(S-dmsu)] (**3**) conducted in acetonitrile was also analysed by DLS scattering. Again the presence of nanoparticles in solution were detected, this time with an average hydrodynamic diameter of 40 nm (polydispersity index: 0.337, standard deviation = 0.3 nm).

3.8.2 Mercury Drop Test

Mercury poisoning is a commonly used technique for distinguishing between homogeneous and heterogeneous metal-particle catalysts.¹⁶⁶ Mercury can deactivate the metal particle by amalgamation or by adsorption onto the surface. The mercury should remain in the reaction solution until the reaction is complete, and ideally only be added once the reaction has started. A large excess of mercury combined with good stirring are necessary for complete poisoning.¹⁹⁷ The method is not entirely fool proof and there are examples where the mercury has reacted with a soluble complex to give what is in effect a false positive and so results from the test must be treated critically.¹⁷¹ Given the observation of particulate platinum at the end of the reaction, it was important to try to ascertain what role, if any, this might play in the observed reaction either in relation to the decarbonylation itself or the coupled hydrogenation.

The mercury drop test was, therefore, performed three times according to the protocol set out in the Experimental Section, and the results are summarised in Table 13. All three tests indicate a large reduction in the formation of butane when mercury is added; however, the peak areas recorded for the experiments are not very reproducible. The mercury drop test results suggest that platinum nanoparticles play an important role in the transformation of cyclohexanone to butane.

Table 13: Summary of the peak areas (a.u.) corresponding to butane measured after mercury was added to the solution of cyclohexanone and [Pt(tolpy)Cl(*S*-dmsol)] (**3**) and heated under standard decarbonylation conditions

Run	Injection 1, peak area	Injection 2, peak area	Injection 3, peak area	Average peak area \pm standard error
1	624	789	507	640 \pm 82
2	482	447	477	468 \pm 11
3	150	77	122	116 \pm 21
Normal Decarbonylation of Cyclohexanone				
1	4727	4731	3140	4119 \pm 530
2	7023	7832	7926	7593 \pm 500

3.8.3 Use of Polyvinylpyrrolidone (PVP)

Polyvinylpyrrolidone is a non-toxic,¹⁹⁸ non-ionic¹⁹⁹ polymer used widely in the synthesis of nanoparticles (NPs).²⁰⁰ The polymer binds to the particle surface through nitrogen and oxygen atoms, and the hydrophobic carbon chains extend into the solvent preventing aggregation.²⁰¹ It is possible, therefore, that PVP may block active sites on the particles inhibiting catalysis or stabilise particles, preventing their aggregation and improve turn-over number, however, it should have no effect on a homogeneous system. The decarbonylation of cyclohexanone was repeated under standard conditions but with the addition of 0.01 molar equivalents of PVP (7.1 mg, average molecular weight = 40,000 g mol⁻¹). When the experiment was performed under these conditions, complete conversion to [Pt(tolpy)Cl(CO)] (**4**) was observed by ¹H NMR spectroscopy showing that decarbonylation does take place, however, the amount of butane observed by GC was reduced (peak area = 749 \pm 27). This suggests that the formation of [Pt(tolpy)Cl(CO)] (**4**) is homogeneous, but that the formation of butane may involve a heterogeneous process.

3.8.4 Synergistic Hetero- and Homogeneous Catalysis

The formation of $[\text{Pt}(\text{tolpy})\text{Cl}(\text{CO})]$ (**4**) by decarbonylation suggests homogeneous catalysis but the mercury test showed a reduction in the butane formed by decarbonylation of cyclohexanone which is consistent with nanoparticle or heterogeneous catalysis. The presence of nanoparticles during the reaction even though no decarbonylation took place may suggest that either the results of the mercury drop test are misleading in this case or that both homogeneous and heterogeneous routes may be important to the reaction mechanism.

3.9 Introduction of Substrate to Metal Centre

During the mechanistic discussion described above the following key observations were made:

- The reaction products, methane, carbon monoxide and butane require three carbon bond cleavages to occur.
- The reaction involves a transfer hydrogenation process as confirmed by deuterium cross labelling studies.
- The decarbonylation of cyclohexanone is a thermal process confirmed by control experiments conducted in the absence of ambient light.
- Deuterium labelling experiments show some evidence of scrambling, which would be consistent with the proposition that the formation of butane goes *via* an alkene intermediate.
- Infrared absorptions consistent with carbon monoxide coordinating to a transition metal particle surface were observed by *in situ* IR spectroscopy and nanoparticles were detected by dynamic light scattering experiments.
- There was no induction period for formation of $[\text{Pt}(\text{tolpy})\text{Cl}(\text{CO})]$ (**4**) by decarbonylation of cyclohexanone during *in situ* IR analysis.
- The addition of mercury inhibited the formation of butane, one of the products of the decarbonylation of cyclohexanone.
- Use of the complex $[\text{Pt}(\text{tolpy})\text{Cl}(\text{H-tolpy})]$ (**2**) did not result in decarbonylation but did lead to the formation of colloidal platinum.
- Use of different cyclic ketones can lead to different product distribution patterns.

What the above observations suggest is that the mechanism is in two parts; a decarbonylation step and a transfer hydrogenation step. The initial product of decarbonylation (from *in situ* infrared evidence) is [Pt(tolpy)Cl(CO)] (**4**) and it is known that this is also an active catalyst precursor. This suggests strongly that the decarbonylation step is homogeneous. This is further supported by the observation that while [Pt(tolpy)Cl(H-tolpy)] (**2**) is not active in decarbonylation (at least as evidenced by the absence of [Pt(tolpy)Cl(CO)] after reaction), it does decompose under reaction conditions to form platinum nanoparticles.

The presence of platinum nanoparticles, however, requires that their potential activity is screened and addition of a large excess of mercury inhibited butane formation. Decarbonylation *per se* does not require a source of hydrogen, but formation of butane as a product does and the studies with 1,3-cyclohexadiene show that this is *via* a transfer hydrogenation route. Inhibition of butane formation would then suggest that the transfer hydrogenation step is mediated heterogeneously, with the hydrogen arising either from cyclohexanone or from a transfer hydrogenation source, when one is added. Having therefore proposed a two-step process, a more detailed mechanism for the homogeneous step can be considered.

Given that decarbonylation is mediated by a series of related complexes of the general formula [Pt(tolpy)Cl(L)] and that the Pt–Cl bond evidently survives reaction, then it is reasonable to assume that as a first step, ligand L is lost and that this loss is accompanied by introduction of cyclohexanone¹ to the metal. This introduction of the ketone most likely occurs *via* an initial coordination, which could be through the oxygen of the carbonyl group, η^2 through the C=O double bond or through the alkene (or alcohol oxygen) of the enol tautomer (Figure 81). Following coordination, then activation of the cyclohexanone could proceed *via* oxidative addition of the C_α–H or C_{CO}–C_α bonds. Oxidative addition of either the C_{CO}–C_α or the C_α–H bonds would be preceded with an interaction between the cyclohexanone and catalyst.

Being a soft acid, Pt^{II} generally does not form very stable complexes with hard oxygen donor ligands but there are a few examples reported, mostly of cationic complexes.²⁰²⁻²⁰⁴ For example, Thayer and Payne obtained the single crystal X-ray crystal structure of *trans*-[Pt(CH₃)(PMe₂Ph)₂(acetone)]⁺ where the acetone

¹ Cyclohexanone is included here as a generic example of the ketones under investigation.

ligand is coordinated to the metal atom through an sp^2 pair of electrons on oxygen.²⁰⁵ The acetone C=O double-bond length of 1.225(7) Å shows no significant lengthening.

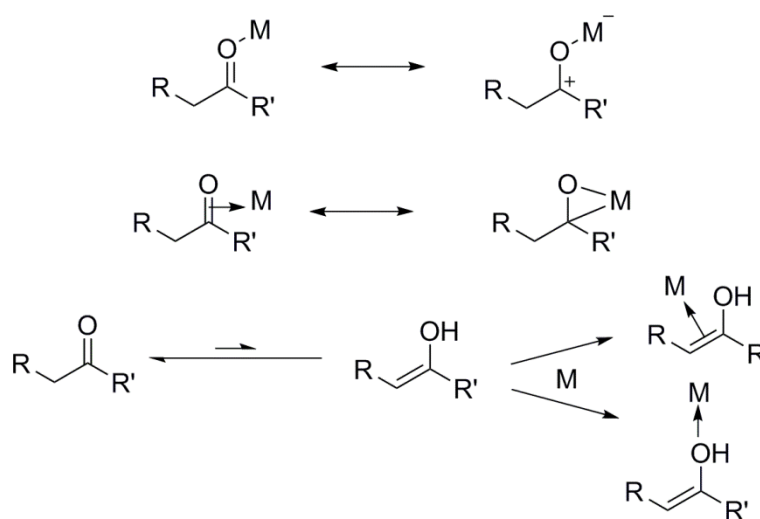


Figure 81: Coordination modes and resonance forms for metal complexes of ketones

3.9.1 Loss of the Neutral Ligand in [Pt(tolpy)Cl(L)]

The formation of [Pt(tolpy)Cl(L)] by decarbonylation of cyclohexanone requires the loss of the neutral ligand, be it *S*-dms, dms, py or PPh₃. The catalyst is a square-planar, 16-electron complex, so a dissociative ligand substitution is unlikely. The possibilities remaining are associative, concerted ligand substitution or oxidative addition to afford the octahedral Pt^{IV} species followed by ligand dissociation. The presence of a neutral electron donor will increase the electron density on the platinum promoting oxidative addition.

3.9.2 Oxidative Addition

Possible Oxidative Addition of the C_{Co}-C_α Bond

Heating cyclopentanone and cyclohexanone with complexes of the general formula, [Pt(tolpy)Cl(L)], led to the cleavage of three C–C bonds. As discussed in the Chapter One, C–C bonds are relatively inert; in addition to strategies reported for decarbonylation reactions, namely strain and chelation, aromatisation for their activation, which is dominated by complexes of Rh and Ir.^{13, 206} There are three main pathways for C–C activation, namely oxidative addition, β -carbon elimination and retro-allylation.¹³

Generally, the complexes that mediate oxidative addition reactions are coordinatively unsaturated complexes with eight or ten *d*-electrons in their outer shell, both Pt⁰ and Pt^{II} complexes fall into this category. The α -keto C–C bond is slightly weaker than other C–C single bonds and so would be the most likely site for oxidative addition. For example the bond dissociation energy of a C–C bond in acetone is 352.9 kJ mol⁻¹ whereas for propane is it 370.3 kJ mol⁻¹.²⁰⁷

Possible Oxidative Addition of C α –H Bonds

There are also examples of platinum-keto complexes where coordination of the ketone is through activation of the acidic C α –H bond,^{84, 208, 209} such as [PtCl{ η^1 -CH₂C(O)R}(N–N)] (where N–N is 1,10-phenanthroline or 2,2-bipyridine and R can be CH₃ or CH₂CH₃, see Figure 82).⁸² In the mechanism proposed by Stahl for dehydrogenation of ketones to cyclic enone, coordination of cyclohexanone to the palladium(II) species is by C α –H activation.²¹⁰

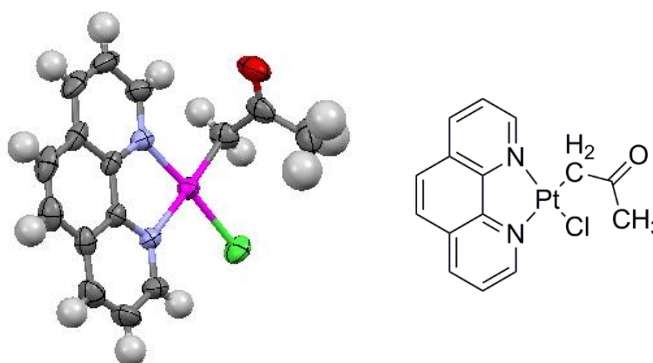


Figure 82: X-ray crystal structure of [PtCl{CH₂C(O)CH₃}(1,10-phenanthroline)] (left) and the packing of the molecules (right) reported by Barone *et al.* with the hydrogen atoms and solvent molecules removed for clarity⁸²

3.10 C–C Bond Scission to Afford an Aldehyde

In considering the activation of cyclohexanone and the product distribution, it seems clear that there is an initial C–C bond activation, which would lead to a C₆ equivalent with a carbonyl at one end. If the carbonyl is regarded as aldehyde-like, then decarbonylation of aldehydes is both well-known and straightforward. However, a simple decarbonylation of this type would generate CO and a C₅ fragment from which generation of methane may be difficult. Another possibility would be that in opening up the C₆ ring, the activation leads to extrusion of an acetaldehyde equivalent by activation of the C α –C β bond, which would could decompose further (with sufficient hydrogen) to generate methane and CO, leaving a C₄ fragment that would lead to butane (Figure 83). In Chapter Two, it

was shown that the aldehyde, pentanal, undergoes decarbonylation readily (identified by GC) under standard conditions and even at room temperature, demonstrating the high reactivity of this functional group.

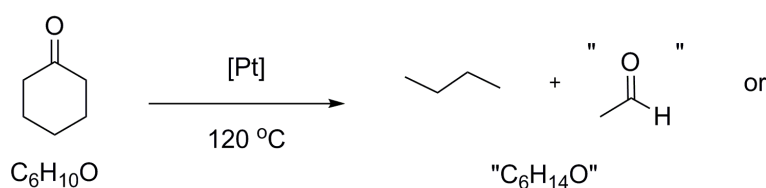


Figure 83: Proposed C-C bond activation of cyclohexanone

3.11 Proposed Mechanistic Route for the Decarbonylation of Cyclohexanone

After initial coordination of the enol form of cyclohexanone, it is proposed that the reaction between cyclohexanone and $[\text{Pt}(\text{tolpy})\text{Cl}(\text{L})]$ proceeds *via* a carbon-carbon σ -bond scission to afford a C_4 hydrocarbon, either butane or butadiene which undergoes transfer hydrogenation to afford the observed product butane. This is supported by the observation of the incorporation of additional hydrogen atoms into the butyl product of the decarbonylation of perdeuterated cyclohexanone. An acetaldehyde like species (C_2OH_2) is also extruded, which undergoes decarbonylation and rapid transfer hydrogenation to afford the carbonyl complex **4** and the other hydrocarbon product methane.

It is believed that the decarbonylation of the acetaldehyde like fragment and its transfer hydrogenation are both homogeneous processes, supported by the deuterium cross labelling experiments. The inhibition in the formation of butane, suggest a heterogeneous process may be involved in the transfer hydrogenation step to afford this product but this has not been confirmed. Substrates can interact with the surface of heterogeneous/nanoparticle catalyst by physisorption or chemisorption.²¹¹ Physisorption may precede chemisorption and is where molecules weakly interact with a solid surface through van der Waals forces. Chemisorption involves a chemical bond between the substrate and the catalyst surface, and once all surface sites are occupied no more substrate can be coordinated. Carbonyls can chemisorb onto the catalyst surface through donation from the oxygen to the surface sites and hydrides can coordinate through sigma donation from the hydride.²¹²

In the present study it is proposed that the decarbonylation of the acetaldehyde fragment goes *via* oxidative addition of the C_{CO}-H bond to give the six coordinate Pt^{IV} species (Figure 84). This is then followed by ligand dissociation, extrusion of the carbonyl and finally reductive elimination to afford methane. This general mechanism may be applied more broadly to other active substrates, for which C-C bond formation was also not observed, such as for acetone, acetophenone and propiophenone. The process begins with initial coordination of the enol form of the ketone to the metal centre, the enol form of acetophenone is less favourable relative to propiophenone and accordingly lower conversion to [Pt(tolpy)Cl(CO)] (**4**) was observed. This is then followed by oxidative addition of the C_α-C_{CO} bond, for propiophenone and acetophenone, insertion will be more favourable into the C_{CH₃/CH₂CH₃}-C_{CO} than the C_{Ar}-C_{CO} bond. Transfer hydrogenation of the CH₃ group will afford the product methane, and the aldehyde like fragment will undergo decarbonylation and rapid transfer hydrogenation to afford carbon monoxide and a second equivalent of methane for acetone and acetophenone and ethane for propiophenone.

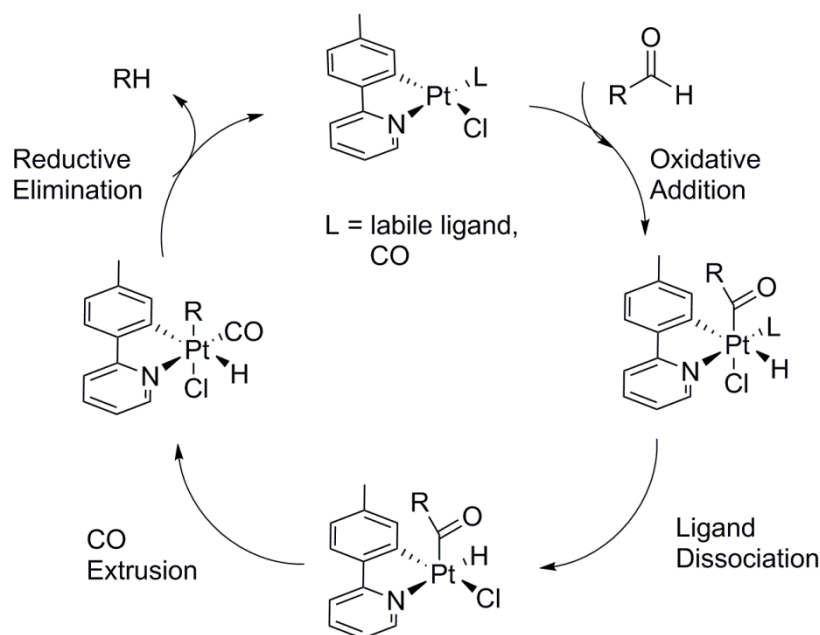


Figure 84: Proposed mechanism for the decarbonylation of an aldehyde by [Pt(tolpy)Cl(L)]

3.11 Mechanism for the Decarbonylation of Cyclooctanone and Cycloheptanone

Both cycloheptanone and cyclooctanone have a similar pattern of reactivity to each other, but different from cyclopentanone and cyclohexanone; observed by the hydrocarbon products identified and the formation of $[\text{Pt}(\text{tolpy})\text{Cl}(\text{CO})]$ (**4**) observed by ^1H NMR and *in situ* IR spectroscopy. For both ketones, ring closed alkenyl products were observed by GC-MS analysis of the reaction headspace and the formation of these products was not mass balanced; two hydrogen atoms are lost during the reaction. It is not known why different reactivity is observed for these substrates but it is suspected to be due to the ring size. A preliminary mechanism was proposed for the decarbonylation of cycloheptanone and cyclooctanone which begins with initial coordination of the metal centre (Figure 85). This is followed by oxidative addition of a $\text{C}_{\text{CO}}\text{-C}_{\alpha}$ bond, then ligand dissociation, followed by carbonyl extrusion to afford a metallocycle. The metallocycle must decompose to afford the alkenyl ring closed product but the mechanism of this requires further study.

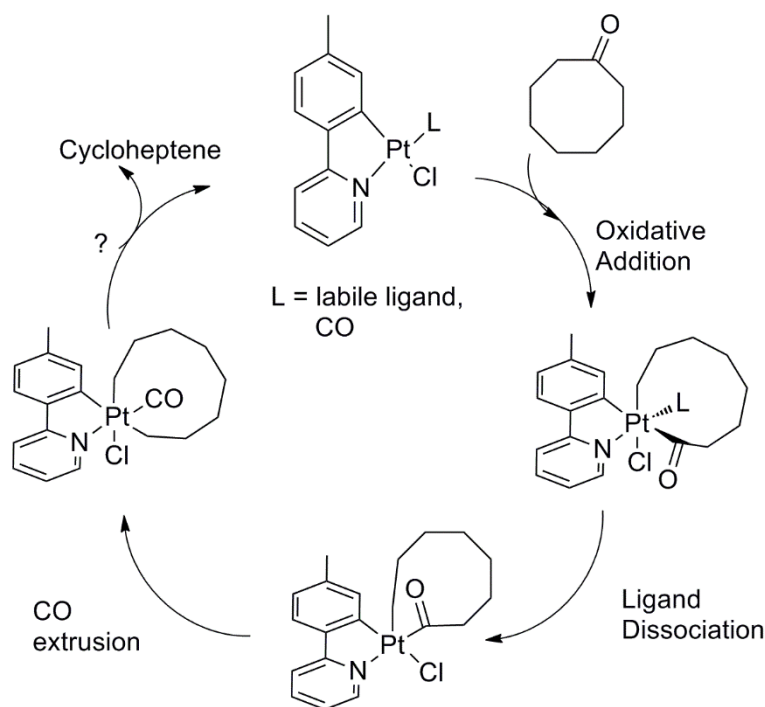


Figure 85: Preliminary mechanism proposed for the decarbonylation of cyclooctanone

3.12 Summary

The decarbonylation of cyclohexanone mediated by $[\text{Pt}(\text{tolpy})\text{Cl}(\text{S-dms})]$ (**3**) affords the products, methane, carbon monoxide and butane which requires four additional hydrogen atoms. Although cyclohexanone can act as a source of additional hydrogen atoms, the reaction is promoted by the addition of a hydrogen donor, such as 1,3-cyclohexadiene. A transfer hydrogenation process was strongly supported by cross deuterium labelling studies. The decarbonylation of the previously inactive substrates, acetone, acetophenone and propiophenone proceeded in the presence of the hydrogen donors 1,3-cyclohexadiene or IPA. The decarbonylation of cyclohexanone mediated by $[\text{Pt}(\text{tolpy})\text{Cl}(\text{S-dms})]$ (**3**) proceeded in the absence of light which confirmed it to be a thermal process rather than a photochemical one.

The formation of $[\text{Pt}(\text{tolpy})\text{Cl}(\text{CO})]$ (**4**) by decarbonylation was often accompanied by the formation of other cycloplatinated species, namely $[\text{Pt}(\text{tolpy})(\mu\text{-Cl})]$ (**1**), $[\text{Pt}(\text{tolpy})\text{Cl}(\text{H-tolpy})]$ (**2**) and $[\text{Pt}^{\text{IV}}(\text{tolpy})_2\text{Cl}_2]$ (**11**), these are thought to be decomposition products, rather than intermediates relevant to the decarbonylation reaction.

When the reactions were monitored by *in situ* IR spectroscopy maximum formation of $[\text{Pt}(\text{tolpy})\text{Cl}(\text{CO})]$ (**4**) occurred within 90 minutes after which it began to decay away. An induction period was not observed for the ketone substrates except for cyclooctanone or β -tetralone. The formation of additional carbonyl species was observed and these signals were thought to be carbon monoxide coordinated to platinum particles formed during the decomposition of $[\text{Pt}(\text{tolpy})\text{Cl}(\text{CO})]$ (**4**).

Nanoparticles were observed in the reaction solution both when the decarbonylation of cyclohexanone proceeded and when it did not using dynamic light scattering experiments. Although, the mercury test showed a reduction in the butane formed by decarbonylation of cyclohexanone which is consistent with nanoparticle or heterogeneous catalysis, the presence of nanoparticles during the reaction even though no decarbonylation took place may suggest that either the results of the mercury drop test are misleading in this case or that both homogeneous and heterogeneous routes may be important to the reaction mechanism.

A speculative mechanism for the decarbonylation of cyclohexanone is proposed where fragmentation and transfer hydrogenation take place to afford an acetaldehyde like fragment. This aldehyde like species then undergoes oxidative addition of the C_{co}-H bond, followed by ligand dissociation, extrusion of the carbonyl and finally reductive elimination to afford methane.

Chapter Four: Investigating the *trans*-Influence using a Combined Spectroscopic and Computational Approach

4.1.0 Introduction

A number of cycloplatinated complexes with the general formula $[\text{Pt}(\text{tolpy})\text{Cl}(\text{L})]$ (where *tolpy* is 2-(4-tolyl)pyridine and *L* is a neutral ligand, *S*-dms, dms, CO, py, *H*-tolpy and PPh_3) were prepared and characterised as described in previous chapters, and the activity of each complex towards the decarbonylation of ketones was evaluated in turn, along with the role of the labile ligand *L*. Given that these complexes had been prepared and characterised, there was then the opportunity to study some thermodynamic aspects of these complexes, specifically the ability of the *trans* ligand, *L*, to weaken the *M*–*L* bond *trans* to itself (*trans*-influence) and to evaluate methods of probing *trans*-influence. The origin of the *trans*-influence will be discussed below in Section 4.1.1 of this chapter.

It was possible to grow single crystals of many of the platinum complexes and hence the platinum–ligand (*Pt*–*L*) bond lengths could be measured following single crystal X-ray diffraction. The chloride ligands provided an additional spectroscopic handle, namely vibrational frequency of the *Pt*–*Cl* bond in the far infrared region. $[\text{Pt}(\text{tolpy})(\mu\text{-Cl})_2]$ can be easily cleaved by dms to afford $[\text{Pt}(\text{tolpy})\text{Cl}(\text{S-dms})]$ and in turn the dms is readily exchanged for other ligands in order to build up a small family of complexes with a range of steric and electronic properties. Towards this end, the family of complexes was extended to include $[\text{Pt}(\text{tolpy})\text{Cl}(\text{L})]$, where *L* is *tht*, *PhCN*, PCy_3 and $\text{P}(\text{OPh})_3$.

In this chapter, the detailed spectroscopic study of these compounds will be discussed, relating the spectroscopic observations to the *trans*-influence of the ligands. Chemical shifts and coupling constants measured from ^1H , $^{13}\text{C}\{^1\text{H}\}$, ^{15}N , and ^{195}Pt NMR and in some cases, $^{31}\text{P}\{^1\text{H}\}$ spectroscopy and *Pt*–*Cl* stretching frequencies will be compared with bond lengths determined by X-ray crystallography and combined with quantum chemical calculations to probe the *trans*-influence exerted by each ligand on the *Pt*–*N* bond.

4.1.1 *Trans*-Influence

The *trans*-influence was defined by Pidcock in 1966 as the extent to which a ligand in a metal complex weakens the metal-ligand (M–L) bond *trans* to itself in the ground state.²¹³⁻²¹⁵ The *trans*-influence is sometimes referred to as the thermodynamic or the structural *trans*-effect. It is a thermodynamic phenomenon, whereas the kinetic *trans*-effect describes the change in the rate of substitution of the *trans*-ligand (Figure 86).²¹⁶ There are related, small effects between the ligands situated *cis* to one another, named the *cis*-effect / influence, where lengthening of a bond or an increased rate of substitution can also be observed. For late transition metals such as square planar d^8 complexes or octahedral d^6 complexes, the magnitude of the *trans*-influence is much greater than the *cis*, however, for octahedral Sn^{IV} and Sb^{V} complexes, similar magnitudes for both *cis*- and *trans*-influences have been reported.²¹⁷

The relative *trans*-influence of different ligands is due to the electronic properties of the said ligand and so can be linked to the spectrochemical series, which lists ligands in order of their increasing ability generate a crystal field splitting. In general, π -donor ligands such as the chloride anion are weak field ligands and π -acceptor ligands such as carbon monoxide are strong field ligands.²¹⁸

Spectrochemical Series:²¹⁸ $\text{CO} > \text{CN}^- > \text{PPh}_3 > \text{NO}_2 > \text{NH}_3 > \text{py} > \text{CH}_3\text{CN} > \text{NCS}^- > \text{H}_2\text{O} > \text{OH}^- > \text{F}^- > \text{SCN}^- > \text{Cl}^- > \text{Br}^- > \text{I}^-$

***Trans*-Effect:**²¹⁹ $\text{H}^- = \text{CH}_3^- = \text{CN}^- = \text{C}_2\text{H}_4 = \text{CO} \gg \text{PR}_3 = \text{SR}_2 > \text{NO}_2 = \text{SCN}^- = \text{I}^- > \text{Br}^- > \text{Cl}^- > \text{py} > \text{RNH}_2 = \text{NH}_3 > \text{OH}^- > \text{H}_2\text{O}$

Figure 86: Spectrochemical and *trans*-effect series (decreasing from left to right)^{220,219}

There have been many explanations suggested for the origin of the *trans*-influence.²¹⁹ The first of these was Grinberg's polarisation theory which predates the definition of the *trans*-influence and, although it is reported as an explanation for the '*trans*-effect', it is in fact the weakening of bonds in the ground state and hence, is the *trans*-influence.²²¹ Grinberg suggests that a strong ligand, T, polarises the opposite ligand, L, by inducing a dipole (Figure 87).²²² This dipole repels the negative charge of the *trans*-ligand (T) weakening the M–L bond. The main limitation to this theory is that the M–L bonds of the late transition metals, such as platinum, have a high degree of covalency.²²³

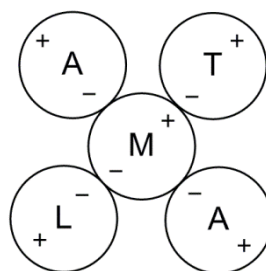


Figure 87: Schematic of Grinberg's polarisation theory where T is a ligand with a strong *trans*-influence, L is the ligand in the *trans*-position to T^{221, 222}

Later Syrkin proposed an explanation of the *trans*-effect, which can also be applied to the *trans*-influence in terms of hybridisation of the orbitals.²²⁴ He suggested that when L forms a strong bond with a metal it dominates the hybrid bonding orbitals, meaning that these are less available to the *trans*-ligand, and hence weakening the M–T bond. In a similar way, the *trans*-influence is most commonly explained in terms of competition for the metal's *d* electrons.

4.1.2 Experimental Techniques to Probe the *trans*-Influence

The *trans*-influence has been probed experimentally using X-ray crystallography as well as FT-IR and NMR spectroscopy.²¹⁹ X-ray crystallography has been used extensively to study the *trans*-influence because it allows the length (related to the strength) of the M–L bonds in the crystal to be determined directly.²²⁵⁻²³² However, changes in the bond lengths when the ligand is varied can be small and often similar to the error associated with bond length determination.²¹⁹ Another limitation of this technique is that intermolecular interactions within the crystal can occasionally have a significant effect on the bond lengths observed.

Metal–ligand bond strengths can also be evaluated using FT-IR spectroscopy particularly for studying metal–halogen and metal–hydride bonds. As a bond weakens, the force constant associated with the vibration of that bond also decreases and hence the vibrational frequency. However, it can be difficult to interpret the change in vibrational frequency because this will also change with the mass of the ligand. In this work, complexes are studied where the molecular weight of the [Pt(tolpy)Cl] fragment is 398.75 g mol⁻¹ and the molecular weight of the largest ligand, PCy₃, is 280.44 g mol⁻¹, whereas the molecular weight of the smallest ligand, CO, is only 28.01 g mol⁻¹. Another factor to consider is vibrational coupling, where an interaction between different vibrations occurs. This may be due two different vibrating groups sharing a common atom or bond and the effect is greater when the vibrations of coupling groups are of similar energy. For solid samples, lattice vibrations may also be observed in the far-infrared region; these

vibration will depend on the symmetry of the crystal, the number of atoms in the unit cell as well as any defects in the crystal lattice.²³³

The Pt–Cl stretching frequencies reported for complexes with the general formula *trans*-[PtCl(L)(PEt₃)₂] and *cis*-[PtCl₂L₂] were collected by Appleton *et al.* and are summarised below (Figure 88, Table 14).²¹⁹ As the *trans*-influence of the ligand, L, increases, a decrease in bond strength of the *trans* Pt–Cl bond would be expected, and hence a reduction in the vibrational frequency. The trend in vibrational frequencies observed does not agree completely with the spectrochemical series with carbon monoxide appearing much lower in this series. They also report the vibrational frequencies of complexes where L = py or dms and observed that the *trans*-influence of these ligands was similar.

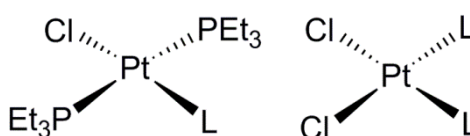


Figure 88: General structure of the platinum complexes for which the $\bar{\nu}(\text{Pt}-\text{Cl})$ vibrational frequencies were collected by Appleton *et al.*²¹⁹

Table 14: Values for the vibrational frequencies for Pt–Cl stretches reported in the literature.

Pt–Cl Vibrational frequency for <i>trans</i> -[PtClL(PEt ₃) ₂] (cm ⁻¹)								
L =	CO >	^t BuNC >	Cl ⁻ >	py >	P(OPh) ₃ >	PPh ₃ >	PEt ₃ >	H ⁺
$\bar{\nu}(\text{Pt}-\text{Cl}),$ cm ⁻¹	344 ²³⁴	341 ²³⁴	340 ²³⁵	337 ²¹⁹	316 ²³⁴	298 ²¹⁹	295 ²³⁴	269 ²³⁵
Pt–Cl Vibrational frequency for <i>cis</i> -PtCl ₂ L ₂ (cm ⁻¹)								
L =	py =	dms >	cod >	NH ₃	PPh ₃	PEt ₃		
$\bar{\nu}(\text{Pt}-\text{Cl}),$ cm ⁻¹	336 ²³⁵	336 ²³⁶	327 ²³⁵	321 ²³⁷	305 ²³⁸	294 ²³⁶		

Chemical shift data and heteronuclear coupling constants have also been used to evaluate the *trans*-influence.^{213, 219, 239-245} Chemical shift is dependent on the electron density surrounding the nucleus and how effectively those electrons shield the nucleus from the applied magnetic field. The shielding constant for a nucleus is the product of the diamagnetic and paramagnetic contributions to shielding (equation 1).

$$\sigma = \sigma_d + \sigma_p \quad (1)$$

Where σ_d and σ_p are the diamagnetic and paramagnetic contributions to shielding.

Lower electron density between two atoms may indicate a weaker bond and cause signals to be shifted downfield. Correlation between hydride chemical shifts of complexes and their position in the *trans*-influence series were reported by Chatt and Shaw,²⁴⁶ while Atkins²⁴⁷ *et al.* later reported linear relationships between hydride chemical shifts or $^1J_{\text{HPt}}$ values and Pt–H stretching frequencies for a range of platinum hydride species.

The J coupling observed between atoms is due to the interaction between magnetic moments caused by nuclear and electron orbital motion and also by dipolar interactions between electron and nuclear spins. The magnitude of J_{AB} , for two atoms, A and B, directly bonded to one another, depends on a number of factors including: the hybridisation of the atoms involved; bond/dihedral angles; bond lengths; the presence of neighbouring π -systems or electronegative atoms. The J coupling of atoms which are directly bonded to each other (A–B) can be described mathematically by the Fermi contact term. This treatment assumes that the contribution due to orbital motion is negligible and states that the coupling constant observed between two nuclei (A–B) is proportional the gyromagnetic ratios of each nuclei and the s -character of the bonding hybrid orbitals used in the A–B bond. As the measured J value varies with changing s character of the hybrid orbitals used by the metal in the M–L bond, it can be related to the *trans*-influence which describes the weakening of that bond.

Finally, Mössbauer spectroscopy (^{129}I) has also been used to evaluate the *trans* influence of different ligands of *cis*-diiodo-platinum(II) complexes.²⁴⁸ They demonstrated that the quadrupole coupling constants recorded of the *cis*-complexes varied systematically with the nature of the neutral ligands, for example, the low coupling constants observed for hydrides indicated a large *trans*-influence for this ligand.

Definitive comparisons can be made by measuring the bond lengths involved by X-ray crystallography, but this can only be carried out if a suitable crystal can be obtained. Useful insight can also be gained using NMR, Mössbauer and FT-IR spectroscopy, but careful analysis is necessary due to the limitations described above. In this study, trends in bond lengths measured using X-ray diffraction will be compared using $^3J_{\text{HPt}}$, ^{195}Pt chemical shifts, and ^{15}N chemical shifts to evaluate the *trans*-influence.

4.1.3 Computational Techniques to Probe the *trans*-Influence

More recently, quantum mechanical calculations have also been used to study this phenomenon^{225, 226, 249-252} allowing expensive, synthetically challenging or unstable complexes to be modelled. The geometries and bond lengths of metal complexes can be calculated, along with the infra-red and NMR spectra, and the bond strengths can also be evaluated using natural bond order analysis.²⁵³⁻²⁵⁵ The terms and principles which underpin this area of research are described in a short appendix (Appendix II).

As described above, the coupling constant between two directly bonded atoms can be related to the strength of the bond between them. Recently, Grief *et al.* calculated NMR chemical shifts (PBE0/def2-TZVP with ECP for Pt and I) in order to study the *trans*-influence on a series of Pt^{II} hydrides, *trans*-[Pt(H)(L)(PMe₃)₂] (Figure 89).²⁵⁶ The PBE0 functional uses an electron core potential (ECP) to treat the core electrons of platinum. They state that the observed correlations between the ¹H chemical shifts and Pt–H distances measured experimentally arise indirectly and are caused by the effect of the *trans*-ligand on the polarization of the metal *d*-orbitals, which in turn affects both the structures and the shifts. The calculated chemical shifts of the hydride ligand were observed downfield as electron density from the Pt–H σ -bonding orbital is donated to the unoccupied π -orbital on platinum. This was most pronounced when L = BH₂ (Figure 90). Shielding was observed when L = Cl, NO₂ or NO₃ as donation of electron density from platinum's occupied *d*-orbitals to the unoccupied Pt–H σ^* -orbital and hence covalency of the Pt–H bond increased.

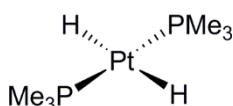


Figure 89: Chemical structure of *trans*-[Pt(H)(L)(PMe₃)₂].

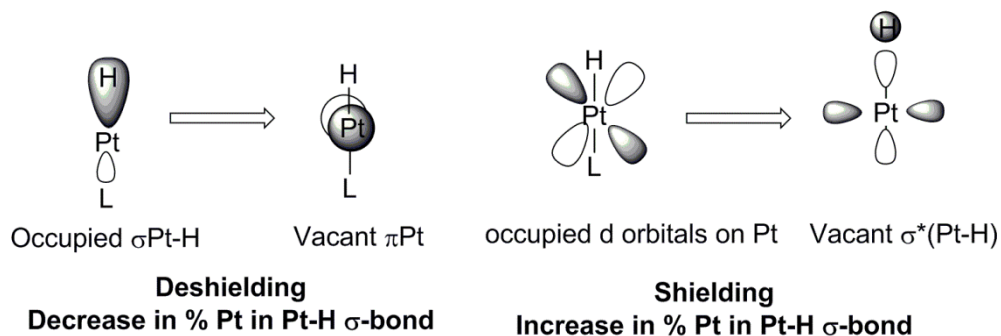


Figure 90: Deshielding and shielding of the hydride ligand caused by electron donation between the orbitals of the Pt–H bond and the orbitals centred on platinum.²⁵⁶

The most common tool used to evaluate the *trans*-influence computationally is calculation of bond strength parameters such as the bond order, which is related to the strength and hence length of a given bond. There are a number of methods for the calculation of bond order from molecular orbital calculations.²⁵⁷ These include the Coulson model (for π -orbitals studied at the Hückel level of theory, bond order between A and B = $\sum c_i A c_i B$, where c_i is the coefficient of the atomic orbital of A in the i^{th} doubly occupied molecular orbital),²⁵⁸ the Wiberg bond order (this gives positive bond orders between all atoms in a molecule) and Mayer (an extension of the Wiberg bond order).^{259, 260} The Wiberg and Mayer bond orders calculated are close to classical bond valences. Pauling and co-workers suggested a function, the Pauling correlation,²⁶¹ to describe the expected correlation between bond order and length, whereby the bond order increases or decreases exponentially as the bond length decreases or increases. Mayer bond orders also agree very well with this expected correlation. Bridgeman *et al.* reviewed the usefulness of calculating Mayer bond orders when studying the strength and nature of chemical bonding for a range of inorganic compounds.²⁵⁷ They report that the value of the Mayer bond order calculated depends on the basis set used, and so comparison between different systems can only be valid if the same basis set is used to calculate them.

Jia *et al.* studied the *trans*-influence of different ligands on the Pt–C bonds in PCP pincer complexes using quantum mechanical calculations, single crystal X-ray crystallography and $^{13}\text{C}\{^1\text{H}\}$ NMR spectroscopy (Figure 91).²²⁶ They carried out natural bond orbital analysis and calculated delocalisation energies which are inversely proportional to the bond length (B3LYP²⁶²/SDD(Pt), 6-31G(d) (other atoms)). In their work, they highlighted the importance of the *trans*-influence in understanding the mechanism of the activation of substrates and used their study to inform the design of new pincer complexes for use in asymmetric organic reactions.

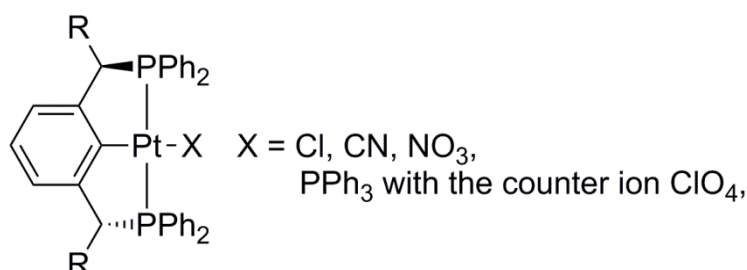


Figure 91: General structure of the PCP pincer complexes studied by Jia *et al.*²²⁶

These selected examples demonstrate a range of methods recently employed to study M–L bonds in organometallic complexes, which provide useful information

about structure and bonding, particularly for complexes for which it is difficult or expensive to synthesise and obtain a single crystal X-ray structure. In this study, the geometries of the complexes will be optimised in order to measure the calculated bond lengths and the bond order will be investigated using natural bond order analysis.

4.1.4 Research Objectives

As there are advantages and limitations to all of the techniques discussed above, a combined experimental and computational approach was chosen to study the platinum complexes with the general formula $[\text{Pt}(\text{tolpy})\text{Cl}(\text{L})]$, where $\text{L} = N$ -2-(4-tolyl)pyridine, *S*-dms_o, CO, py, CH₃CN, dms, tht, PPh₃ as well as the dimer $[\text{Pt}(\text{tolpy})(\mu\text{-Cl})_2]$ (in effect $\text{L} = \mu\text{-Cl}$) (Figure 92). FT-IR spectra collected in the far-infrared region and, together with data from NMR spectroscopy (¹H, ¹³C, ¹⁵N, ¹³C{¹H} and ¹⁹⁵Pt{¹H}), were compared to the bond lengths determined by single-crystal X-ray diffraction and those calculated using quantum chemistry. Using this approach, trends in the spectral data could be identified and a *trans*-influence series for these ligands proposed. The calculated geometries and bond lengths will be compared to those obtained by X-ray crystallography; if they are in good agreement it will suggest that quantum mechanical calculations may provide a quick, cost effective and safe way of comparing different ligands. Finally, the different techniques used to probe the *trans*-influence were evaluated by comparison to the change in metal–ligand bond lengths measured by X-ray diffraction.

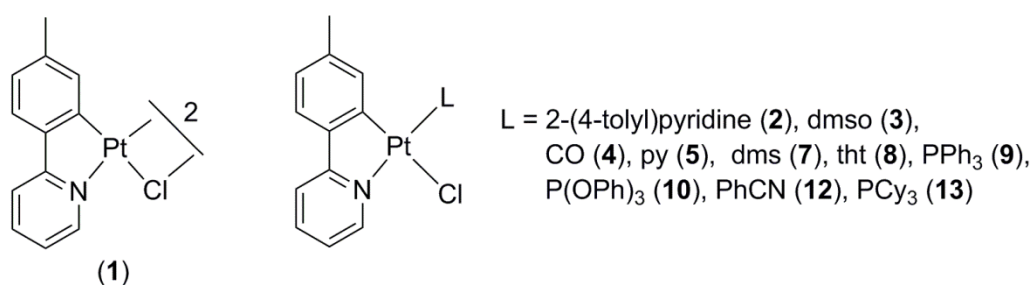


Figure 92: General structures for the cyclometallated platinum complexes studied in this chapter, with the complex numbers given in brackets

2.0 Summary of the Spectroscopic Properties of the $[\text{Pt}(\text{tolpy})\text{Cl}(\text{L})]$ Complexes

2.1 $[\text{Pt}(\text{tolpy})(\mu\text{-Cl})_2]$ (1)

Halo-bridged, square-planar, dinuclear platinum complexes including $[\text{Pt}(\text{tolpy})(\mu\text{-Cl})_2]$ (1) can form either the *cis*- or *trans*-isomers and may adopt

planar or bent (jointed at the two bridging chlorine atoms) geometries.²⁶³ [Pt(tolpy)(μ -Cl)]₂ (**1**) is very insoluble and so it is difficult to obtain spectroscopic data, it was, however, possible to obtain an X-ray single crystal structure for the *cis*-isomer and to measure $\bar{\nu}(\text{Pt}-\text{Cl})$ in the solid state using infrared spectroscopy; these data are discussed here and complemented with geometry optimisations of both isomers. Together, this data will allow for analysis of the geometry of each isomer, and determination of their relative energies.

A computational study by Aullón *et al.* surveying 139 different dimers of the general formula, [L₂M(μ -X)₂ML₂] (M = Ni, Pd, Pt, Rh, Ir, X = bridging atom or group) investigated the energy difference between bent and planar geometries. In all cases the energy difference, as calculated using MP2/LANL2DZ, between the planar and the bent form was within 42 kJ mol⁻¹. They report that the driving force for the bending of the molecules is the attractive metal–metal interaction involving the occupied d_{z^2} and the empty p_z orbitals, the extent of which depends on the metal and the terminal and bridging ligands. They compared different bridging atoms and found that the stability of the bent form increased in the order F⁻ < Cl⁻ < Br⁻ < I⁻, and for different metal atoms it increased in the order Ni^{II} < Pd^{II} < Pt^{II} < Rh^I < Ir^I. Applying this to isomers of [Pt(tolpy)(μ -Cl)]₂ (**1a** and **b**) studied here, a bent geometry would be expected.

Computational Study

Initially a range of combinations of DFT functionals and basis sets were evaluated for eight of the compounds discussed in this chapter and compared based on their agreement to experimental data and computational cost. Three hybrid DFT functionals widely used for geometry optimisation of transition metal complexes were chosen; M06, BP86 and B3LYP.²⁵⁵ The post-Hartree-Fock method, MP2 was also considered but initial calculations proved too costly, especially when used with larger basis sets, and so was not studied further.

For the elements, H, C, N, Cl, two basis sets were investigated, 6-31G(d) and 6-311+G(d,p), the latter being larger and more computationally expensive. Both of these basis sets are suitable for atoms H through to Cl but for heavy atoms, such as Pt, relativistic effects must be accounted for. A popular method for correcting for relativistic effects is by using an electron core potential (ECP). This is where an ECP is used to replace the core electrons so that only the valence electrons are included in the calculation. For platinum, four basis sets were investigated; LANL2DZ, LANL2TZ, SDD and def2TVZP. These were chosen

because they are relatively large basis sets which include ECP. There are different approaches to dealing with dispersion,²⁶⁴ in this work the D3 version of Grimme's dispersion correction combined with Becke-Johnson damping (D3-BJ)²⁶⁵ was employed for the DFT functionals except for M06 for which it is already parameterised.

The results of the different combinations of basis sets and functionals were compared and the combination of BP86 with 6-31G(d) and LAND2DZ for platinum was chosen using a balance of agreement with the experimental data and computational cost (a summary of the results obtained using different combinations of functionals and basis sets are given in the Experimental Section). In this study, only trends in bond lengths, relative energies and vibrational frequencies across a series of compounds are required, not exact values. Any calculations which took longer than 96 hours to converge using four nodes on the YARC cluster were eliminated from the study. For the different complexes studied, the trends in platinum-ligand bond length showed good agreement with the X-ray data, no matter which combination was used.

[Pt(tolpy)(μ -Cl)]₂ (1a and b)

The chosen combination for both isomers of dimer **1** was the functional BP86 combined with the basis sets, 6-311+G(d,p) and LAND2DZ (for Pt, results summarised in Table 15, Figures 94 and 93). Unlike the other complexes studied, the larger basis set, 6-311+G(d,p), was required to achieve good agreement with experimentally determined geometry, namely a bend angle between the two Pt-L planes of less than 3°. In all cases where 6-311+G(d,p) was used, a planar geometry was predicted for the *cis*-isomer. A bent geometry was also predicted for the *trans* isomer in all cases except for B3LYP/6-311+G(d,p)/def2TZVP.

For all combinations studied, the Pt-Cl bond *trans* to the carbanion was longer than the bond *trans* to the pyridyl nitrogen which is in agreement with the experimental X-ray data discussed later for **1a**. Furthermore, except when using B3LYP with 6-311+G(d,p) and LAND2DZ, the *trans*-isomer was lower in energy than the *cis*. The difference in energy between the isomers was small; the *trans*-isomer was only 3 kJ mol⁻¹ lower in energy using the values obtained using the chosen method.

Table 15: Summary of the geometry optimisation for **1a** and **b**

Isomer	Functional	Basis set, H, C, N, Cl	Basis set Pt	Geometry	E , Ha	ΔE , kJ mol ⁻¹
1a , <i>cis</i>	BP86	6-311+G(d,p)	LANL2DZ	planar, 0.21°	-2195.71732548	3.26
1b , <i>trans</i>	BP86	6-311+G(d,p)	LANL2DZ	Bent 62.85°	-2195.71857966	0

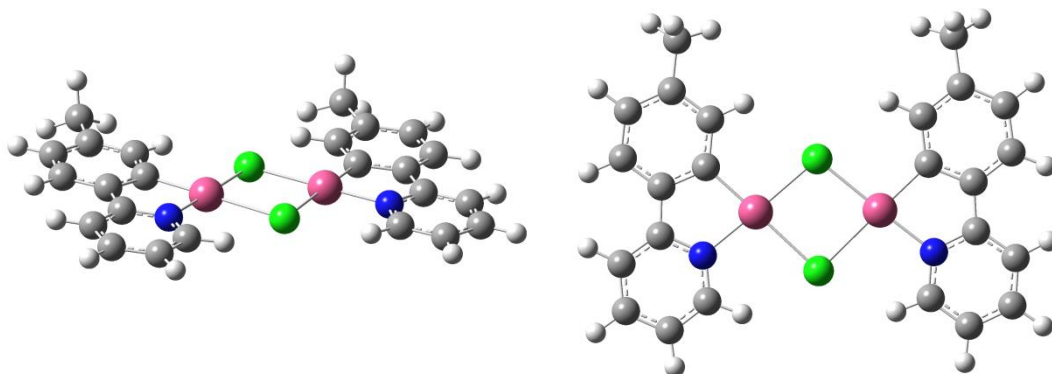


Figure 93: Geometry optimisation of the *cis*-isomer **1a** using the DFT functional BP86 and the basis sets 6-311+G(d,p) and LANL2DZ (for Pt), which includes ECP and the D3-BJ correction

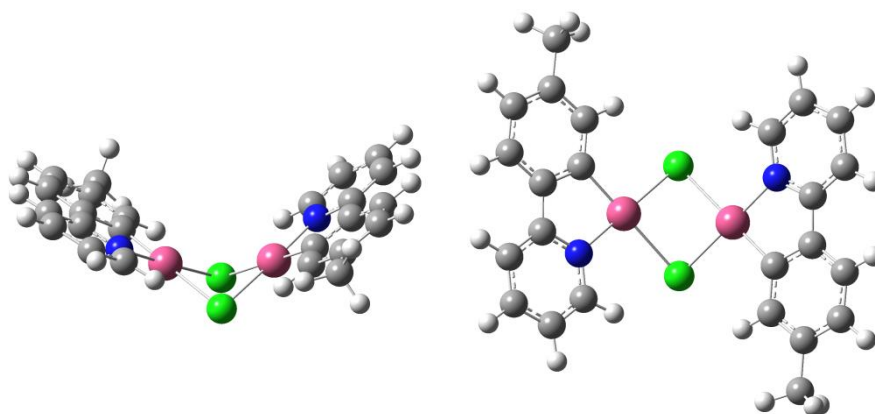


Figure 94: Geometry optimisation of the *trans*-isomer **1b** using the DFT functional BP86 and the basis sets 6-311+G(d,p) and LANL2DZ (for Pt), which includes ECP and the D3-BJ correction

2.1.1 Far-infrared Spectroscopy

The far-infrared spectrum was recorded for complex **1** in the solid state and compared to the calculated infra-red spectra (Figure 95) obtained using the method described above for the geometry optimisation. The calculations are not able to predict exact vibrational frequencies but they can be used to predict relative vibrational frequencies and intensities. For the *cis*-isomer, one large peak is expected around 315 cm^{-1} and for the *trans*-isomer, two smaller absorptions are expected around 300 and 280 cm^{-1} . On comparison with the calculated spectra, it would appear that both isomers are present in the solid state which is unsurprising as the calculated energy difference between the two is small. When the *cis* isomer, **1a**, was isolated and then analysed, its spectrum was very similar to the predicted one but shifted to slightly higher wavenumbers ($\sim 15\text{ cm}^{-1}$).

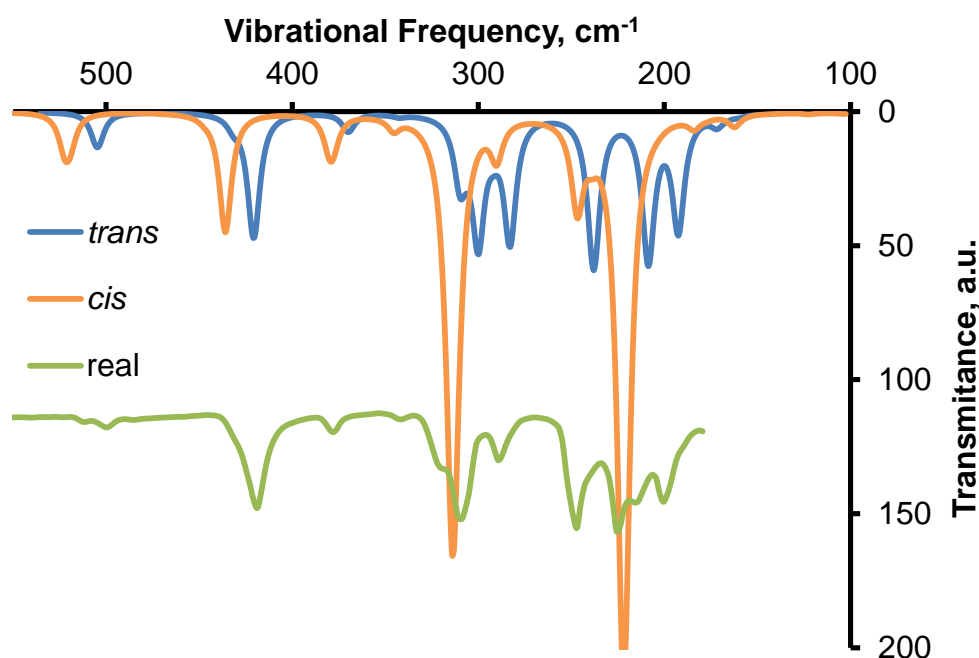


Figure 95: Calculated far-infrared spectra for the *cis*- (orange) and *trans*-isomers (blue) of $[\text{Pt}(\text{tolpy})(\mu\text{-Cl})_2]$ (**1**), overlaid with the measured spectrum (green) for which the transmittance values have been shifted down for clarity.

2.1.2 X-ray Diffraction

Both *cis*- and *trans*-isomers of the dimer complex are present at the end of the reaction, as evidenced by ^1H NMR and FT-IR spectroscopy but the *cis*-isomer is less soluble and crystallises out of solution first. A single crystal suitable for X-ray diffraction was obtained for **1a**, but only a disordered and twinned crystal was obtained for **1b**.

Crystal structure analysis confirms that the single crystal obtained of the *cis*-[Pt(tolpy)(μ -Cl)]₂ (**1a**) has an almost planar geometry (bend angle = 1.69°, each plane defined by platinum and the four atoms bound directly to it) and that it is the *cis*-isomer with C₂ symmetry (Figure 96). The unit cell contains one molecule of **1** and two molecules of disordered CHCl₃, modelled over two positions with refined occupancies of 0.570:0.430(7) and 0.721:0.279(7). C–Cl distances were restrained to be 1.75 Å and Cl··Cl interatomic distances were restrained to be 2.88 Å. Due to close proximity, equivalent atoms of the major and minor component were constrained to have the same atomic displacement parameter. The packing in the crystal is shown in Figure 97, where π - π stacking of the aromatic rings between pairs of molecules was observed. The molecules are stacked in an antiparallel arrangement with respect to the methyl groups to avoid steric clash and the angle between parallel planes is 0°. The aromatic rings are offset to allow alignment of positive electrostatic potential on one ring with negative electrostatic potential on the other ring. A Pt··Pt interaction was not observed with the inter-platinum distance (3.6101(5) Å) being greater than the sum of the van der Waals radii (3.50 Å).

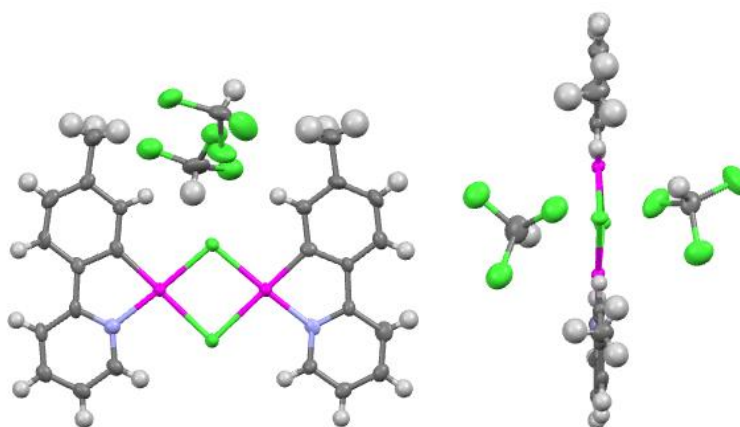


Figure 96: Single crystal X-ray structure of [Pt(tolpy)(μ -Cl)]₂·2CHCl₃ (**1**), with ellipsoids at 50% probability. Images show the front on (left) and side on (right) views. The solvent molecules exhibited disorder and each was modelled with refined occupancies of 0.570:0.430(7) and 0.721:0.279(7).

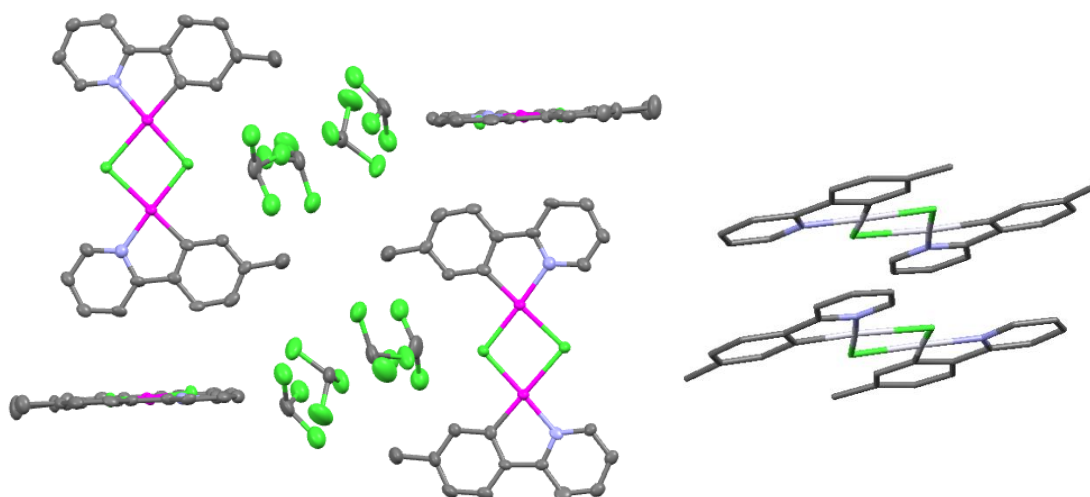


Figure 97: Packing in the crystal for $[\text{Pt}(\text{tolpy})(\mu\text{-Cl})]_2 \cdot 2\text{CHCl}_3$ (**1**) in the unit cell (left), with ellipsoids at 50% probability and the H atoms removed for clarity and a view of one of the π - π stacked pairs (right)

When comparing the two Pt–Cl bond lengths, it can be seen that the two *trans* to the carbanion of the 2-(4-tolyl)pyridine ligand are longer, 2.448(2) and 2.467(2) Å compared with 2.326(2) and 2.331(3) Å for those *trans* to the tolpy nitrogen. This is because the carbanion exerts a stronger *trans*-influence than the coordinating pyridine, dominating the bonding to platinum and thus weakening and lengthening the Pt–Cl bond *trans* to it. Interestingly, different bond lengths were measured for the two different platinum atoms in a molecule of **1a**; for Pt–Cl *trans* to nitrogen the difference in values is not mathematically significant but it is for Pt–Cl *trans* to carbanion. It is surprising that the two Pt–Cl *trans* to carbanion are different in length and it may be due a solvent or intermolecular interaction in the crystal lattice.

1b *Trans*-Isomer

A crystal of the *trans*-isomer was analysed by X-ray diffraction, although it the crystal was severely twinned and too disordered to obtain a good quality structure. Nonetheless, the geometry observed during the refinement was bent (angle between planes of the complex $\sim 25^\circ$, Figure 98), consistent with the calculated geometry.

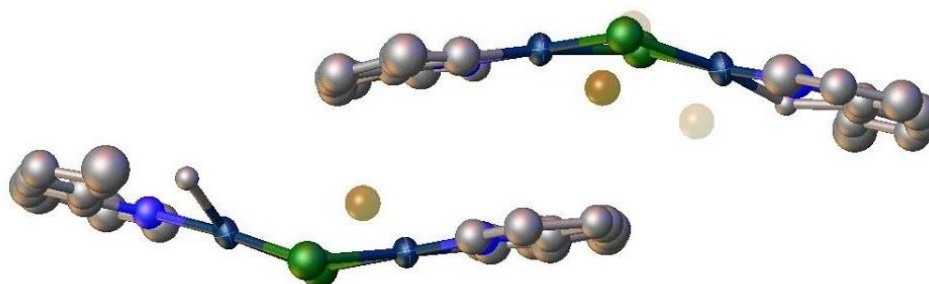


Figure 98: Partly solved crystal of **1b** by X-ray crystallography, with carbon in grey, chlorine in green, nitrogen in purple, platinum in dark blue and the residual electron density (Q peaks) in gold.

2.1.3 NMR Spectroscopy

The ^1H NMR spectrum of the *cis*-isomer **1a** was then fully assigned using 2D COSY spectra and selective 1D difference spectra (the full assignment is detailed in the Experimental Section). Due to the low solubility of complex **1**, it was not possible to observe the ^{15}N or ^{195}Pt chemical shifts and the ^1H NMR spectrum was obtained in solution in acetonitrile (Figure 99). The formation of $[\text{Pt}(\text{tolpy})\text{Cl}(\text{NCMe})]$ (**6**) by cleavage of the dimer was not observed within the timeframe of the NMR experiments (one hour), although it was observed at timescales longer than twelve hours.

The ^1H NMR spectrum was assigned as described above using the chemical shift data, splitting patterns, ^1H - ^{195}Pt coupling and the ^1H - ^1H couplings observed in the ^1H - ^1H COSY spectra (Figures 99 and 100). The ^1H NMR spectrum contained eight proton signals, with ^{195}Pt couplings observed for the protons three bonds away from platinum, namely H^1 and H^8 . The doublet at 8.76 ppm is assigned to the H^1 ($^3J_{\text{HPt}} = 46$ Hz) and the singlet at 7.61 ppm is assigned to the proton adjacent to the coordinating anionic carbon, H^8 ($^3J_{\text{HPt}} = 44$ Hz). Coupling was observed between H^1 and the signal at 7.15 ppm which can hence be assigned as H^2 . H^2 in turn couples to the triplet of doublets at 7.95 ppm which is assigned as H^3 . H^3 couples to H^4 which is assigned as the doublet at 7.73 ppm. This leaves three signals unassigned, H^5 , H^6 and H^7 . Immediately, the up field signal at 2.28 ppm is assigned to the methyl protons, H^7 . Selective 1D nuclear Overhauser effect (NOE) experiments, which detect through space interactions between nearby nuclei, were used to distinguish between the doublets H^5 and H^6 and it was found that H^5 is more downfield than H^6 , which is sensible as H^6 is *ortho* to the electron donating methyl group. Long range w-coupling were not observed; for example, a dd splitting pattern would be expected for H^1 rather than d. For H^3 ,

a ddd splitting pattern was expected but instead a td was observed due to overlap of the peaks.

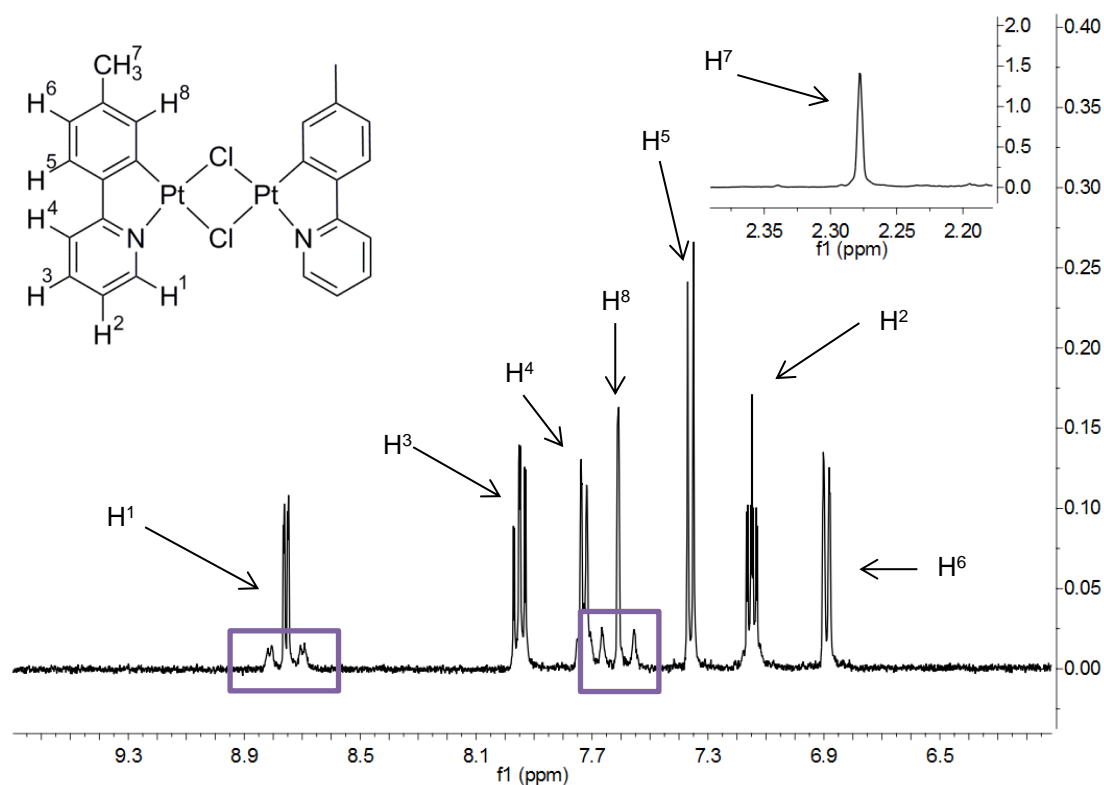


Figure 99: Annotated ^1H NMR spectrum of $[\text{Pt}(\text{tolpy})(\mu\text{-Cl})_2]$ (1) recorded in CD_3CN at 400 MHz. The platinum satellites are highlighted in purple.

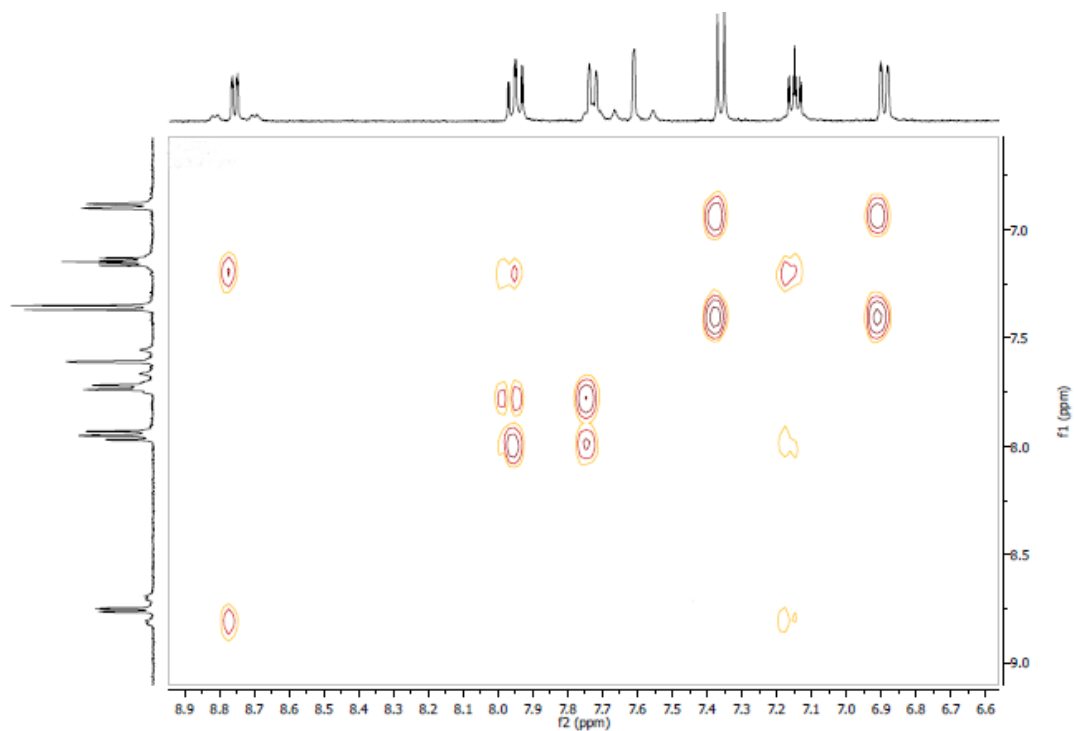


Figure 100: ^1H - ^1H DQF-COSY NMR spectra of $[\text{Pt}(\text{tolpy})(\mu\text{-Cl})_2]$ (1) recorded in CD_3CN

2.2 Nitrogen Donor Ligands

The spectroscopic properties of complexes with the nitrogen donor ligands H-tolpy are discussed here. The lone pair on the nitrogen of pyridine and 2-(4-tolyl)pyridine is not involved in resonance around the pyridine ring system and so instead can be used to coordinate to the metal through σ -donation. [Pt(C[^]N)Cl(H-C[^]N)] complexes (where C[^]N is a bidentate ligand coordinated through C and N donors), such as [Pt(tolpy)Cl(H-tolpy)] (**2**), have been reported as by-products of the synthesis of cyclometallated platinum dimers.^{120, 189} The nitrile complexes, [Pt(tolpy)Cl(NCCH₃)] (**6**) and [Pt(tolpy)Cl(NCPh)] (**12**) were investigated, but both complexes had poor stability, readily undergoing decomposition and thus the spectroscopic data collected for these complexes were limited.

2.2.1 [Pt(tolpy)Cl(H-tolpy)] (**2**)

X-ray Diffraction

The crystal structure obtained (Figure 102) is consistent with that reported by Rodriguez-Castro *et al.* except that the Pt–Cl bond length is slightly shorter than reported previously and it has crystallised in the monoclinic space group rather than triclinic.²⁶⁶ The crystal reported here is a co-crystal with CH₂Cl₂ but the goodness of fit (F^2 value 1.097 vs. 1.069) is better. There are four molecules of [Pt(tolpy)Cl(H-tolpy)] (**2**) and four molecules of CH₂Cl₂ in the unit cell. No interaction between the platinum atoms was observed (Figure 103), but the off-set stacking of the aromatic rings suggests that there is a π - π interaction. The crystallographic data show that there is a twisting angle of 47.61° between the tolyl and pyridyl groups of the monodentate 2-(4-tolyl)pyridine. The proton adjacent to the coordinating carbanion is positioned 3.282 Å from the centre of the pyridyl ring, which suggests a T-shaped C_{Ar}-H \cdots π _{py} interaction. This type of interaction has been reported previously by Fuertes *et al.* for similar cycloplatinated complexes, [Pt(C[^]C)ClL] (C[^]C = 1-(4-cyanophenyl)-3-methyl-1H-imidazol-2-ylidene, L' = Cl, L = PPh₃, py, see Figure 101).²⁶⁷ The pyridyl ligand is orientated so that the plane that goes through the ring is at an angle of 69° to the plane defined by platinum and the four atoms bound to it.

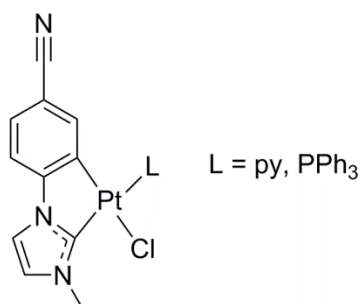


Figure 101: General chemical structure of the complexes reported by Fuertes *et al.* to exhibit a T-shaped C_{Ar}-H... π _{py} interaction²⁶⁷

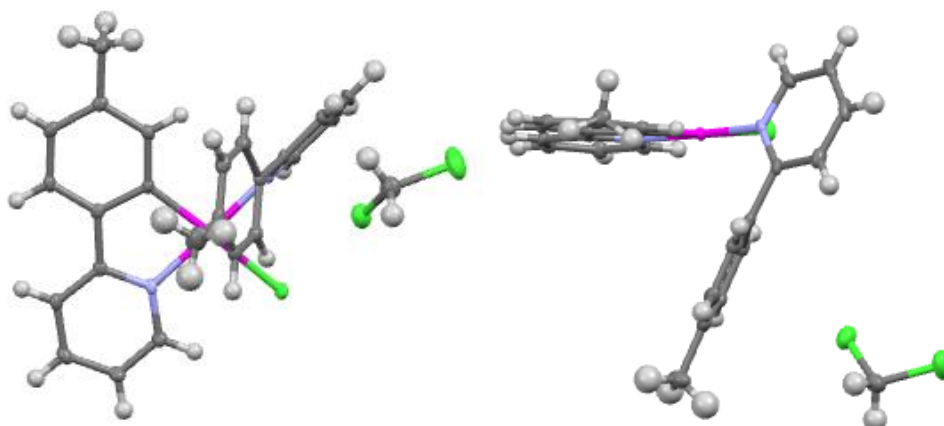


Figure 102: Single crystal X-ray structure for [Pt(tolpy)Cl(H-tolpy)].CH₂Cl₂ (**2**), with ellipsoids at 50% probability, images show the front on (left) and top down (right) views.

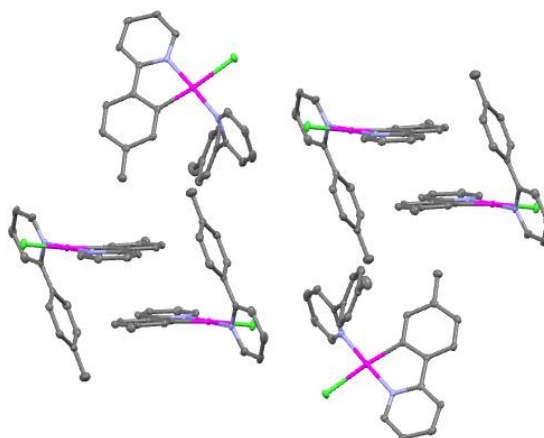


Figure 103: Single crystal X-ray crystal structure showing the packing of [Pt(tolpy)Cl(H-tolpy)].CH₂Cl₂ (**2**), the hydrogen atoms and solvent molecules were removed for clarity

Table 16: Comparison of the bond lengths reported for [Pt(tolpy)Cl(H-tolpy)] (**2**) here and by Rodriguez-Castro *et al.* with [Pt(ppy)Cl(H-ppy)]

Bond	[Pt(tolpy)Cl(H-tolpy)]	[Pt(tolpy)Cl(H-tolpy)] (Lit.) ²⁶⁶	[Pt(ppy)Cl(H-ppy)] ²⁶⁸
------	------------------------	--	-----------------------------------

Pt-C	1.983(2)	1.982(3)	1.976(6)
Pt-N _{tolpy}	2.008(2)	2.017(3)	2.005(5)
Pt-N _{H-tolpy}	2.038(2)	2.036(3)	2.029(6)
Pt-Cl	2.4034(8)	2.4104(8)	2.405(5)

NMR Spectroscopy

For this compound, assignment of the $^{13}\text{C}\{^1\text{H}\}$ and ^{15}N NMR spectra will be explained in detail. For all subsequent compounds, only additional interesting features will be considered. The protons on the tolpy and H-tolpy ligands appear at similar chemical shifts and so ^1H - ^1H COSY and selective 1D NOE NMR experiments were used to assign the different environments (Figures 104). With the key protons on the tolpy and H-tolpy ligands assigned, the chemical shift, splitting and coupling observed in the COSY experiment (Figure 105) were used to assign the remaining signals as described above for complex **1**. The spectrum contained 15 proton environments with three-bond ^1H - ^{195}Pt couplings observed for the bidentate tolpy (H^8 , s, $^3J_{\text{HPt}} = 48$ Hz and H^1 , d, $^3J_{\text{HH}} = 5.7$ Hz, $^3J_{\text{HPt}} = 36$ Hz) and the monodentate H-tolpy (H^9 , d, $^3J_{\text{HH}} = 5.7$ Hz, $^3J_{\text{HPt}} = 40.0$ Hz) ligands. The chemical shift observed for H^8 (6.01 ppm) is consistent with a T-shaped $\text{C}_{\text{Ar}}\text{-H}\cdots\pi_{\text{py}}$ interaction, owing to the high degree of shielding that originates from the position of this proton, pointing directly towards the centre of the pyridyl ring as shown in the X-ray crystal structure (Figure 102). This means that this proton experiences anisotropic shielding due to the aromatic ring current of the pyridyl group.

The AA'XX' spin system of the tolyl protons, H^{13} and H^{14} of the monodentate ligand, was observed in the ^1H NMR spectrum and selective 1D NOE spectra were used to assign these protons. NOE enhancements were observed for H^{12} , and H^8 , as well as the other doublet of the spin system when the more deshielded doublet signal was irradiated, and hence this signal was assigned as H^{13} . The signals at 2.27 and 2.15 ppm are due to the methyl groups; selective 1D NOE spectra were used to distinguish between them. When the signal at 2.15 ppm was irradiated a strong NOE enhancement was observed for H^8 , identifying this peak as H^7 and the signal at 2.27 ppm as H^{15} . When H^8 was irradiated, NOE enhancements were observed for the methyl group, H^7 and also for H^{13} and the doublet at 9.24 ppm. Due to the downfield chemical shift and the platinum

satellites observed, it is known that this signal is due to a proton *ortho* to the coordinating nitrogen, H¹ or H⁹. The observation of an NOE enhancement on irradiation of H⁸ means that this signal is assigned at H⁹ and the other downfield signal at 9.59 ppm is assigned as H¹.

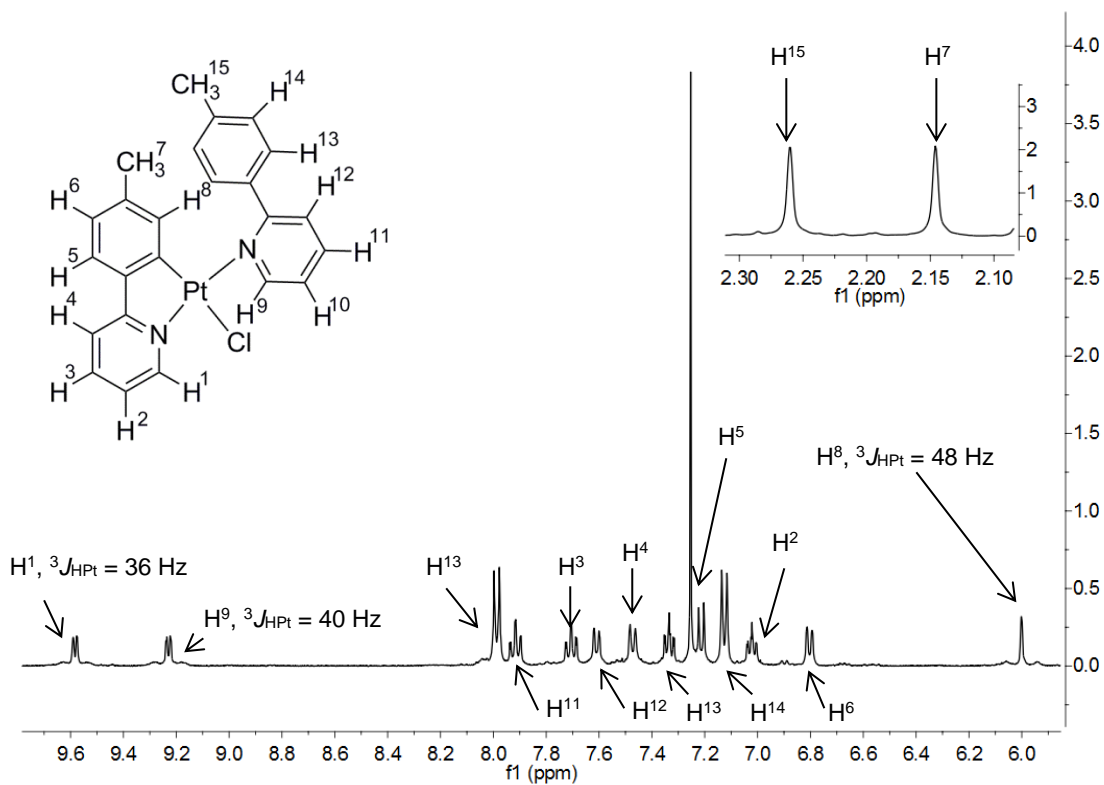


Figure 104: Annotated ¹H NMR spectrum of [Pt(tolpy)Cl(H-tolpy)] (2) recorded in CDCl₃.

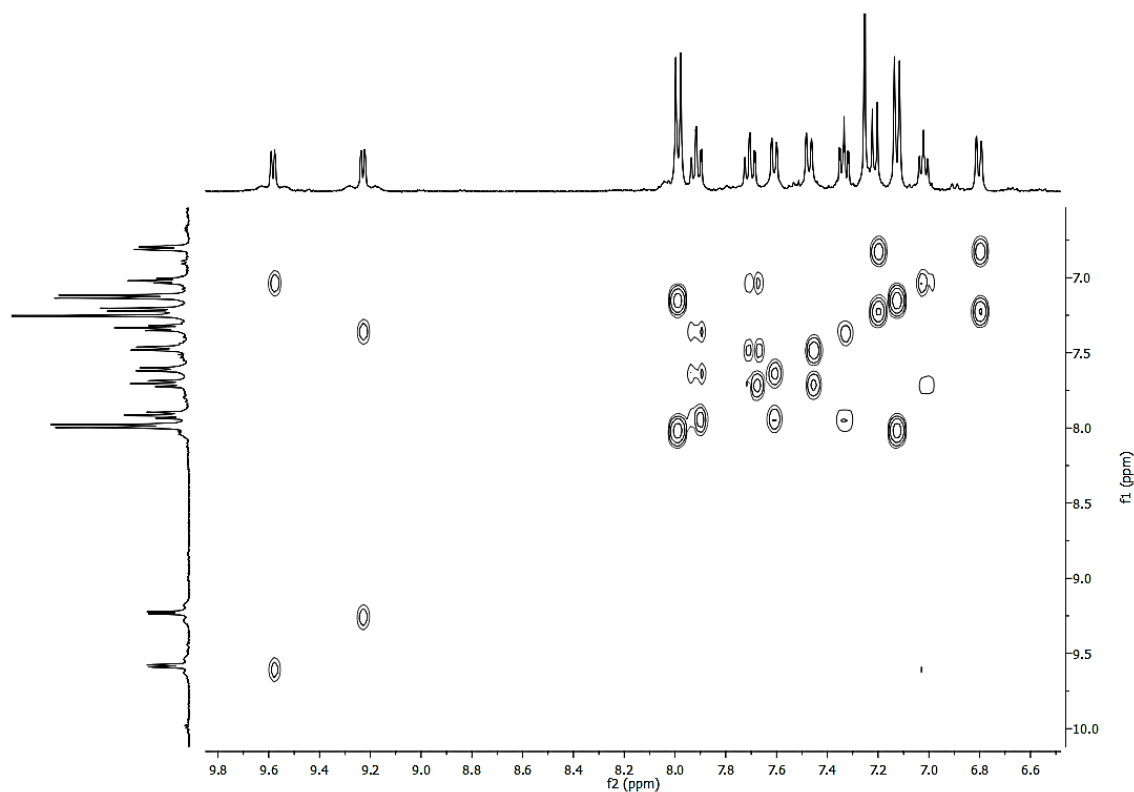
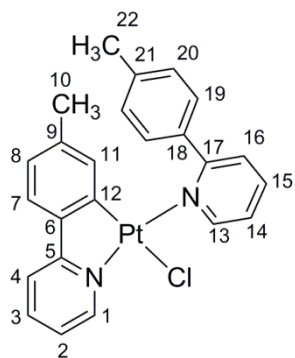


Figure 105: ^1H - ^1H DQF-COSY NMR spectra of $[\text{Pt}(\text{tolpy})\text{Cl}(\text{H-tolpy})]$ (**2**) recorded in CDCl_3

$^{13}\text{C}\{^1\text{H}\}$ NMR Spectroscopy

The non-quaternary signals observed in the $^{13}\text{C}\{^1\text{H}\}$ NMR spectrum were assigned using the 2D HMQC ^1H - ^{13}C correlation experiment (Figures 106 and 107) and the remaining seven unassigned quaternary carbon signals (underlined) were assigned using a 2D HMBC ^1H - ^{13}C correlation experiment. Coupling between carbon and platinum was observed for the signal at 137.23 ppm ($^3J_{\text{CPt}} = 28$ Hz) which also couples to H^{15} and H^{14} , and was assigned as C^{18} . The quaternary signal at 141.08 ppm does not couple to anything but by a process of elimination is assigned to C^{12} . Coupling between C^{12} and ^{195}Pt was not observed even though they are directly bound, this is thought to be due to faster relaxation through the chemical anisotropy mechanism, which will be discussed in more detail in Section 3.3.²⁶⁹



$^{13}\text{C}\{^1\text{H}\}$ -NMR δ_{C} (100.5 MHz, CDCl_3): 167.32 (q, C5), 162.43 (q, C17), 154.41 (C13), 151.17 (C1), 141.62 (q, C6), 141.08 (q, C12), 139.88 (q, C9), 139.27 (q, C21), 138.30 (C16 $3J_{\text{CPt}} = 34$ Hz), 137.60 (C15), 137.23 (q, C18, $3J_{\text{CPt}} = 28$ Hz), 131.71 (C11), 129.37 (C19, $4J_{\text{CPt}} = 36$ Hz), 128.73 (C20), 127.30 (C16), 123.92 (C8), 123.57 (C14), 123.10 (C7), 121.19 (C2), 117.73 (C4), 21.90 (C10), 21.48 (C22).

Figure 106: Structure of $[\text{Pt}(\text{tolpy})\text{Cl}(\text{H-tolpy})]$ (2) with the carbon atoms labelled from 1 to 22 and the assignment of the signals observed in the ^1H NMR spectrum. The quaternary carbon signals are underlined.

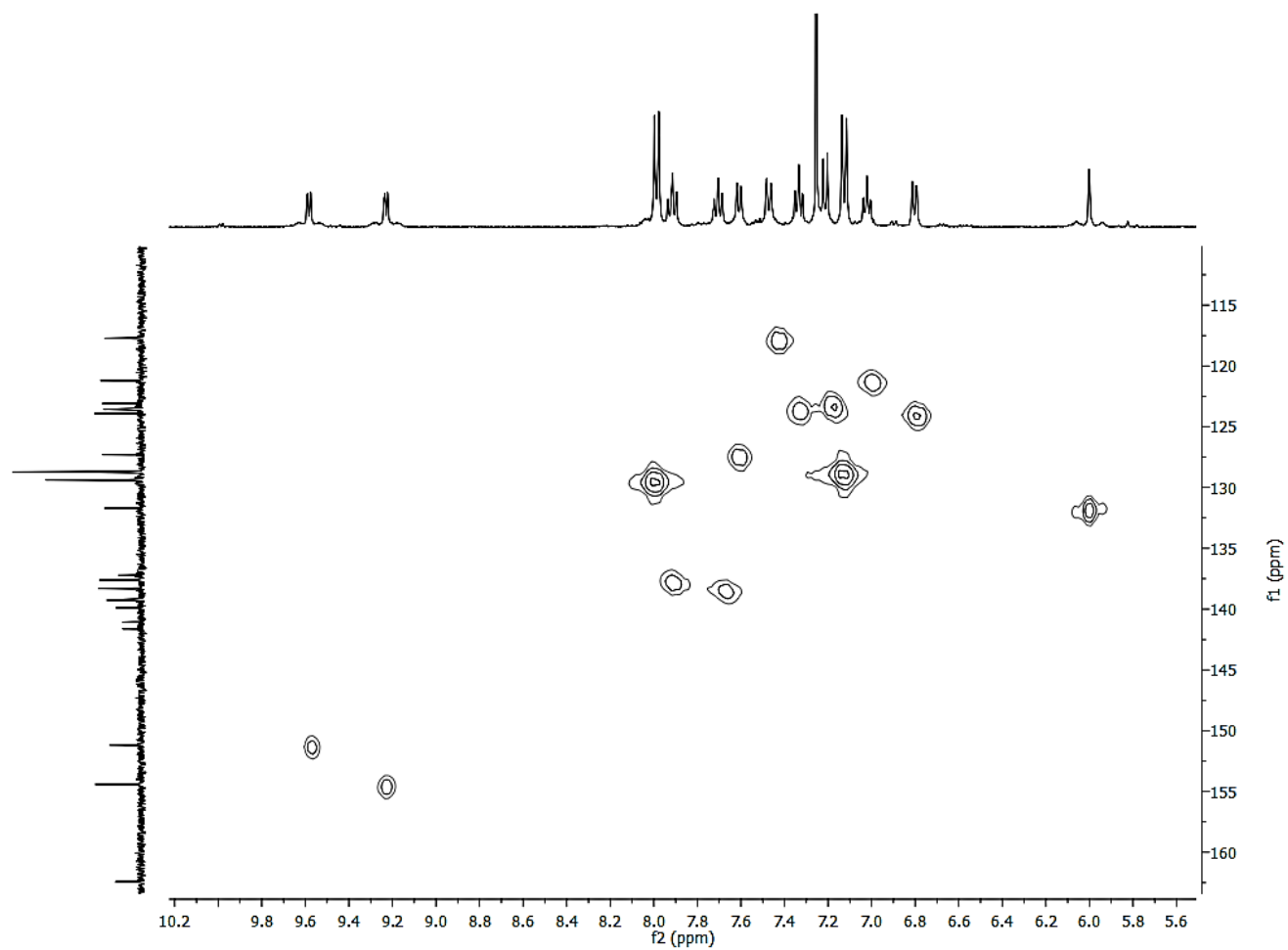


Figure 107: ^1H - ^{13}C HMQC spectra for $[\text{Pt}(\text{tolpy})\text{Cl}(\text{H-tolpy})]$ (**2**) recorded in CDCl_3

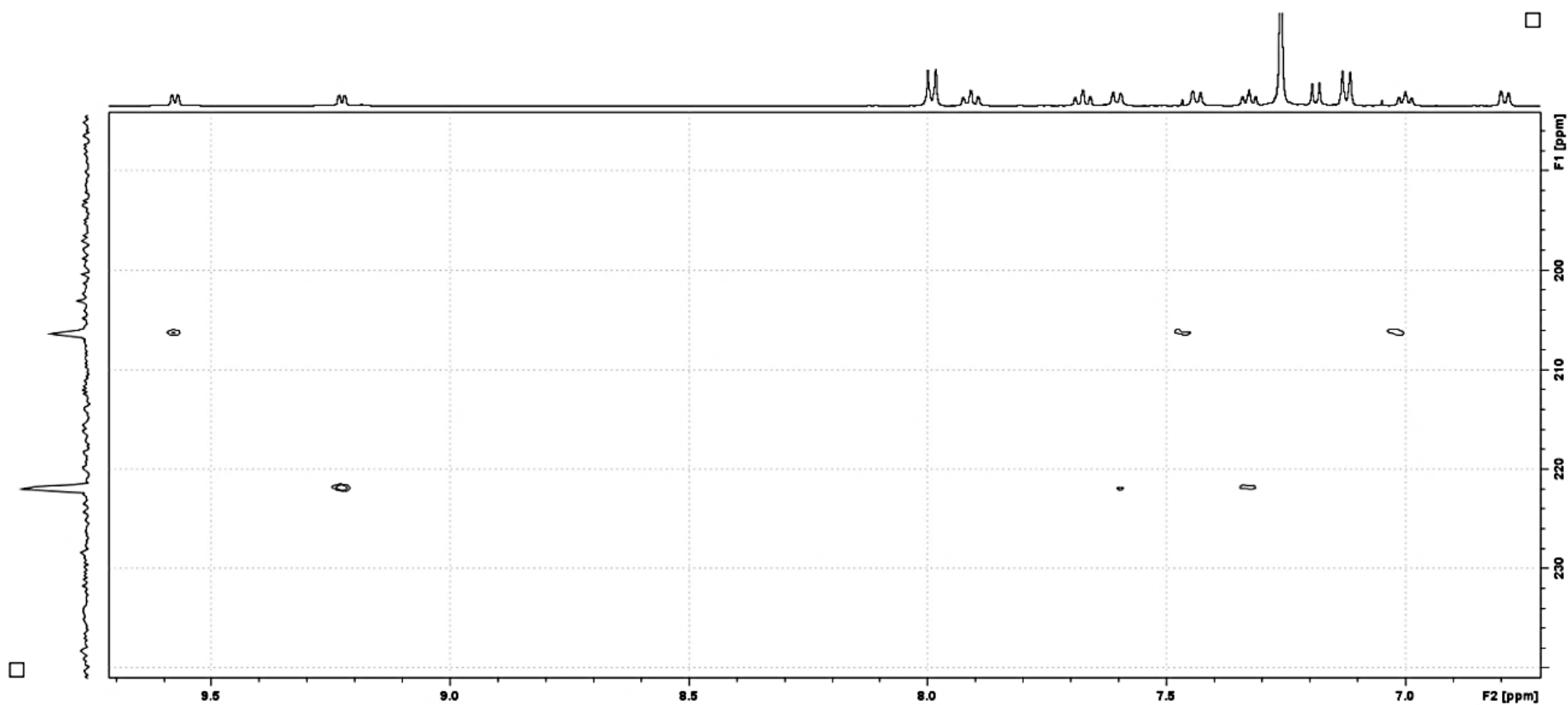
^{15}N NMR Spectroscopy

Figure 108: ^1H - ^{15}N HMBC spectra for $[\text{Pt}(\text{tolpy})\text{Cl}(\text{H-tolpy})]$ (**2**) recorded in CDCl_3 and the data were acquired over 32 scans. The 1D projection for the ^{15}N spectrum is on the x-axis and the previously recorded ^1H spectrum is on the y-axis.

^{15}N NMR spectra are not recorded routinely because of the low sensitivity of the nucleus which has a natural abundance of 0.46% and this nucleus also has a negative gyromagnetic ratio (-27.1), which means that smaller or even negative signals can be observed under conditions of proton decoupling. Here, a 2D method was used to reduce the time required to collect a spectrum; ^{15}N chemical shifts were obtained using 2D ^1H - ^{15}N correlation *via* heteronuclear zero and double quantum coherence. This method was optimised for long-range couplings (using a ^1H - ^{15}N coupling constant of 2 Hz), with no decoupling during acquisition and using gradient pulses for selection. ^{15}N chemical shifts were referenced relative to external 2-(4-tolyl)pyridine in CDCl_3 (306 ppm).

The two nitrogen peaks were observed in the spectra recorded for $[\text{Pt}(\text{tolpy})\text{Cl}(\text{H-tolpy})]$ (**2**) (Figure 108). The peak at 206 ppm couples to H^1 , H^4 and H^2 , and is assigned to the bidentate tolpy ligand. The peak at 222 ppm couples to protons at H^9 , H^{12} and H^{10} and is assigned as the nitrogen of the monodentate ligand (H-tolpy). Coupling between nitrogen and platinum was not observed.

2.2.2 $[\text{Pt}(\text{tolpy})\text{Cl}(\text{py})]$ (**5**)

The title complex was synthesised by ligand exchange from the dmsO complex **3** in acetone. Attempts were also made to prepare the analogous pentafluoropyridine and 2-fluoropyridine analogues, but these were unsuccessful due to the low basicity of the nitrogen lone pair. Furthermore it has been reported that 2,3,5,6-tetra-fluoropyridyl ligands binds preferentially to the carbanion though C–H activation rather than the pyridyl nitrogen lone pair.²⁷⁰ The tolylpyridine ligand is expected to be a stronger Lewis base than pyridine due to the electron donating tolyl substituent and so a weaker Pt– N_{py} bond is suspected for complex **5**.

X-ray Diffraction

The X-ray structure has not previously been reported in the literature and was determined from a crystal obtained from CDCl_3 and diethyl ether (Figure 109). The unit cell contains 16 molecules of complex **5** and none of solvent. Two molecules in the unit cell which appear to be stacked one on top of the other are slightly offset but the angle measured between each molecular plane, defined by the platinum and four atoms directly coordinated to it, is 13.62° indicating that there is no π - π stacking interaction (Figure 110). The pyridyl ligand is twisted out of the plane by an average of 70.26° ($65.18^\circ - 74.42^\circ$) amongst the molecules in the unit cell, which is consistent with the twisting angle observed for the pyridyl group of the monodentate H-tolpy ligand of complex **2**.

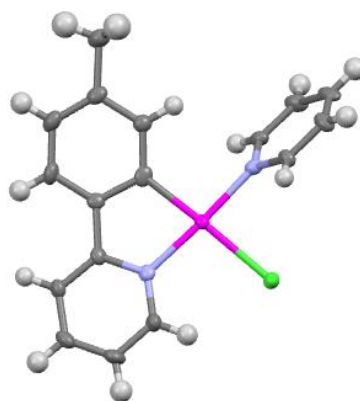


Figure 109: Single crystal X-ray structure of [Pt(tolpy)Cl(py)] (**5**) with ellipsoids at 50% probability.

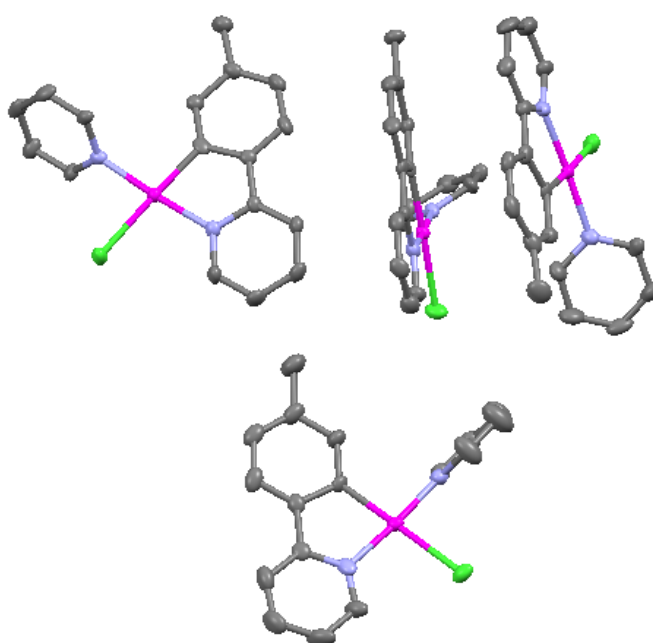


Figure 110: Packing of [Pt(tolpy)Cl(py)] determined by single crystal X-ray crystallography with ellipsoids at 50% probability and the hydrogen atoms omitted for clarity.

Notable Features of the NMR and FT-IR Spectra

The magnitude of the coupling between platinum and the proton *ortho* to the pyridyl nitrogen of the pyridyl ligand (^9H , $^3J_{\text{HPt}} = 42$ Hz) observed in the ^1H NMR spectrum of [Pt(tolpy)Cl(py)] (**5**) was greater than that observed for the related proton on the bidentate ligand (^1H , $^3J_{\text{HPt}} = 36$ Hz). As with complex **2**, the proton *ortho* to the carbanion, H^8 , has been shifted up-field to 6.13 ($^3J_{\text{HPt}} = 48$ Hz) caused by shielding by the pyridyl ring. Two peaks, one at 206 ppm and one at 221 ppm, were present in the 2D ^1H - ^{15}N HMBC spectra and coupling to ^{195}Pt was observed. The peak at 206 ppm coupled to protons at H^1 , H^2 and H^4 and is assigned to the bidentate ligand. The peak at 221 ppm coupled to protons at H^{11} and H^{10} and is assigned to the

pyridine ligand. The $^1J_{\text{NPt}}$ coupling constant for the nitrogen of the pyridyl ligand ($^1J_{\text{NPt}} = 454$ Hz) was observed and a smaller coupling to the nitrogen of the bidentate ligand was also observed ($^1J_{\text{NPt}} = 395$ Hz). The value of the coupling constant is similar to those reported by Chikuma and Pollock for *cis*-diamine platinum(II) complexes (300 – 410 Hz).²⁷¹

In addition to the Pt–Cl stretching frequency, additional absorptions for the pyridine ligand were observed in the infrared region using FT-IR spectroscopy. When pyridine forms metal complexes the in plane ring deformation at 604 cm^{-1} and the out-of-plane ring deformation at 405 cm^{-1} are shifted to higher frequencies.²⁷²

2.3 Sulfur Donor Ligands

Sulfur donor ligands can coordinate to transition metals by σ -donation from one of the sulfur lone pairs. They are soft bases which form stable complexes with soft acids such as platinum(II).²⁷³ In this study, complexes of the ligands dimethyl sulfide (dms), dimethyl sulfoxide (dmsO) and tetrahydrothiophene (tht) were evaluated. These complexes were synthesised by heating the dimer complex **1** in the neat ligand under reflux.

2.3.1 [Pt(tolpy)Cl(S-dmsO)] (**3**)

The dmsO ligand can coordinate to a metal centre through either the oxygen atom or the sulfur and it can have both terminal and bridging modes.²⁷⁴ Generally, the hardness or softness of the metal centre determines the preferred mode of coordination, with soft metals preferentially binding to the sulfur atom. Ruthenium sulfoxide complexes have been reported to undergo photochemical isomerisation between oxygen- and sulfur-coordination modes.²⁷⁵⁻²⁷⁷

X-ray Diffraction

The single crystal X-ray structure confirms that coordination of the dmsO ligand is through a Pt–S bond. Two different geometries were observed for the coordinated dmsO ligand, one with the methyl groups of the dmsO ligand pointing out of the plane of the molecule, and one with the oxygen atom and one of the methyl groups pointing out of the plane (Figure 112). For the molecule where the sulfur–oxygen bond is pointing out of the plane, the angle between it (plane defined by the oxygen, sulfur and platinum atoms) and the molecular plane (defined by platinum and the four surrounding atoms) was 57° . The sulfur–oxygen bond lengths measured by X-ray diffraction of the molecules of the unit cell were in the range 1.466(6) - 1.479(6)

Å, which is shorter than the value for free dmsO, which was measured by Thomas *et al.* to be 1.513(5) Å.²⁷⁸ The shortening of the sulfur–oxygen bond length is consistent with the neutral resonance form of dmsO (Figure 111). There are twelve molecules of complex **3** (and no solvent molecules) in the unit cell (Figure 113), each stacking infinitely in one direction with the dmsO ligand orientated on the alternate side. Evidence for intermolecular Pt⋯Pt or π - π interactions between aromatic rings, such as offset stacking of the aromatic rings or a reduced Pt⋯Pt, was not observed.

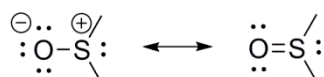


Figure 111: Resonance forms of the ligand dmsO

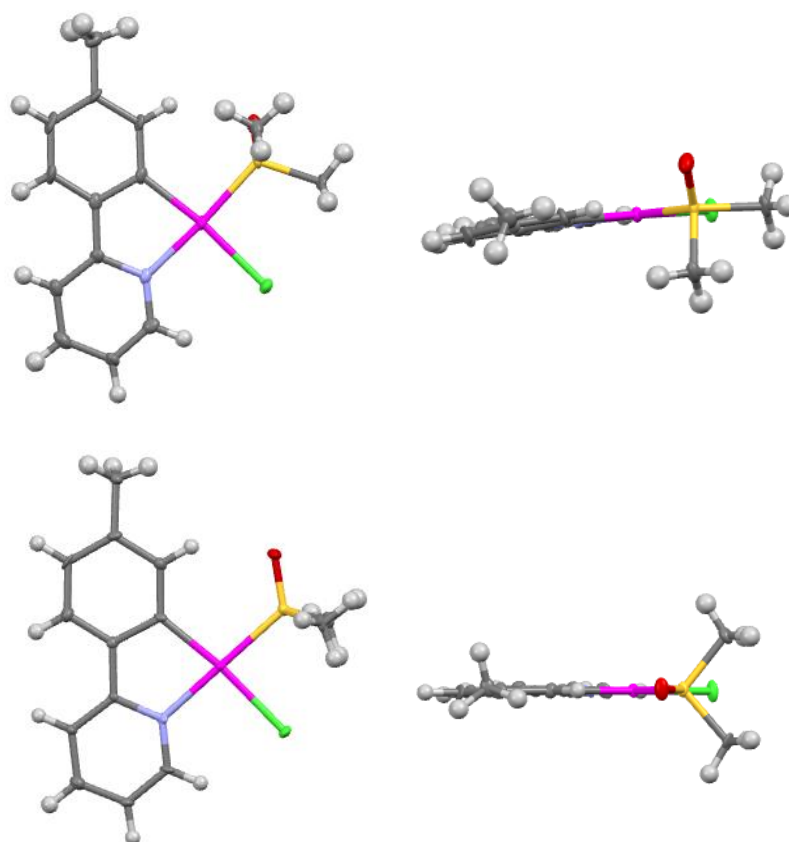


Figure 112: Single crystal X-ray crystal structure for [Pt(tolpy)Cl(S-dmsO)] (**3**), with ellipsoids at 50% probability. The images show the front on (left) and top down (right) views with the dmsO ligand coordinated with two different geometries in the unit cell (upper and lower images).

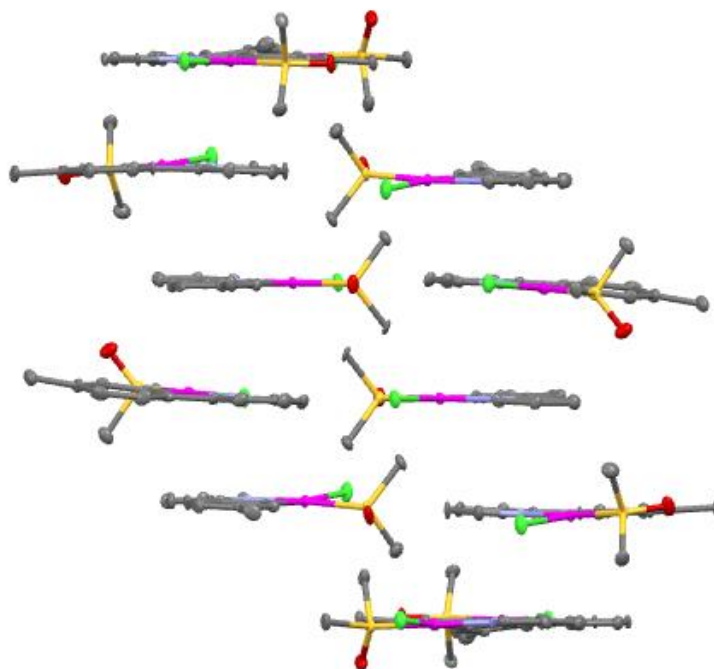


Figure 113: Packing of [Pt(tolpy)Cl(S-dmsO)] (**3**) in the unit cell determined by X-ray crystallography, with ellipsoids at 50% probability and the hydrogen atoms omitted for clarity.

The single crystal X-ray structure of the phenylpyridine analogue, [Pt(ppy)Cl(S-dmsO)] was reported by Kobayashi and co-workers (Figure 114, Table 17).²⁷⁹ Here, only one geometry of the S-bound dmsO ligand was observed, with the methyl groups pointing out from the molecular plane. However, the stacking of the molecules is very similar to **3** and the bond lengths are statistically the same.

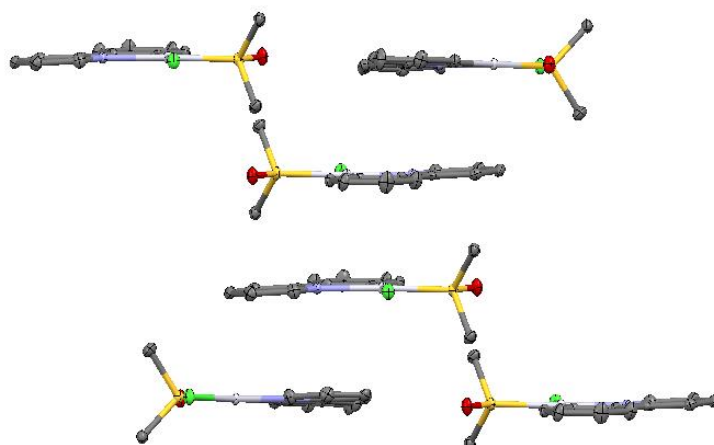


Figure 114: Packing of [Pt(ppy)Cl(S-dmsO)] determined by single crystal X-ray diffraction reported by Kobayashi and co-workers, with ellipsoids at 50% probability and the hydrogen atoms omitted for clarity.²⁷⁹

Table 17: Comparison of the bond lengths reported for [Pt(tolpy)Cl(S-dmsO)] (**3**) reported here and [Pt(ppy)Cl(S-dmsO)] reported by Kobayashi and co-workers.²⁷⁹

Bond	[Pt(tolpy)Cl(S-dmsO)]	[Pt(ppy)Cl(S-dmsO)] ²⁷⁹
Pt–C	2.012(7)	2.003(4)
Pt–N	2.053(6)	2.070(3)
Pt–S	2.216(2)	2.2181(9)
Pt–Cl	2.409(2)	2.420(1)

Infra-red Spectroscopy

Metal complexes of dmsO bound through oxygen show absorption bands at lower wavenumbers than free dmsO, whereas metal complexes bound through sulfur show absorption bands at higher wavenumbers. The increase in wavenumber is due to stabilisation of the neutral resonance form of dmsO when bound through sulfur (Figure 111). The intense band at 1118 cm⁻¹ present in the FT-IR spectrum is assigned to the S=O stretch by comparison with the literature values for other platinum sulfoxide complexes.^{280, 281} The position of the S=O band is higher than that of free dmsO (1062 cm⁻¹),²⁸² which is consistent with the crystal structure described in 2.3.1 in which the dmsO ligand binds to platinum through sulfur.

NMR Spectroscopy

Coupling between ¹⁹⁵Pt and the methyl protons of the dmsO ligand was observed in the ¹H NMR spectrum of [Pt(tolpy)Cl(S-dmsO)] (**3**) (3.64 ppm, ³J_{HPt} = 23 Hz) which were shifted down-field compared to the free ligand (2.62 ppm in CDCl₃).²⁸³ The magnitude of the coupling constant is similar to that reported for [Pt(ppy)Cl(S-dmsO)].¹⁸⁹ The down-field shift of approximately 1 ppm observed is consistent with coordination through the sulfur atom; a downfield shift is also observed for oxygen-bound dmsO but the magnitude is smaller.²⁸⁴ The magnitude of the coupling observed is smaller than the other vicinal ³J couplings to the protons of the bidentate ligand. Similar to the ¹H spectrum, the ¹³C{¹H} NMR spectrum also shows an increase in chemical shift for the methyl groups present on the bound dmsO ligand from 40.76 ppm for the free ligand to 47.30 ppm.²⁸³ Coupling between the magnetically equivalent methyl carbon atoms and ¹⁹⁵Pt was observed with a coupling constant, ²J_{CPt} = 60 Hz.

2.3.2 [Pt(tolpy)Cl(dms)] (7)

X-ray Diffraction

The crystal structure obtained for complex **7** shows that the methyl groups are orientated pointing out of the molecular plane (defined by platinum and the four surrounding atoms, Figure 115) and that both of the S–C_{Me} bonds are equal in length. The unit cell contains four molecules of **7** and no solvent molecules. Although in the unit cell the molecules do not orientate themselves so that the bidentate ligand is stacked above another (Figure 116), there is evidence for π - π interactions between tolpy ligands in the crystal phase. There was no evidence for Pt...Pt interactions but close contacts were observed between chlorine and some of the hydrogen atoms of the pyridyl ring and also of the dms ligand.

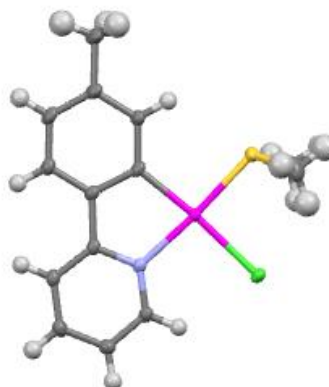


Figure 115: Single crystal X-ray crystal structure of [Pt(tolpy)Cl(dms)] (**7**) with ellipsoids shown at 50% probability

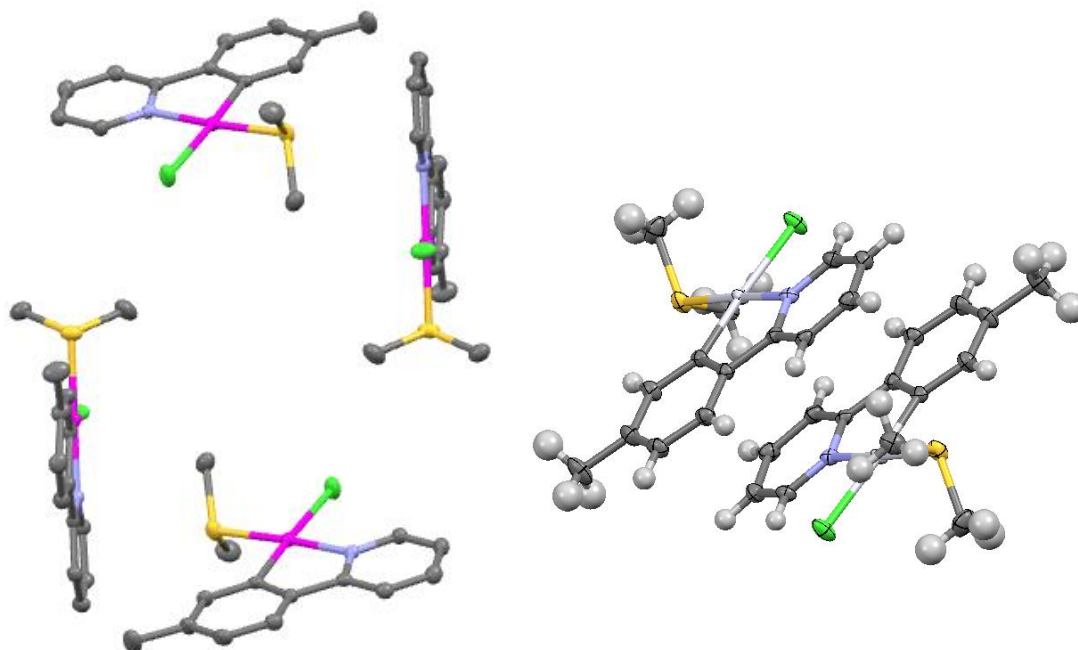


Figure 116: Packing of [Pt(tolpy)Cl(dms)] (**7**) in the unit cell determined by X-ray crystallography (left) and image showing π - π stacking of tolpy ligands (right) with ellipsoids at 50% probability and the hydrogen atoms omitted for clarity

NMR Spectroscopy

Coupling between ^{195}Pt and the methyl protons of the dms ligand was observed in the ^1H NMR spectrum of **7** (2.77 ppm, $^3J_{\text{HPt}} = 52.5$ Hz) which were shifted down-field compared to the free ligand (2.11 ppm in CDCl_3).²⁸³ The magnitude of the $^3J_{\text{HPt}}$ coupling observed is larger than the other vicinal $^3J_{\text{HPt}}$ couplings to the protons of the bidentate ligand and, interestingly, it is significantly larger than the $^3J_{\text{HPt}}$ observed for the protons of the dmsO ligand in complex **3**. Similar to the ^1H spectrum, the $^{13}\text{C}\{^1\text{H}\}$ NMR spectrum also shows a small increase in chemical shift for the methyl groups present on the bound dms ligand from 23.50 ppm for the free ligand to 18 ppm. Coupling between the magnetically equivalent methyl carbon atoms and ^{195}Pt was observed with a coupling constant, $^2J_{\text{CPt}} = 31$ Hz, much lower than that observed for the dmsO complex **3** ($^2J_{\text{CPt}} = 60$ Hz).

2.3.3 [Pt(tolpy)Cl(tht)] (**8**)

X-ray Diffraction

The crystal structure for [Pt(tolpy)Cl(tht)] (**8**) contains four molecules in the unit cell (Figure 117). The tht ligand is twisted out of the molecular plane of complex by 84° (defined by the platinum atom and the four directly coordinated atoms). The molecules pack in the crystal with the tolyl group alternating between pointing up and down (Figure 118) and there were no obvious π - π or Pt \cdots Pt interactions. As with the dms complex **7**, short contacts were observed between the chloride ligand and the hydrogen atoms of the tolpy ligand and the tht ligand. The distance between the chloride ligand and the hydrogen atom is 98% of the sum of the van der Waals radii for these atoms, indicating a very weak interaction (Figure 119).

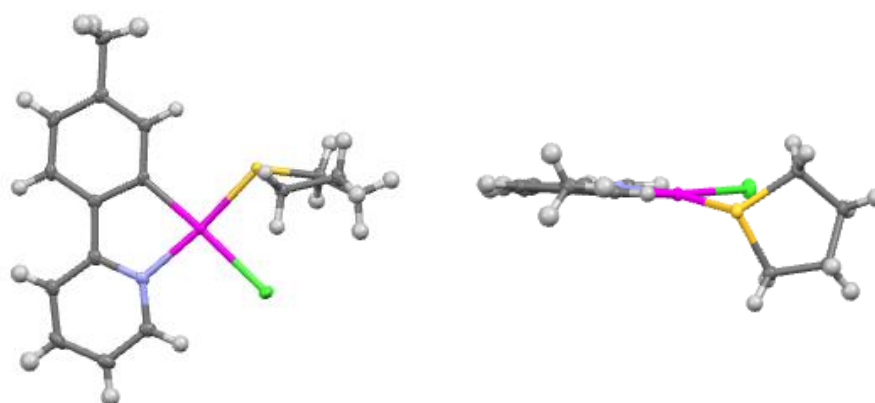


Figure 117: Front on (left) and side on (right) views of the single crystal X-ray crystal structure of [Pt(tolpy)Cl(tht)] (**8**), with ellipsoids at 50% probability.

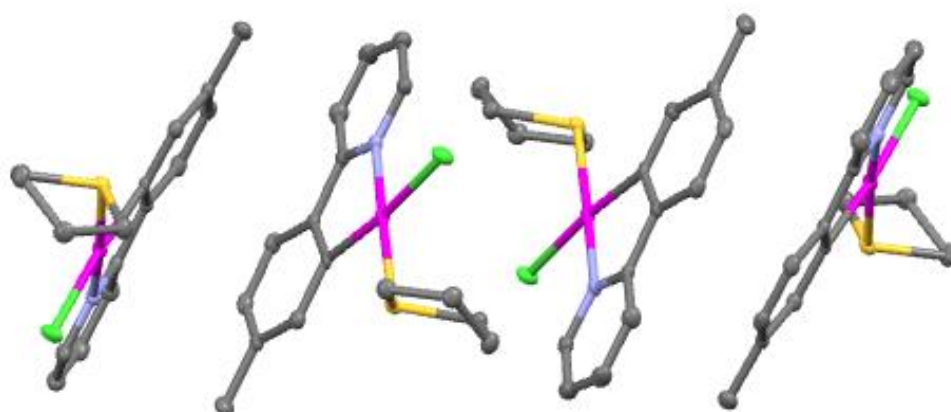


Figure 118: Packing of [Pt(tolpy)Cl(tht)] (**8**) in the unit cell determined by X-ray crystallography with ellipsoids at 50% probability and the hydrogen atoms omitted for clarity

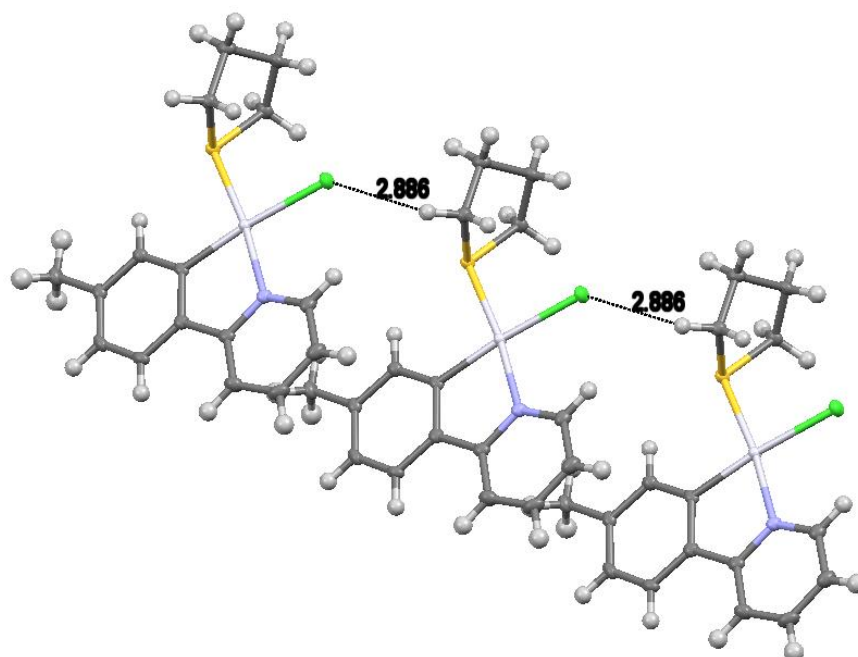


Figure 119: View of the packing in the crystal structure of **8** highlighting the short contact between the chloride ligand and a hydrogen atom of the tht ligand with ellipsoids at 50% probability

NMR Spectroscopy

The proton environments of the 2-(4-tolyl)pyridine ligand were assigned as described previously. Four broad signals were observed for the tht ligand, and for two of these, platinum satellites were observed (Figure 120). Only two signals were observed for carbon atoms of the tht ligand in the $^{13}\text{C}\{^1\text{H}\}$ NMR spectrum, which suggests that the two α -carbons are equivalent and the two β -carbons are equivalent on the NMR timescale but that the protons bonded to these carbon environments are not chemically or magnetically equivalent.

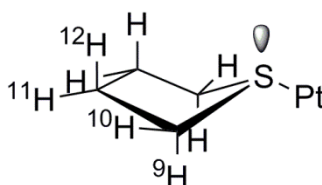


Figure 120: Geometry and Proton assignment of the tht ligand

Both the Karplus^{285, 286} and the Bothner-By²⁸⁷ equations (see below) can be used to relate the magnitude of the coupling constant between vicinal protons to the dihedral angle. If we apply these equations for the $^3J_{\text{HPt}}$ couplings, a larger value would be predicted for H^9 relative to H^{10} . Therefore the more deshielded signal at 3.87 ppm with the larger $^3J_{\text{HPt}}$ value was speculatively assigned to H^9 (Figure 120). The broadness of the proton signals suggests a fluxional process, such as stereo-chemical inversion at the sulfur, is occurring.

Karplus equation:²⁸⁶ ${}^3J_{\text{HH}'} = 4.22 - 0.5\cos\phi + 4.5\cos 2\phi$

Bothner-By equation:²⁸⁷ ${}^3J_{\text{HH}'} = 7 - \cos\phi + 5\cos 2\phi$

2.4 Carbon Donor Ligands

2.4.1 [Pt(tolpy)Cl(CO)] (4)

The carbonyl ligands of certain cycloplatinated complexes can undergo thermal and photochemical ejection and for this reason they have found application as therapeutic CO-releasing molecules (CORMs).²⁸⁸ Although carbon monoxide is fatal on inhalation, small quantities can be beneficial to cells.²⁸⁹ For example, CO has anti-inflammatory effects, can provide protection against hyperoxia and ischemia and can regulate blood pressure under stress conditions.²⁹⁰

In a similar way to nitriles, carbon monoxide demonstrates synergic bonding to metals, acting as both a σ -donor and a π -acceptor, but it has greater π -acidity.²⁹¹ Carbon monoxide has four modes of coordination to metals, terminal, bridging μ^2 , triply bridging and asymmetric bridging. Both isomers of [Pt(tolpy)Cl(CO)] (**4**) were prepared and analysed, one with the carbonyl group *trans* to the pyridyl nitrogen (**4a**) and one *trans* to the carbanion (**4b**). Previously, all the published structures for platinum carbonyl complexes with C[^]N cyclometallating ligands reported are where the carbonyl is *trans* to the pyridyl nitrogen. The relative energies of the two isomers were calculated and the minor isomer (in terms of isolated yield), **4b**, was found to be significantly higher in energy than the major isomer, **4a** ($\Delta E = 45 \text{ kJ mol}^{-1}$).

FT-IR Spectroscopy

The carbon monoxide stretching frequency is dependent on the coordination mode and the degree of back-bonding from the metal. The strong absorption at 2098 cm^{-1} present in the FT-IR spectrum of **4a** and 2113 cm^{-1} for **4b** are assigned to the $\bar{\nu}(\text{C}\equiv\text{O})$ stretch and the relative order of the stretching frequencies is the same as those predicted by the vibrational frequency calculations (BP86/6-31G(d)/LanD2DZ on Pt, Table 18). These values are similar to those reported for the related cyclometallated complexes of the general formula [Pt(C[^]N)Cl(CO)] reported by Newman *et al.*; where C[^]N is ppy $\bar{\nu}(\text{C}\equiv\text{O})$ is 2104 cm^{-1} , for 2-(4-fluorophenyl)pyridine $\bar{\nu}(\text{C}\equiv\text{O})$ is 2108 cm^{-1} and for 2-(4-methoxyphenyl) the $\bar{\nu}(\text{C}\equiv\text{O})$ is 2101 cm^{-1} .¹⁸⁹ The variation in vibrational frequency observed for these complexes is quite small, which is consistent with limited availability of the platinum *d*-orbitals for π -back-bonding.

Table 18: Comparison of the calculated and experimental vibrational frequencies and the relative energies of the isomers **4a** and **4b**

	E , Ha	E , kJ mol ⁻¹	ΔE , kJ mol ⁻¹	Calculated $\bar{\nu}(\text{C}\equiv\text{O})$	Experimental $\bar{\nu}(\text{C}\equiv\text{O})$
4 a	-1210.96	-3179379	0	2081	2098
4 b	-1210.94	-3179334	45.29	2155	2113

Calculating the Frontier Molecular orbitals

In order to understand the metal-ligand bonding, specifically the π -back donation, the HOMO and LUMO orbitals of complex **4** were studied using computational chemistry. Unlike octahedral or tetrahedral complexes, the relative ordering of the d -orbitals in square planar complexes vary with the nature of the ligand.²⁹² For ligands which are purely σ -donors, the LUMO is the b_{1g} (derived from the $d_{x^2-y^2}$ atomic orbital). This is raised in energy by strong M–L antibonding interactions in the x - y plane. The HOMO is the a_{1g} orbital (derived from the d_{z^2} atomic orbital) which is higher in energy than the other molecular orbitals because the ring shaped lobe also takes part in some M–L anti-bonding interactions in the x - y plane. The molecular orbitals derived from the d_{xy} , d_{xz} and d_{yz} atomic orbitals are non-bonding. In most cases, metal complexes of π -acceptor ligands show the same energetic ordering of orbitals. For π -donating ligands such as Cl, the LUMO remains the b_{1g} orbital but the HOMO changes depending on the complex.²⁹³⁻²⁹⁵ For [PdCl₄], the HOMOs are the two degenerate e_g orbitals (derived from d_{xz} and d_{yz}).²⁹² The e_g orbitals take part in π -antibonding interactions with the lone pairs of the ligand which raise the energy of the molecular orbitals, whereas the a_{1g} (d_{z^2}) orbital is stabilised by weak σ -donation from the ligand.

Complex **4** contains π -acceptor (tolpy and CO) and π -donor (Cl) ligands. Computational methods have been used to determine the energetic ordering of d -orbitals.²⁹⁶⁻²⁹⁸ The HOMO and LUMO were visualised after the geometry optimisation of complex **4** (BP86/6-31G(d)/LANL2DZ for Pt), using the Cubegen utility within Gaussian09 (Figure 121 and Figure 122). The calculated HOMO appears to be derived from a platinum d_{yz} atomic orbital.

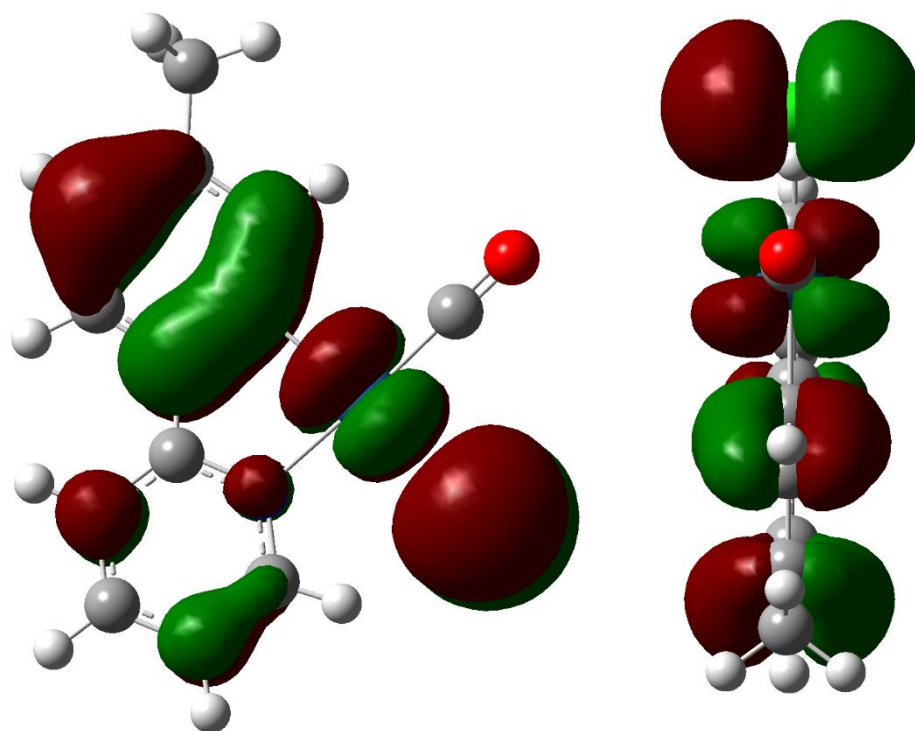


Figure 121: The calculated HOMO for complex **4a** using BP86 with 6-31G(d) and LANL2DZ (for Pt) for the geometry optimisation and the utility Cubegen within Gaussian09

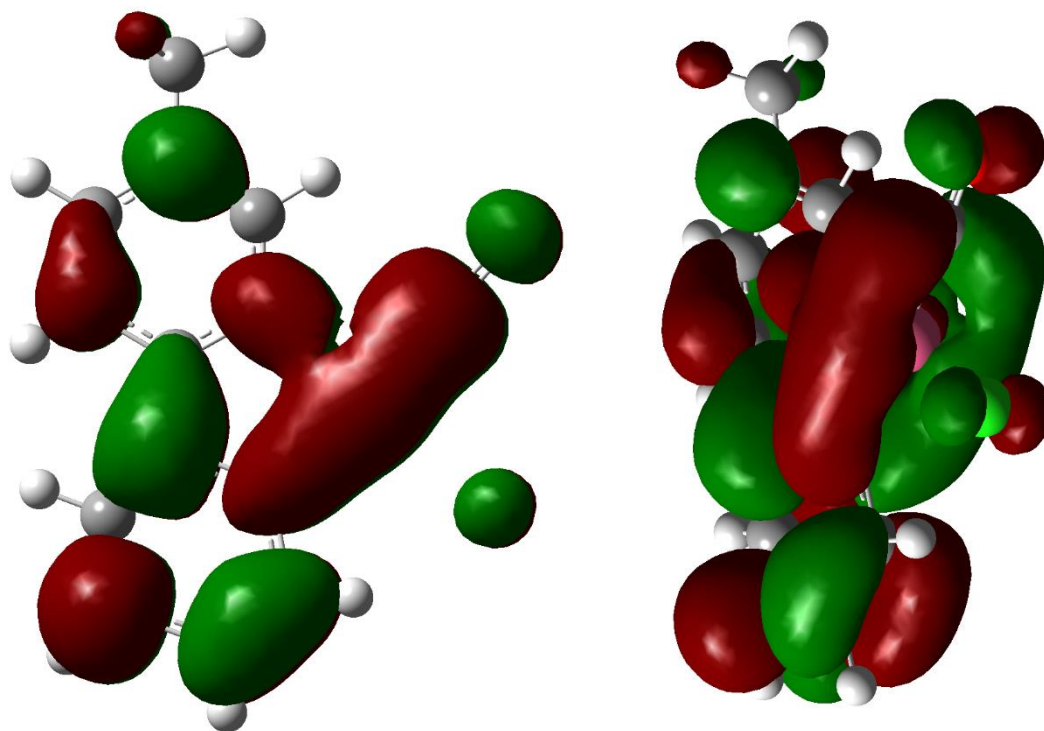


Figure 122: The calculated LUMO for complex **4a** using BP86 with 6-31G(d) and LANL2DZ (for Pt) for the geometry optimisation and the utility Cubegen within Gaussian09

The donation of electron density from the partly anti-bonding 5σ -orbital to the empty metal orbital raises the vibrational frequency of $\bar{\nu}(\text{C}\equiv\text{O})$. Back-bonding from the metal d -orbitals to the $2p\pi^*$ anti-bonding orbital weakens the $\text{C}\equiv\text{O}$ bond, reducing the vibrational frequency of $\bar{\nu}(\text{C}\equiv\text{O})$. The small decrease in vibrational frequency when compared to free CO (2143 cm^{-1}),²⁹⁹ suggests that there is a small degree of back bonding. This is consistent with the electronic configuration of $\text{Pt}^{\text{II}} d^8$ square-planar complexes, where the HOMO is d_{yz} (as shown by the quantum chemical calculations) and will have poor overlap with the $2p\pi^*$ anti-bonding orbital.

X-ray Diffraction

Isomer 4a

The structure is consistent with that reported by Mdleleni *et al.* (Figure 123).¹²⁰ There are four molecules in the unit cell and each packs with the carbonyl and chloride ligands arranged on top of each other (Figure 124) and as with complex **3**, these molecules stack infinitely on top of one another with the CO and Cl groups alternating position. The aromatic rings stack on top of each other, slightly offset, with an angle between each molecular plane (defined by the platinum atom and the four atoms directly bonded to it) measured as 0.54° . Although the platinum atoms stack one on top of another, the separation is greater than the sum of the van der Waals radii ($3.5989(3)\text{ \AA}$ vs. 3.50 \AA). The CO bond length measured is very similar to that of free CO (Free CO bond length = 1.131 \AA , bond length of CO in complex **4** = $1.133(9)\text{ \AA}$), indicating that there is little π -back-donation from platinum to the CO ligand. The similarity of coordinated CO to free CO for this complex also suggests that the σ -donation from the anti-bonding orbital on carbon is almost exactly counterbalanced by π -back donation from platinum.

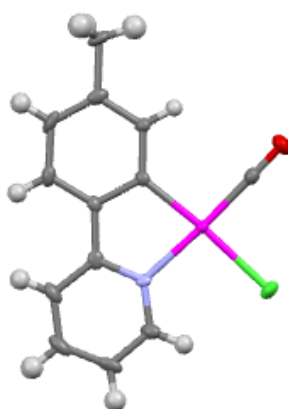


Figure 123: Single crystal X-ray structure for $[\text{Pt}(\text{tolpy})\text{Cl}(\text{CO})]$ (**4a**) with ellipsoids at 50% probability.

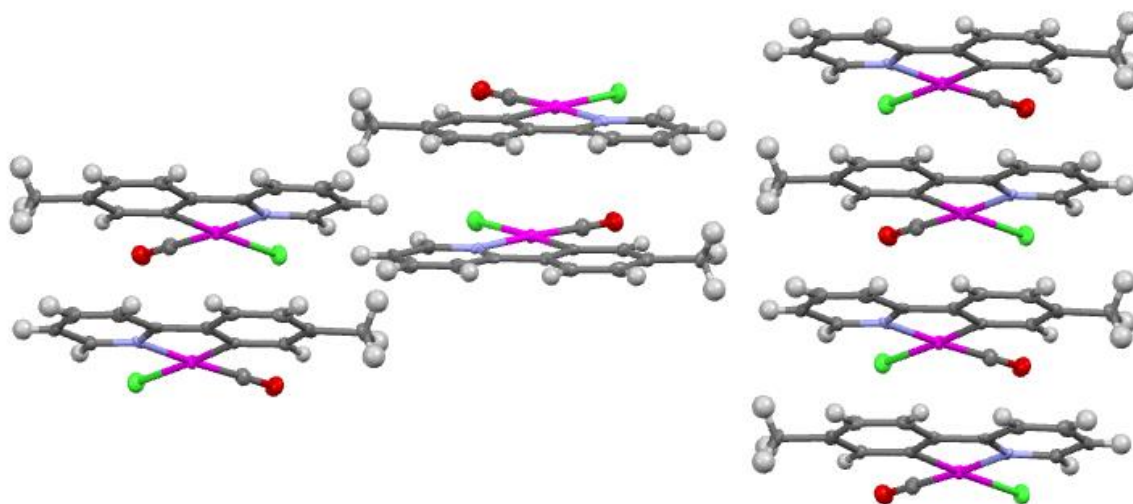


Figure 124: Packing of [Pt(tolpy)Cl(CO)] (**4**) in the unit cell of the single crystal X-ray crystal structure (left), and top view of two molecules arranged on top of each other (right), with ellipsoids at 50% probability.

Isomer 4b

The crystal structure obtained for the minor isomer **4b** also has four molecules in the unit cell (Figure 125). For this isomer, a Pt...Pt interaction was observed with an interatomic distance measured as 3.3435(6) Å, which is 95% of the sum of the van der Waals radii (Figure 126). Stacking of the pyridyl and tolyl aromatic rings of the tolpy ligands was also observed, indicating a π - π interaction. The stacking rings were almost parallel with one another, with the angle between molecular planes (as defined by the platinum atoms and the four atoms directly bonded to it) measured as 0.012° and the distance between the rings was 3.583 Å. Some of the bond lengths for each isomer are compared in Table 19, the CO bond lengths are very similar to each other and to free CO, as found in **4a**. However, the Pt-C_{co} bond is appreciably longer for **4b** (1.94(1) vs. 1.845(7) Å), indicating that it is weaker; this is likely due to the greater *trans*-influence of the carbanion versus the pyridyl group. This is also evident when comparing the chloride ligands, for which the platinum-chloride bond *trans* to the carbanion (2.397(2) Å) is longer than the one *trans* to the pyridyl nitrogen (2.318(3) Å). The CO ligand has a greater *trans*-influence than chloride even though there appears to be limited back-bonding and so a longer Pt-N bond length is observed for isomer **4a**.

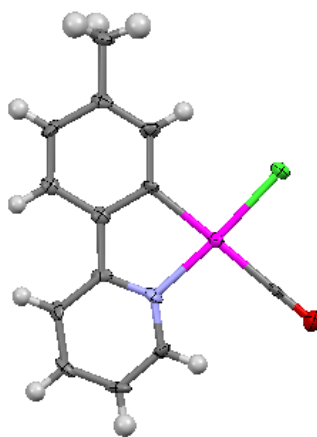


Figure 125: Molecular structure of [Pt(tolpy)Cl(CO)] (**4b**) with ellipsoids at 50% probability.

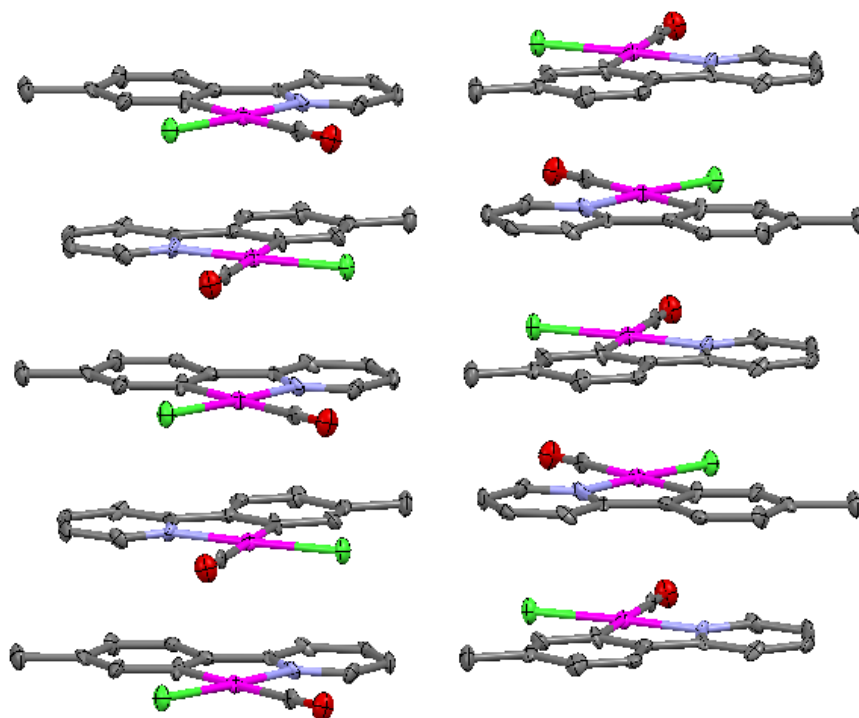


Figure 126: Packing of [Pt(tolpy)Cl(CO)] (**4b**) in the unit cell of the single crystal X-ray crystal structure (left), and top view of two molecules arranged on top of each other (right), with ellipsoids at 50% probability and the hydrogen atoms removed for clarity.

Table 19: Comparison of the bond lengths measure by X-ray crystallography for isomers **4a** and **4b**

Isomer	Pt–C	Pt–N	Pt–Cl	Pt–CO	C≡O
4a	1.999(6)	2.065(5)	2.397(2)	1.845(7)	1.133(9)
4b	2.05(1)	2.024(9)	2.318(3)	1.94(1)	1.13(1)

NMR Spectroscopy

The ^1H NMR spectrum of **4b** was very similar to that of the major isomer **4a**, in terms of chemical shifts and coupling constants observed. A very large coupling to ^{195}Pt was observed for the proton bound to the carbon adjacent to the coordinating carbon (^8H , $^3J_{\text{HPt}} = 70$ Hz for **4a**) which was shifted up-field. This is surprising, as the carbonyl ligand is *cis* to the carbanion and a large coupling constant was not observed for the H^1 ($^3J_{\text{HPt}} = 32$ Hz for **4a** and **4b**). Carbonyl ligands are strongly π -acidic; a reduction in the electron density at the metal centre may be compensated by strengthening of the $\text{Pt}-\text{C}_{\text{phenyl}}$ bond, causing an increase in coupling constant. However, it is unlikely for there to be a significant reduction of electron density on platinum as the eight d -electrons are involved in bonding.

2.5 Phosphorus Donor Ligands

The steric and electronic properties of phosphine ligands, PR_3 , can be tuned by varying the R groups. These ligands are strong σ -donors and they can also act as π -acids, the extent of which depends on the nature of the R groups.³⁰⁰ Electronegative substituents bonded to phosphorus stabilise the σ^* -orbital on phosphorus and increase its π -acidity. The order of increasing π -acidity for a range of phosphine ligands was reported by Crabtree (with CO included for reference):³⁰⁰



2.5.1 [Pt(tolpy)Cl(PPh₃)] (**9**)

X-ray Diffraction

The crystal structure obtained for [Pt(tolpy)Cl(PPh₃)] (**9**) contains two molecules of **9** in the unit cell (Figure 127). The phosphine ligand has a pyramidal geometry which is slightly distorted due to proximity to the adjacent chloride ligand. Close contacts were observed between the chloride ligand and a hydrogen atom of the triphenylphosphine ligand (2.8579 Å, 97% of the sum of the van der Waals radii, Figure 129). The tolyl rings of the tolpy ligand are slightly offset but stacked on-top of each other, which suggests a π - π interaction; the angle between the tolyl planes was measured to be 0° (Figure 128).

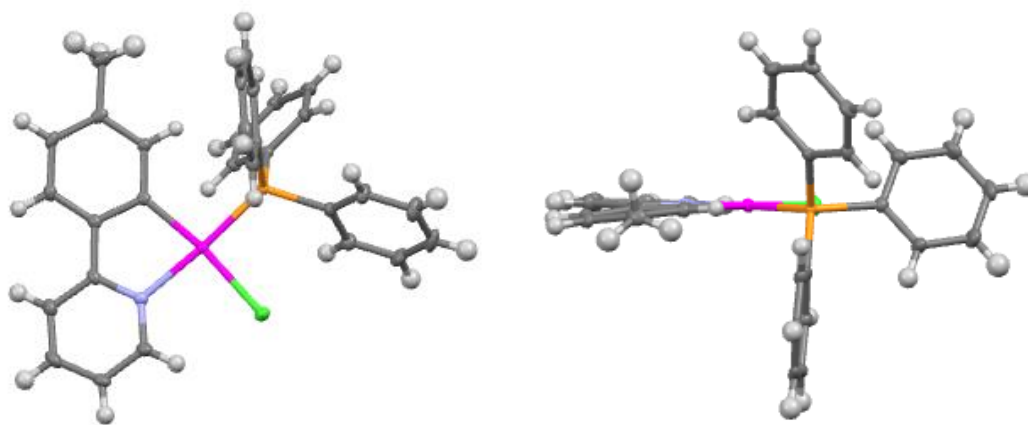


Figure 127: Front on (left) and side on (right) views of the single crystal X-ray crystal structure of $[\text{Pt}(\text{tolpy})\text{Cl}(\text{PPh}_3)]$ (**9**), with ellipsoids at 50% probability.

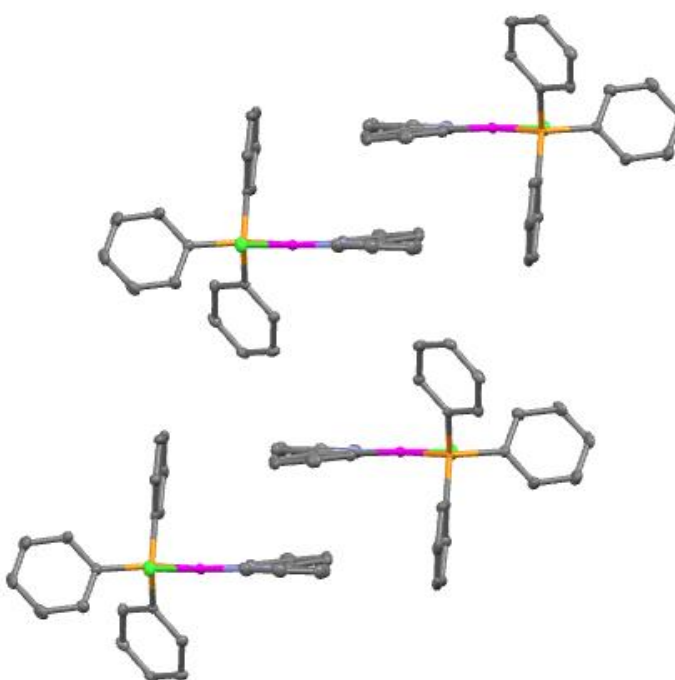


Figure 128: Packing of $[\text{Pt}(\text{tolpy})\text{Cl}(\text{PPh}_3)]$ (**9**) determined by X-ray crystallography with ellipsoids at 50% probability and the hydrogen atoms omitted for clarity.

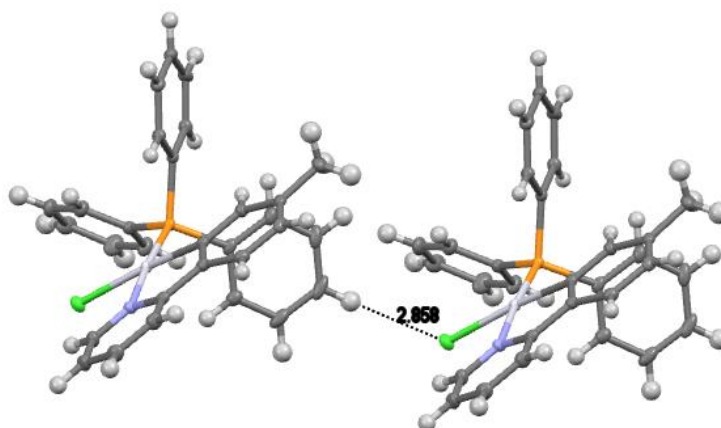


Figure 129: Close contact observed between the chloride ligand and a hydrogen atom of the PPh₃ ligand by X-ray diffraction with ellipsoids at 50% probability

NMR Spectroscopy

In addition to coupling to ^{195}Pt , protons H¹ and H⁸ also couple to ^{31}P in the ^1H NMR spectrum for complex **9**. For H¹, the proton *ortho* to the tolyl nitrogen, a complicated multiplet is observed due to coupling to the vicinal proton, a four-bond coupling to ^{31}P and a three-bond coupling to ^{195}Pt leading to a quartet of doublets which, due to the similar coupling constants, overlap (Figure 130). The dd splitting pattern observed for all the earlier complexes reported here is observed in the $^1\text{H}\{^{31}\text{P}\}$ spectrum, shown in Figure 130. In the $^{31}\text{P}\{^1\text{H}\}$ NMR spectrum (Figure 131), a single peak is observed at 23.7 ppm with ^{195}Pt satellites ($^1J_{\text{PPt}} = 4345$ Hz). The peak is shifted downfield relative to the free ligand (-5.9 ppm).³⁰¹ In the $^{195}\text{Pt}\{^1\text{H}\}$ spectrum a doublet is observed with the corresponding $^1J_{\text{PPt}}$ constant of 4350 Hz. Waddell *et al.* studied platinum complexes with $^1J_{\text{PPt}}$ between 3450 and 5750 Hz and reported strong linear correlation between the $^1J_{\text{PPt}}$ coupling constant and the Pt–P bond length.³⁰² They reported that the $^1J_{\text{PPt}}$ constant observed increased with increasing π -acidity of the phosphine ligand and that this value could be used to compare the relative *trans*-influence of phosphine ligands.

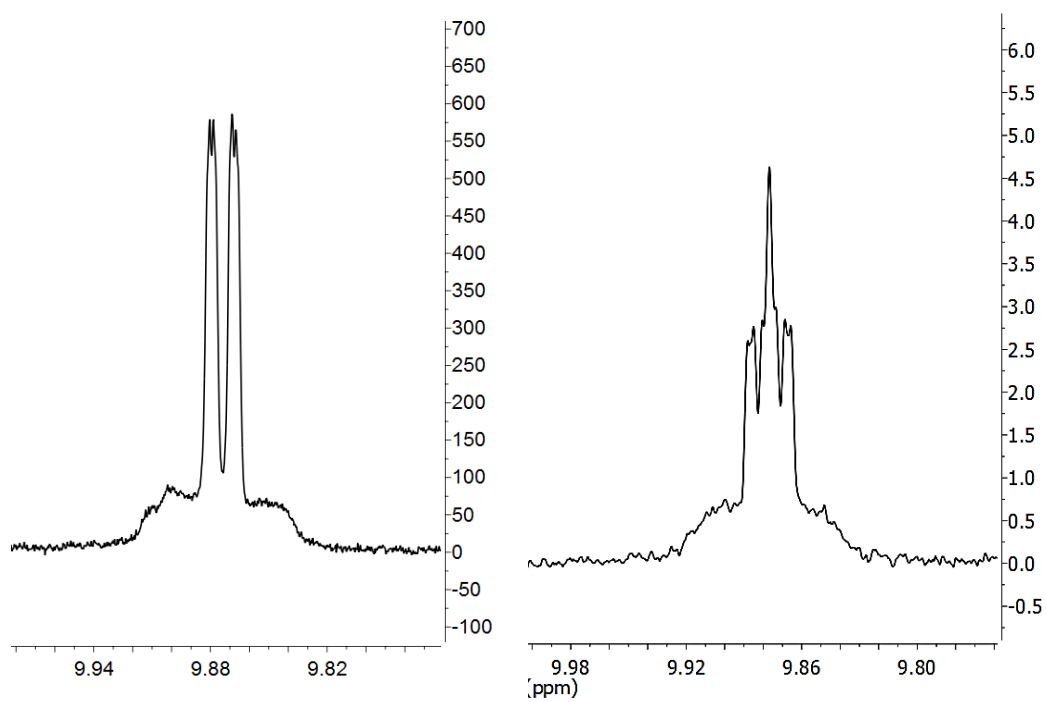


Figure 130: ^1H (left) and $^1\text{H}\{^{31}\text{P}\}$ (right) NMR spectra of $[\text{Pt}(\text{tolpy})\text{Cl}(\text{PPh}_3)]$ (**9**) recorded in CDCl_3 in region of H^1

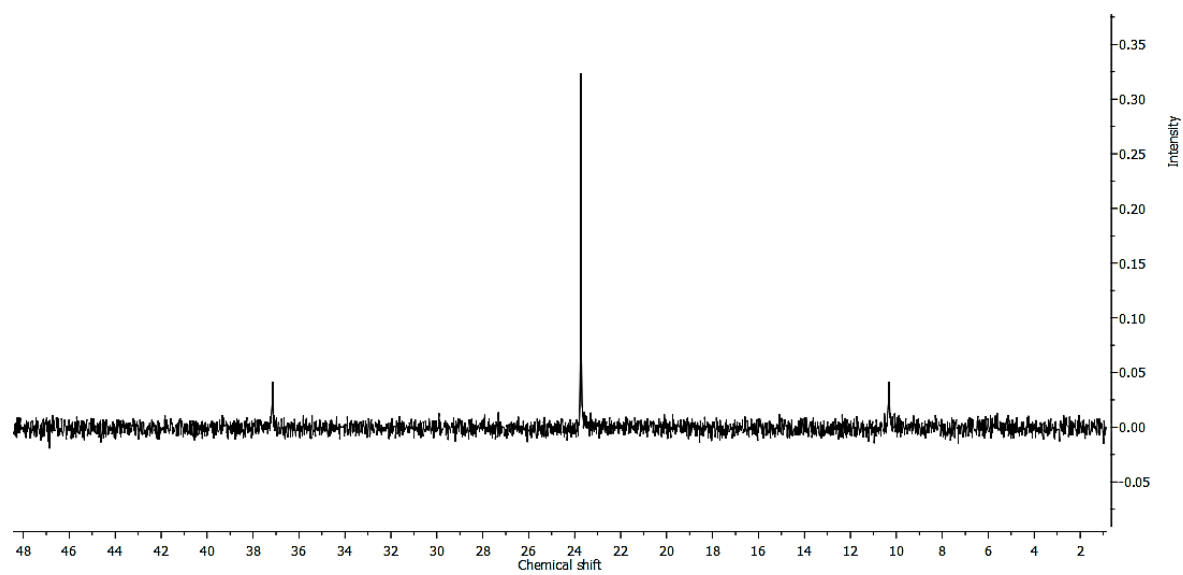


Figure 131: ^{31}P NMR spectrum of $[\text{Pt}(\text{tolpy})\text{Cl}(\text{PPh}_3)]$ (**9**) recorded in CDCl_3

2.5.2 [Pt(tolpy)Cl(P(OPh)₃)] (**10**)

X-ray Diffraction

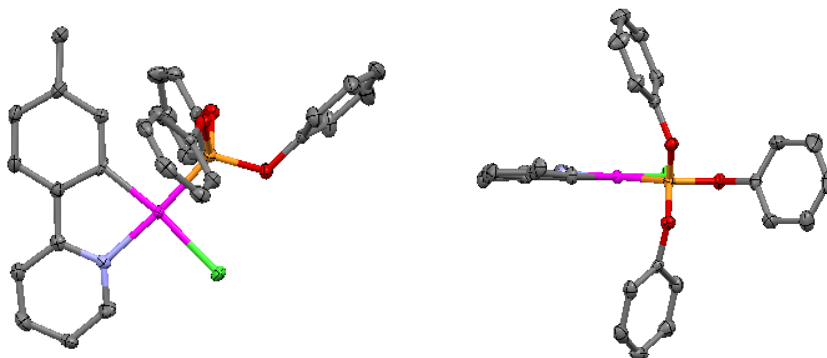


Figure 132: Front on (left) and side on (right) views of the single crystal X-ray crystal structure of [Pt(tolpy)Cl(P(OPh)₃)] (**10**), with ellipsoids at 50% probability and the hydrogen atoms omitted for clarity.

The crystal structure is shown in Figure 132 and there are four molecules of **10** in the unit cell. The packing of the molecules is shown in Figure 133, for which no π - π stacking or Pt...Pt interactions were observed. A short contact was observed between the chloride ligand and a hydrogen of the tolyl group (99% of the sum of the van der Waals radii, Figure 134) and there are also short contacts between the oxygen atoms and phenyl hydrogen atoms (Figure 135).

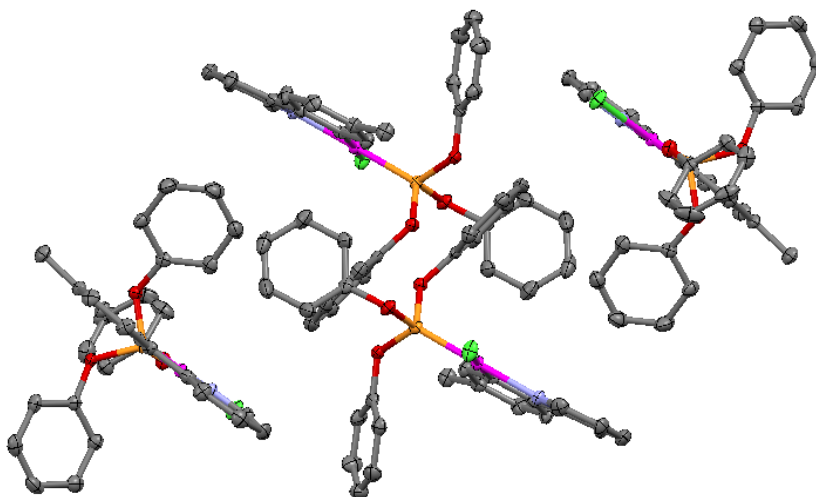


Figure 133: Packing of [Pt(tolpy)Cl(P(OPh)₃)] (**10**) determined by X-ray crystallography with ellipsoids at 50% probability and the hydrogen atoms omitted for clarity.

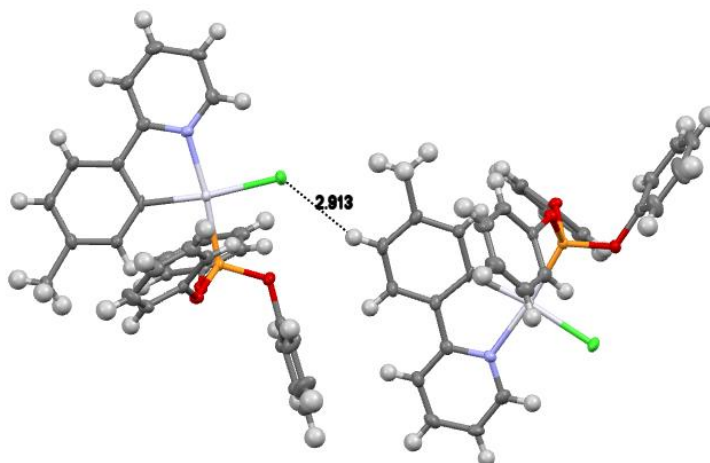


Figure 134: Short contact between the chloride ligand and a hydrogen atom of the tolyl ring observed in the packing of **10** in the X-ray crystal structure, with ellipsoids at 50% probability.

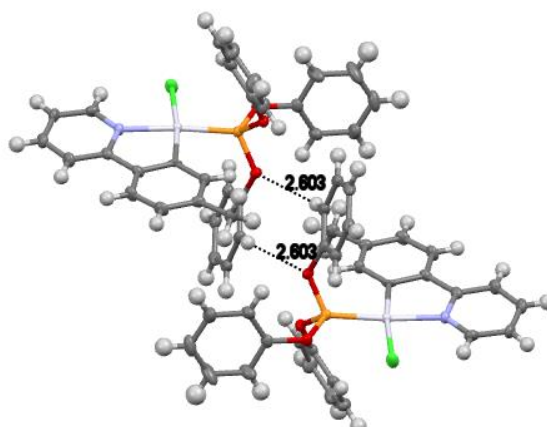


Figure 135: Short contact between the oxygen atoms and hydrogen atoms of the phenyl rings observed in the packing of **10** in the X-ray crystal structure, with ellipsoids at 50% probability.

NMR Spectroscopy

For H¹ a triplet of doublets was observed in the ¹H spectrum due to coupling to the vicinal proton and a four-bond coupling to ³¹P and the three-bond coupling to ¹⁹⁵Pt was observed as satellites. A doublet of doublets splitting pattern was observed in the ¹H{³¹P} spectrum, shown in Figure 130. Coupling to ³¹P was not observed for H⁸, the proton bound to the adjacent carbon to the carbanion, but a large ³J_{HPt} of 62 Hz was observed. A very large ¹J_{PPt} value was recorded – 7000 Hz – larger than that of PPh₃, which is consistent with the greater π-acidity of the P(OPh)₃ ligand and indicative of a strong Pt–P bond for complex **10**.

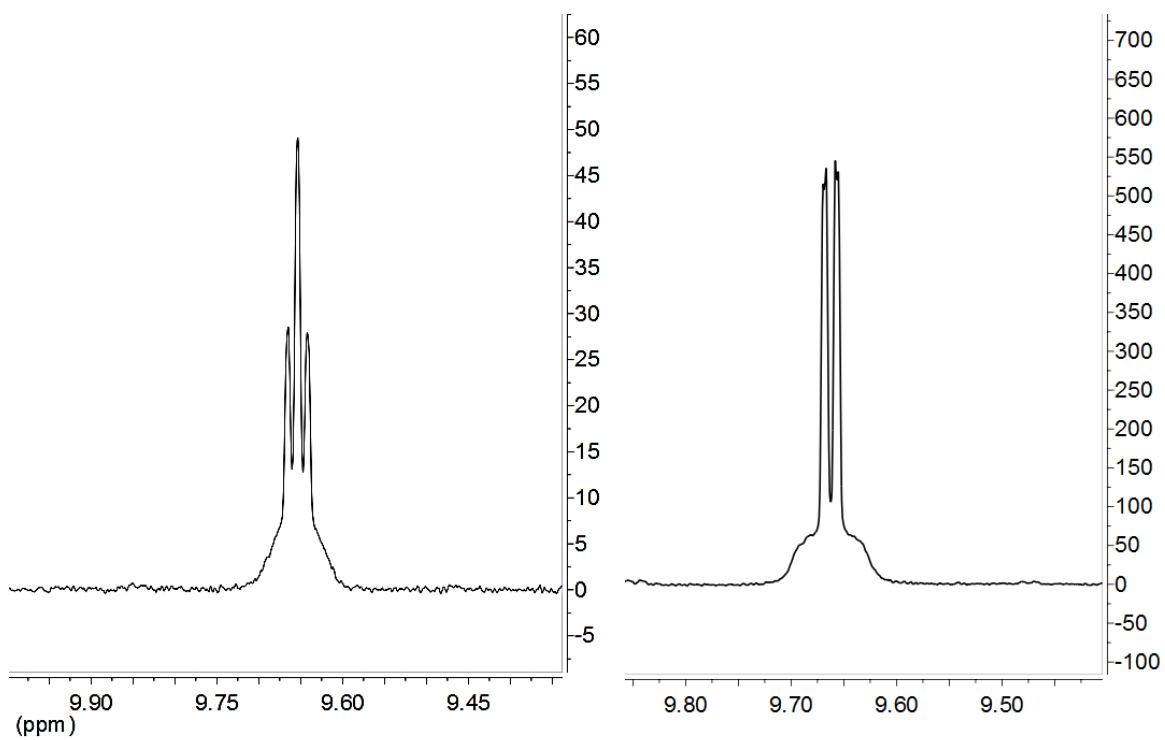


Figure 136: ^1H NMR (left) and $^1\text{H}\{^{31}\text{P}\}$ (right) spectra of $[\text{Pt}(\text{tolpy})\text{Cl}(\text{P}(\text{OPh})_3)]$ (**10**) recorded in CDCl_3 in region of H^1

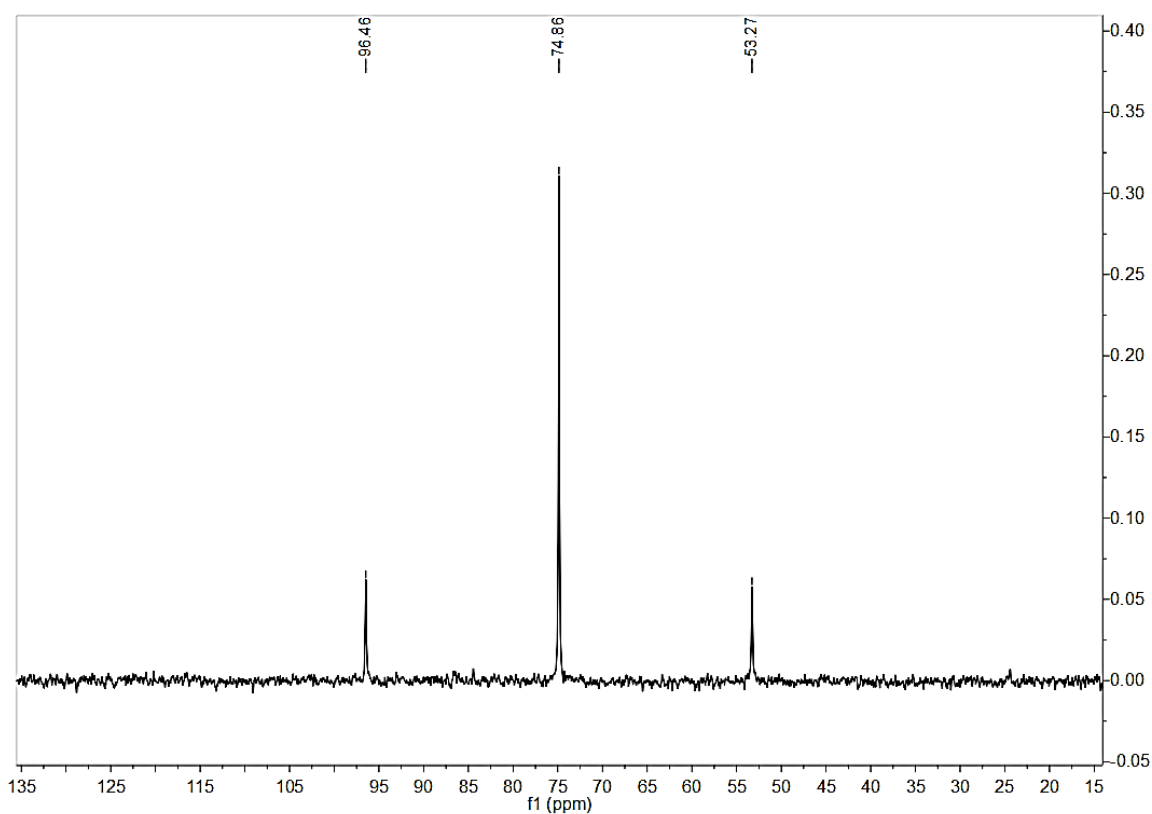


Figure 137: ^{31}P NMR spectrum of $[\text{Pt}(\text{tolpy})\text{Cl}(\text{P}(\text{OPh})_3)]$ (**10**) recorded in CDCl_3

2.5.3 [Pt(tolpy)Cl(PCy₃)] (13)

X-ray Diffraction

The molecular structure of **13** is shown in Figure 138 and there are four molecules of **13** in the unit cell and four molecules of dichloromethane. The packing of **13** is shown in Figure 139, where no π - π stacking or Pt \cdots Pt interaction was observed. Short contacts were observed between the chloride ligand and hydrogen atoms of the CH₂Cl₂ solvent molecule and the pyridyl ring of the tolpy ligand (Figure 140).

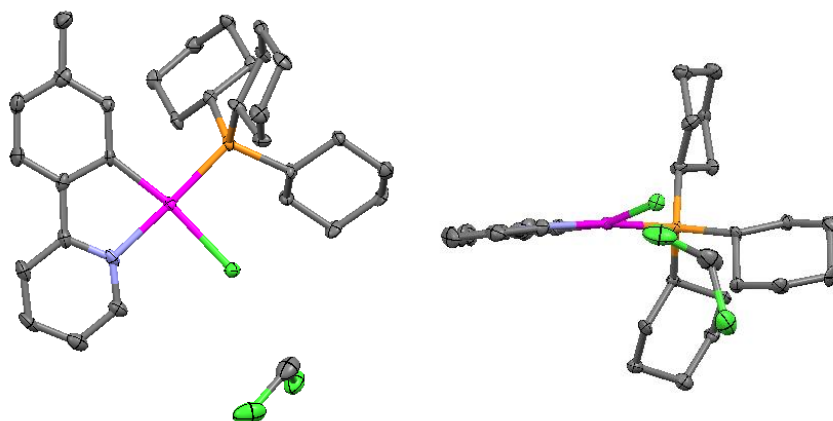


Figure 138: Front on (left) and side on (right) views of the single crystal X-ray crystal structure of [Pt(tolpy)Cl(PCy₃)]·CH₂Cl₂ (**13**), with ellipsoids at 50% probability and the hydrogen atoms omitted for clarity.

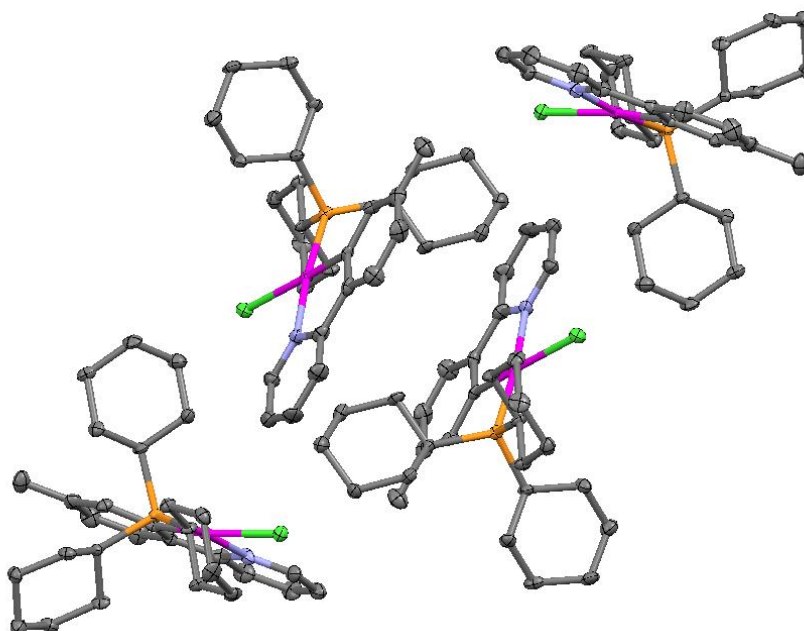


Figure 139: Packing of [Pt(tolpy)Cl(PCy₃)]·CH₂Cl₂ (**13**) determined by X-ray crystallography with ellipsoids at 50% probability and the hydrogen atoms and solvent molecules omitted for clarity.

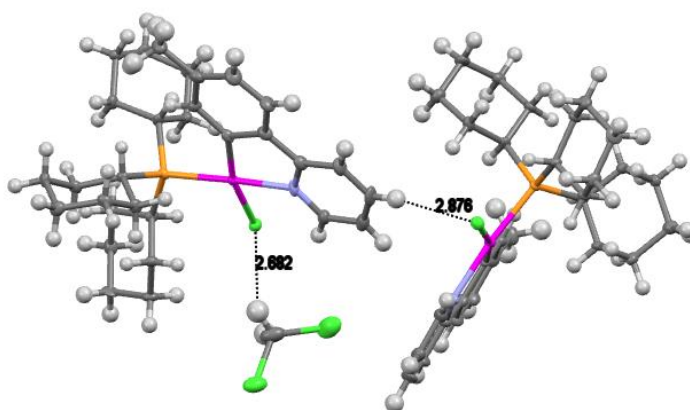


Figure 140: Short contacts observed between the chloride ligand and hydrogen atoms of the CH_2Cl_2 solvent molecule and the pyridyl ring of the tolyl ligand.

NMR Spectroscopy

For H^1 , the proton *ortho* to the pyridyl nitrogen, a complicated multiplet was observed due to coupling to the vicinal proton, a four-bond coupling to ^{31}P and a three-bond coupling to ^{195}Pt leading to a quartet of doublets which, due to the similar coupling constants, overlap (Figure 141). The $^1J_{\text{PPt}}$ coupling constant observed ($^{31}\text{P}\{^1\text{H}\}$ -NMR δ_{P} recorded at 162.0 MHz in CDCl_3 19.15 ppm, s, $^1J_{\text{PPt}} = 4010$ Hz) was slightly lower than the value observed for the PPh_3 complex **9**, indicating that this ligand is less π -acidic.

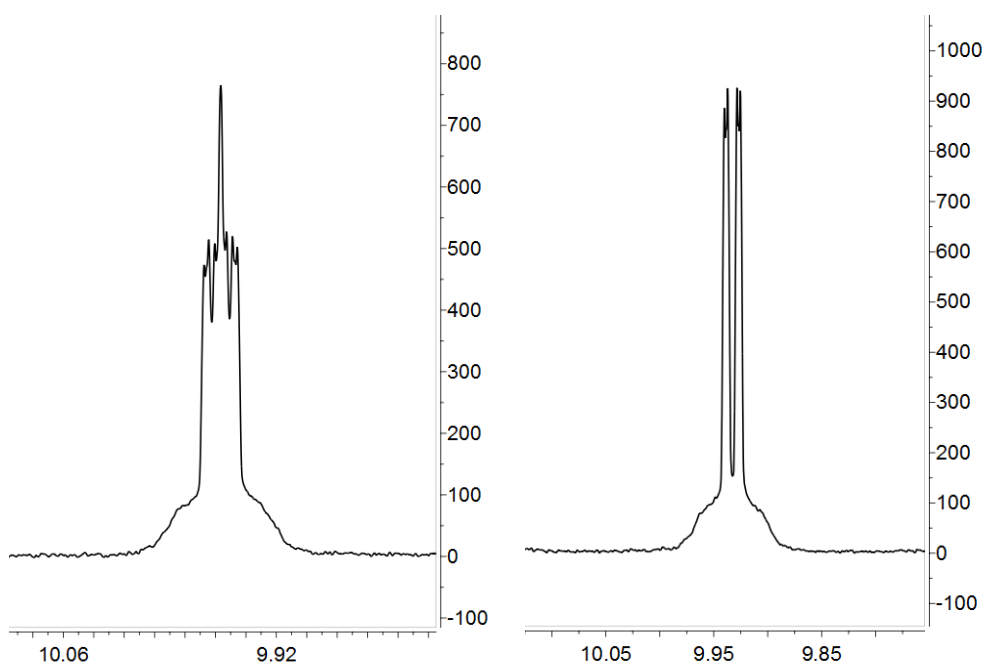


Figure 141: ^1H (left) and $^1\text{H}\{^{31}\text{P}\}$ (right) NMR spectrum of $[\text{Pt}(\text{tolpy})\text{Cl}(\text{PCy}_3)]$ (**13**) recorded in CDCl_3

3.0 Probing the *trans*-Influence of Different Ligands using Spectroscopic Techniques

3.1 X-ray Diffraction

Despite the synthetic route, whether from cleavage of the dimer **1** or by ligand exchange from **3**, in all cases the incoming ligand L is *trans* to the pyridyl nitrogen except for the carbonyl complex **4**, where a small amount of isomer **4b** was isolated. A distorted square-planar geometry was observed in the crystal structures of all platinum complexes due to the steric requirements of the ligands and the bidentate tolpy ligand, which has a C^{Pt}N angle with a small range between 80.3 and 81.8°. The orientation of the molecules within the crystal is dominated by efficient packing and intermolecular interactions, for example in many of the complexes interactions between the chloride ligand and the hydrogen atoms of other ligands were observed. Stacking of the aromatic rings in the crystal structures suggested a π - π interaction for complexes **1**, **2**, **4a**, **4b**, **7** and **9**. A Pt...Pt was observed for the carbonyl complex **4b**, with an interatomic distance measured as 3.3435(6) Å which is 95% of the sum of the van der Waals radii.

As discussed in Section 4.1.2, X-ray crystallography has been the most popular way of investigating the *trans*-influence of ligands, however changes in the bond length can be small and often similar to the error associated with bond length determination and this as observed here. The bond lengths will be discussed first and then used as a bench mark for which to compare the other techniques to. The platinum-ligand bond lengths are listed in Table 20, and of most interest are the Pt–N bond lengths, as this bond is *trans* to the neutral ligand which was varied in this series of compounds. In considering these data, it is observed that between many pairs of compounds the difference in the Pt–N bond length is not statistically significant, yet there are real differences between the shortest and longest distances. This leads to an overall trend that is in agreement with what might be expected for a *trans*-influence series except for the position of CO, which as a stronger π -acid would be expected to have the greatest *trans*-influence (Figure 142 and Figure 143). However, the spectroscopic data collected for the carbonyl complex **4a**, in particular the position of the stretching frequency, $\bar{\nu}(\text{CO})$, suggested that there is very little back-bonding to the carbonyl ligand in this complex.

Trans-influence (X-ray data) : Cl < H-tolpy < py < tht \approx dms < S-dmso < CO < P(OPh)₃ < PPh₃ \approx PCy₃

Table 20: Bond lengths measured using single crystal X-ray diffraction; the estimated standard deviation is given in brackets

L =	Pt–C	Pt–N	Pt–L (<i>trans</i> to N)	Pt–Cl (<i>trans</i> to carbanion)
Cl, dimer (1a)	1.978(9)	2.0045(8)	2.326(2)	2.448(2)
H-tolpy (2)	1.983(2)	2.008(2)	2.038(2)	2.4034(8)
S-dmso (3)	2.012(7)	2.053(6)	2.216(2)	2.409(2)
CO (4a)	1.999(6)	2.065(5)	1.845(7)	2.397(2)
py (5)	1.966(8)	2.024(7)	2.024(6)	2.41(2)
dms (7)	2.004(3)	2.046(2)	2.2677(9)	2.4012(8)
tht (8)	1.994(2)	2.044(2)	2.2587(6)	2.3987(6)
PPh ₃ (9)	2.018(4)	2.097(2)	2.2274(7)	2.3814(9)
P(OPh) ₃ (10)	2.012(4)	2.082(3)	2.157(1)	2.374(1)
PCy ₃ (13)	2.017(6)	2.093(5)	2.266(2)	2.401(2)

The Pt–N bond lengths for the related H-tolpy (**2**) and py (**5**) complexes are very similar; this suggests that the electron donating tolyl group has had a very small effect on the *trans*-influence of the pyridyl ligand. When comparing the sulfur donor ligands, very similar bond lengths and hence *trans*-influences were observed for the dms (**7**) and tht (**8**) complexes. For the phosphorus donor ligands, the Pt–N bond lengths are the same within error for the PPh₃ (**9**) and PCy₃ (**10**) complexes, but a shorter bond was observed for P(OPh)₃ (**13**). This at first seemed a surprising result, due to the greater π -acidity of P(OPh)₃ compared to the other phosphine ligands, but the bond lengths measured are not solely affected by the bonding, the large bulky ligands must be accommodated. On the basis of π -acidity, the P(OPh)₃ ligand would be expected to have the greatest *trans*-influence of the phosphines studied, however, although the greatest coupling constant was observed for complex **13**, evidence for a greater *trans*-influence was not observed in the X-ray or ¹⁹⁵Pt chemical shift data for this family of complexes.

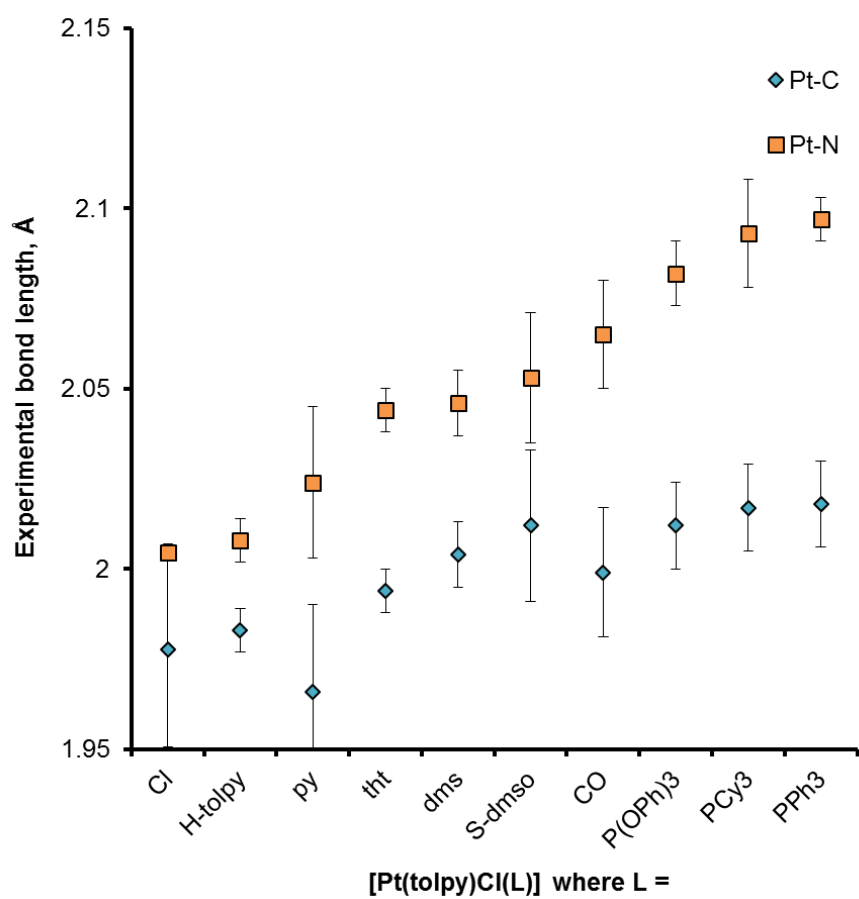


Figure 142: The Pt–C and Pt–N bond lengths measured using single crystal X-ray diffraction for the series of complexes, $[\text{Pt}(\text{tolpy})\text{Cl}(\text{L})]$, the error bars are given as ± 3 estimated standard deviations.

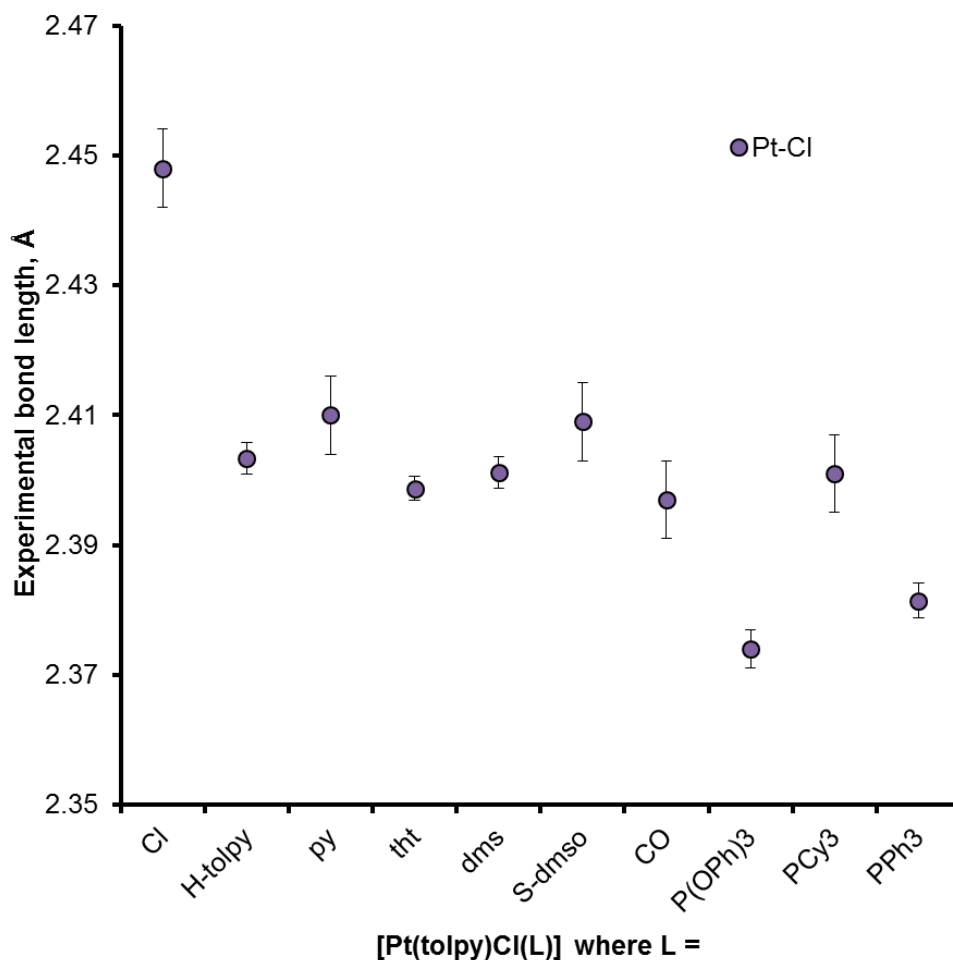


Figure 143: The Pt–Cl bond lengths measured using single crystal X-ray diffraction for the series of complexes, $[\text{Pt}(\text{tolpy})\text{Cl}(\text{L})]$, the error bars are given as \pm three estimated standard deviations.

The adjacent Pt–C and Pt–Cl bond lengths also change across the series (Figure 142). As the *trans*-influence of L increases and the Pt–N bond length increases, a general increase in the Pt–C bond length was also observed, indicating a decrease in bond strength. Very generally a decrease in the Pt–Cl bond was observed but the correlation was very poor (Figure 143).

The N–Pt–L bond angle should be 180° for a square-planar Pt^{II} complex and deviation from this could mean poorer orbital overlap which should cause a weakening and lengthening of the Pt–N and Pt–L bonds. To evaluate this, the deviation of the N–Pt–L bond angle from 180° was plotted against the Pt–N bond lengths (Figure 144) and no correlation was observed. The deviation of the C–Pt–Cl bond angle from 180° against the Pt–C bond lengths was also plotted. Overall there is a general increase in bond length as the deviation in bond angle increases but the correlation is poor.

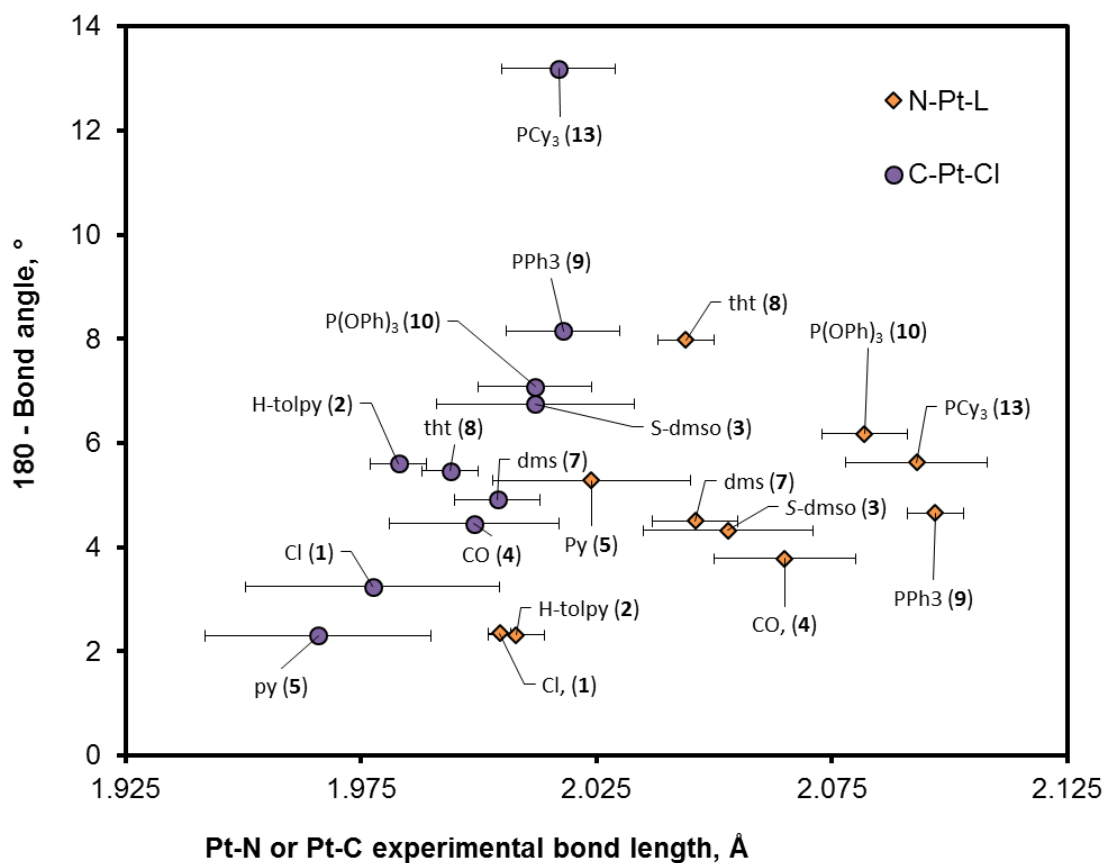


Figure 144: The difference from 180° of the angle between *trans*-ligands was compared to the Pt-bidentate ligand bond lengths, the error bars are given as \pm three estimated standard deviations.

3.2 Far-infrared Spectroscopy

The far-infrared spectra for a range of [Pt(tolpy)Cl(L)] complexes were measured in order to determine vibrational frequency of the Pt–Cl stretching mode. This will facilitate evaluation of a possible *cis*-effect when varying L. Assignment of the Pt–Cl stretching mode was carried out with the aid of vibrational frequency calculations which allowed visualisation of each frequency and by comparison to literature values.²⁷² Only one $\bar{\nu}$ (Pt–Cl) absorption was expected for each complex, however, two were observed in the experimental and calculated spectra for complexes **9** and **10**, this is suspected to be due to coupling to the vibrational modes of the phosphine ligand.

Table 21: Comparison of the $\bar{\nu}(\text{Pt}-\text{Cl})$ compared to the Pt–Cl bond length, the complexes are ordered in terms of increasing Pt–Cl bond length

L	Pt–Cl (<i>trans</i> to carbanion) Bond length, Å	$\bar{\nu}(\text{Pt}-\text{Cl})$ far-infrared, cm^{-1}
P(OPh) ₃	2.374(1)	268, 295
PPh ₃	2.3814(9)	274, 295
CO	2.398(3)	297
tht	2.3987(6)	269
dms	2.4012(8)	261
tolpy	2.4034(8)	257
S-dmso	2.409(2)	264
py	2.408(2)	252

The vibrational frequencies for the complexes decrease in the order: CO > tht > dms > H-tolpy > S-dmso > py (Table 21). These frequencies were then compared to the experimentally measured Pt–Cl bond lengths (Figure 145), although, complexes with L = P(OPh)₃ or PPh₃ were not included as the Pt–Cl stretch was coupled to other vibrational modes to give two stretches. There is a general decrease in vibrational frequency of the Pt–Cl stretch as the Pt–Cl bond length increases, with the exception of [Pt(tolpy)Cl(S-dmso)] for which the vibrational frequency is higher than for L = py even though the bond is very slightly longer. However, the correlation is not good; this would suggest that although the vibrational frequency of the Pt–Cl stretch should increase as the bond strength increases, the effect of changing the masses of the ligands is so great that the vibrational frequency data cannot be used to get sensible information about the bond strengths in this study. In this work, complexes with a large range of molecular weights were studied, where the molecular weight of the largest ligand, PCy₃, is 280 g mol⁻¹, whereas the molecular weight of the smallest ligand, CO, is only 28 g mol⁻¹.

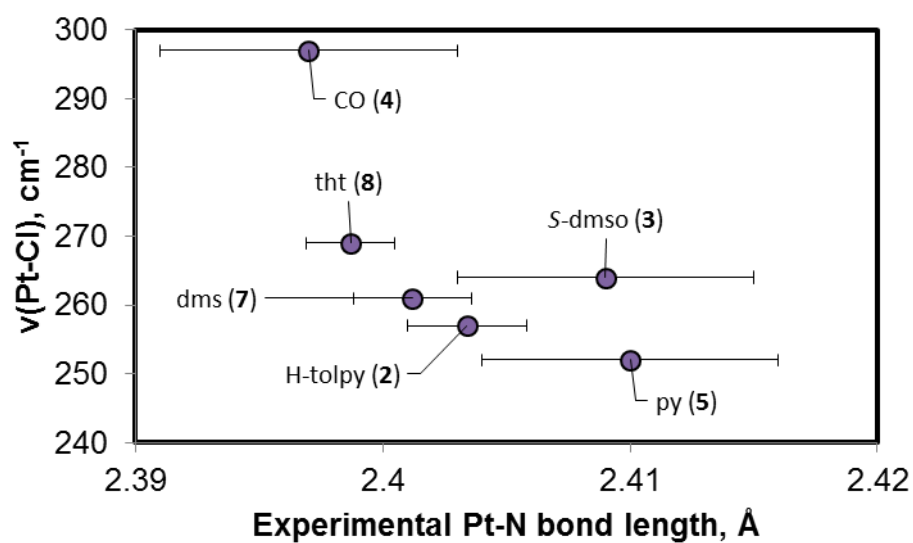


Figure 145: Comparison of the vibrational frequency of the Pt–Cl stretching mode with the experimentally measured Pt–N bond length for $[\text{Pt}(\text{tolpy})\text{Cl}(\text{L})]$, where $\text{L} = \text{CO}$, tht, dms, tolpy, S-dmso, py. The error bars are given as \pm three estimated standard deviations.

3.3 NMR spectroscopy

A summary of the ^1H , $^{13}\text{C}\{^1\text{H}\}$, ^{15}N and $^{195}\text{Pt}\{^1\text{H}\}$ NMR spectroscopic data collected for complexes studied is given in Table 22. The assignments of H^1 and H^8 and C^{12} are shown in Figure 146.

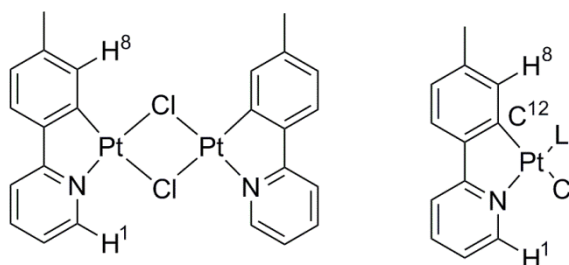


Figure 146: Proton and carbon assignments for dinuclear and mononuclear platinum complexes

Table 22: NMR spectral data for the platinum complexes synthesised recorded in CDCl₃.

Nuclei	¹ H				¹³ C		¹⁹⁵ Pt	¹⁵ N	
	H ¹		H ⁸		C ^{12c}				
	L	δ / ppm	³ J _{HPt} / Hz	δ / ppm	³ J _{HPt} / Hz	δ / ppm	¹ J _{CPt} / Hz	δ / ppm	δ / ppm
Cl, dimer (1)a	8.76	45	7.61 ^b	44	-	-	-	-	-
tolpy (2) ^b	9.22	43	6.00	49	141.19	1139	-3195	206 (C [^] N), 222 (H-tolpy)	
py (5)	9.65	36	6.13	48	141.82	1126	-3261	206 (C [^] N), 221 (py)	
tht (8)	9.68	38	7.50	51	139.98	1050	-3799	225	
dmsO (3)	9.59	36	8.18	46	140.00	1063	-3816	221	
dms (7)	9.65	35	7.44	52	139.73	1044	-3858	224	
CO (4)	9.39	33	7.31	70	142.10	938	-3947	226	
PPh ₃ (9)	9.85	27	6.45	56	-	-	-4368	-	
P(OPh) ₃ (10)	9.61	27	7.83	59	141.28	1013	-4148	237	
PCy ₃ (13)	9.99	26	7.43	57	140.34	1111	-4011	242	

^a NMR data collected in acetonitrile ^bNMR data are for the cyclometallated ligand, ^c The ¹³C{¹H} NMR spectra of [Pt(tolpy)Cl(L)] were recorded at 75.4 Hz using a 300 MHz (7.0 T) spectrometer.

^1H and $^1\text{H}\{^{31}\text{P}\}$ NMR Spectroscopy

The ^1H NMR data show that changing the ligand *trans* to the nitrogen on the pyridyl ring has a significant effect on the chemical shift of both H^1 and H^8 . The chemical shift of H^8 was particularly sensitive with the chemical shift recorded ranging from 6.00 – 8.18 ppm, the large range is in part due to a π -interaction between this proton and the aromatic rings of the ligands where $\text{L} = \text{py}$, H-tolpy or PPh_3 ligands. The chemical shifts observed by ^1H NMR cannot, however, be used to evaluate the *trans*-influence of the different ligands, which are very sensitive to environment; being affected both by the change in strength of bonds but also by anisotropic shielding caused by proximity of some proton environments to aromatic ring currents. There appears to be no correlation between the chemical shift of H^1 (*ortho* to N) and the Pt–N bond length (Figure 147).

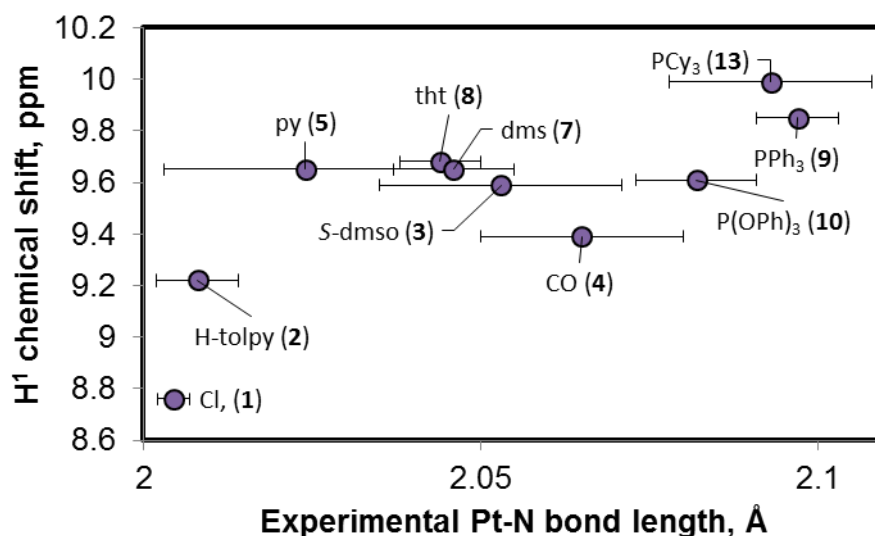


Figure 147: Comparison of the chemical shift data for H^1 and the Pt–N bond length showing no correlation. The error bars are given as \pm three estimated standard deviations.

A range of coupling constants $^3J_{\text{HPt}}$ were recorded for H^1 (26 - 45 Hz) and H^8 (44 - 70 Hz). A small decrease in the coupling constant between H^1 and ^{195}Pt was observed as the Pt–N bond length increases except where $\text{L} = \text{py}$ (Figure 148). However, no correlation was observed between either the chemical shift (Figure 149) or the $^3J_{\text{HPt}}$ coupling constant (Figure 150) for H^8 with the Pt–C bond length measured by X-ray diffraction. A very large value for $^3J_{\text{HPt}}$ coupling constant was recorded for H^8 , this phenomenon was also reported by Newman *et al.* for the equivalent proton environment of the related $[\text{Pt}(\text{ppy})\text{Cl}(\text{CO})]$ complex.¹⁸⁹ This may be due to the π -acidity of the carbonyl ligand, but if this was the case, a similar effect on the $^3J_{\text{HPt}}$ recorded for H^1 would be expected as well as for the

complexes with the π -acidic phosphorus donor ligands. The origin of this large coupling constant is not yet known but it may be due to a through space interaction between H^8 and the carbonyl ligand.

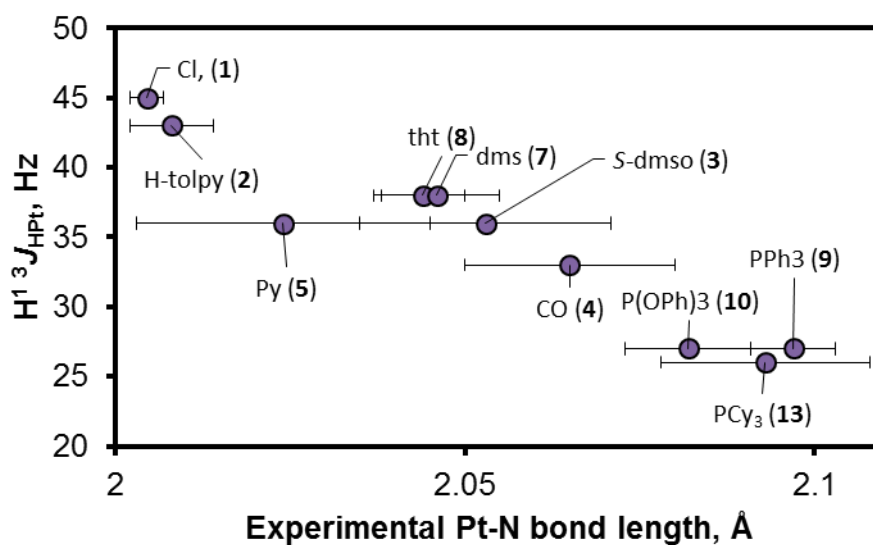


Figure 148: Comparison of the $^3J_{\text{HPt}}$ for H^1 and the Pt-N bond length for $[\text{Pt}(\text{tolpy})\text{Cl}(\text{L})]$

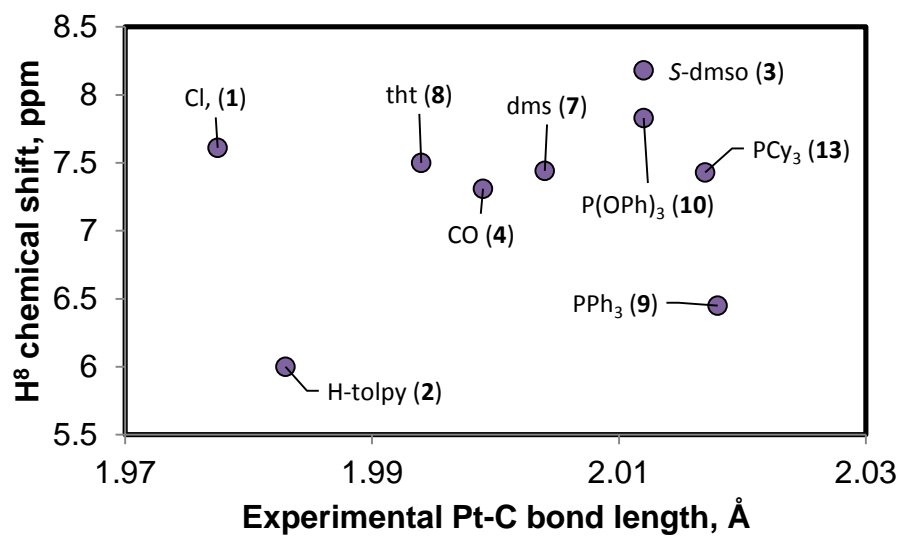


Figure 149: Comparison of the chemical shift data for H^8 and the Pt-C bond length showing no correlation

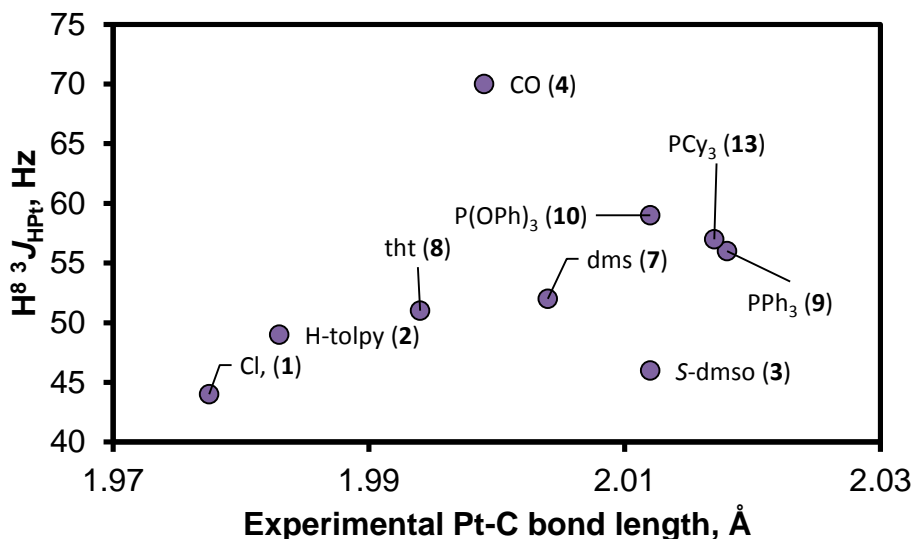


Figure 150: Comparison of the $^3J_{HPt}$ for H^8 and the Pt–C bond length for [Pt(tolpy)Cl(L)]

$^{13}\text{C}\{^1\text{H}\}$ NMR Spectroscopy

There is only a small change in chemical shift observed for the carbanion carbon amongst the platinum complexes studied (140.00 – 142.10 ppm). Coupling between the carbanion carbon and platinum was not observed in the $^{13}\text{C}\{^1\text{H}\}$ NMR experiments conducted using the 400 and 500 MHz instruments which is believed to be due to fast relaxation caused by the chemical shift anisotropy mechanism (CSA).²⁶⁹ Thus, the chemical shifts of nuclei are changing constantly as the molecule tumbles in solution, which can cause relaxation if it occurs at a specific frequency. The increase in relaxation rate leads to line broadening in the recorded spectra and may cause to loss of coupling information. Relaxation by this mechanism is not observed for protons or for carbon atoms which are chemically bonded to hydrogen. Nuclei with large chemical shift ranges such as ^{195}Pt do however, undergo relaxation by this mechanism, in fact, for non-octahedral platinum complexes this is the dominant method of relaxation.³⁰³

The rate of relaxation *via* the CSA mechanism is a function of the gyromagnetic ratio of the nucleus, the chemical shift anisotropy and the applied magnetic field strength.²⁶⁹ As relaxation by this mechanism is proportional to the square of the field strength, the $^{13}\text{C}\{^1\text{H}\}$ NMR experiments were repeated using a lower-field, 300 MHz instrument. Using this instrument, platinum satellites could now be observed for the peak corresponding to the coordinating carbanion and for many of the other carbon signals. Jia *et al.* studied the Pt–C bonds in PCP pincer ligated complexes using $^{13}\text{C}\{^1\text{H}\}$ NMR spectroscopy and the $^1J_{CPt}$ values as a measure

of the Pt–C bond strength and so there is precedent for using this as an indicator of bond strengths.²²⁶ The $^1J_{\text{CPt}}$ coupling constants they recorded ranged from 677 to 951 Hz (Figure 91).

[Pt(tolpy)Cl(dms)] (**7**) was investigated first as it is readily soluble in chloroform and a concentrated solution was prepared. A good quality $^{13}\text{C}\{^1\text{H}\}$ NMR spectrum was obtained within 4 hours and platinum satellites could be observed for the peak corresponding to the coordinating carbanion (Figures 151 and 152). The magnitude of the $^1J_{\text{CPt}}$ coupling observed was 1393 Hz. Additional two bond coupling was also observed for carbons C⁵ and C⁶ ($^2J_{\text{CPt}} = 134$ and 55 Hz respectively). When the delay time was increased from two seconds to four and six seconds in order to account for slow relaxation of quaternary carbon nuclei, no improvement to the peak intensities was observed and so further spectra were acquired with the shorter delay time.

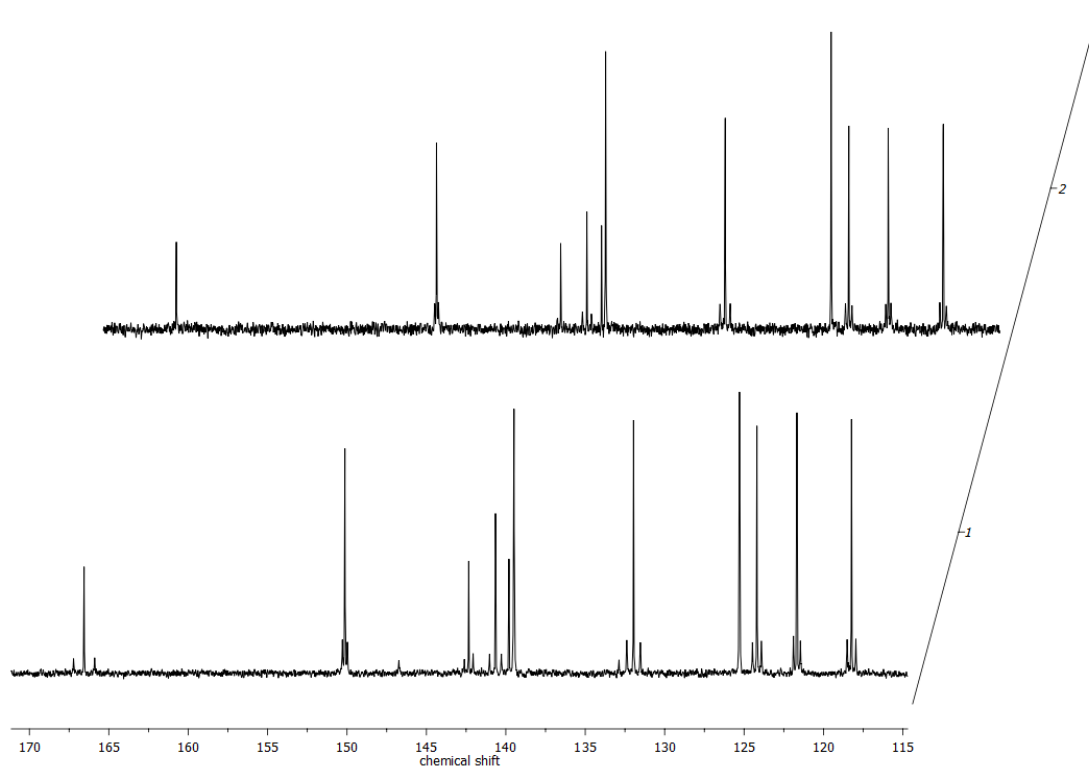


Figure 151: Stacked $^{13}\text{C}\{^1\text{H}\}$ NMR spectra of [Pt(tolpy)Cl(dms)] (**7**) recorded using a 400 MHz (upper) and 300 MHz (lower) instruments.

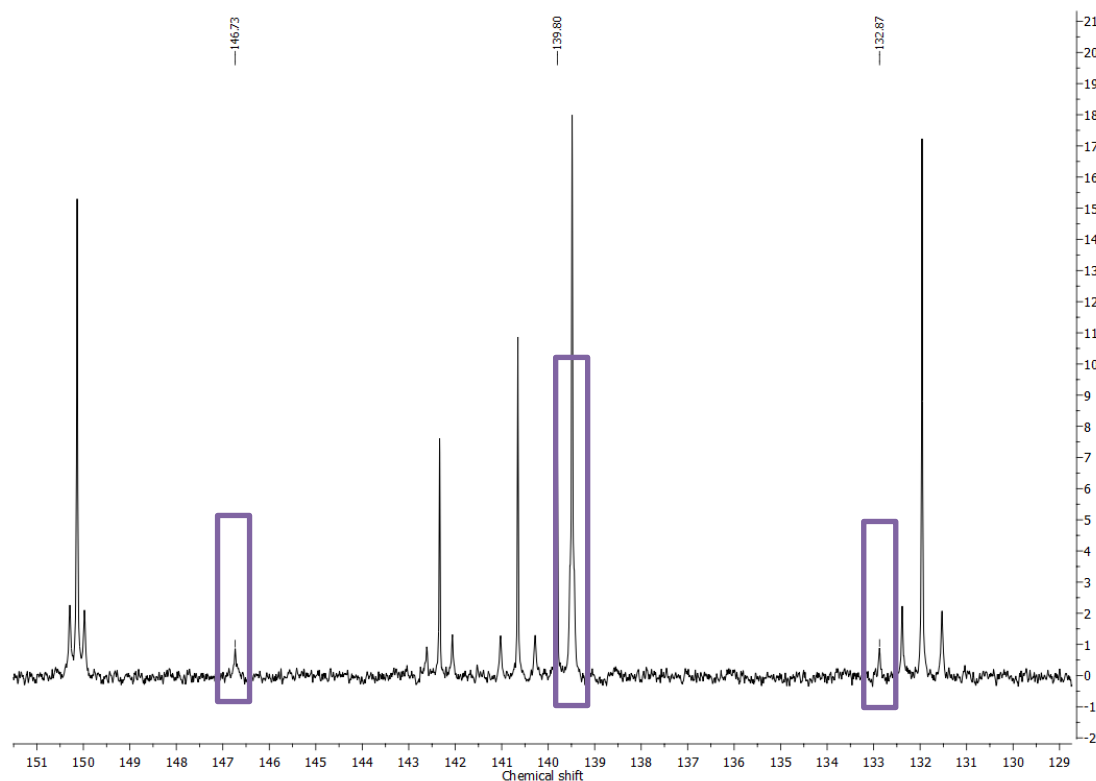


Figure 152: $^{13}\text{C}\{^1\text{H}\}$ NMR spectra of $[\text{Pt}(\text{tolpy})\text{Cl}(\text{dms})]$ recorded using a 300 MHz zoomed in of the carbanion signal

When the $^1J_{\text{CPt}}$ values for the complexes were compared an almost linear relationship between the coupling constant observed and the Pt–N bond lengths was observed and hence the *trans*-influence of the ligands (Figure 153). However, much poorer correlation was observed between the $^1J_{\text{CPt}}$ values and the Pt–C bond lengths (Figure 154).

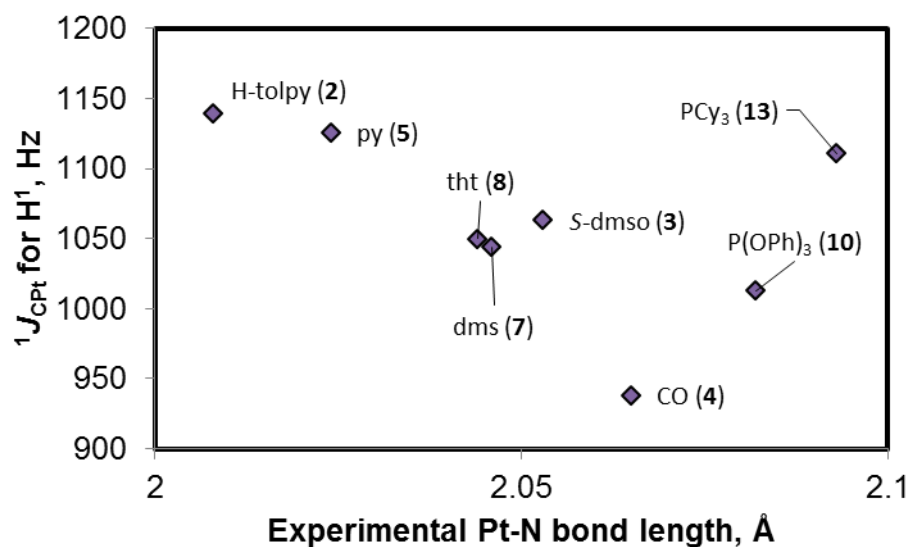


Figure 153: The relationship between $^1J_{\text{CPt}}$ coupling constant and the experimentally determined Pt–N bond lengths

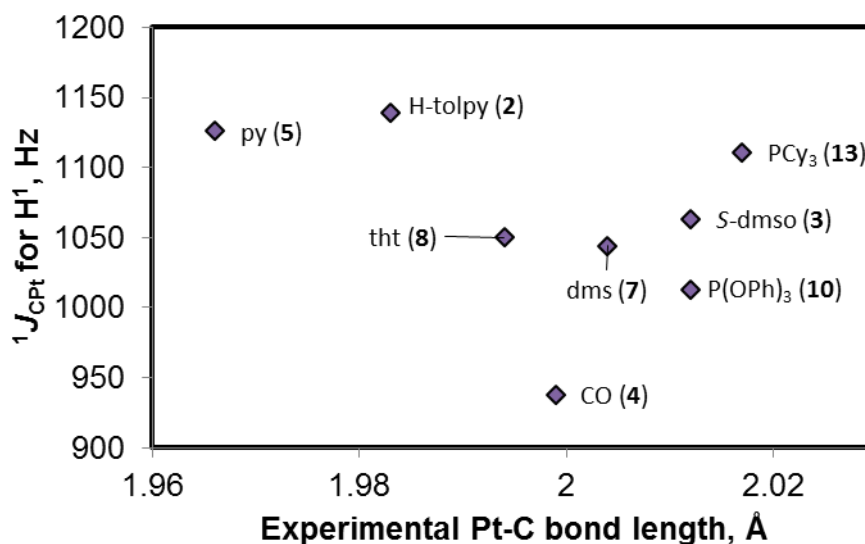


Figure 154: The relationship between $^1J_{\text{C}_{\text{Pt}}}$ coupling constant and the experimentally determined Pt–C bond lengths

^{15}N NMR Spectroscopy

While nitrogen-containing ligands are present in many coordination compounds, due to low natural abundance, ^{15}N NMR data are not routinely collected.³⁰⁴ The sensitivity of ^{15}N in NMR experiments can be enhanced by the use of concentrated samples, higher fields, lower temperatures and isotopic enrichment. In this study, the ^{15}N - ^1H HETCOR NMR spectra were obtained at natural isotopic abundance using 2-(4-tolyl)pyridine as the external reference (δ 305.4 ppm). Studies have been published which have shown that ^{15}N NMR spectroscopy of metal compounds has the potential to provide information on ligand binding, geometry and electronic structure.^{305, 306}

During the optimisation of the 2D method, different combinations of pulse programs (hmbcgpndqf and hsqcetgpsi2) and coupling constants were evaluated. The best results in terms of sensitivity were obtained using 2D ^1H - ^{15}N correlation *via* heteronuclear zero and double quantum coherence (pulse program: hmbcgpndqf). This method was optimised for long-range couplings (using a ^1H - ^{15}N coupling constant of 2 Hz), with no decoupling during acquisition and using gradient pulses for selection. The hsqcetgpsi2 pulse program, for which a poorer signal-to-noise ratio was observed, involved 2D ^1H - ^{15}N correlation *via* double inept transfer, using sensitivity improvement and Echo/Antiecho-TPPI gradient selection, with decoupling during acquisition and using trim pulses in inept transfer with gradients in back-inept. Although different signal-to-noise

ratios were observed, in all cases the ^{15}N chemical shift for 2-(4-tolyl)pyridine was 306 ppm.

The ^{15}N chemical shifts for these complexes have not been reported in the literature and a notable decrease in chemical shift was observed on cyclometallation with platinum. The ^{15}N chemical shift of the 2-(4-tolyl)pyridine ligand for the complexes $[\text{Pt}(\text{tolpy})\text{Cl}(\text{L})]$ increases in the order: 2-(4-tolyl)pyridine (206 ppm) = py (206 ppm) < dms (221 ppm) < dms (224 ppm) < tht (225 ppm) < CO (226 ppm) < $\text{P}(\text{OPh})_3$ (237 ppm) < PCy_3 (242 ppm) << free ligand (306 ppm).

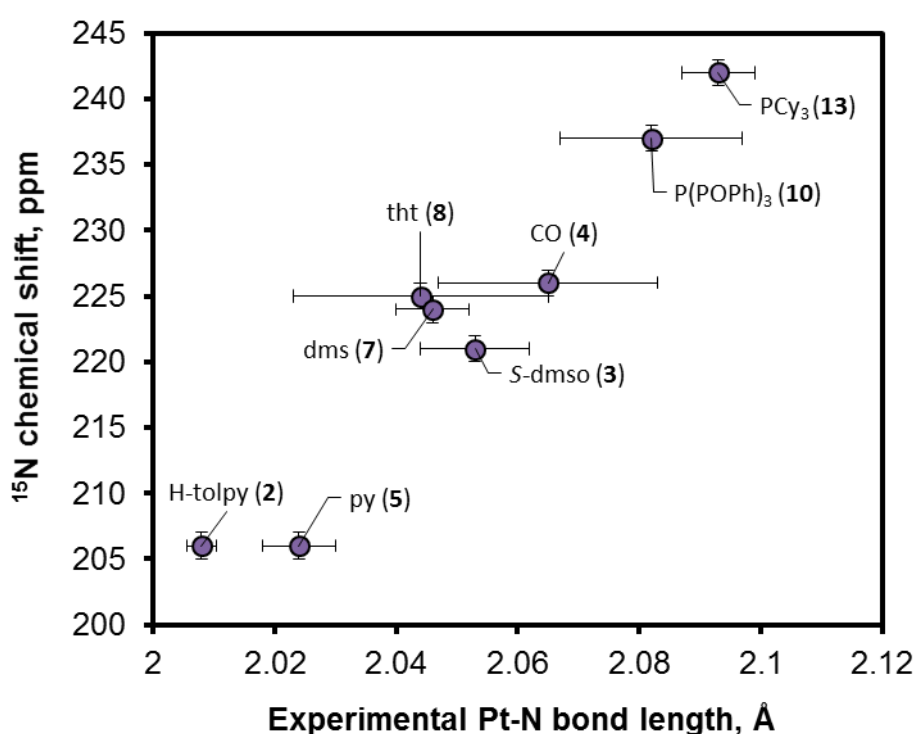


Figure 155: Comparison of the ^{15}N chemical shift and the Pt–N bond length for $[\text{Pt}(\text{tolpy})\text{Cl}(\text{L})]$. The error bars are given as \pm three estimated standard deviations.

The ^{15}N chemical shift of the nitrogen of the cyclometallated 2-(4-tolyl)pyridine ligand does not appear to be very sensitive to the labile ligand, with only 30 ppm difference between the highest and lowest values recorded here. There is a correlation with the Pt–N bond lengths measured by X-ray diffraction (Figure 155) although sulfur donor ligands and CO give rise to complexes with very similar ^{15}N chemical shifts. No correlation observed between ^{15}N chemical shift and the deviation from the linear N–Pt–L bond angle was observed.

Typical values of $^1J_{\text{PtN}}$ for Pt^{II} complexes found in the literature appear between 270 and 400 Hz and are sensitive to the ligand *trans* to nitrogen.^{305, 307} For the majority of complexes $^1J_{\text{PtN}}$ coupling was not observed, but coupling was observed for complex **5** (395 Hz) and **7** (426 Hz), for which concentrated solutions could be prepared due to the solubility of their complexes in CDCl₃.

¹⁹⁵Pt{¹H} NMR Spectroscopy

As discussed in section 1.2, the ¹⁹⁵Pt chemical shift provides information about the effect of the ligands on platinum. All of the ¹⁹⁵Pt spectra were recorded in CDCl₃; it was important to use the same solvent, as solvent interactions with the *d*_{z² orbital on platinum can cause significant variations in chemical shift for platinum(II) complexes. For the set of data collected it was observed that the chemical shift of ¹⁹⁵Pt generally decreases as the Pt–N bond increases (Figure 156) and the *trans*-influence of the ligand, L, increases. The decrease in chemical shift could be indicative of a decrease in electron density at platinum caused by reduced σ -donation from the pyridyl group of the tolpy ligand.}

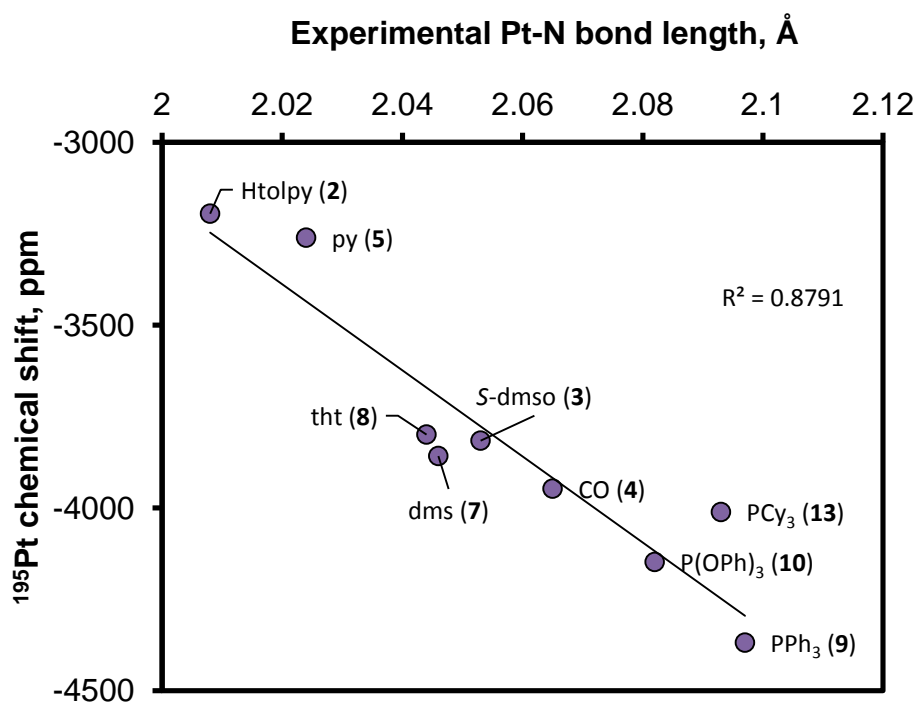


Figure 156: Comparison of the ¹⁹⁵Pt chemical shift and the Pt–N bond length for [Pt(tolpy)Cl(L)] with a line of best fit showing correlation ($R^2 = 0.879$)

Comparison of the Spectroscopic Techniques

In considering many of the data sets above, it is evident that not so many turn out to be faithful reporters of the *trans*-influence of the different neutral ligands, L. For example, although X-ray crystallography is a popular technique for evaluating the *trans*-influence, the Pt–N bond lengths of many of the ligands were reasonably similar; many of the differences were within the limits of three times the estimated standard deviation (3 e.s.d.). That said, an overall trend could be observed that suggested that, in terms of donors, the *trans*-influence series progressed as *N*-donor < *S*-donor < *P*-donor.

From the various sets of NMR data, by far the most sensitive was ^{195}Pt spectroscopy, where the wide chemical shift range was better able to distinguish the different ligands (Figure 157). Thus, it can be proposed that the Pt chemical shift reflects differing electron density on Pt, which in turn reflects electron donation from L (other ligands remain constant) for this family of complexes.

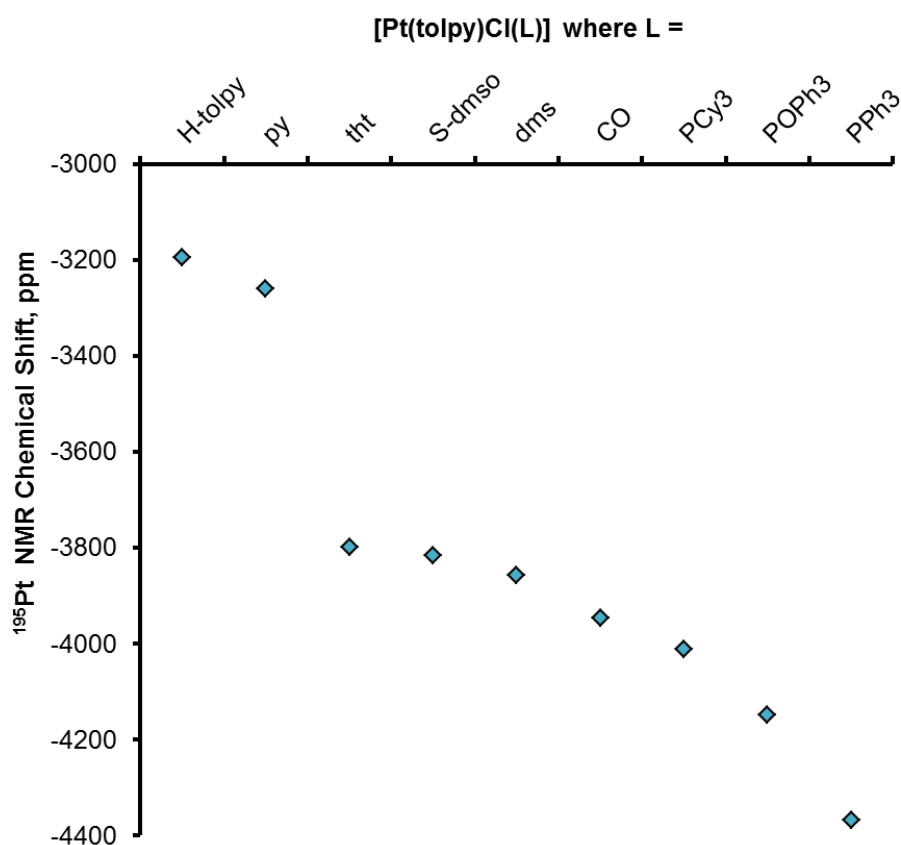


Figure 157: Variation in ^{195}Pt chemical shift among the family of [Pt(tolpy)Cl(L)] complexes.

Thus from all the data collected, properties related to the electron density on Pt appear to give the most reliable estimation of the relative *trans* influence of the

ligands under study. The correlations observed above between the Pt–N bond length and the $^3J_{\text{HPt}}$ coupling constant for H¹ (Figure 158), the $^1J_{\text{CPt}}$ coupling constant for C¹² (Figure 159) and the ^{15}N chemical shift (Figure 161) were re-evaluating using the ^{195}Pt chemical shift. Correlation was still observed for these variables when compared to the ^{195}Pt chemical shift, although complexes **4** and **13** appear outside of the trend when the $^1J_{\text{CPt}}$ coupling constants were considered.

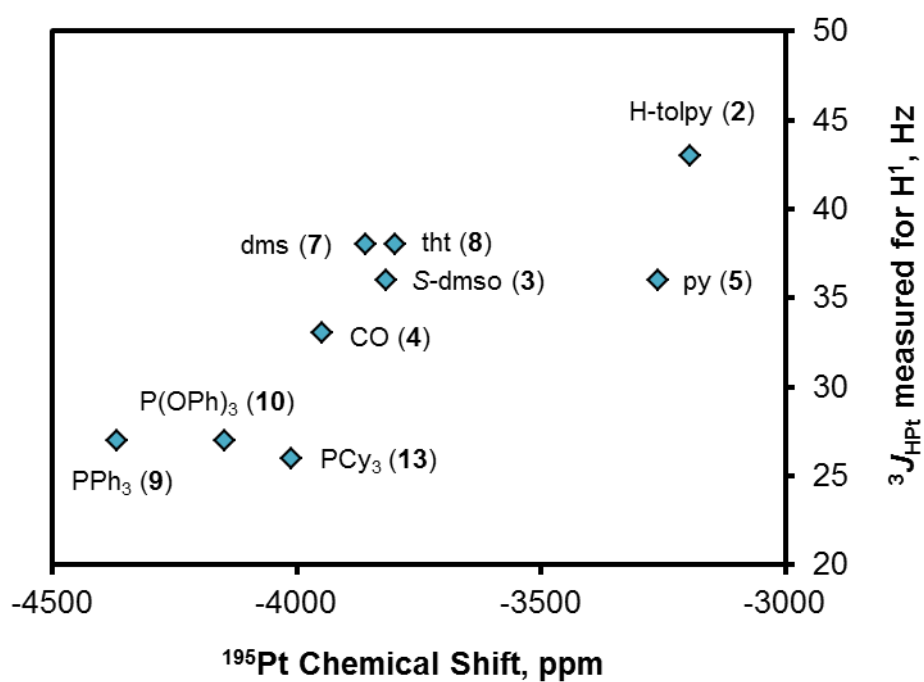


Figure 158: The correlation between $^3J_{\text{HPt}}$ for H¹ and ^{195}Pt chemical shift

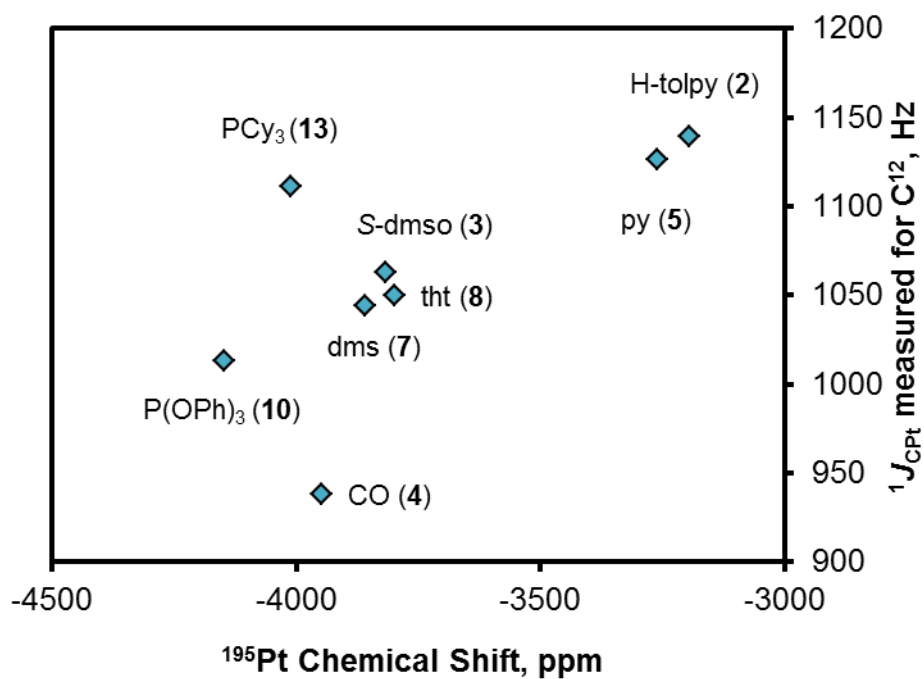


Figure 159: The correlation between $^1J_{\text{C}^{12}\text{Pt}}$ for C^{12} and ^{195}Pt chemical shift

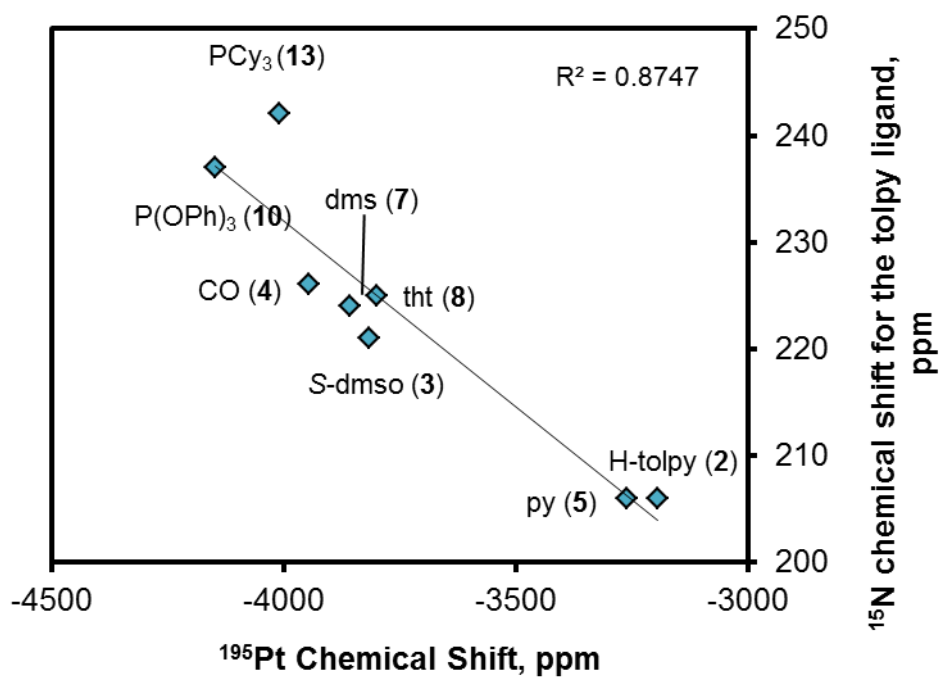


Figure 160: The correlation between ^{15}N and ^{195}Pt chemical shifts

4.0 Probing the *Trans*-Influence of Different Ligands using Natural Bond Order Analysis

Methods of analysing the population of orbitals can be used to probe the electronic structure of transition metal complexes and the relative *trans*-influence of ligands.^{257, 308-310} Quantum chemical calculations on the family of Pt^{II} complexes, [Pt(tolpy)Cl(L)], were performed by M. Shafikov³¹¹ and carried out using Gaussian09 in order to calculate the bond strength parameters; natural (semi-localised) molecular orbitals (MLMO), Mayer-Mulliken population (MM), natural binding index (NBI) and Wiberg index (WI).³¹² The geometries were optimised using B3LYP/def2TZVP which includes an effective core potential (ECP) applied to the Pt atom.

Although the error bars for the bond lengths measured by X-ray diffraction are large compared to the variation between the complexes, the trend observed is consistent with the calculated bond lengths. Comparison of the calculated and experimental structural data (Table 23, Figure 161) shows good agreement in the trend of Pt–N distances, although a general overestimation of the bond lengths is also apparent in the calculated data. All of the bond strength parameters decrease with increasing bond length (X-ray and calculated) which demonstrates that the Pt–N bond lengthens as the population of the molecular orbitals of the Pt–N bond decreases (Figure 162). However, poor correlation was observed when the Wiberg bond order was plotted against the experimentally recorded ¹⁹⁵Pt chemical shifts (Figure 163).

Table 23: Summary of bond strength parameters and bond lengths for the Pt–N bond in [Pt(tolpy)Cl(L)] and [Pt(tolpy)(μ -Cl)]₂

L =	Pt–N bond length, Å		Pt–N bond strength parameters, a.u.			
	Experimental	Calculated	NLMO	MM	NBI	WI
Cl, dimer	2.006(7)	2.0270	0.3648	0.6852	0.6682	0.4465
py	2.024(7)	2.0395	0.3063	0.6279	0.6633	0.4400
dms	2.046(2)	2.0694	0.2401	0.5867	0.6156	0.3790
tht	2.044(2)	2.0670	0.2384	0.5862	0.6158	0.3792
S-dmso	2.052(7)	2.0853	0.2263	0.5394	0.5963	0.3556
CO	2.065(5)	2.0933	0.2004	0.5042	0.5600	0.3136
PPh ₃	2.097(2)	2.1228	0.1887	0.4641	0.5533	0.3061

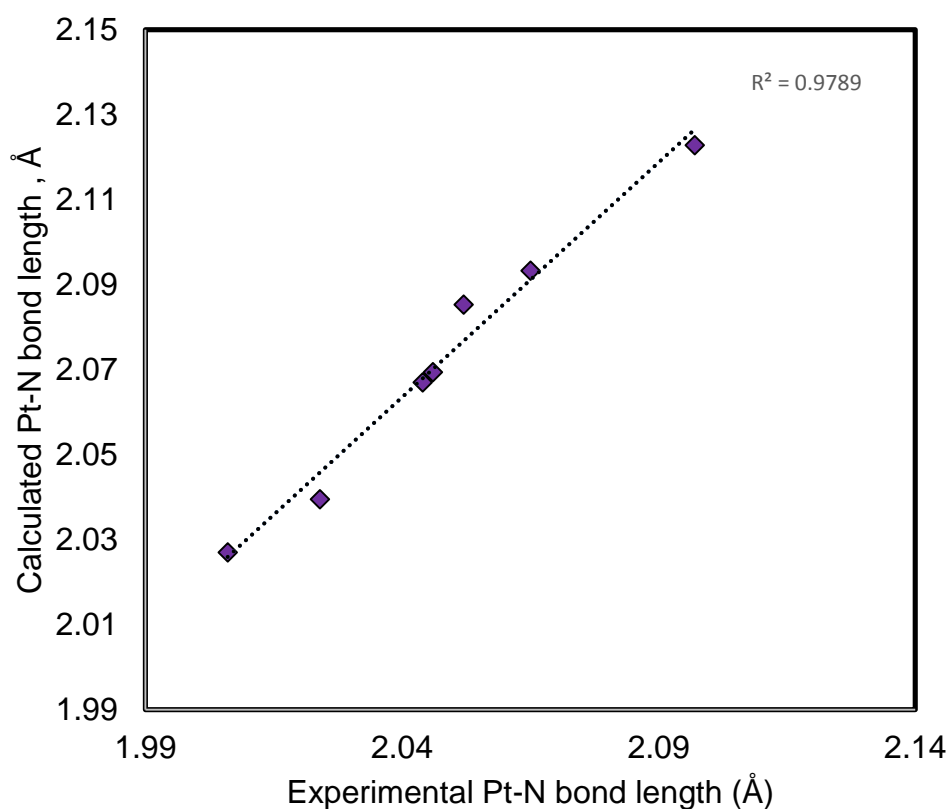


Figure 161: Comparison between experimental and calculated Pt–N bond lengths, with a line of best fit showing good correlation ($R^2 = 0.979$)

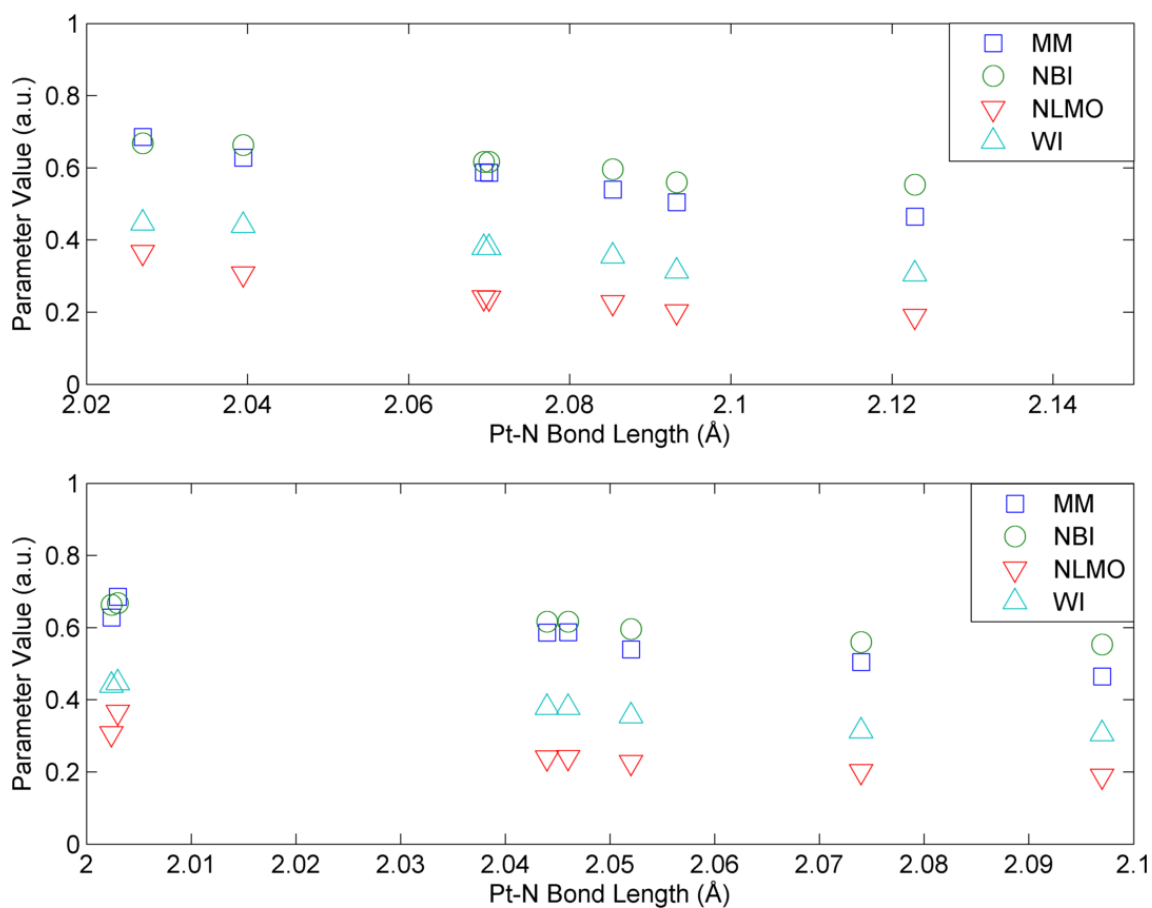


Figure 162: Comparison of bond strength parameters calculated using population analysis *versus* Pt–N bond length calculated using DFT (upper) and determined from X-ray crystallography (lower); where: MM are Mayer-Mullikan populations, NBI are the natural binding indices, NLMO are the natural (semi-)localised molecular orbital and WI refers to the Wiberg indices.

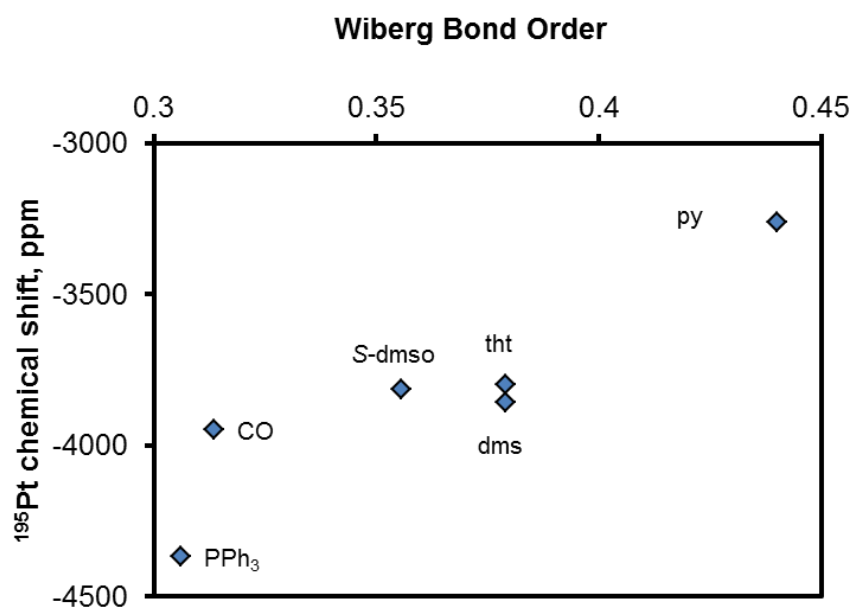


Figure 163: Variation in ^{195}Pt chemical shift experimentally recorded with the calculated Wiberg bond order

5.0 Conclusion

The *trans*-influence exerted by a ligand on the platinum-nitrogen bond in each complex was studied using a range of spectroscopic and computational techniques. An order for the *trans*-influence of the ligands was identified using X-ray analyses of the single crystal X-ray structure (see below) which reproduced the spectrochemical series apart from the ordering of the phosphine and CO ligands. The variation in bond lengths is very small which highlights the need to consider other techniques such as computational chemistry and NMR spectroscopy to compliment this data. The trend in bond lengths measured by X-ray diffraction was consistent with quantum mechanical calculations, where the calculated bond lengths increased and the population of the Pt–N bond decreased as the *trans*-influence of L increased.

When other analytical techniques were investigated it was found that the ^1H chemical shifts of nearby protons did not correlate with the Pt–N bond lengths as they were also sensitive to groups close in space to them. A linear relationship between ^{195}Pt NMR chemical shift and the Pt–N bond length was observed for this series of compounds. Therefore, you can use ^{195}Pt chemical shifts or quantum calculations to estimate the *trans*-influence in the absence of a crystal structure. When the $^1J_{\text{PPt}}$ coupling constants were compared, they were consistent with the relative π -acidity of the ligands, where the strongest π -acid, P(OPh)_3 had the greatest coupling constant (7000 Hz). Although it was expected that a greater $^1J_{\text{PPt}}$ coupling constant would indicate a stronger Pt–P bond and hence a weaker Pt–N bond, this trend was not consistent with the Pt–N bond lengths measured by X-ray diffraction.

When far-infrared spectroscopy was used to investigate a possible *cis*-effect, a general decrease in vibrational frequency of the Pt–Cl stretch as the bond length increased was observed, however, the correlation was poor. Much better correlation was observed when comparing the $^1J_{\text{CPt}}$ coupling constants with the Pt–N bond length for this series of compounds.

This study has demonstrated the usefulness of ^{195}Pt NMR spectroscopy, $^1J_{\text{CPt}}$ coupling constants and calculated bond lengths for evaluating the relative *trans*-influence of ligands and the strength of M–L bonds. It would be beneficial to build on this study and evaluate a larger range of ligands, including electron rich and poor derivatives of the ligands studied, and extend further to different classes of ligands such as carbenes. It would be interesting to investigate the palladium analogues, especially given the interest in palladium complexes with regard to cross coupling reactions.

Experimental Section

1.0 Analytical Techniques

^1H , ^2H , $^{13}\text{C}\{^1\text{H}\}$, ^{15}N , ^{19}F , $^{31}\text{P}\{^1\text{H}\}$ and $^{195}\text{Pt}\{^1\text{H}\}$ NMR Spectroscopy

^1H , $^{13}\text{C}\{^1\text{H}\}$, ^{19}F and $^{31}\text{P}\{^1\text{H}\}$ NMR spectra were recorded using a Jeol ECS400 spectrometer (9.4 T) operating at 400 MHz, 100.5 MHz, 376 MHz and 164 MHz, respectively. For ^1H NMR, the residual protic solvent was used as the internal standard (CHCl_3 : 7.26 ppm, CD_2Cl_2 : 5.32 ppm, CH_3CN : 1.94 ppm, CD_3COCD_3 : 2.04 ppm), for $^{13}\text{C}\{^1\text{H}\}$ NMR, the solvent was also used as the internal standard (CDCl_3 : 77.16 ppm, CD_2Cl_2 : 53.84 ppm, CH_3CN : 1.32 ppm) and the ^{19}F and $^{31}\text{P}\{^1\text{H}\}$ NMR experiments were run unreferenced. The $^{13}\text{C}\{^1\text{H}\}$ NMR spectrum of $[\text{Pt}(\text{tolpy})\text{Cl}(\text{CO})]$ was obtained using HMBC with a coupling constant of 5 Hz and non-uniform sampling. The $^{13}\text{C}\{^1\text{H}\}$ NMR experiments were repeated using a Bruker 300NB AVANCE III instrument (7.0 T) operating at 75 MHz, in order to observe the ^{13}C - ^{195}Pt coupling for the $[\text{Pt}(\text{tolpy})\text{Cl}(\text{L})]$ family of complexes. DEPT-135 spectra were recorded using a Jeol ECS400 spectrometer (9.4 T) and using a 135° pulse.

^2H , ^{15}N , $^{31}\text{P}\{^1\text{H}\}$ and $^{195}\text{Pt}\{^1\text{H}\}$ NMR spectra were recorded using a Bruker 500 AVANCE III spectrometer (11.7 T) operating at 76.8 MHz, 50.7 MHz, 202.4 MHz and 107 MHz, respectively. ^{15}N chemical shifts were obtained using 2D ^1H - ^{15}N correlation *via* heteronuclear zero and double quantum coherence without decoupling during acquisition. This method was optimised for long-range couplings (using a ^1H - ^{15}N coupling constant of 2 Hz) and used gradient pulses for selection (pulse program: hmbcgpndqf). $^{195}\text{Pt}\{^1\text{H}\}$ NMR chemical shifts were referenced relative to external $\text{K}_2[\text{PtCl}_4]$ in D_2O . ^{15}N NMR chemical shifts were referenced relative to external 2-(4-tolyl)pyridine in CDCl_3 (305.7 ppm). 1D NOESY difference spectra were obtained using selective refocusing with a shaped pulse.³¹³⁻³¹⁵

2D ^1H - ^1H correlation (COSY) experiments were conducted using gradient double-quantum-filtered COSY (gDQF-COSY), 2D ^1H - ^{13}C heteronuclear correlation experiments were obtained using gradient HSQC with *y*-projection for one bond couplings and heteronuclear multiple-bond correlation (HMBC) was used to investigate long-range couplings. All chemical shifts are given in ppm.

IR Spectroscopy

FT-IR spectra in the range 4000 to 600 cm^{-1} were recorded using a Shimadzu IR Prestige-21 with Specac Golden Gate diamond ATR-IR insert. *In situ* ATR FT-IR spectra were recorded using a React-IR 4000 Instrument (Mettler Toledo AutoChem ReactIR) equipped with a silicon ATR probe (SiComp, optical range 4400–650 cm^{-1}). The silicon probe was introduced into the reaction vessel and spectra were recorded every two minutes using a thermocouple to record the temperature of the reaction solution. Spectra in the range 600 to 150 cm^{-1} were recorded on a Bruker TENSOR 37 instrument using a Bruker platinum ATR stage.

Single Crystal X-ray Diffraction

Diffraction data were collected at 110 K on an Oxford Diffraction SuperNova diffractometer with Mo- K_{α} radiation ($\lambda = 0.071073$ nm) or Cu- K_{α} radiation ($\lambda = 0.15418$ nm) using a Cannon EOS CCD camera. The crystal was cooled with liquid nitrogen to 110 K using an Oxford Instruments Cryojet. Diffractometer control, data collection, initial unit cell determination, frame integration and unit-cell refinement was carried out with 'CrysAlisPro'.³¹⁶ Face-indexed absorption corrections were applied using spherical harmonics, implemented in SCALE3 ABSPACK scaling algorithm.³¹⁷ OLEX2³¹⁸ was used for overall structure solution, refinement and preparation of computer graphics and publication data. Within OLEX2, the structures were solved with the Superflip Structure solution program using 'charge flipping'³¹⁹ or with the ShelXS/ShelXT structure solution programs using Direct Methods.³²⁰ Refinement by full-matrix least-squares used the SHELXL-97³²¹ algorithm within OLEX2. All non-hydrogen atoms were refined anisotropically and hydrogen atoms were placed using a 'riding model' and included in the refinement at calculated positions. The crystallographic parameters for the single crystal structures in this chapter are shown in Tables in Appendix I. The images of the crystal structures obtained were processed using the program Mercury.

UV-Vis Spectroscopy

Absorption spectra in solution were measured using a Shimadzu UV-2401 instrument using quartz cuvettes of 1 cm path length and a spectral window between 190 and 900 nm.

Dynamic Light Scattering

The average hydrodynamic radii of particles in solution were determined using a Zetasizer Nano (Malvern Instruments Ltd.). The samples (0.1 ml) were diluted with the reaction solvent (0.9 ml), filtered through a syringe filter (0.22 μm) and then measured at 25 °C and adjusted to this temperature for 2 min prior to the measurement. The autocorrelation functions were analysed using the DTS v5.1 software provided by Malvern. Measurements were done in quintuplicate with 15–20 runs per single measurement and the calculated mean values (based on intensity distribution) were used.

High Resolution Mass Spectrometry

Mass spectrometry was carried out using a Bruker microTOF instrument. All data were acquired in positive ion mode using ESI ionisation.

CHN Elemental Analysis

Values were obtained using an Exeter Analytical Inc. CE-440 Analyser and Sartorius S2 analytical balance. Calibration was performed against acetanilide standards and checked by the use of *S*-benzyl thiuronium chloride as internal standard (analytical grade, Exeter Analytical).

Peroxide Test

The peroxide levels were tested using Quantofix[®] peroxides test sticks (1-100 mg/L range of application). To test for peroxides in organic solvents the test zone was wetted with one drop of water after evaporation of the solvent.

Gas Chromatography (GC)

Five GC instruments were used to undertake headspace analysis. GC-A was used to identify hydrocarbons present in the reaction headspace by comparison to known standards. This instrument was fitted with a hydrocarbon trap for pre-concentration and parallel columns for separating out low molecular weight hydrocarbons and oxygenated species. GC-B was used for routine reaction headspace analysis, it is equipped with two detectors, TCD and FID in series. Peak identification was achieved by referencing to a number of certified gas standard mixtures combined with injection of single hydrocarbons (C₂-C₈). GC-C, GC-D and GC-E were GC-MS instruments used to confirm the identity of the analytes and determine the isotopic distribution. GC-D was used to identify

methane and carbon monoxide present in the reaction headspace by analysis of the mass spectra. GC-E was used for the quantitative analysis of butane using a calibration curve.

GC-A

The reaction headspace was transferred to an evacuated canister (internal volume: 700 mL), which was then pressurised with nitrogen to 40 psi. Samples (5 ml) from the canister were drawn through a condensation trap, and then pre-concentrated on a dual-bed adsorbent trap containing Carboxen 1000 and Carbotrap B (Supelco) (approximately 90 mg in total). The dual-bed adsorbent trap, was held at -20 °C during trapping and then heated to 325 °C during desorption. The eluent was split in an approximately 9:1 ratio between a Na₂SO₄ deactivated aluminium oxide (Al₂O₃) porous layer open tubular (PLOT) column (50 m, 0.53 mm id, Varian Netherlands) and two LOWOX columns (10 m, 0.53 mm id, Varian Netherlands) in series. The initial oven temperature of 40 °C was held for 3 min, and then ramped at 12 °C min⁻¹ to 110 °C, followed by 7 °C min⁻¹ to 200 °C and held for 20 min, giving a total run time of 42 min. Analytes were eluted from the GC columns into two separate flame ionisation detectors.

GC-B

Samples (1 ml, sampled at 25 °C split injection, 10:1) of the reaction headspace were passed through a GS-AL/KCl column (50 m, 0.535 mm id, Agilent Technologies) using an Agilent 7820A system with helium carrier gas. The initial oven temperature of 100 °C was held for 1 min, then ramped at 5 °C min⁻¹ to 195 °C and held for 5 min; giving a total run time of 25 min. Analytes were eluted from the GC column into a thermal conductivity detector and then a flame ionisation detector in series.

In order to identify the peaks observed after sampling the reaction headspace, a number of hydrocarbon references were analysed. The retention times for the references are summarised in

Table 24, and overall it was observed that an increase in unsaturation leads to an increase in retention time for this system.

Table 24: Summary of GC retention times including study of C₄₋₇ hydrocarbons using GC method described above for GC-B

Compound	Retention Time, minutes	Boiling Point, °C	Compound	Retention Time, minutes	Boiling Point, °C
Butane	5.8	-1	1-Hexene	16.1	63
1-Butene	6.8	-6	DMS	17.5	37
Cyclopentane	9.0	49	1,3-Cyclohexadiene	18.3	80
Cyclohexane	12.8	81	Cycloheptane	20.0	118
Hexane	13.8	69	Benzene	20.5	80
Cyclohexene	15.9	83	Cycloheptene	21.7	113

GC-C, GC-MS

Samples of the reaction headspace were passed through a HP-AL/S column (30 m, 0.25 mm id, 5 mm film thickness, Agilent Technologies) using an Agilent 7890 GC system. The carrier gas was helium (flow rate: 1.5 mL min⁻¹) and the injection was split with a ratio, 10:1. The initial oven temperature of 100 °C was held for 1 min, then ramped at 5 °C min⁻¹ to 195 °C and held for 5 min, giving a total run time of 25 min. Analytes were eluted from the GC column into a Waters GCT Premier time of flight instrument (scan time = 0.19 s, interscan = 0.01 s, internal standard = perfluorotributylamine also known as heptacosyl) equipped with an electron impact ionisation source.

GC-D, GC-MS

For the analysis of butane, the samples were first transferred to a pre-concentration trap, where the sample was frozen using liquid nitrogen and the gases which do not condense at that temperature (such as N₂, He, Ar and O₂) were evacuated from the cryo-trap by a pressure differential created by the two-stage rotary pump. Following the removal of any non-condensable gases, the vacuum pump is isolated from the sample, and a flow of ultra-pure He is passed through the trap. The liquid nitrogen bath was then removed from the cryo-trap and replaced with a bath of boiling water. This results in the sample rapidly being flushed from the trap by the flow of helium. The helium carrier gas

(the GC mobile phase) then passes the sample into the GC system where the components are separated and passed to a mass detector for selected ion mode optimised for butane analysis for detection.

Samples of reaction headspace (1 ml) were transferred to serum vials (120 ml, flushed with helium). Samples (1 ml) were taken from the serum vial and injected into a condensation trap, cooled with liquid nitrogen and a small portion of sample (approx. 0.04 ml) was delivered to a PoraBondQ column (25 m, 0.32 mm id, 5 μm film thickness, Varian) using an Hewlett Packard GCD plus 91800B system. The volume of gas delivered was accurately determined by measuring the change in pressure. The carrier gas was helium (flow rate: 4.0 mL min⁻¹ for 2 min followed by 1 mL min⁻¹) and the initial oven temperature of 35 °C was held for 2 min, then ramped at 18 °C min⁻¹ to 115 °C. Analytes were eluted from the GC column into a mass detector (selected ion mode: 57. 58 a.m.u.) equipped with an electron impact ionisation source.

Calculation for Butane Analysis

1) Calculation moles of gas injected:

$$\text{moles of gas injected} = \frac{(\text{injection pressure in atm} \times \text{volume})}{(\text{temperature} \times \text{gas constant})}$$

$$\text{moles of gas injected} = \frac{(\text{injection pressure in atm} \times 0.2956 \text{ L})}{(293 \text{ K} \times 0.082057 \text{ L atm K}^{-1} \text{ mol}^{-1})}$$

2) Apply linear calibration

$$\text{moles of butane} = \frac{\text{peak area}}{\text{gradient of linear fit } (1.25 \times 10^{16})}$$

3) Molar ratio of butane in injection (ppm):

$$\text{Butane ppm} = \frac{(\text{moles of butane} \times 10^6)}{(\text{moles of gas injected})}$$

4) Calculation of moles of butane in serum vial:

$$\text{Butane in serum vial moles} = \frac{\text{butane ppm}}{10^6} \times \frac{\text{volume of serum vial (120 ml)}}{22400}$$

5) Calculation of butane in headspace:

$$\text{Butane in headspace mmol} = \text{butane in serum vial} \times 23 \times 1000$$

6) Calculation of the turnover number (TON)

$$TON = \frac{\text{butane in headspace mmol}}{\text{mmol catalyst used}}$$

GC-E, GC-MS

The effluent separated in the GC column is split between a mass spectrometer, used to obtain mass spectral data for compound identification, and a combustion column leading to an IRMS detector. IRMS is carbon stable isotope ratio mass spectrometry, which analyses the carbon dioxide formed after the analytes which have passed through the GC system undergo combustion.

Samples (0.05 ml) were injected from a standard volume loop onto a condensation trap and passed through a MolSeive 5A column (30 m, 0.32 mm id, 15 μm film thickness, Supelco) using an Agilent 7890B system. The carrier gas was helium (flow rate: 1.0 mL min⁻¹) and the initial oven temperature of 30 °C was held for 15 min, then ramped at 50 °C min⁻¹ to 200 °C and held for 5 min. Analytes were eluted from the GC column were then split between two mass spectrometers. One portion (10%) is transferred into an Agilent inert MSD 5975C with a triple axis detector (selected ion mode: 15, 16, 27, 28 a.m.u) equipped with an electron impact ionisation source. For full isotopomer analysis of methane the ions, 15, 16, 17, 18, 19 and 20 a.m.u, were studied. The second portion (90%) is transferred to a combustion column leading to a Delta Advantage IRMS (ThermoFinnigan). A known CO₂ isotopic reference gas is used to calibrate the isotope ratio measurements, which is added *via* the Conflow 3 (ThermoFinnigan) after four minutes and twenty minutes for 30 seconds at the beginning of each analysis. All stable carbon isotope values are subsequently reported as $\delta^{13}\text{C}$ per mille (‰) relative to the Vienna PeeDee Belemnite reference standard (VPDB).³²²

Calculation for Quantification of Methane

The methane produced by the reaction was observed and quantified using GC-MS analysis of the reaction headspace and the method used was first reported by Archbold and co-workers.³²³ The peak areas observed using the first mass spectrometer can be compared to a calibration curve of methane in air (Figure 164).

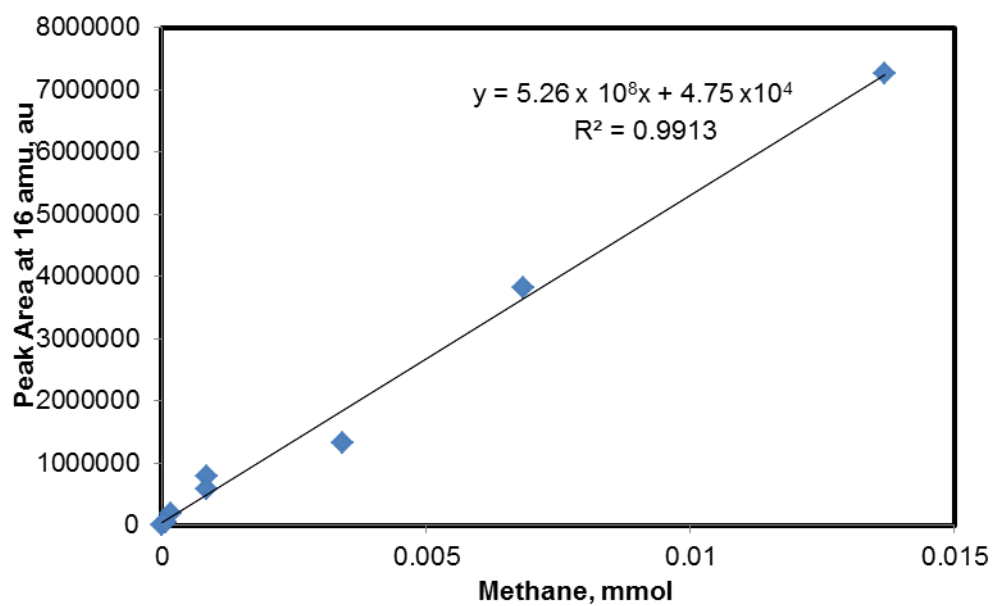


Figure 164: Calibration curve for methane analysed using a mass spectral detector, GC-E

Gradient = $5.26 \times 10^8 \pm 3.8\%$

Standard error of regression was calculated using the data analysis tool in Microsoft Excel.

2.0 Materials

The $K_2[PtCl_4]$ was obtained from Johnson Matthey and Alfa Aesar. Ultra-high purity carbon monoxide was purchased from Air Products. 2-(4-Tolyl)pyridine and the ketone substrates, including cyclohexanone- d_{10} and were obtained from Sigma Aldrich and used without further purification unless otherwise stated. 1,2-Bis(diphenylphosphino)ethane (dppe), 4,4'-di-tert-butyl-2,2'-dipyridyl (^tBubipy) and 4,4',4''-tri-tert-butyl-2,2',2''-terpyridine (^tButerpy) were obtained from Fluorochem. All solvents were HPLC grade and all materials were used without further purification unless otherwise stated. $[PtCl_2(dppe)]$,³²⁴ $[PtCl_2(^tBubipy)]$,³²⁵ and $[PtCl(^tButerpy)]Cl$ ³²⁶ were synthesised in house according to literature procedures by Iman Khazal.³²⁷

3.0 Purification of Solvents and Reagents

Solvents (dichloromethane, hexane, acetonitrile) were purchased from Fisher Scientific UK and dried by percolation over activated alumina prior to use. $CDCl_3$ were treated with K_2CO_3 and stored in an amber vial over molecular sieves (4 Å). Unless otherwise stated, reagents were purified according to procedures described by Armarego and Chai.³²⁸

Acetone

Acetone was dried over calcium sulfate under an atmosphere of nitrogen for 20 h, distilled under atmospheric pressure (oil bath temperature: 80 °C, head temperature: 56 - 57 °C) and stored temporarily over molecular sieves (3 Å). Note: long term storage over molecular sieves is not advisable as acetone can undergo aldol condensation when in the presence of a base.³²⁹

Acetophenone

Acetophenone was stirred with calcium hydride under an atmosphere of nitrogen for 20 h, distilled under reduced pressure, and stored under an atmosphere of nitrogen over molecular sieves (4 Å).

Cyclic Ketones

Cyclic ketones were stirred with magnesium sulfate under an atmosphere of nitrogen for 20 h, distilled under reduced pressure, and stored under an atmosphere of nitrogen over molecular sieves (4 Å).

α -Tetralone: pressure: 8 mbar, oil bath temperature: 140 °C, head temperature: 116 - 117 °C

Cyclohexanone: pressure: 10 mbar, oil bath temperature: 80 °C, head temperature: 42 - 43 °C

Cyclopentanone: pressure: 15 mbar, oil bath temperature 40 °C, head temperature: 30 - 31 °C

Cycloheptanone: 10 mbar, oil bath temperature: 90 °C, head temperature: 46 - 47 °C

Cyclopentylmethylether

Cyclopentylmethyl ether was passed through a plug of basic alumina (Brockmann 1, standard grade, ~ 150 mesh) to remove peroxides and then dried over calcium chloride under an atmosphere of nitrogen for 20 h, distilled under reduced pressure (pressure: 10 mbar, oil bath temperature: 50 °C, head temperature: 28 - 29 °C), and stored under an atmosphere of nitrogen, over molecular sieves (4 Å).

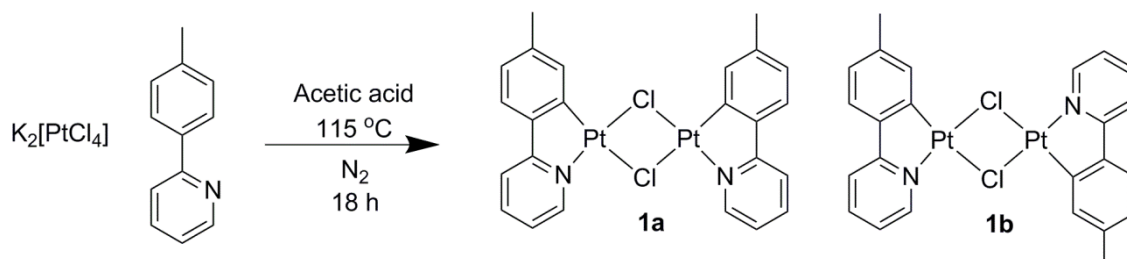
Dioxane

Dioxane was dried over calcium hydride (5% w/v) under an atmosphere of nitrogen for 24 h, distilled under atmospheric pressure (oil bath temperature: 125 °C, head temperature: 101 - 103 °C), and stored under an atmosphere of nitrogen, over molecular sieves (4 Å).³³⁰

4.0 Synthesis

4.1 Synthesis of Platinum(II) Complexes

Synthesis of $[\text{Pt}(\text{tolpy})(\mu\text{-Cl})]_2$ (**1**)



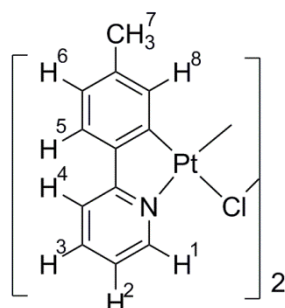
An outgassed solution of $\text{K}_2[\text{PtCl}_4]$ (0.603 mmol, 250.5 mg) in hot water (1.5 ml), was added to an outgassed solution of 2-(4-tolyl)pyridine (0.585 mmol, 99 mg, 0.1 ml) in acetic acid (50 ml) under an atmosphere of dry nitrogen. The mixture was heated under reflux, with stirring for 18 h. Water (40 ml) was added, yielding a yellow precipitate, which was recovered by filtration. The filtrate was then washed successively with water (2 x 5 ml), hexane (2 x 2 mL), ethanol (2 x 5 ml) and cold diethyl ether (2 x 2 ml) affording a mixture of *cis* (**1a**) and *trans* (**1b**) isomers as a yellow/green solid, which was dried *in vacuo*.

Yield 151 mg (65%).

CHN data for $\text{C}_{24}\text{H}_{20}\text{Cl}_2\text{N}_2\text{Pt}_2$ found (expected)/%: C 36.36 (36.15), H 2.59 (2.53), N 3.36 (3.51).

For the mixture of *cis* and *trans* isomers, FT-IR (ATR, $\bar{\nu}$ max, cm^{-1}) selected bands: 419, 310, 289, 246

Spectroscopy data for isomer **1a**:



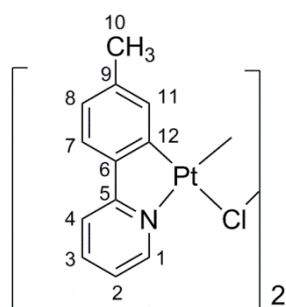
$^1\text{H-NMR}$ δ_{H} (400 MHz, CD_3CN): 8.76 (2H¹, d, $^3J_{\text{HH}} = 5.6$ Hz, $^3J_{\text{HPt}} = 45$ Hz), 7.95 (2H³, td, $^3J_{\text{HH}} = 7.2$ Hz, $^4J_{\text{HH}} = 1.2$ Hz), 7.73 (2H⁴, d, $^3J_{\text{HH}} = 8$ Hz), 7.61 (2H⁸, s, $^3J_{\text{HPt}} = 44$ Hz), 7.36 (2H⁵, d, $^3J_{\text{HH}} = 8$ Hz), 7.15 (2H², td, $^3J_{\text{HH}} = 7.6$ Hz, $^4J_{\text{HH}} = 1.6$ Hz), 6.89 (2H⁶, d, $^3J_{\text{HH}} = 8.8$ Hz), 2.28 (6H⁷, s)

Table 25: Summary of the data collected using the selective 1D NOE Spectra recorder for **1a**

H irradiated	Enhancement observed for
H ⁴	H ⁵ (d)
H ⁵	H ⁴ (d), H ⁶ (d)

Table 26: Summary of the coupling observed in the ¹H-¹H COSY experiment for **1a**

H	δ_{H} , ppm	Coupling observed with
H ¹	8.76	7.15 (H ²)
H ²	7.15	8.76 (H ¹), 7.95 (H ³)
H ³	7.95	7.73 (H ⁴), 7.15 (H ²)
H ⁴	7.73	7.95 (H ³)
H ⁵	7.36	6.89 (H ⁶)
H ⁶	6.89	7.36 (H ⁵)
H ⁷	2.28	6.89 (H ⁶)



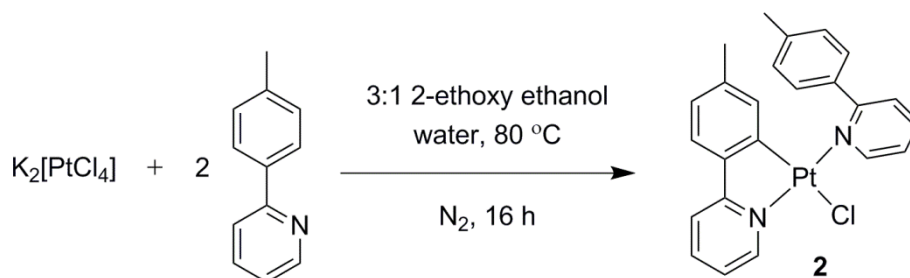
¹³C{¹H} NMR δ_{C} (125.7 MHz, CDCl₃): 149.30 (C¹), 139.22 (C¹²), 138.96 (C⁹), 134.24 (C³), 124.95 (C¹¹), 123.23 (C⁸), 122.82 (C⁷), 118.82 (C²), 118.92 (C⁴), 20.86 (C¹⁰). The solution was very dilute due to the poor solubility of complex **1a** and as a consequence two (C⁵ and C⁶) of the quaternary carbon signals were not observed.

Due to the low solubility of the complex, it was not possible to observe the ¹⁵N or ¹⁹⁵Pt chemical shifts.

For isolated *cis* isomer **1a**, FT-IR (ATR, $\bar{\nu}$ max, cm⁻¹) selected bands: 332 (Pt–Cl)

Structure of **1a** confirmed by single-crystal X-ray crystallography see appendix I. A suitable crystal was obtained from layering a dilute solution of complex **1** in chloroform with diethyl ether.

Synthesis of [Pt(tolpy)Cl(H-tolpy)] (2)

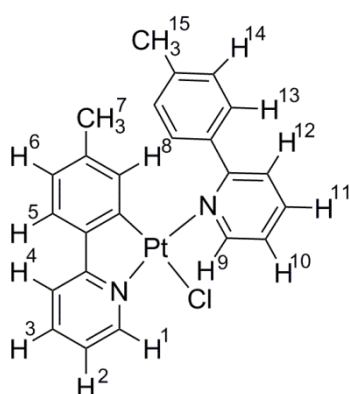


A solution of $K_2[PtCl_4]$ (0.612 mmol, 254.2 mg) in hot water (1.5 ml) was added to an outgassed solution of 2-(4-tolyl)pyridine (1.17 mmol, 0.2 ml) in 2-ethoxyethanol and water (3:1, 50 ml) under an atmosphere of dry nitrogen. The mixture was heated ($80\text{ }^\circ\text{C}$) with stirring for 14 h. Water (50 ml) was added, yielding a grey/green precipitate, which was recovered by filtration. The filtrate was then washed successively with water (2 x 5 ml) and hexane (1 x 5 ml) affording the title compound as a grey/green solid, which was dissolved in dichloromethane and filtered through a Celite™ pad and recrystallised from dichloromethane and hexane to yield the yellow crystalline product. A crystal suitable for X-ray crystallography was obtained by layering a solution of [Pt(tolpy)Cl(H-tolpy)] (2) in dichloromethane with hexane.

Yield 198 mg (58%).

CHN data for $C_{24}H_{21}Cl_2N_2Pt$ found (expected)/%: 49.26 (50.75), 3.82 (3.73), 4.72 (4.93)

MS-ESI (m/z): [$M^+ - Cl^-$] for [$C_{24}H_{21}N_2Pt$] $^+$ 532.1362 (expected: 532.1349)



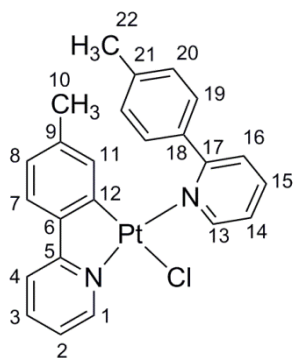
1H -NMR δ_H (400 MHz, $CDCl_3$): 9.59 (1 H^1 , d, $^3J_{HH} = 5.7$ Hz, $^3J_{HPt} = 36.0$ Hz), 9.24 (1 H^9 , d, $^3J_{HH} = 5.7$ Hz, $^3J_{HPt} = 40.0$ Hz), 7.99 (2 H^{13} , AA'XX', $^3J_{HH} = 8.0$ Hz), 7.93 (1 H^{11} , t, $^3J_{HH} = 8.2$ Hz), 7.71 (1 H^3 , t, $^3J_{HH} = 6.7$ Hz), 7.61 (1 H^{12} , d, $^3J_{HH} = 7.9$ Hz), 7.48 (1 H^4 , d, $^3J_{HH} = 8.0$ Hz), 7.34 (1 H^{10} , t, $^3J_{HH} = 7.6$ Hz), 7.22 (1 H^5 , d, $^3J_{HH} = 7.6$ Hz), 7.13 (1 H^{14} , d, $^3J_{HH} = 7.9$ Hz), 7.03 (1 H^2 , t, $^3J_{HH} = 7.4$ Hz), 6.81 (1 H^6 , d, $^3J_{HH} = 8.0$ Hz), 6.01 (1 H^8 , s, $^3J_{HPt} = 48.0$ Hz), 2.27 (3 H^{15} , s), 2.15 (3 H^7 , s).

Table 27: Summary of the data collected using the selective 1D NOE Spectra for **2**

H irradiated	Enhancement observed for
H ¹	H ² (s)
H ⁵	H ⁴ (s), H ⁶ (m)
H ⁶	H ⁵ (s), H ⁷ (s)
H ⁷	H ¹³ (w), H ⁶ (m), H ⁸ (s)
H ⁸	H ⁷ (w), H ¹³ (m), H ⁹ (s)
H ¹³	H ¹² , (m), H ¹⁴ (s), H ⁸ (w)
H ¹⁴	H ¹³ (s), H ¹⁵ (s)

Table 28: Summary of the coupling observed in the ¹H-¹H COSY experiment for **2**

H	δ_{H} , ppm	Coupling observed with
H ¹	9.59	7.03 (H ²)
H ²	7.03	9.59 (H ¹), 7.71 (H ³)
H ³	7.71	7.48 (H ⁴), 7.03 (H ²)
H ⁴	7.48	7.71 (H ³)
H ⁵	7.22	6.81 (H ⁶)
H ⁶	6.81	7.22 (H ⁵), 2.15 (H ⁷)
H ⁷	2.15	6.81 (H ⁶)
H ⁹	9.24	7.34 (H ¹⁰)
H ¹⁰	7.34	9.24 (H ⁹), 7.93 (H ¹¹)
H ¹¹	7.93	7.61 (H ¹²), 7.34 (H ¹⁰)
H ¹²	7.61	7.99 (H ¹³)
H ¹³	7.99	7.13 (H ¹⁴)
H ¹⁴	7.13	7.99 (H ¹³), 2.27 (H ¹⁵)
H ¹⁵	2.27	7.13 (H ¹⁴)



$^{13}\text{C}\{^1\text{H}\}$ -NMR δ_{C} (100.5 MHz, CDCl_3): 167.32 (q, C^5), 162.43 (q, C^{17}), 154.41 (C^{13}), 151.17 (C^1), 141.62 (q, C^6), 141.08 (q, C^{12}), 139.88 (q, C^9), 139.27 (q, C^{21}), 138.30 (C^{16} , $^3J_{\text{CPt}} = 34$ Hz), 137.60 (C^{15}), 137.23 (q, C^{18} , $^3J_{\text{CPt}} = 28$ Hz), 131.71 (C^{11}), 129.37 (C^{19} , $^4J_{\text{CPt}} = 36$ Hz), 128.73 (C^{20}), 127.30 (C^3), 123.92 (C^8), 123.57 (C^{14}), 123.10 (C^7), 121.19 (C^2), 117.73 (C^4), 21.90 (C^{10}), 21.48 (C^{22}).

$^{13}\text{C}\{^1\text{H}\}$ -NMR δ_{C} (75.4 MHz, CDCl_3): 167.36 (C^2 , q, $^3J_{\text{CPt}} = 108$ Hz), 162.47 (C^{17} , q), 154.45 (C^{13}), 151.19 (C^1 , $^2J_{\text{CPt}} = 19$ Hz), 141.68 (C^6 , q, $^2J_{\text{CPt}} = 59$ Hz), 141.13 (C^{12} , q, $^1J_{\text{CPt}} = 1139$ Hz), 139.90 (C^9 , q, $^3J_{\text{CPt}} = 57$ Hz), 139.31 (C^{21} , q), 138.30 (C^{16}), 137.64 (C^{15}), 137.31 (C^{18} , q, $^3J_{\text{CPt}} = 25$ Hz), 131.75 (C^{11} , $^2J_{\text{CPt}} = 60$ Hz), 129.44 (C^{19}), 128.77 (C^{20}), 127.34 (C^3 , $^4J_{\text{CPt}} = 34$ Hz), 123.97 (C^8), 123.60 (C^{14}), 123.20 (C^7 , $^3J_{\text{CPt}} = 47$ Hz), 121.20 (C^2 , $^3J_{\text{CPt}} = 35$ Hz), 117.79 (C^4 , $^3J_{\text{CPt}} = 44$ Hz), 21.94 (C^{10}), 21.51 (C^{22}).

Table 29: Summary of the coupling was observed in the HMQC spectra for **2**

^{13}C	δ , ppm	Couples to protons, δ , ppm
C^1	151.17	9.59 (H^1)
C^2	121.19	7.03 (H^2)
C^3	138.30	7.71 (H^3)
C^4	117.73	7.48 (H^4)
C^7	123.10	7.22 (H^5)
C^8	123.92	6.81 (H^6)
C^{10}	21.90	2.15 (H^7)
C^{11}	131.71	6.01 (H^8)
C^{13}	154.41	9.24 (H^9)
C^{14}	123.57	7.34 (H^{10})
C^{15}	137.60	7.93 (H^{11})
C^{16}	127.30	7.61 (H^{12})

¹³ C	δ , ppm	Couples to protons, δ , ppm
C ¹⁹	129.37	7.99 (H ¹³)
C ²⁰	128.73	7.13 (H ¹⁴)
C ²²	21.48	2.27 (H ¹⁵)

Table 30: Summary of the coupling was observed in the HMBC spectra for **2**

¹³ C	¹³ C δ , ppm	Couples to protons, δ , ppm
C ⁵	167.32	9.59 (H ¹), 7.71 (H ³), 7.48 (H ⁴) and 7.22 (H ⁵)
C ¹⁷	162.43	9.24 (H ⁹), 7.99 (H ¹³) and 7.93 (H ¹¹)
C ⁶	141.62	6.81 (H ⁶) and 6.01 (H ⁸)
C ⁹	139.88	7.22 (H ⁵) and 2.15 (H ⁷)
C ¹⁸	137.23	2.27 (H ¹⁵) and 7.13 (H ¹⁴)
C ²¹	139.27	7.99 (H ¹³) and 2.27 (H ¹⁵)

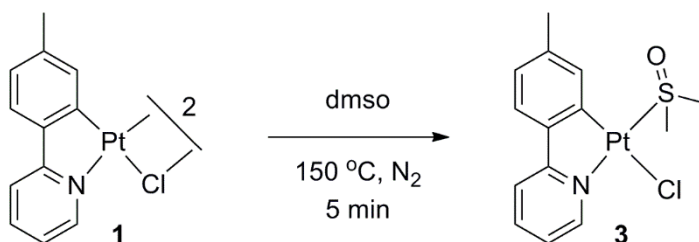
¹⁵N-NMR δ_N (51 MHz, CDCl₃): 206 (C^N tolpy) coupled to H¹, H⁴ and H², 222 (H-tolpy) coupled to protons at H⁹, H¹² and H¹⁰.

¹⁹⁵Pt{¹H}-NMR δ_{Pt} (107 MHz, CDCl₃): -3195 ppm.

FT-IR (ATR, $\bar{\nu}$ max, cm⁻¹) selected bands: 520, 257 (Pt-Cl), 243.

Structure confirmed by single-crystal X-ray crystallography see appendix I.

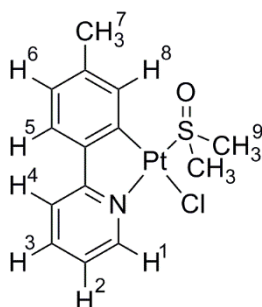
Synthesis of [Pt(tolpy)Cl(S-dmsO)] (3) from [Pt(tolpy)Cl]₂ (1)



A solution of [Pt(tolpy)(μ Cl)]₂ (**1**) (0.1442 mmol, 115.0 mg) in dmsO (24 ml) was heated to 150 °C with stirring for 5 min under an atmosphere of dry nitrogen. The mixture was cooled to room temperature and water (11.5 ml) was added, affording a yellow precipitate. After collecting by filtration and washing successively with water (2 x 2.5 ml) and ethanol (1 ml), the title compound was obtained as a yellow solid and dried *in vacuo*.

Yield 90 mg (66%).

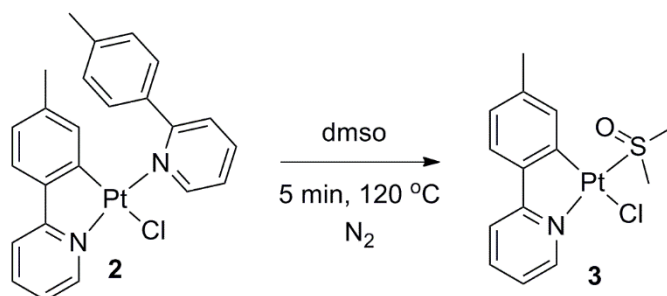
CHN data for C₁₄H₁₆ClNOPS found (expected)/%: C 34.82 (35.26), H 3.26 (3.38), N 2.68 (2.94).



¹H-NMR δ_{H} (400 MHz, CDCl₃): 9.52 (1H¹, d, ³J_{HH} = 5.5 Hz, ³J_{HPt} = 36 Hz), 8.11 (1H⁸, s, ³J_{HPt} = 48 Hz), 7.77 (1H³, t, ³J_{HH} = 7.9 Hz), 7.62 (1H⁴, d, ³J_{HH} = 8.0 Hz), 7.34 (1H⁵, d, ³J_{HH} = 8.0 Hz), 7.13 (1H², t, ³J_{HH} = 5.6 Hz), 6.93 (1H⁶, d, ³J_{HH} = 7.6 Hz), 3.58 (6H⁹, s, ³J_{HPt} = 23 Hz), 2.33 (3H⁷, s).

FT-IR (ATR, $\bar{\nu}$ max, cm⁻¹) selected bands: 2924, 2855, 1118 (S=O), 264 (Pt–Cl).

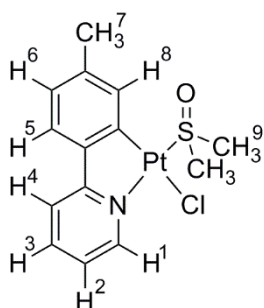
Synthesis of [Pt(tolpy)Cl(S-dmsO)] (3) from [Pt(tolpy)Cl(H-tolpy)] (2)



A solution of [Pt(tolpy)Cl(H-tolpy)] (2) (0.2016 mmol, 114.51 mg) in dmsO (6 ml) was heated to 150 °C with stirring for 5 min under an atmosphere of dry nitrogen. Formation of Pt⁰ *via* decomposition of the platinum complex was observed from the start of the reaction. The mixture was filtered twice through a Celite™ pad to remove the Pt⁰ and afford a yellow solution. Water (12 ml) was added to this solution, affording a yellow precipitate. After collecting by filtration and washing successively with water (1 ml), ethanol (1 ml) and diethyl ether (3 x 1 ml), the title compound was obtained as a yellow solid.

Yield 38 mg (40%).

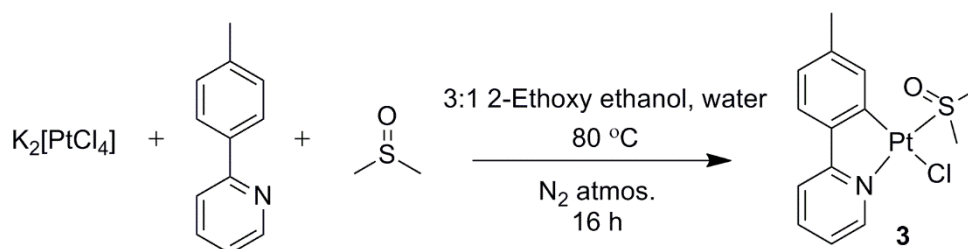
CHN data for C₁₄H₁₆ClNOPS found (expected)%: C 34.78 (35.26), H 3.13 (3.38), N 2.60 (2.94).



¹H-NMR δ_H (400 MHz, CDCl₃): 9.52 (1H¹, d, ³J_{HH} = 5.5 Hz, ³J_{HPt} = 36 Hz), 8.11 (1H⁸, s, ³J_{HPt} = 48 Hz), 7.77 (1H³, t, ³J_{HH} = 7.9 Hz), 7.62 (1H⁴, d, ³J_{HH} = 8.0 Hz), 7.34 (1H⁵, d, ³J_{HH} = 8.0 Hz), 7.13 (1H², t, ³J_{HH} = 5.6 Hz), 6.93 (1H⁶, d, ³J_{HH} = 7.6 Hz), 3.58 (6H⁹, s, ³J_{HPt} = 23 Hz), 2.33 (3H⁷, s).

FT-IR (ATR, ν̄ max, cm⁻¹) selected bands: 2924, 2855, 1118 (S=O), 264 (Pt-Cl).

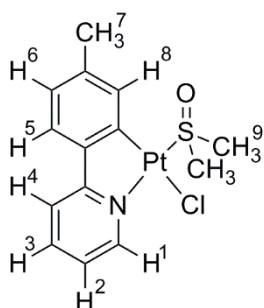
Synthesis of [Pt(tolpy)Cl(S-dms)] (3) from K₂[PtCl₄]



An outgassed solution of K₂[PtCl₄] (618.9 μmol, 256.9 mg) in water (1.5 ml) was added to an outgassed solution of 2-(4-tolyl)pyridine (0.585 mmol, 0.1 ml) and dms (1.408 mmol, 0.1 ml) in 2-ethoxyethanol and water (3:1, 30 ml) and heated to 80 °C with stirring for 16 h under an atmosphere of nitrogen. Water was added (75 ml) yielding a yellow precipitate, which was recovered by filtration. The filtrate was then washed successively with water (2 x 5 ml) and dried *in vacuo*, affording the title compound as a pale yellow solid. A single crystal suitable for X-ray diffraction was obtained by layering a concentrated solution of the title compound in CH₂Cl₂ with hexane in a Durham tube.

Yield 234 mg (84%).

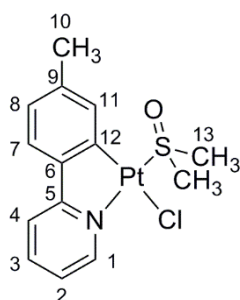
CHN data for C₁₄H₁₆ClNOPtS found (expected)/%: C 35.66 (35.26), H 3.27 (3.38), N 2.85 (2.94).



¹H-NMR δ_H (400 MHz, CDCl₃): 9.59 (1H¹, d, ³J_{HH} = 6.0 Hz, ³J_{HPt} = 34 Hz), 8.18 (1H⁸, s, ³J_{HPt} = 46 Hz), 7.84 (1H³, td, ³J_{HH} = 8 Hz, ⁴J_{HH} = 1.2 Hz), 7.69 (1H⁴, d, ³J_{HH} = 8 Hz), 7.41 (1H⁵, d, ³J_{HH} = 7.6 Hz), 7.20 (1H², td, ³J_{HH} = 7.2 Hz, ⁴J_{HH} = 1.2 Hz), 7.00 (1H⁶, d, ³J_{HH} = 8 Hz), 3.64 (6H⁹, s, ³J_{HPt} = 23 Hz), 2.39 (3H⁷, s).

Table 31: Summary of the coupling observed in the ^1H - ^1H COSY experiment for **3**

H	δ_{H} , ppm	Coupling observed with
H ¹	9.59	7.20 (H ²)
H ²	7.20	9.69 (H ⁴), 7.84 (H ³)
H ³	7.84	7.20 (H ²)
H ⁴	7.69	7.20 (H ²)
H ⁵	7.41	7.00 (H ⁶)
H ⁶	7.00	7.41 (H ⁵), 2.39 (H ⁷)
H ⁷	2.39	8.18 (H ⁸), 7.00 (H ⁶)
H ⁸	8.18	7.00 (H ⁶), 2.39 (H ⁷)



$^{13}\text{C}\{^1\text{H}\}$ -NMR δ_{C} (100.5 MHz, CDCl_3): 166.15 (q, C⁵), 149.96 (C¹), 141.74 (q, C⁶), 141.40 (q, C⁹), 140.30 (C³), 140.00 (q, C¹²), 134.80 (C¹¹, $^2J_{\text{CPt}} = 50$ Hz), 126.15 (C⁸), 123.81 (C⁷, $^3J_{\text{CPt}} = 44$ Hz), 121.40 (C², $^3J_{\text{CPt}} = 29$ Hz), 118.35 (C⁴, $^3J_{\text{CPt}} = 39$ Hz), 47.31 (C¹³, $^2J_{\text{CPt}} = 60$ Hz), 22.29 (C¹⁰).

$^{13}\text{C}\{^1\text{H}\}$ -NMR δ_{C} (75.4 MHz, CDCl_3): 166.31 (C⁵, $^1J_{\text{CPt}} = 100$ Hz), 150.07 (C¹, $^2J_{\text{CPt}} = 26$ Hz), 141.85 (C⁶, $^2J_{\text{CPt}} = 42$ Hz), 141.52 (C⁹, $^3J_{\text{CPt}} = 56$ Hz), 140.35 (C³), 140.20 (C¹², $^1J_{\text{CPt}} = 1063$ Hz), 134.92 (C¹¹, $^2J_{\text{CPt}} = 54$ Hz), 126.23 (C⁸), 123.87 (C⁷, $^3J_{\text{CPt}} = 44$ Hz), 121.45 (C², $^3J_{\text{CPt}} = 32$ Hz), 118.40 (C⁴, $^3J_{\text{CPt}} = 39$ Hz), 47.40 (C¹³, $^2J_{\text{CPt}} = 60$ Hz), 22.34 (C¹⁰).

DEPT-135 (CDCl_3): 149.98, 140.30, 134.81, 126.17, 123.83, 121.43, 118.37, 47.31, 22.30 (all signals were positive, CH or CH₃)

Table 32: Summary of the coupling was observed in the HMQC spectra for **3**

¹³ C	δ , ppm	Couples to protons, δ , ppm
C ¹	149.96	9.59 (H ¹)
C ²	121.40	7.20 (H ²)
C ³	140.30	7.84 (H ³)
C ⁴	118.35	7.69 (H ⁴)
C ⁷	123.81	7.49 (H ⁵)
C ⁸	126.15	7.00 (H ⁶)
C ¹⁰	22.29	2.39 (H ⁷)
C ¹¹	134.80	8.78 (H ⁸)
C ¹³	47.31	3.64 (H ⁹)

Table 33: Summary of the coupling was observed in the HMBC spectra for **3**

¹³ C	δ_c , ppm	Couples to protons, δ_H , ppm
C ¹	149.96	7.84 (H ³)
C ²	121.40	9.59 (H ¹), 7.69 (H ⁴)
C ³	140.30	9.59 (H ¹), 7.20 (H ²)
C ⁴	118.35	7.20 (H ²)
C ⁵	166.15	9.59 (H ¹), 7.85 (H ³), 7.69 (H ⁴), 7.41 (H ⁵)
C ⁶	141.74	8.18 (H ⁸), 7.00 (H ⁶)
C ⁹	141.40	7.41 (H ⁵), 2.39 (H ⁷)
C ⁸	126.15	8.18 (H ⁸), 2.39 (H ⁷)
C ¹⁰	22.29	8.18 (H ⁸), 7.00 (H ⁶)
C ¹¹	134.80	7.00 (H ⁶), 2.39 (H ⁷)
C ¹³	47.31	3.64 (H ⁹)

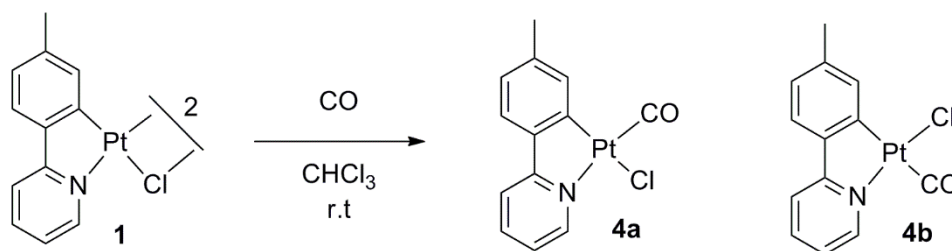
^{15}N -NMR δ_{N} (51 MHz, CDCl_3): 222 ppm coupled to H^1 , H^4 and H^2 .

$^{195}\text{Pt}\{^1\text{H}\}$ -NMR δ_{Pt} (107 MHz, CDCl_3): -3816 ppm.

FT-IR (ATR, $\bar{\nu}$ max, cm^{-1}) selected bands: 2924, 2855, 1118 (S=O), 264 (Pt-Cl).

Structure confirmed by single-crystal X-ray crystallography, see Appendix I.

Synthesis of [Pt(tolpy)Cl(CO)] (4) via Carbonylation of [Pt(tolpy)(μ -Cl)]₂ (1)



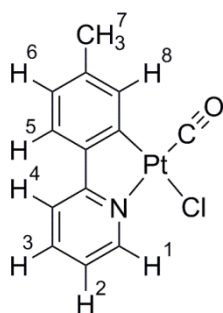
[Pt(tolpy)(μ -Cl)]₂ (**1**) (39.1 mg, 49.0 μ mol) was added to dry outgassed dichloromethane (20 ml) and carbon monoxide was bubbled through for 6 h. The precipitate was collected by filtration, crystallisation from chloroform and diethyl ether affording the title compound as a yellow solid.

Analytical data for **4a**:

Yield = 32 mg, 76%

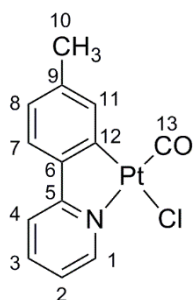
CHN data for C₁₃H₁₀ClOPt found (expected)/%: C 36.69 (36.50), H 2.25 (2.59), N 3.06 (3.27).

MS-ESI (*m/z*): [M⁺-Cl⁻] for [C₁₃H₁₀NOPt]⁺ found (expected) 391.0429 (391.0406).



¹H-NMR δ_{H} (400 MHz, CD₂Cl₂): 9.38 (1H¹, d, ³J_{HH} = 5.6 Hz, ³J_{HPt} = 32 Hz), 7.93 (1H², td, ³J_{HH} = 8 Hz, ⁴J_{HH} = 1.6 Hz), 7.75 (1H⁴, d, ³J_{HH} = 8 Hz), 7.50 (1H⁵, d, ³J_{HH} = 8.0 Hz), 7.33 (1H³, td, ³J_{HH} = 7.6 Hz, ⁴J_{HH} = 1.2 Hz), 7.31 (1H⁸, s, ³J_{HPt} = 70.4 Hz), 7.06 (1H⁶, d, ³J_{HH} = 8.4 Hz), 2.34 (3H⁷, s).

¹H-NMR δ_{H} (500 MHz, CDCl₃): 9.46 (1H¹, d, ³J_{HH} = 5.9 Hz, ³J_{HPt} = 32 Hz), 7.93 (1H³, td, ³J_{HH} = 7.8 Hz, ⁴J_{HH} = 1.6 Hz), 7.73 (1H⁴, d, ³J_{HH} = 7.9 Hz), 7.47 (1H⁵, d, ³J_{HH} = 7.6 Hz), 7.32 (1H², td, ³J_{HH} = 6.7 Hz, ⁴J_{HH} = 1.2 Hz), 7.30 (1H⁸, s, ³J_{HPt} = 70.1 Hz), 7.05 (1H⁶, d, ³J_{HH} = 7.7 Hz), 2.37 (3H⁷, s).



$^{13}\text{C}\{^1\text{H}\}$ -NMR δ_{C} (100.5 MHz, CD_2Cl_2): 148.36 (C^1), 143.12 (C^6), 142.00 (C^{12}), 141.71 (C^9), 140.73 (C^3), 137.39 (C^{11}), 126.75 (C^8), 124.54 (C^7), 122.23 (C^2), 119.00 (C^4), 21.38 (C^{10}).

C^5 and C^{13} were not observed.

^{13}C - ^1H HMBC-NMR δ_{C} (125.75 MHz, CDCl_3): 184.88 (C^{13}), 166.75 (C^5), 148.55 (C^1), 143.03 (C^6 , $^3J_{\text{CPt}} = 67$ Hz), 141.88 (C^{12}), 141.39 (C^9), 140.49 (C^3), 137.34 (C^{11} , $^2J_{\text{CPt}} = 108$ Hz), 126.71 (C^8), 124.47 (C^7), 121.97 (C^2), 118.88 (C^4), 21.60 (C^{10}).

$^{13}\text{C}\{^1\text{H}\}$ -NMR δ_{C} (75.4 MHz, CDCl_3): 166.77 (C^5 , q, $^2J_{\text{CPt}} = 94$ Hz), 165.41 (C^{13}), 148.81 (C^1 , $^2J_{\text{CPt}} = 24$ Hz), 143.18 (C^6 , $^3J_{\text{CPt}} = 69$ Hz), 142.10 (C^{12} , $^1J_{\text{CPt}} = 938$ Hz), 141.54 (C^9), 140.68 (C^3), 137.52 (C^{11} , $^2J_{\text{CPt}} = 108$ Hz), 126.94 (C^8), 124.67 (C^7 , $^3J_{\text{CPt}} = 38$ Hz), 122.10 (C^2 , $^3J_{\text{CPt}} = 30$ Hz), 118.93 (C^4 , $^3J_{\text{CPt}} = 38$ Hz), 21.81 (C^{10}).

^{15}N -NMR δ_{N} (51 MHz, CDCl_3): 226 coupled to protons at H^1 , H^4 and H^2 ppm.

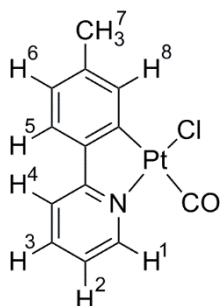
$^{195}\text{Pt}\{^1\text{H}\}$ -NMR δ_{Pt} (107 MHz, CDCl_3): -3947 ppm.

FT-IR (ATR, $\bar{\nu}$ max, cm^{-1}) selected bands: 2098 ($\text{C}=\text{O}$), 297 ($\text{Pt}-\text{Cl}$).

Structure confirmed by single-crystal X-ray crystallography, see Appendix I. A crystal suitable for X-ray crystallography was grown from chloroform by slow evaporation.

Analytical data for 4b:

Yield = 4 mg, 10%

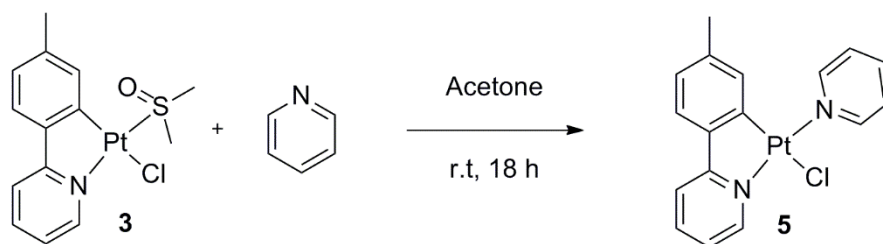


$^1\text{H-NMR}$ δ_{H} (400 MHz, CHCl_3): 9.47 (1H¹, dd, $^3J_{\text{HH}} = 5$ Hz, $^4J_{\text{HH}} = 1$ Hz $^3J_{\text{HPt}} = 32$ Hz), 7.93 (1H², td, $^3J_{\text{HH}} = 8$ Hz, $^4J_{\text{HH}} = 2$ Hz), 7.74 (1H⁴, d, $^3J_{\text{HH}} = 8$ Hz), 7.48 (1H⁵, d, $^3J_{\text{HH}} = 8$ Hz), 7.35-7.30 (m, 1H³ and 1H⁸), 7.06 (1H⁶, d, $^3J_{\text{HH}} = 8$ Hz), 2.37 (3H⁷,s).

FT-IR (ATR, $\bar{\nu}$ max, cm^{-1}) selected bands: 2013 (C=O),

Structure confirmed by single-crystal X-ray crystallography see appendix I. A suitable crystal was obtained by vapour diffusion from chloroform and diethyl ether.

Synthesis of [Pt(tolpy)Cl(py)] (5)

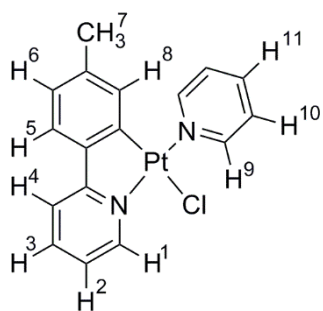


Pyridine (0.25 ml 3.15 mmol) was added to a solution of [Pt(tolpy)Cl(S-dms)] (**3**) (150 mg, 0.313 mmol) in acetone (10 ml) and stirred for 18 h. The pyridine and solvent were removed *in vacuo* and the precipitate washed with diethyl ether affording the title compound as a yellow solid.

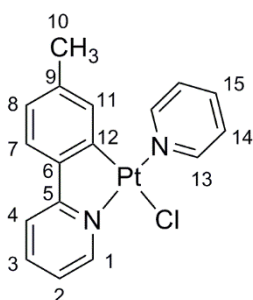
Yield: 87 mg, 58%

CHN data for $C_{17}H_{15}ClN_2Pt$ found (expected) %: C 42.90 (42.72), H 3.18 (3.16), N 5.72 (5.86).

MS-ESI (m/z): [M - Cl] for $[C_{17}H_{15}N_2Pt]^+$ found (expected) 441.0886 (442.0879).



1H -NMR δ_H (400 MHz, $CDCl_3$): 9.65 (1H¹, d, $^3J_{HH} = 6.8$ Hz, $^3J_{HPt} = 36$ Hz), 9.00 (2H¹¹, d, $^3J_{HH} = 6.4$ Hz, $^3J_{HPt} = 42$ Hz), 7.90 (1H⁹, tt, $^3J_{HH} = 7.6$, $^4J_{HH} = 1.2$ Hz), 7.78 (1H³, td, $^3J_{HH} = 8.0$ Hz, $^4J_{HH} = 1.6$ Hz), 7.59 (1H⁴, d, $^3J_{HH} = 7.6$ Hz), 7.44 (2H¹⁰, td, $^3J_{HH} = 6.4$ Hz, $^4J_{HH} = 1.2$ Hz), 7.36 (1H⁵, d, $^3J_{HH} = 7.6$ Hz), 7.09 (1H², td, $^3J_{HH} = 7.2$ Hz, $^4J_{HH} = 1.2$ Hz), 6.91 (1H⁶, d, $^3J_{HH} = 7.6$ Hz), 6.13 (1H⁸, s, $^3J_{HPt} = 48$ Hz), 2.20 (3H⁷, s).



$^{13}C\{^1H\}$ -NMR δ_C (100.5 MHz, $CDCl_3$): 167.39 (C⁵, q), 154.15 (C¹⁵, $^4J_{CPt} = 11$ Hz), 151.16 (C¹), 142.18 (C⁶, q), 141.68 (C¹², q), 140.49 (C⁹, q), 138.85 (C³), 137.86 (C¹³), 131.88 (C¹¹, $^2J_{CPt} = 59$ Hz), 126.07 (C¹⁴, $^3J_{CPt} = 50$ Hz), 124.64 (C⁸), 123.68 (C⁷), 121.50 (C², $^3J_{CPt} = 34$ Hz), 117.99 (C⁴), 21.92 (C¹⁰).

$^{13}\text{C}\{^1\text{H}\}$ -NMR δ_{C} (75.4 MHz, CDCl_3): 167.51 (C^5 , q, $^2J_{\text{CPt}} = 103$ Hz), 154.24 (C^{15} , $^4J_{\text{CPt}} = 12$ Hz), 151.44 (C^1 , $^2J_{\text{CPt}} = 21$ Hz), 142.27 (C^6 , q, $^2J_{\text{CPt}} = 56$ Hz), 141.82 (C^{12} , q, $^1J_{\text{CPt}} = 1126$ Hz), 140.54 (C^9 , q, $^2J_{\text{CPt}} = 58$ Hz), 138.87 (C^3), 137.89 (C^{13} , $^2J_{\text{CPt}} = 58$ Hz), 131.66 (C^{11} , $^2J_{\text{CPt}} = 63$ Hz), 126.10 (C^{14} , $^3J_{\text{CPt}} = 51$ Hz), 124.68 (C^8), 123.73 (C^7 , $^3J_{\text{CPt}} = 45$ Hz), 121.54 (C^2 , $^3J_{\text{CPt}} = 33$ Hz), 118.03 (C^4 , $^3J_{\text{CPt}} = 44$ Hz), 21.92 (C^{10}).

Table 34: Summary of the coupling was observed in the HMQC spectra for **7**

^{13}C	δ , ppm	Couples to protons, δ , ppm
C^1	151.16	9.65 (H^1)
C^2	121.50	7.09 (H^2)
C^3	138.85	7.78 (H^3)
C^4	117.99	7.59 (H^4)
C^7	123.68	7.36 (H^5)
C^8	124.64	6.91 (H^6)
C^{10}	21.92	2.20 (H^7)
C^{11}	131.88	6.13 (H^8)
C^{13}	137.86	7.90 (H^9)
C^{14}	126.07	7.44 (H^{10})
C^{15}	154.15	9.00 (H^{11})

Table 35: Summary of the coupling was observed in the HMBC spectra for **5**

^{13}C δ , ppm	Couples to protons, δ , ppm
167.39	9.65 (H ¹), 7.78 (H ³), 7.59 (H ⁴) and 7.36 (H ⁵)
154.15	9.00 (H ¹¹), 7.90 (H ⁹) and 7.44 (H ¹⁰)
151.16	7.78 (H ³) and 7.09 (H ²)
142.18	7.36 (H ⁵), 6.91 (H ⁶), 6.13 (H ⁸)
140.49	7.59 (H ⁴) and 7.36 (H ⁵)
138.85	9.65 (H ₁)
137.86	9.00 (H ¹¹)
131.88	6.91 (H ⁶)
126.07	9.00 (H ¹¹) and 7.44 (H ¹⁰)
124.64	6.13 (H ⁸)
121.50	9.65 (H ¹) and 7.59 (H ⁴)
117.99	7.09 (H ²)
21.92	6.91 (H ⁶) and 6.13 (H ⁸)

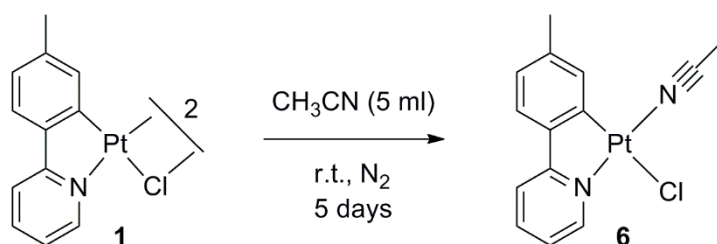
^{15}N -NMR δ_{N} (51 MHz, CDCl_3): 206 (C^N, toly, $^1J_{\text{NPt}} = 395$ Hz) coupled to protons at H¹, H² and H⁴, 221 (py, $^1J_{\text{NPt}} = 454$ Hz) coupled to protons at H¹¹ and H¹⁰.

$^{195}\text{Pt}\{^1\text{H}\}$ -NMR δ_{Pt} (107 MHz, CDCl_3): -3261 ppm.

FT-IR (ATR, $\bar{\nu}$ max, cm^{-1}) selected bands: 422, 304, 269, 252 (Pt-Cl).

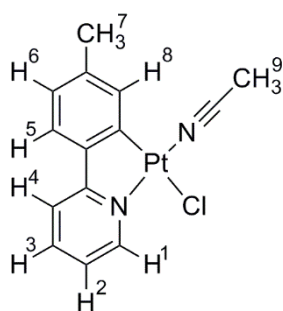
Structure confirmed by single-crystal X-ray crystallography see Appendix I, a suitable crystal was obtained by layering a solution of **5** in CDCl_3 with diethyl ether.

Synthesis of [Pt(tolpy)Cl(CH₃CN)] (6)



[Pt(tolpy)(μ -Cl)]₂ (**1**, 50 mg, 0.0627 mmol) and acetonitrile (5 ml) were stirred at room temperature under an atmosphere of nitrogen for 5 days. The solution was filtered through Celite™ after which the solvent was removed *in vacuo* to yield a yellow oil. The oil was then crystallised from dichloromethane and hexane to afford the title compound. ¹H NMR data was obtained by decomposition of the complex occurred before further analysis was possible.

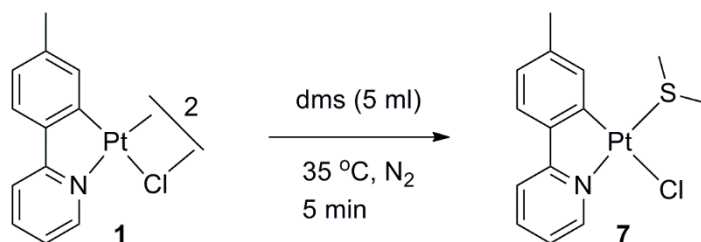
Yield: 21 mg, 38%



¹H-NMR δ_{H} (400 MHz, CDCl₃): 9.56 (1H¹, d, ³J_{HH} = 6 Hz, ³J_{HPt} = 45 Hz), 7.76 (1H³, td, ³J_{HH} = 8 Hz, ⁴J_{HH} = 1.6 Hz), 7.54 (1H⁴, d, ³J_{HH} = 7.6 Hz), 7.30 (1H⁵, d, ³J_{HH} = 7.6 Hz), 7.07 (2H, m, overlapping signals H² and H⁸), 6.93 (1H⁶, d, ³J_{HH} = 8.8 Hz), 2.57 (3H⁸, s, ⁴J_{HPt} = 12 Hz), 2.35 (3H⁷, s).

Due to the poor stability of complex **6**, it was not possible to obtain further analytical data.

Synthesis of [Pt(tolpy)Cl(dms)] (7)

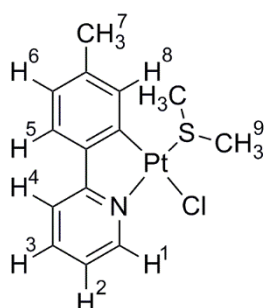


A solution of [Pt(tolpy)(μ -Cl)]₂ (**1**) (0.126 mmol, 100.0 mg) in dms (5 ml) was heated under reflux with stirring for 5 min under an atmosphere of dry nitrogen. The solution was cooled to room temperature and the dms was removed *in vacuo*. The residue was re-dissolved in CH₂Cl₂ (3 ml), filtered through Celite™, and then hexane (20 ml) was added, affording the yellow microcrystalline product. After collecting by filtration and washing successively with water (1 x 2.5 ml) and ethanol (1 ml), the title compound was obtained as a yellow crystalline solid.

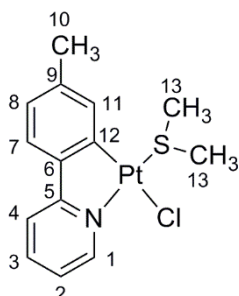
Yield = 77 mg, 66%

CHN data for C₁₄H₁₆ClNPtS found (expected)%: C 36.49 (36.49), H 3.48 (3.50), N 2.89 (3.04).

MS-ESI (*m/z*): [M⁺-Cl⁻] for [C₁₄H₁₆NPtS]⁺ found (expected) 425.0658 (425.0647).



¹H-NMR δ_{H} (400 MHz, CDCl₃): 9.65 (1H¹, d, ³J_{HH} = 6.0 Hz, ³J_{HPt} = 35 Hz), 7.79 (1H³, td, ³J_{HH} = 8.5 Hz, ⁴J_{HH} = 1.5 Hz), 7.63 (1H⁴, d, ³J_{HH} = 7.5 Hz), 7.44 (1H⁸, s, ³J_{HPt} = 52 Hz), 7.36 (1H⁵, d, ³J_{HH} = 7.5 Hz), 7.15 (1H², t, ³J_{HH} = 7.5 Hz), 6.95 (1H⁶, d, ³J_{HH} = 7.0 Hz), 2.77 (6H⁹, s, ³J_{HPt} = 52.5 Hz), 2.36 (3H⁷, s).



¹³C{¹H}-NMR δ_{C} (100.5 MHz, CDCl₃): 166.50 (C⁵, q), 150.12 (C¹, ²J_{CPt} = 25 Hz), 142.30 (C⁶, q), 140.65 (C⁹, q, ¹J_{CPt} = 57 Hz), 139.73 (C¹², q), 139.47 (C³), 131.94 (C¹¹, ²J_{CPt} = 65 Hz), 125.27 (C⁸), 124.16 (C⁷, ³J_{CPt} = 41 Hz), 121.67 (C², ³J_{CPt} = 33 Hz), 118.21 (C⁴, ³J_{CPt} = 41 Hz), 23.50 (C¹³, ²J_{CPt} = 31 Hz), 21.99 (C¹⁰)

$^{13}\text{C}\{^1\text{H}\}$ -NMR δ_{C} (75.4 MHz, CDCl_3): 166.52 (C^5 , q, $^2J_{\text{Cpt}} = 100$ Hz), 150.09 (C^1 , $^2J_{\text{Cpt}} = 24$ Hz), 142.30 (C^6 , q, $^2J_{\text{Cpt}} = 42$ Hz), 140.61 (C^9 , q, $^3J_{\text{Cpt}} = 56$ Hz), 139.76 (C^{12} , q, $^1J_{\text{Cpt}} = 1044$ Hz), 139.45 (C^3 , $^4J_{\text{Cpt}} = 7$ Hz), 131.92 (C^{11} , $^2J_{\text{Cpt}} = 64$ Hz), 125.25 (C^8), 124.15 (C^7 , $^3J_{\text{Cpt}} = 42$ Hz), 121.63 (C^2 , $^3J_{\text{Cpt}} = 33$ Hz), 118.20 (C^4 , $^3J_{\text{Cpt}} = 42$ Hz), 23.49 (C^{13} , $^2J_{\text{Cpt}} = 23$ Hz), 22.00 (C^{10})

Table 36: Summary of the coupling was observed in the HMQC spectra for **7**

^{13}C	δ , ppm	Couples to protons, δ , ppm
C^1	151.12	9.65 (H^1)
C^2	121.67	7.15 (H^2)
C^3	139.47	7.79 (H^3)
C^4	118.21	7.63 (H^4)
C^7	124.16	7.36 (H^5)
C^8	125.27	6.95 (H^6)
C^{10}	21.99	2.36 (H^7)
C^{11}	131.94	7.44 (H^8)
C^{13}	23.50	2.77 (H^9)

Table 37: Summary of the coupling was observed in the HMBC spectra for **5**

^{13}C δ , ppm	Couples to protons, δ , ppm
166.50	9.65 (H ¹), 7.79 (H ³), 7.63 (H ⁴) and 7.36 (H ⁵)
150.12	7.79 (H ³) and 7.15 (H ²);
142.30	6.95 (H ⁶) and 7.44 (H ⁸);
140.65	7.36 (H ⁵) and 2.36 (H ⁷)
139.47	9.65 (H ¹)
131.94	6.95 (H ⁶) and 2.36 (H ⁷)
125.27	7.44 (H ⁸) and 2.36 (H ⁷)
121.67	9.65 (H ¹) and 7.63 (H ⁴)
118.21	7.15 (H ²)
23.5	2.77 (H ⁹)
21.99	7.44 (H ⁸), 6.95 (H ⁶) and 2.36 (H ⁷).

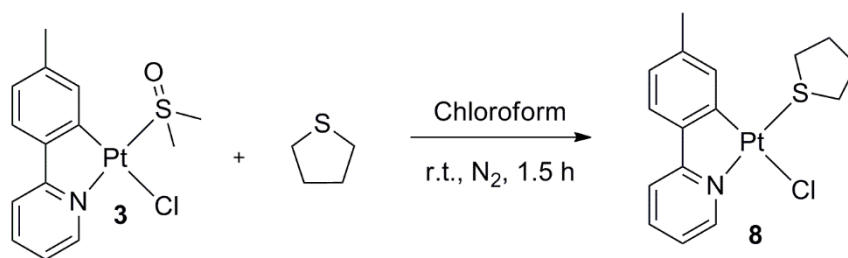
^{15}N -NMR δ_{N} (51 MHz, CDCl_3): 224 ($^1J_{\text{NPt}} = 426$ Hz) coupled to protons at H¹, H⁴ and H⁹ ppm.

$^{195}\text{Pt}\{^1\text{H}\}$ -NMR δ_{Pt} (107 MHz, CDCl_3): -3858 ppm.

FT-IR (ATR, $\bar{\nu}$ max, cm^{-1}) selected bands: 261 (Pt-Cl).

Structure confirmed by single-crystal X-ray crystallography, see Appendix I.

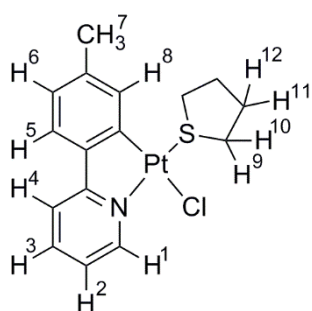
Synthesis of [Pt(tolpy)Cl(tht)] (8)



Prepared under supervision by Alice Mcellin, undergraduate summer project student, 2015. [Pt(tolpy)Cl(S-dmsO)] (91.2 mg, 0.191 mmol) and tetrahydrothiophene (0.2 ml, 2.268 mmol) was stirred for 1.5 hours in chloroform (10 ml) under an atmosphere of dry nitrogen. The solvent was removed *in vacuo* and the resulting precipitate was washed with successively ice cold water, ice cold ethanol (2 x 1 ml) and ice cold diethyl ether (2 x 1 ml) giving the title compound as a yellow solid.

Yield: 33 mg, 28%

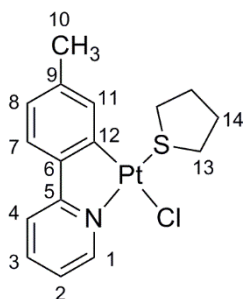
CHN data for C₁₆H₁₈ClNPtS found (expected)%: C 39.21 (39.47), H 3.89 (3.73), and N 2.53 (2.88)



¹H-NMR δ_{H} (500 MHz, CDCl₃): 9.68 (1H¹, dd, ³J_{HH} = 5.8 Hz, ⁴J_{HH} = 1.7 Hz, ³J_{HPt} = 38 Hz), 7.80 (1H³, td, ³J_{HH} = 7.4 Hz, ⁴J_{HH} = 1.66 Hz), 7.64 (1H⁴, d, ³J_{HH} = 8.2 Hz), 7.50 (1H⁸, s, ³J_{HPt} = 51 Hz), 7.38 (1H⁵, d, ³J_{HH} = 7.85 Hz), 7.17 (1H², td, ³J_{HH} = 5.93 Hz, ⁴J_{HH} = 1.5 Hz), 6.96 (1H⁶, d, ³J_{HH} = 7.76 Hz), 3.87 (2H⁹, s, br, ³J_{HPt} = 69 Hz), 3.13 (2H¹⁰, s, br, ³J_{HPt} = 53 Hz), 2.45 (2H¹¹ or H¹², s, br), 2.38 (3H⁷, s), 2.05 (2H¹¹ or H¹², s, br).

Table 38: Summary of the coupling observed in the ^1H - ^1H COSY experiment for **8**

H	δ_{H} , ppm	Coupling observed with
H ¹	9.68	7.17 (H ²)
H ²	7.17	9.68 (H ¹), 7.80 (H ³)
H ³	7.80	7.17 (H ²)
H ⁵	7.38	6.96 (H ⁶)
H ⁶	6.96	7.38 (H ⁵)
H ⁷	2.38	7.50 (H ⁸)
H ⁸	7.50	6.96 (H ⁶), 2.38 (H ⁷)
H ⁹	3.87	3.13 (H ¹⁰)
H ¹⁰	3.13	3.87 (H ⁹), 2.05 (H ¹¹ or H ¹²)
H ¹¹ or H ¹²	2.05	2.45 (H ¹¹ or H ¹²)
H ¹¹ or H ¹²	2.45	2.05 (H ¹¹ or H ¹²)



$^{13}\text{C}\{^1\text{H}\}$ NMR δ_{C} (100.5 MHz, CDCl_3): 166.55 (C⁵, q), 150.05 (C¹, $^2J_{\text{CPt}} = 24$ Hz), 142.40 (C⁹, q), 140.59 (C⁶, q), 139.91 (C¹², q), 139.37 (C³), 132.52 (C¹¹, $^2J_{\text{CPt}} = 61$ Hz), 125.20 (C⁸), 124.14 (C⁷, $^3J_{\text{CPt}} = 41$ Hz), 121.70 (C², $^3J_{\text{CPt}} = 33$ Hz), 118.24 (C⁴, $^3J_{\text{CPt}} = 42$ Hz), 38.92 (C¹³, $^2J_{\text{CPt}} = 19$ Hz), 30.60 (C¹⁴, $^3J_{\text{CPt}} = 15$ Hz), 22.09 (C¹⁰).

$^{13}\text{C}\{^1\text{H}\}$ NMR δ_{C} (75.4 MHz, CDCl_3): 166.62 (C⁵, q, $^2J_{\text{CPt}} = 101$ Hz), 150.11 (C¹, $^2J_{\text{CPt}} = 25$ Hz), 142.42 (C⁹, q, $^3J_{\text{CPt}} = 42$ Hz), 140.58 (C⁶, q, $^3J_{\text{CPt}} = 55$ Hz), 139.98 (C¹², q, $^1J_{\text{CPt}} = 1050$ Hz), 139.31 (C³), 132.55 (C¹¹, $^2J_{\text{CPt}} = 63$ Hz), 125.19 (C⁸), 124.13 (C⁷, $^3J_{\text{CPt}} = 41$ Hz), 121.66 (C², $^3J_{\text{CPt}} = 33$ Hz), 118.14 (C⁴, $^3J_{\text{CPt}} = 42$ Hz), 38.89 (C¹³, $^2J_{\text{CPt}} = 20$ Hz), 30.57 (C¹⁴, $^3J_{\text{CPt}} = 16$ Hz), 22.05 (C¹⁰).

Table 39: Summary of the coupling was observed in the HMQC spectra of **8**

¹³ C	δ , ppm	Couples to protons, δ , ppm
C ¹	150.06	9.68 (H ¹)
C ²	121.70	7.17 (H ²)
C ³	139.37	7.80 (H ³)
C ⁴	118.24	7.64 (H ⁴)
C ⁷	124.14	7.38 (H ⁵)
C ⁸	125.20	6.96 (H ⁶)
C ¹⁰	22.09	2.38 (H ⁷)
C ¹¹	132.52	7.50 (H ⁸)
C ¹³	38.92	9.87 (H ⁹), 3.13 (H ¹⁰)
C ¹⁴	30.60	2.45 (H ¹¹ or H ¹²), 2.05 (H ¹¹ or H ¹²)

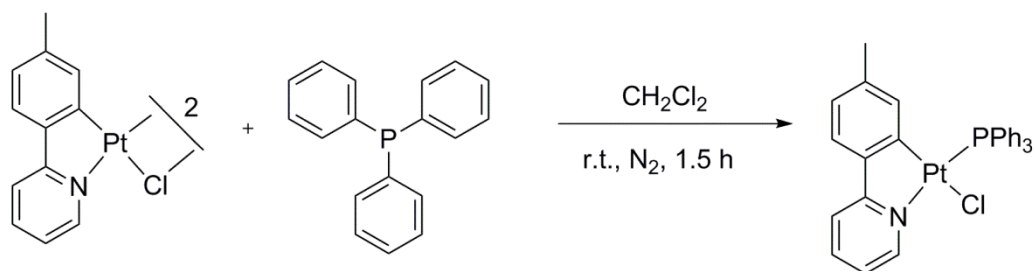
¹⁵N-NMR δ_N (51 MHz, CDCl₃): 225 coupled to protons at H¹, H⁴ and H².

¹⁹⁵Pt{¹H}-NMR δ_{Pt} (107 MHz, CDCl₃): -3799 ppm.

FT-IR (ATR, $\bar{\nu}$ max, cm⁻¹) selected bands: 269 (Pt–Cl).

Structure confirmed by single-crystal X-ray crystallography, see Appendix I. Suitable crystals were obtained by crystallisation from CDCl₃.

Synthesis of [Pt(tolpy)Cl(PPh₃)] (9)

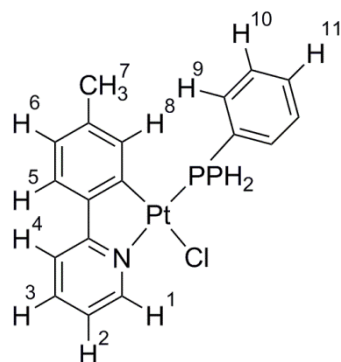


Prepared, under supervision, by Alice Mcellin, undergraduate summer project student, 2015. Triphenylphosphine (80.1 mg, 0.305 mmol) was added to a suspension of [Pt(tolpy)(μ -Cl)]₂ (1, 99.7 mg, 0.127 mmol) in dichloromethane (10 mL) and stirred at room temperature for 1.5 h under an atmosphere of nitrogen. The solvent was removed *in vacuo* and the yellow solid was washed with ice cold diethyl ether (1 x 1 ml). This was then crystallised from CH₂Cl₂ and methanol to afford the title compound as yellow green crystals.

Yield: 120 mg, 78%

CHN data for found (expected)%: 53.86 (54.51), H 3.78 (3.81), and N 1.93 (2.12)

MS-ESI (*m/z*): [M⁺-Cl⁻] for [C₃₀H₂₅NPt]⁺ found (expected) 625.1358(625.1370).



¹H-NMR δ_{H} (500 MHz, CDCl₃): δ 9.95 – 9.75 (1H¹, m/ddd, ³J_{HPt} = 27 Hz), 7.84 – 7.78 (1H³ and 7H⁹, m), 7.72 (1H⁴, d, ³J_{HH} = 8.5 Hz), 7.46 – 7.41 (3H¹¹, m), 7.41 – 7.35 (1H⁵ and 6H¹⁰, m), 7.24 (1H², tt, ³J_{HH} = 6 Hz, ⁴J_{HH} = 1.5 Hz), 6.76 (1H⁶, d, ³J_{HH} = 7.9 Hz), 6.45 (1H⁸, d, ³J_{HPt} = 56 Hz, ⁴J_{HP} = 3.5 Hz), 1.69 (3H⁷, s).

³¹P{¹H}-NMR δ_{P} (164.0 MHz, CDCl₃): 23.74 (s, ¹J_{PPt} = 4345 Hz).

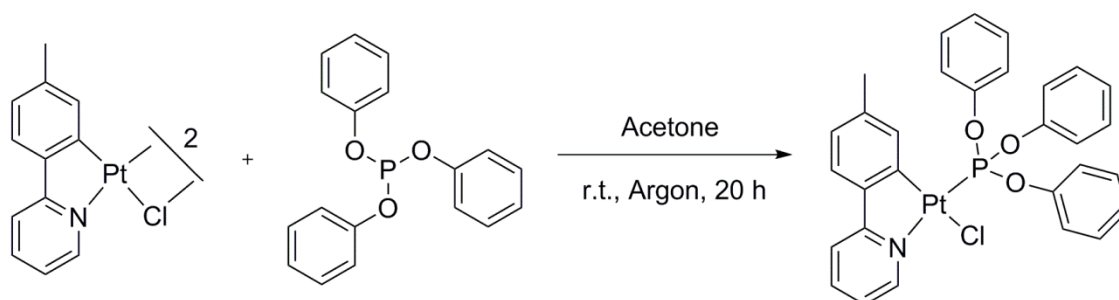
¹⁹⁵Pt{¹H}-NMR δ_{Pt} (107 MHz, CDCl₃): 4184 (d, ¹J_{PPt} = 4350 Hz)

Due to the low solubility of the complex it was not possible to record the ¹⁵N-NMR spectrum.

FT-IR (ATR, $\bar{\nu}$ max, cm⁻¹) selected bands: 295 (Pt–Cl), 274 (Pt–Cl).

Structure confirmed by single-crystal X-ray crystallography, see Appendix I. Suitable crystals were obtained by crystallisation from dichloromethane and methanol.

Synthesis of [Pt(tolpy)Cl(P(OPh)₃)] (10)

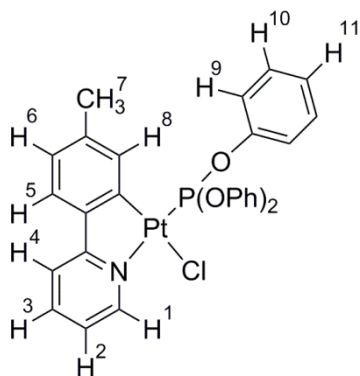


A solution of [Pt(tolpy)(μ -Cl)]₂ (**1**) (0.0756 mmol, 60.0 mg) and triphenyl phosphite (0.21 ml, 0.799 mmol) in acetone (10 ml) was stirred at room temperature for 20 h under an atmosphere of dry argon. The solution was filtered through Celite™ and then hexane was layered on top of the resulting yellow solution to afford the desired complex as a crystalline yellow solid.

Yield: 79 mg, 74%

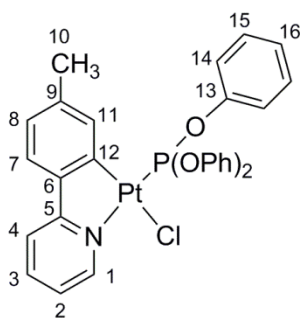
CHN data for found (expected) %: C 50.88 (50.82), H 3.59 (3.55), N 1.82 (1.98)

MS-ESI (m/z): [M⁺-Cl⁻] for [C₃₀H₂₅NO₃PPt]⁺ found (expected) 673.1198(673.1217).



¹H-NMR δ_{H} (400 MHz, CDCl₃): δ 9.61 (1H¹, td, ³J_{HPt} = 32 Hz), 7.80 (1H⁸, s, ³J_{HPt} = 62 Hz), 7.72 (1H³, td, ³J_{HH} = 7 Hz, ⁴J_{HH} = 1.6 Hz), 7.55 (1H⁴, d, ³J_{HH} = 8 Hz), 7.39 (6H⁹, d, ³J_{HH} = 8 Hz), 7.30 - 7.21 (m, overlap of 6H¹⁰ and 1H⁵), 7.16 (1H², td, ³J_{HH} = 6 Hz, ⁴J_{HH} = 1.6 Hz), 7.09 (3H¹¹, t, ³J_{HH} = 8 Hz), 6.85 (1H⁶, d, ³J_{HH} = 8 Hz), 2.30 (3H⁷, s).

¹H-NMR δ_{H} (500 MHz, CDCl₃): 9.66 (1H¹, dd, ³J_{HH}, ⁴J_{HH} = 1.1 Hz, ³J_{HPt} = 27 Hz), 7.83 (1H⁸, s, ³J_{HPt} = 59 Hz), 7.74 (1H³, td, ³J_{HH} = 8 Hz, ⁴J_{HH} = 1.6 Hz), 7.57 (1H⁴, d, ³J_{HH} = 8 Hz), 7.41 (6H⁹, d, AA'BB', ³J_{HH} = 8 Hz), 7.31 - 7.25 (m, overlap of 6H¹⁰ and 1H⁵), 7.18 (1H², td, ³J_{HH} = 6 Hz, ⁴J_{HH} = 1.5 Hz), 7.11 (3H¹¹, tt, ³J_{HH} = 8 Hz, ⁴J_{HH} = 1 Hz), 6.88 (1H⁶, d, ³J_{HH} = 8 Hz), 2.32 (3H⁷, s).



$^{13}\text{C}\{^1\text{H}\}$ -NMR δ_{C} (100.5 MHz, CDCl_3): 165.90 (C^5 , q), 151.16 (C^1 , d, $^3J_{\text{CP}} = 6$ Hz), 148.93 (C^{13} , q), 142.08 (C^7), 141.19 (C^{12} , q, d, $^2J_{\text{CP}} = 6$ Hz), 140.94 (C^6 , q, d, $^3J_{\text{CP}} = 2$ Hz), 140.06 (C^3), 137.68 (C^{11} , d, $^3J_{\text{CP}} = 6$ Hz), 129.8 (C^{15}), 125.18 (C^8), 125.07 (C^{16}), 123.92 (C^9 , q), 121.50 (C^2 , d, $^4J_{\text{CP}} = 6$ Hz), 120.75 (C^{14} , d, $^3J_{\text{CP}} = 6$ Hz), 118.16 (C^4 , d, $^4J_{\text{CP}} = 4$ Hz), 22.04 (C^{10}).

$^{13}\text{C}\{^1\text{H}\}$ -NMR δ_{C} (75.4 MHz, CDCl_3): 166.00 (C^5 , d, $^3J_{\text{CP}} = 4$ Hz, $^2J_{\text{CPt}} = 91$ Hz), 151.22 (C^1 , d, $^3J_{\text{CP}} = 6$ Hz), 148.92 (C^{13} , q, $^3J_{\text{CPt}} = 24$ Hz), 142.11 (C^7 , $^3J_{\text{CPt}} = 26$ Hz), 141.28 (C^{12} , d, $^2J_{\text{CP}} = 8$ Hz, $^1J_{\text{CPt}} = 1013$ Hz), 140.91 (C^6 , q, d, $^3J_{\text{CP}} = 2$ Hz), 140.04 (C^3), 137.72 (C^{11} , d, $^3J_{\text{CP}} = 6$ Hz, $^2J_{\text{CPt}} = 100$ Hz), 129.79 (C^{15}), 125.17 (C^8), 125.07 (C^{16}), 123.94 (C^9 , q, $^3J_{\text{CPt}} = 40$ Hz), 121.44 (C^2 , d, $^4J_{\text{CP}} = 6$ Hz, $^3J_{\text{CPt}} = 25$ Hz), 120.78 (C^{14} , d, $^3J_{\text{CP}} = 6$ Hz), 118.16 (C^4 , d, $^4J_{\text{CP}} = 4$ Hz, $^3J_{\text{CPt}} = 30$ Hz), 22.02 (C^{10}).

Table 40: Summary of the coupling was observed in the HMQC spectra for **10**

^{13}C	δ , ppm	Couples to protons, δ , ppm
C^1	151.16	9.61 (H^1)
C^2	121.50	7.16 (H^2)
C^3	140.06	7.74 (H^3)
C^4	118.16	7.55 (H^4)
C^7	142.08	7.72 (H^5)
C^8	129.8	6.85 (H^6)
C^{10}	22.04	2.30 (H^7)
C^{11}	137.68	7.80 (H^8)
C^{14}	120.75	7.39 (H^9)
C^{15}	129.8	7.25 (H^{10})
C^{16}	125.07	7.09 (H^{11})

^{15}N -NMR δ_{N} (51 MHz, CDCl_3): 237 ppm coupled to protons, H^1 , H^2 and H^4 .

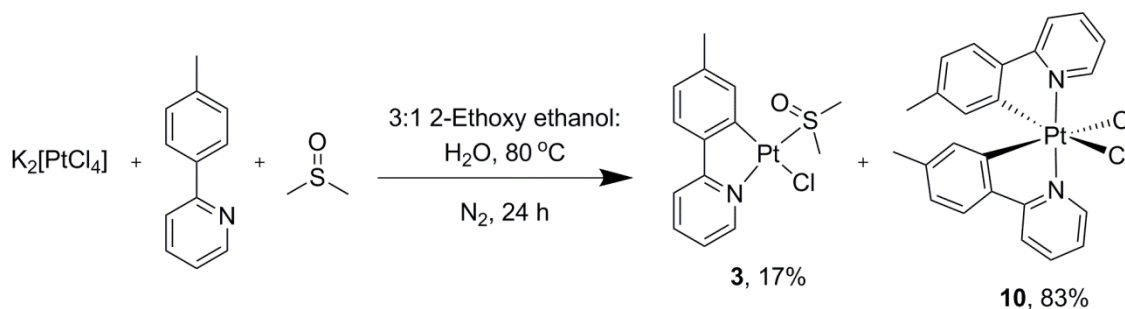
$^{31}\text{P}\{^1\text{H}\}$ -NMR δ_{P} (164.0 MHz, CDCl_3): 74.86 (s, $^1J_{\text{PPt}} = 7000$ Hz).

$^{195}\text{Pt}\{^1\text{H}\}$ -NMR δ_{Pt} (107 MHz, CDCl_3): -4148 (d, $^1J_{\text{PPt}} = 6980$ Hz)

FT-IR (ATR, $\bar{\nu}$ max, cm^{-1}) selected bands: 540, 421, 295 (Pt–Cl), 268 (Pt–Cl), 243

Structure confirmed by single-crystal X-ray crystallography, see Appendix I. Suitable crystals were obtained by crystallisation from acetone and hexane.

Synthesis of [Pt(IV)(tolpy)₂Cl₂] (11)



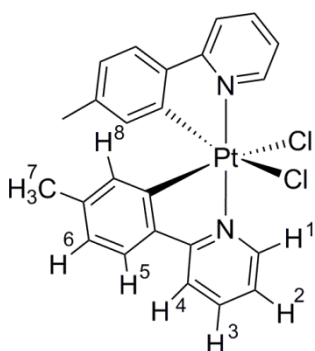
An outgassed solution of K₂[PtCl₄] (618.9 μmol, 256.9 mg) in water (1.5 ml) was added to an outgassed solution of 2-(4-tolyl)pyridine (1.17 mmol, 0.2 ml) and dmsO (1.408 mmol, 0.1 ml) in 2-ethoxyethanol and water (3:1, 30 ml) and heated to 80 °C, with stirring, for 24 h under an atmosphere of nitrogen. Water was added (75 ml) yielding a white precipitate, which was recovered by filtration. The filtrate was then washed successively with water (2 x 5 ml) and dried *in vacuo*, affording the title compound as a white solid.

Conversion: 83% by integration of the ¹H NMR spectrum

Yield: 149 mg, 40%

CHN data for C₂₄H₂₀Cl₂N₂Pt found (expected)%: C 47.61 (47.85), H 3.29 (3.35), N 4.55 (4.65)

MS-ESI (*m/z*): [MNa⁺] for [C₂₄H₂₀Cl₂N₂NaPt]⁺ found (expected) 624.0546 (624.0546).



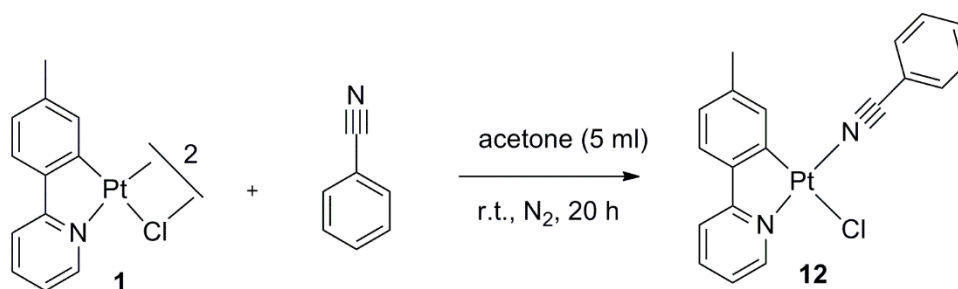
¹H-NMR δ_H (400 MHz, CDCl₃): 10.00 (2H¹, d, ³J_{HH} = 6.0 Hz, ³J_{HPt} = 29 Hz), 8.06 (2H³, td, ³J_{HH} = 7.6 Hz, ⁴J_{HH} = 1.2 Hz), 7.92 (2H⁴, d, ³J_{HH} = 8.0 Hz), 7.48 (2H⁵, d, ³J_{HH} = 8.0 Hz), 7.45 (2H², td, ³J_{HH} = 6.4 Hz, ⁴J_{HH} = 1.2 Hz), 6.92 (2H⁶, d, ³J_{HH} = 8.0 Hz), 5.83 (2H⁸, s, ³J_{HPt} = 33 Hz), 2.10 (6H⁷, s).

Due to the low solubility of the complex it was not possible to collect ¹³C{¹H}, ¹⁹⁵Pt{¹H}, or ¹⁵N spectra.

FT-IR (ATR, ν̄ max, cm⁻¹) selected bands: 307, 266 (symm. Pt–Cl stretch), 250 (assym. Pt–Cl stretch)

Structure confirmed by single-crystal X-ray crystallography, see Appendix I. Suitable colourless crystals were obtained by vapour diffusion from chloroform and hexane.

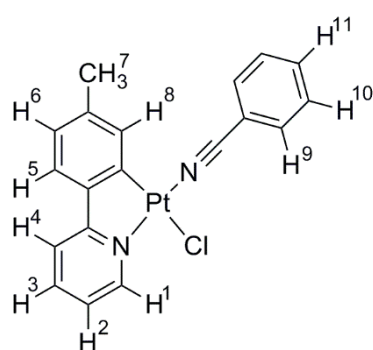
Synthesis of [Pt(tolpy)Cl(PhCN)] (12)



A solution of [Pt(tolpy)(μ-Cl)₂] (**1**, 0.075 mmol, 60 mg) and benzonitrile (0.78 ml, 0.75 mmol) in acetone (5 ml) was stirred at room temperature for 20 hours under an atmosphere of dry nitrogen. The solution was filtered through Celite™ and the solvent was removed *in vacuo*. The resulting precipitate was dissolved in a minimum of CH₂Cl₂ and layered with hexane. After collecting the precipitate by filtration and washing successively with hexane (2 x 2.5 ml), the title compound was obtained as a yellow solid.

Yield: 25 mg, 33%

MS-ESI (*m/z*): [M⁺-Cl⁻] for [C₁₉H₁₅N₂Pt]⁺ found (expected) 466.0894(466.0879).

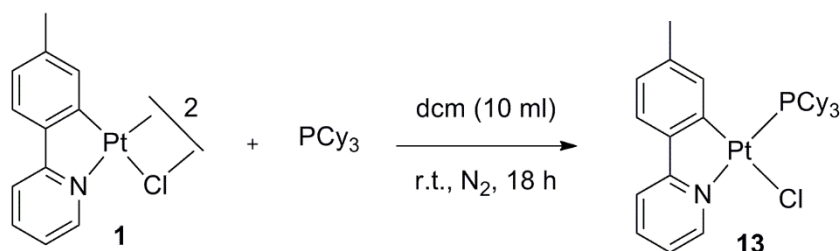


¹H-NMR δ_H (500 MHz, CDCl₃): 9.67 (1H¹, d, ³J_{HH} = 7 Hz, ⁴J_{HH} = 1.5 Hz, ³J_{HPt} = 46 Hz), 7.96 – 7.93 (2H⁹, m,), 7.86 – 7.78 (2H, overlap of H³, td and H¹¹, td), 7.66 – 7.60 (3H, overlap of H⁴, d and H¹⁰, dd), 7.39 (1H⁵, d, ³J_{HH} = 8 Hz), 7.24 (1H⁸, s, ³J_{HPt} = 47 Hz), 7.15 (1H², td, ³J_{HH} = 6 Hz, ⁴J_{HH} = 1.5 Hz), 7.01 (1H⁶, d, ³J_{HH} = 8 Hz), 2.40 (3H⁷, s).

FT-IR (ATR, $\bar{\nu}$ max, cm⁻¹) selected bands: 493, 296, 277

Due to the poor stability of complex **12**, it was not possible to obtain further analytical data.

Synthesis of [Pt(tolpy)Cl(PCy₃)] (13)

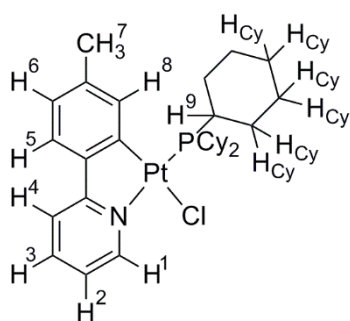


A solution of [Pt(tolpy)(μ -Cl)]₂ (**1**, 0.125 mmol, 100 mg) and PCy₃ (85 mg, 0.305 mmol) in CH₂Cl₂ (10 ml) was stirred at room temperature for 18 hours under an atmosphere of dry nitrogen. The solution was filtered through Celite™ and hexane (15 ml) was added, affording a yellow precipitate. After collecting by filtration and washing successively with hexane (2 x 2.5 ml), the title compound was obtained as a yellow crystalline solid.

Yield: 112 mg, 66%

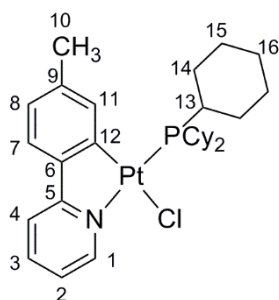
CHN data for found (expected)%: 54.29 (53.05), H 6.76 (6.38), and N 1.91 (2.06)

MS-ESI (*m/z*): [M⁺-Cl⁻] for [C₃₀H₄₃NPt]⁺ found (expected): 643.2764 (643.2778)



¹H-NMR δ_{H} (400 MHz, CDCl₃): 9.93 (1H¹, m), 7.77 (1H³, td, ³J_{HH} = 8 Hz, ⁴J_{HH} = 1.6 Hz), 7.66 (1H⁴, d, ³J_{HH} = 8 Hz), 7.42 (1H⁸, s, ³J_{HPt} = 55 Hz), 7.41 (1H⁵, d, ³J_{HH} = 8 Hz), 7.20 (1H², tt, ³J_{HH} = 6 Hz, ⁴J_{HH} = 1.2 Hz), 6.91 (1H⁶, d, ³J_{HH} = 8 Hz), 2.80 (3H⁹, td, ³J_{HP} = 11 Hz, ³J_{HH} = 11 Hz), 2.33 (3H⁷, s), 2.08 (6H^{Cy}, d, ³J_{HH} = 11 Hz), 1.88 - 1.76 (6H^{Cy}, m), 1.76 - 1.63 (9H^{Cy}, m), 1.37 - 1.18 (9H^{Cy}, m)

¹H{³¹P}-NMR δ_{H} (500 MHz, CDCl₃): 9.93 (1H¹, ddd, ³J_{HH} = 6 Hz, ⁴J_{HH} = 1.6 Hz, ⁵J_{HH} = 0.7 Hz, ³J_{HPt} = 26 Hz), 7.77 (1H³, dd, ³J_{HH} = 7 Hz, ⁴J_{HH} = 1.6 Hz), 7.66 (1H⁴, d, ³J_{HH} = 8 Hz), 7.43 (1H⁸, s, ³J_{HPt} = 57 Hz), 7.41 (1H⁵, d, ³J_{HH} = 8 Hz), 7.19 (1H², td, ³J_{HH} = 6 Hz, ⁴J_{HH} = 1.4 Hz), 6.90 (1H⁶, d, ³J_{HH} = 8 Hz), 2.80 (3H⁹, t, ³J_{HH} = 11 Hz), 2.33 (3H⁷, s), 2.08 (6H^{Cy}, d, ³J_{HH} = 11 Hz), 1.85 - 1.77 (6H^{Cy}, m), 1.75 - 1.65 (9H^{Cy}, m), 1.35 - 1.20 (9H^{Cy}, m)



$^{13}\text{C}\{^1\text{H}\}$ -NMR δ_{C} (100.5 MHz, CDCl_3): 165.55 (C^5), 148.91 (C^1), 143.37 (C^7), 140.42 (C^{12} , d, $^2J_{\text{CP}} = 6$ Hz), 139.29 (C^6), 138.92 (C^{11}), 138.88 (C^3), 124.22 (C^8), 123.81 (C^7), 121.37 (C^2 , d, $^4J_{\text{CP}} = 3$ Hz), 117.88 (C^4 , d, $^2J_{\text{CP}} = 2$ Hz), 33.52 (C^{13} , d, $^2J_{\text{CPt}} = 31$ Hz), 30.22, (C^{14}), 27.86 (C^{15} , d, $^3J_{\text{CP}} = 11$ Hz), 26.63 (C^{16}), 21.96 (C^{10}).

$^{13}\text{C}\{^1\text{H}\}$ -NMR δ_{C} (75.4 MHz, CDCl_3): 165.45 (C^5 , d, $^3J_{\text{CP}} = 2$ Hz, $^2J_{\text{CPt}} = 87$ Hz), 145.79 (C^1 , $^2J_{\text{CPt}} = 24$ Hz), 143.25 (C^7 , $^3J_{\text{CPt}} = 24$ Hz), 140.34 (C^{12} , d, $^2J_{\text{CP}} = 6$ Hz, $^1J_{\text{CPt}} = 1111$ Hz), 139.13 (C^6 , d, $^3J_{\text{CP}} = 1$ Hz), 138.75 (C^{11} , d, $^3J_{\text{CP}} = 3$ Hz), 138.69 (C^{11}), 124.07 (C^8), 123.67 (C^7 , $^3J_{\text{CPt}} = 42$ Hz), 121.19 (C^2 , d, $^4J_{\text{CP}} = 3$ Hz, $^3J_{\text{CPt}} = 17$ Hz), 117.71 (C^4 , d, $^4J_{\text{CP}} = 2$ Hz, $^3J_{\text{CPt}} = 24$ Hz), 33.47 (C^{13}) 30.11, (C^{14} , $^3J_{\text{CPt}} = 24$ Hz), 27.70 (C^{15} , d, $^3J_{\text{CP}} = 11$ Hz), 26.49 (C^{16} , d, $^3J_{\text{CP}} = 1$ Hz), 21.78 (C^{10}).

Table 41: Summary of the coupling was observed in the HMQC spectra for **13**

^{13}C	δ , ppm	Couples to protons, δ , ppm
C^1	148.91	9.93 (H^1)
C^2	121.37	7.20 (H^2)
C^3	138.88	7.77 (H^3)
C^4	117.88	7.66 (H^4)
C^7	123.81	7.41 (H^5)
C^8	124.22	6.91 (H^6)
C^{10}	21.96	2.33 (H^7)
C^{11}	138.92	7.42 (H^8)
C^{13}	33.56	2.80 (H^9)
C^{14}	30.22	2.08 (H^{Cy}), 1.76 – 1.63 (H^{Cy})
C^{15}	27.86	1.88 – 1.76 (H^{Cy})
C^{16}	26.22	1.76 – 1.63

^{15}N -NMR δ_{N} (51 MHz, CDCl_3): 243.79 (d, $^2J_{\text{NP}} = 49$ Hz) couples to proton at 9.93 H¹, 7.66 H⁴ and 7.20 H²

$^{31}\text{P}\{^1\text{H}\}$ -NMR δ_{P} (164.0 MHz, CDCl_3): 19.15 (s, $^1J_{\text{PPt}} = 4010$ Hz)

$^{195}\text{Pt}\{^1\text{H}\}$ -NMR δ_{Pt} (107 MHz, CDCl_3): -4011 (d, $^1J_{\text{PPt}} = 4000$ Hz)

Structure confirmed by single-crystal X-ray crystallography see Appendix I. Suitable crystals were obtained by vapour diffusion from CH_2Cl_2 and hexane.

4.2 Decarbonylation Reactions

General Procedure for Decarbonylation of Neat Substrates

The metal complex (0.021 mmol) was added to the substrate (9.7 mmol) and heated to 120 °C, unless otherwise stated, with stirring in a sealed constant volume reaction vessel. After 16 h the mixture was allowed to cool to 25 °C, the reaction headspace was sampled (1 ml) and analysed by GC or GC-MS and the substrate volume was reduced *in vacuo*. For the reactions launched for monitoring by ^1H NMR spectroscopy, the yellow-green residue was dissolved in CDCl_3 and analysed by NMR spectroscopy. To isolate $[\text{Pt}(\text{tolpy})\text{Cl}(\text{CO})]$ (**4**), after the volume of cyclohexanone was reduced *in vacuo*, diethylether (1.5 ml) was added to the green residue and placed in the fridge. The yellow-green precipitate was obtained by filtration and washed with diethyl ether (2 x 1.5 ml).

^1H -NMR δ_{H} (400 MHz, CDCl_3): 9.45 (1, dd, $^3J_{\text{HH}} = 6$ Hz, $^3J_{\text{HPt}} = 31$ Hz, $^4J_{\text{HH}} = 1.2$ Hz), 7.92 (1, td, $^3J_{\text{HH}} = 7.6$ Hz, $^4J_{\text{HH}} = 1.6$ Hz), 7.73 (1, d, $^3J_{\text{HH}} = 4$ Hz), 7.47 (1, d, $^3J_{\text{HH}} = 8.0$ Hz), 7.31 (1, td, $^3J_{\text{HH}} = 6.8$ Hz, $^4J_{\text{HH}} = 1.2$ Hz), 7.30 (1, s, $^3J_{\text{HPt}} = 70$ Hz), 7.05 (1, d, $^3J_{\text{HH}} = 7.2$ Hz), 2.34 (3,s).

$^{195}\text{Pt}\{^1\text{H}\}$ -NMR δ_{Pt} (107 MHz, CDCl_3): -3946 ppm.

FT-IR (ATR) selected bands: 2098 cm^{-1} $\bar{\nu}(\text{C}\equiv\text{O})$.

Structure confirmed by single-crystal X-ray crystallography.

Results for when $[\text{Pt}(\text{tolpy})\text{Cl}(\text{S-dmsO})]$ (**3**)

GC and GC-MS analysis when:

The headspace of the reaction was sampled and analysed using GC-A (Table 42) and butane was identified as the major component. The formation of butane as the major hydrocarbon product for the decarbonylation of cyclohexanone was further confirmed by GC (GC-B, $R_T = 5.8$ min, Table 43) and GC-MS (GC-C, $R_T = 2.95$ min, $M^{+\bullet} = 58$ amu and GC-D $R_T = 15.2$ min, $M^{+\bullet} = 58$ amu) analysis of the reaction. Carbon monoxide and methane were observed in the reaction headspace using GC-E (CH_4 $R_T = 8.5 - 9.2$ min, $M^{+\bullet} = 16$ amu and CO $R_T = 11.7 - 13.8$ min, $M^{+\bullet} = 58$ amu).

Table 42: Head space analysis after decarbonylation of cyclohexanone mediated by complex (3), (GC-A)

Compound	Retention Time / min	Peak Area / %	Column
Ethane	2.17	0.39	PLOT
Ethene	3.19	0.67	PLOT
Propane	4.10	3.95	PLOT
Propene	6.94	0.02	PLOT
Butane	7.53	94.9	PLOT
Isobutene	9.494	0.03	PLOT
Cyclohexanone	18.0	-	LOWOX

Table 43: Head space analysis after decarbonylation of cyclohexanone mediated by complex (3), (GC-B)

Run	Injection 1, peak area	Injection 2, peak area	Injection 3, peak area	Average peak area \pm standard error
1	4727	4731	3140	4119 \pm 530
2	7023	7832	7926	7593 \pm 500

Dynamic light scattering:

Particles with an average hydrodynamic diameter of 47 nm were observed (polydispersity index = 0.34), these particles accounted for 88% of those observed. The second peak relates to larger particles with diameters between 480 – 860 nm.

Effect of Air and Light on the Decarbonylation of Cyclohexanone

The general procedure for decarbonylation described above was employed unless otherwise stated and the results are summarised in Table 44.

Table 44: Initial studies of the decarbonylation of cyclohexanone mediated by [Pt(tolpy)Cl(S-dmsO)] (**3**) under different conditions

Temp.	Ambient Light	Atmos.	Water	Conversion to 4	GC-HS peak area for butane
120 °C	yes	N ₂ ^a	no	0	na ^b
120 °C	yes	Air	no	100	5900 ± 800
120 °C	no ^c	Air	no	100	1160 ± 28

^a In order to rigorously exclude oxygen Schlenk apparatus was used: A solution of [Pt(tolpy)Cl(S-dmsO)] (10 mg, 21 μmol) in freshly dried and distilled cyclohexanone (1 ml, 0.97 mmol) was outgassed using three cycles of freeze-pump-thaw before it was heated to 120 °C with stirring for 16 hours.

^b It is not possible to rigorously exclude oxygen in the Fisher-Porter vessel required for head-space analysis

^c The decarbonylation of cyclohexanone mediated by [Pt(tolpy)Cl(S-dmsO)] was repeated in the dark using amber stained glassware under an atmosphere of air.

Irradiation of [Pt(tolpy)Cl(S-dmsO)] and Cyclohexanone

A solution of [Pt(tolpy)Cl(S-dmsO)] (**3**, 10 mg, 0.021 mmol) in cyclohexanone (0.5 ml, 4.85 mmol) was irradiated using a 125 W medium pressure mercury vapour lamp ($\lambda > 250$ nm) in a Young's tube at room temperature for 16 h. CDCl₃ was added and the solution was analysed by ¹H and ¹⁹⁵Pt{¹H} NMR spectroscopy, which showed that only [Pt(tolpy)Cl(S-dmsO)] was present.

¹H-NMR δ_{H} (400 MHz, CDCl₃): 9.59 (1H, d, ³J_{HH} = 5.6 Hz, ³J_{HPt} = 34 Hz), 8.18 (1H, s, ³J_{HPt} = 46 Hz), 7.84 (1H, td, ³J_{HH} = 8.4 Hz, ⁴J_{HH} = 1.6 Hz), 7.69 (1H, d, ³J_{HH} = 8.0 Hz), 7.42 (1H, d, ³J_{HH} = 8.0 Hz), 7.20 (1H, td, ³J_{HH} = 5.6 Hz, ⁴J_{HH} = 1.2 Hz), 7.00 (1H, d, ³J_{HH} = 8.8 Hz), 3.65 (6H, s, ³J_{HPt} = 22 Hz), 2.40 (3H, s).

¹H-¹⁹⁵Pt HMQC δ_{Pt} (107 MHz, CDCl₃): - 3815 ppm (**3**)

FT-IR (ATR, $\bar{\nu}$ max, cm⁻¹) selected band: 1118 $\bar{\nu}$ (S=O)

The Effect of Additives to the Decarbonylation of Cyclohexanone

The general procedure for decarbonylation described above was employed unless otherwise stated and the results are summarised in Table 46.

Mercury

Mercury (600 equivalents, 200 μ L, 12.6 mmol) [Pt(tolpy)Cl(S-dmsO)] (10 mg, 0.021 mmol) was added to the substrate (9.7 mmol) and heated to 120 °C with vigorous stirring in a sealed constant volume reaction vessel.

Table 45: Summary of the peak areas (a.u.) corresponding to butane measured after mercury was added to the solution of cyclohexanone and [Pt(tolpy)Cl(S-dmsO)] (**3**) and heated under standard decarbonylation conditions

Run	Injection 1, peak area	Injection 2, peak area	Injection 3, peak area	Average peak area \pm standard error
1	624	789	507	640 \pm 82
2	482	447	477	468 \pm 11
3	150	77	122	116 \pm 21

Polyvinyl Pyrrolidone (PVP)

The decarbonylation of cyclohexanone was repeated under standard conditions but with the addition of 0.01 molar equivalents of PVP (7.1 mg, average molecular weight = 40,000 g mol⁻¹).

Phenothiazine (PTZ)

The decarbonylation of cyclohexanone was repeated under standard conditions but with the addition of 0.5 molar equivalents of PTZ (2 mg, 0.0100 mmol).

Table 46: Summary of the effect of additives on the decarbonylation of cyclohexanone mediated by [Pt(tolpy)Cl(S-dmsO)] (3)

Additive	Atmos.	No. Molar Equiv. w.r.t 3	Conversion to 4	Average peak area using GC- B ± standard error
Mercury	air	600	- ^a	408 ± 81
PVP	air	0.01	100	749 ± 27
PTZ	air	0.5	100	505 ± 17

^a Isolation of the platinum complex/es from the mixture with mercury was not attempted, after the headspace analysis, sulfur flowers were added to the reaction mixture and then disposed of.

Substrate Scope

The general procedure for decarbonylation (S.D.C) described above was employed unless otherwise stated and the results are summarised in Table 47.

Table 47: Decarbonylation of the different substrates mediated by [Pt(tolpy)Cl(S-dmsO)] (**3**), the abbreviation S.D.C denoted standard decarbonylation conditions

Substrate	Conditions	Analytical Data	Additional
Cyclopentanone	S.D.C.	¹ H NMR (CDCl ₃): 89% [Pt(tolpy)Cl(CO)] (4), 11% [Pt ^{IV} (tolpy) ₂ Cl ₂] (11) IR: $\bar{\nu}$ (C=O) 2100 cm ⁻¹ GC: Propane identified by GC-A and GC-B	Darkening of the reaction solution and the formation of precipitate observed
Cycloheptanone	S.D.C.	¹ H NMR (CDCl ₃): 100% [Pt(tolpy)Cl(CO)] (4) IR: $\bar{\nu}$ (C=O) 2099 cm ⁻¹ GC-B: C ₅ -C ₆ carbon fragment GC-C: major component cyclohexene GC-MS(EI) m/z: 8 (M ^{+•}), 67, 54, 39	Darkening of the reaction solution and the formation of precipitate observed. For one of the three repeats non-quantitative conversion was observed: 68% [Pt(tolpy)Cl(CO)] (4), 25% [Pt(tolpy)Cl(S-dmsO)] (3), 7% [Pt ^{IV} (tolpy) ₂ Cl ₂] (11)
Cycloheptanone	S.D.C.	GC-C: major component cyclohexene	using [PtCl ₂ (^t Bu) ₂ -bipy)] 19
Cyclooctanone	S.D.C.	¹ H NMR (CDCl ₃): 100% [Pt(tolpy)Cl(CO)] (4) IR: $\bar{\nu}$ (C=O) 2098 cm ⁻¹ GC-MS: cycloheptene identified as major component (GC-C) GC-MS(EI) m/z: 96 (M ^{+•})	Darkening of the reaction solution and an increase in viscosity was observed
Cyclohex-2-en-1-one	S.D.C.	¹ H NMR (CDCl ₃): 5% [Pt(tolpy)Cl(CO)] (4), 77% [Pt(tolpy)Cl(S-dmsO)] (3), 8% [Pt(tolpy)(μ -Cl)] ₂ (1) GC-B: small amount of butane	No visual signs of decomposition of the platinum complexes

Substrate	Conditions	Analytical Data	Additional
1,2-Cyclohexadione	S.D.C	$^1\text{H NMR (CDCl}_3\text{)}$: 100% [Pt(tolpy)Cl(CO)] (4) IR: 2098 cm^{-1} $\bar{\nu}(\text{C}\equiv\text{O})$ GC-B: butane, hexane, cyclohexene, dimethylsulfide (dms) and benzene	Darkening of the reaction solution was observed
1,2-Cyclohexadione	Control reaction	GC-B: butane, cyclohexadiene and benzene observed	Reaction conducted without 3
2-Pentanone	S.D.C	$^1\text{H NMR (CDCl}_3\text{)}$: 87% [Pt(tolpy)Cl(CO)] (4) IR: 2098 cm^{-1} $\bar{\nu}(\text{C}\equiv\text{O})$	No obvious signs of decomposition of the platinum complexes were observed between 0-10 hours, but after heating for 16 hours a dark precipitate, suspected to be Pt^0 , could be seen visibly
2-Hexanone	S.D.C	$^1\text{H NMR (CDCl}_3\text{)}$: <1% [Pt(tolpy)Cl(CO)] (4), 0.5%, [Pt(tolpy)(μ -Cl)] ₂ (1) IR: 2098 cm^{-1} $\bar{\nu}(\text{C}\equiv\text{O})$	No obvious signs of decomposition of the platinum complexes
2-Heptanone	S.D.C	$^1\text{H NMR (CDCl}_3\text{)}$: 0% [Pt(tolpy)Cl(CO)] (4), 24% [Pt(tolpy)(μ -Cl)] ₂ (1) IR: 2098 cm^{-1} $\bar{\nu}(\text{C}\equiv\text{O})$	No obvious signs of decomposition of the platinum complexes
Acetone	Reflux, open system, 60 $^\circ\text{C}$	$^1\text{H NMR (CDCl}_3\text{)}$: 1-1% [Pt(tolpy)Cl(CO)] (4) IR: 2098 cm^{-1} $\bar{\nu}(\text{C}\equiv\text{O})$	No obvious signs of decomposition of the platinum complexes
Acetone	S.D.C	$^1\text{H NMR (CDCl}_3\text{)}$: 1-4% [Pt(tolpy)Cl(CO)] (4) IR: 2098 cm^{-1} $\bar{\nu}(\text{C}\equiv\text{O})$	Darkening of the reaction solution and the formation of precipitate observed.

Substrate	Conditions	Analytical Data	Additional
α -Tetralone	S.D.C	^1H NMR (CDCl_3): 29% [Pt(tolpy)Cl(CO)] (4), 56% [Pt(tolpy)Cl(S-dmsol)] (3), 15% [Pt ^{IV} (tolpy) ₂ Cl ₂] (11) IR: 2098 cm^{-1} $\bar{\nu}(\text{C}\equiv\text{O})$	dark precipitates observed
α -Tetralone	reaction time extended to 20 h	^1H NMR (CDCl_3): 71% [Pt(tolpy)Cl(CO)] (4), 16% [Pt(tolpy)Cl(S-dmsol)] (3), 13% [Pt ^{IV} (tolpy) ₂ Cl ₂] (11) IR: 2098 cm^{-1} $\bar{\nu}(\text{C}\equiv\text{O})$	dark precipitates observed
β -Tetralone	S.D.C	^1H NMR (CDCl_3): 50% [Pt(tolpy)Cl(CO)] (4), 50% [Pt(tolpy)Cl(S-dmsol)] (3),	dark precipitates observed
2-Fluorocyclohexanone	S.D.C	^{19}F -NMR δ_{H} (376 MHz, CDCl_3): -152.65 (d, $J = 19$ Hz) GC-C: cyclohexene was observed by mass spectrometry. CHN data for: %C 68.04, %H 6.90, %N 0.14	The entire vessel contents had been transformed from a pale yellow liquid to a black solid.
Acetophenone	S.D.C	^1H NMR (CDCl_3): 0% [Pt(tolpy)Cl(CO)] (4) IR: 2098 cm^{-1} $\bar{\nu}(\text{C}\equiv\text{O})$	Darkening of the reaction solution observed.
Propiophenone	S.D.C	^1H NMR (CDCl_3): 0% [Pt(tolpy)Cl(CO)] (4) IR: 2098 cm^{-1} $\bar{\nu}(\text{C}\equiv\text{O})$	Darkening of the reaction solution observed.
Buterophenone	S.D.C	^1H NMR (CDCl_3): 0% [Pt(tolpy)Cl(CO)] (4), 7% [Pt(tolpy)(μ -Cl)] ₂ (1), 15% [Pt(tolpy)Cl(H-tolpy)] (2), 70% [Pt(tolpy)Cl(S-dmsol)] (3), 8% [Pt ^{IV} (tolpy) ₂ Cl ₂] (11) IR: 2098 cm^{-1} $\bar{\nu}(\text{C}\equiv\text{O})$	Darkening of the reaction solution observed.

Substrate	Conditions	Analytical Data	Additional
Di-cyclohexyl ketone	S.D.C	¹ H NMR (CDCl ₃): 58% [Pt(tolpy)Cl(CO)] (4), 20% [Pt(tolpy)(μ-Cl)] ₂ (1), 22% [Pt(tolpy)Cl(S-dmsO)] (3) IR: 2098 cm ⁻¹ $\bar{\nu}$ (C≡O)	No obvious signs of decomposition observed
Benzophenone	S.D.C.	¹ H NMR (CDCl ₃): 9% [Pt(tolpy)Cl(CO)] (4), 20% [Pt(tolpy)(μ-Cl)] ₂ (1), 41% [Pt(tolpy)Cl(H-tolpy)] (2), 12% [Pt(tolpy)Cl(S-dmsO)] (3), 18% [Pt ^{IV} (tolpy) ₂ Cl ₂] (11) IR: 2098 cm ⁻¹ $\bar{\nu}$ (C≡O)	Darkening of the reaction solution observed and the formation of dark precipitates
Pentanal	S.D.C.	GC-B: formation of butane was observed.	It was not possible to calculate the conversion from [Pt(tolpy)Cl(S-dmsO)] (3) to [Pt(tolpy)Cl(CO)] (4) because of extensive decomposition of the platinum complexes
Pentanal	Rxn. temp. 19 °C	¹ H NMR (CDCl ₃): 28% [Pt(tolpy)Cl(CO)] (4), 72% [Pt(tolpy)Cl(S-dmsO)] (3) IR: 2098 cm ⁻¹ $\bar{\nu}$ (C≡O)	Darkening of the reaction solution observed and the formation of dark precipitates
Hexanal	S.D.C.	¹ H NMR (CDCl ₃): 100% [Pt(tolpy)Cl(CO)] (4) IR: 2098 cm ⁻¹ $\bar{\nu}$ (C≡O) GC-B and GC-C: cyclopentane observed	Darkening of the reaction solution observed
Caprolactone	S.D.C.	¹ H NMR (CDCl ₃): 4% [Pt(tolpy)Cl(CO)] (4), 19% [Pt(tolpy)(μ-Cl)] ₂ (1), 7% [Pt(tolpy)Cl(H-tolpy)] (2), 63% [Pt(tolpy)Cl(S-dmsO)] (3), 7% [Pt ^{IV} (tolpy) ₂ Cl ₂] (11) IR: 2099 cm ⁻¹ $\bar{\nu}$ (C≡O)	Darkening of the reaction solution observed and the formation of dark precipitates

Substrate	Conditions	Analytical Data	Additional
1,4-Dioxane	S.D.C.	^1H NMR (CDCl_3): 62% [Pt(tolpy)Cl(CO)] (4) δ_{Pt} (CDCl_3): -3947 ppm IR: 2094 cm^{-1} $\bar{\nu}$ (CO) peroxides: below 1 ppm	Darkening of the reaction solution observed Large pressure increase observed due to formation of gaseous products. N.B. Do not repeat in closed system.
1,4-Dioxane	rb. flask	GC-E: Carbon monoxide and methane observed. IR: 2094 cm^{-1} $\bar{\nu}$ (CO)	Reaction repeated to identify hydrocarbon products using round bottom flask (rb.) fitted with empty balloon instead of Fisher-Porter vessel
CPME	S.D.C.	IR: 2091 cm^{-1} $\bar{\nu}$ (CO)	Darkening of the reaction solution observed and the formation of dark precipitates. Due to extensive decomposition platinum complexes were not observed in the ^1H NMR spectrum
CPME	reaction time: 1 hour	^1H NMR (CDCl_3): 2% [Pt(tolpy)Cl(CO)] (4), 98% [Pt(tolpy)Cl(S-dmsO)] (3) IR: 2091 cm^{-1} $\bar{\nu}$ (CO)	No obvious signs of decomposition observed
CPME	reaction time: 2 hour	^1H NMR (CDCl_3): 9% [Pt(tolpy)Cl(CO)] (4), 91% [Pt(tolpy)Cl(S-dmsO)] (3) IR: 2091 cm^{-1} $\bar{\nu}$ (CO)	No obvious signs of decomposition observed
CPME	reaction time: 3 hour	^1H NMR (CDCl_3): 15% [Pt(tolpy)Cl(CO)] (4), 85% [Pt(tolpy)Cl(S-dmsO)] (3) IR: 2091 cm^{-1} $\bar{\nu}$ (CO)	No obvious signs of decomposition observed

Variation of the Metal Catalyst

The activity of different platinum complexes were studied using the general decarbonylation conditions described above, unless otherwise stated and the results are summarised in Table 48. Additional analytical data are given below.

Table 48: The decarbonylation of cyclohexanone mediated by different metal complexes

Complex	Conversion to [4], ^a %	CH ₄ , peak area	CO, peak area	<i>n</i> -C ₄ H ₁₀ , peak area
[Pt(tolpy)(μ -Cl)] ₂ (1)	100	17060	0	1514586
[Pt(tolpy)Cl(S-dmsO)] (3)	100	110766	115089925	63703
[Pt(tolpy)Cl(CO)] (4)	Na	217529	36509824	4421008
[Pt(tolpy)Cl(py)] (5)	78	-	-	-
[Pt(tolpy)Cl(dms)] (7)	100	28172	26238698	589874
[Pt(tolpy)Cl(PPh ₃)] (9)	100	212820	20990604	1492472
dppe complex 18	Na	-	-	0
[PtCl ₂ (^t Bu) ₂ -bipy)] 19	Na	0	54872958	2565358
terpyridine complex 20	Na	-	-	0

^a Estimated using the integration of the proton *ortho* to the nitrogen of the coordinated tolpy ligand in the ¹H NMR spectrum

^b observed using GC-E

^c butane observed using GC-D

[Pt(tolpy)Cl(H-tolpy)] (2)

Dynamic light scattering: particles with an average hydrodynamic particle diameter of 250 nm were observed. During the five DLS experiments (of 56 scans of ten seconds) the average particle size increased from 160 nm to 310 nm.

[Pt(tolpy)Cl(CO)] (4)

Dynamic light scattering: When the post-reaction solution was analysed where [Pt(tolpy)Cl(CO)] (4) was used as the catalyst, nanoparticles with average diameters of 11 and 180 nm were observed (Figure 80).

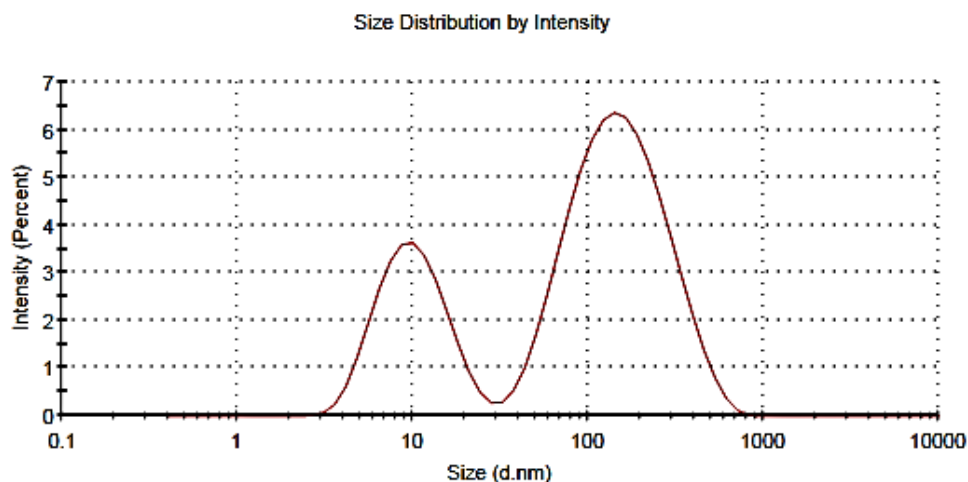


Figure 165: Plot of average hydrodynamic diameter *versus* intensity obtained *via* dynamic light scattering from the reaction solution after decarbonylation of cyclohexanone mediated by [Pt(tolpy)Cl(CO)] (4).

Rhodium Complexes**Repeat of the conditions reported by Rusina and Vlcek¹**

RhCl₃ (300 mg, 1.43 mmol) and PPh₃ (404 mg, 1.54 mmol) were heated to reflux for three hours in cyclohexanone (2.5 ml, 9.7 mmol) according to the method reported by Rusina and Vlcek, but in a constant volume Fisher-Porter vessel.¹ The reaction vessel was allowed to cool to 25 °C, after which the headspace was sampled (3 x 1 mL) and analysed by GC. Butane, cyclohexane, cyclohexene and benzene were observed by GC analysis of the reaction head-space (Table 49). The response for hydrocarbons using a FID detector, is approximately proportional to the chain length and so the relative peak areas, given in Table 49, were scaled accordingly.

³¹P{¹H} (CDCl₃): 30.64 ppm

Table 49: Relative peak areas of hydrocarbon products observed using GC-B

Butane	Cyclohexane	Cyclohexene	Benzene
1.1	1	1.5	4.4
Including scaling factor for chain length			

1.1

0.7

1

2.9

Decarbonylation of cyclohexanone using $[\text{RhCl}_3(\text{PPh}_3)]$ under standard conditions

RhCl_3 (30 mg, 0.143 mmol), PPh_3 (40 mg, 0.154 mmol) and cyclohexanone (1 ml, 9.7 mmol) were heated to 120 °C, under an atmosphere of air for 16 hours in a Fisher-Porter vessel. After 16 hours, the reaction headspace was sampled (3 x 1 ml) and the main components of the headspace were identified as butane, cyclohexane, cyclohexene and benzene using GC-B analysis and comparison to the references. Visible signs of decomposition observed, namely darkening of the reaction solution and formation of dark precipitates.

Decarbonylation of cyclohexanone using $[\text{RhCl}_3(\text{PPh}_3)_3]$ under an atmosphere of nitrogen

RhCl_3 (30 mg, 0.143 mmol), PPh_3 (40 mg, 0.154 mmol) and cyclohexanone (1 ml, 9.7 mmol) were heated to 120 °C, under an atmosphere of nitrogen for 16 hours in a Fisher-Porter vessel. After 16 hours, the reaction headspace was sampled and the main components of the headspace were identified were butane, cyclohexane, cyclohexene and benzene using GC-B analysis. Less visible signs of decomposition compared to the reaction conducted under an atmosphere of air and described above.

Decarbonylation of cyclohexanone using Wilkinson's catalyst, $[\text{RhCl}(\text{PPh}_3)_3]$

$[\text{RhCl}(\text{PPh}_3)_3]$ (19 mg, 0.021 mmol) was added to the cyclohexanone (1 ml, 9.7 mmol) and heated to 120 °C, with stirring in a sealed constant volume reaction vessel. After 16 h the mixture was allowed to cool to 25 °C, the reaction headspace was sampled (1 ml) and analysed by GC. GC:B: the formation of butane was not observed. Benzene and additional peaks with retention times similar to butene ionomers were observed in the headspace.

Heterogeneous Catalysis

Cyclohexanone (1 ml, 9.7 mmol) was added to either platinum on charcoal (Pt/C, 10 wt%) or palladium on carbon (Pd/C, 5 wt) and heated to 120 °C, with stirring in a sealed constant volume reaction vessel. After 16 h the mixture was allowed to cool to 25 °C, the reaction headspace was sampled (1 ml) and analysed by GC.

GC-B analysis of Pt/C:

At least 15 organic components were observed by GC analysis of the headspace, all with small peak areas

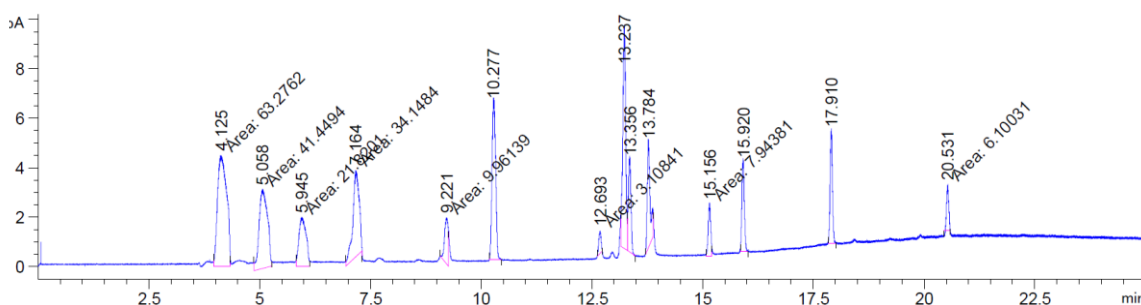


Figure 166: Gas Chromatogram of the reaction headspace after attempted decarbonylation of cyclohexanone mediated by Pt/C

GC-B analysis of Pd/C:

Four main peaks were observed but not identified but the peak areas were low (<400 pA).

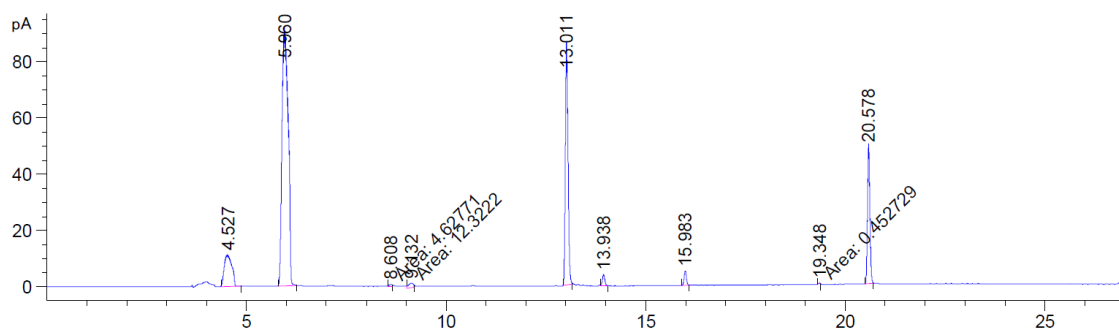


Figure 167: Gas Chromatogram of the reaction headspace after attempted decarbonylation of cyclohexanone mediated by Pd/C

***In situ* IR Monitoring of Decarbonylation Reactions**

The substrate (9.7 mmol) was added to a boiling tube equipped with a silicon ATR probe (SiComp, optical range 4400–650 cm^{-1}) and a thermocouple to record the internal reaction temperature. A background spectrum was recorded at 120 $^{\circ}\text{C}$ after which the metal complex (0.021 mmol) was charged to the reaction vessel and spectra were recorded every two minutes under an atmosphere of air. After 16 h the reaction mixture was allowed to cool and the substrate volume was reduced *in vacuo*; the yellow-green residue was dissolved in CDCl_3 and analysed by NMR spectroscopy.

Determination of the Onset Temperature for Decarbonylation of Cyclohexanone Mediated by [Pt(tolpy)Cl(S-dmsO)] (3)

Cyclohexanone (6 ml, 9.7 mmol) was charged to a boiling tube equipped with a silicon ATR probe (SiComp, optical range 4400–650 cm^{-1}) and a thermocouple to record the internal reaction temperature. A background spectrum was recorded at room temperature (18 $^{\circ}\text{C}$) after which [Pt(tolpy)Cl(S-dmsO)] (10 mg, 0.021 mmol) was charged to the reaction vessel and spectra were recorded every two min. The temperature was gradually increased and the peak area at 2098 cm^{-1} ($\bar{\nu}(\text{CO})$, **4**) was monitored (Figure 56). After 3 h, the reaction mixture was allowed to cool and the substrate volume was reduced *in vacuo*; the yellow-green residue was dissolved in CDCl_3 and analysed by NMR spectroscopy.

^1H NMR (CDCl_3): 50% conversion from [Pt(tolpy)Cl(S-dmsO)] (**3**) to [Pt(tolpy)Cl(CO)] (**4**) was estimated by integration of the ^1H NMR spectrum.

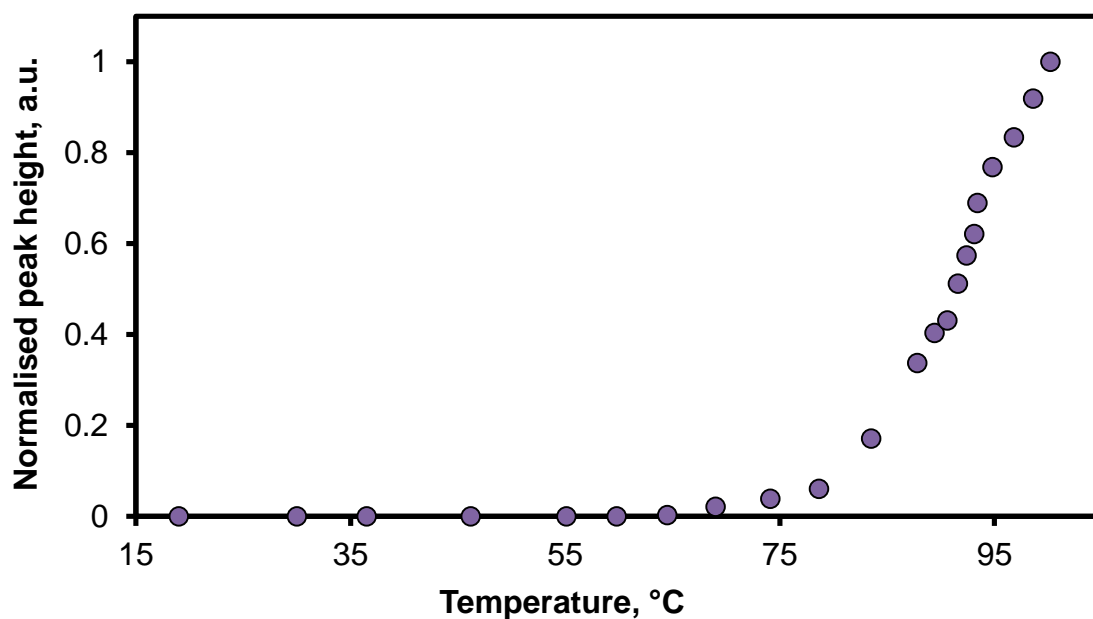


Figure 168: A plot of the normalised intensity of the vibration at 2098 cm^{-1} versus temperature for the decarbonylation of mediated by $[\text{Pt}(\text{tolpy})\text{Cl}(\text{S-dmsO})]$ (**3**)

General Procedure for Control Solvent Reactions

$[\text{Pt}(\text{tolpy})\text{Cl}(\text{S-dmsO})]$ (**3**) was heated to $120\text{ }^{\circ}\text{C}$ for 16 hours in the chosen solvent (2 ml) under an atmosphere of air in a constant volume Fisher-Porter vessel. The solvent was then removed *in vacuo* and the residue dissolved in CDCl_3 for ^1H NMR analysis. The results of the experiments are summarised below in Table 50.

Table 50: Summary of the results of the solvent control experiments using [Pt(tolpy)Cl(S-dmsO)] (**3**)

Solvent	Decomposition observed	Reaction with solvent observed	Details
Acetonitrile	No	Yes	Formation of [Pt(tolpy)Cl(NCMe)] (6)
Cyclopentyl methyl ether (CPME)	Yes	Yes	Formation of [Pt(tolpy)Cl(CO)] (4)
Dichlorobenzene	Yes	No	Free ligand observed in the ¹ H NMR spectrum and small amounts of Pt ⁰ observed.
Dichloroethane (DCE)	Yes	No	Minor decomposition observed
1,4-Dioxane	Yes	Yes	Significant decomposition and the formation of [Pt(tolpy)Cl(CO)] (4)
Ethyl acetate	No	No	Inert solvent
<i>iso</i> -propyl alcohol (IPA)	No	Yes	Formation of [Pt(IV)(tolpy) ₂ Cl ₂] (10 , <0.01%) and suspected [Pt(tolpy)(<i>μ</i> -Cl)] ₂ (1 , 8%)
Nitromethane	Yes	No	Free ligand observed in the ¹ H NMR spectrum
Tetrachloroethene (TCE)	Yes	No	Minor decomposition observed.
Tetrahydrofuran (THF)	No	No	Inert Solvent.
Toluene	No	No	[Pt(tolpy)Cl(S-dmsO)] (3) not fully soluble
Xylene	na	Na	[Pt(tolpy)Cl(S-dmsO)] (3) not soluble
Hexane	na	Na	[Pt(tolpy)Cl(S-dmsO)] (3) not soluble

General Procedure for Decarbonylation of Cyclohexanone in Solvent

The [Pt(tolpy)Cl(S-dmso)] (10 mg, 0.021 mmol) was added to a solution of cyclohexanone in solvent (2 ml) and heated to 120 °C (unless otherwise stated) with stirring in a constant volume Fisher-Porter vessel. After 16 h the mixture was allowed to cool to room temperature and the solvent removed *in vacuo* and the residue re-dissolved in CDCl₃ for ¹H NMR analysis. Details of the specific reaction conditions and the results are given in Table 51 and Table 52.

Table 51: Summary of the experimental conditions and results for the solvent optimisation study

Solvent	No. equiv. cyclohexanone w.r.t [Pt]	T. °C	Atmos.	Residual 3, % ^a	Conversion to 4, % ^a
1,2-Dichlorobenzene	100	120	Air	19	81
1,2-Dichlorobenzene	10	120	Air	96	4
1,2-Dichlorobenzene	5	120	N ₂	0	0
1,2-Dichlorobenzene	1	120	Air	0	0
Dichloroethane (DCE)	10	120	Air	86	0
Tetrachloroethene (TCE)	10	120	Air	96	0
THF	10	120	Air	0	0
Nitromethane	10	120	Air	85	12
Ethyl acetate	10	120	Air	90	10
Toluene	5	110	Air	97	3
Toluene	50	110	N ₂	0	0
Toluene	60	110	Air	71	29

MeCN ^b	10	120	Air	36	0
-------------------	----	-----	-----	----	---

^a Estimated using the integration of H¹ in the ¹H NMR spectrum

^b The presence of nanoparticles in solution were detected with an average hydrodynamic diameter of 40 nm (polydispersity index: 0.337, standard deviation = 0.3 nm)

Table 52: The effect of varying the equivalents of cyclohexanone in the decarbonylation reactions mediated by [Pt(tolpy)Cl(S-dms)] and performed in acetonitrile

Solvent	Equiv. cyclohexanone	Atmos.	Conversion to 4, % ^a	Conversion to 6, % ^a
MeCN	10	Air	0	64
MeCN	5	Air	0	62
MeCN	3	Air	0	44
MeCN	2	Air	0	41
MeCN	1	Air	0	33
MeCN	1	N ₂	0	52

^a Estimated using the integration of H¹ in the ¹H NMR spectrum

General Procedure for Decarbonylation of Substrates in Solvent with a Transfer Hydrogenation Donor (THD)

The metal complex (0.021 mmol) was added to a solution of substrate (10 equiv., 0.21 mmol) and THD (*iso*-propyl alcohol or 1, 3-cyclohexadiene, 2 equivalents, 0.041 mmol) in acetonitrile (2 ml) and heated to 120 °C with stirring in a constant volume reaction vessel. After 16 h the mixture was allowed to cool to room temperature and the solvent removed *in vacuo* and the residue re-dissolved in CDCl₃ for ¹H NMR analysis.

Table 53: The effect of adding a transfer hydrogenation donor (THD) on the decarbonylation reactions mediated by [Pt(tolpy)Cl(*S*-dmsu)]

Substrate	THD	No. equiv. THD	Solvent	Conversion to 4 , % ^a	Conversion to 6 ^b , %
Cyclohexanone	1,3-Cylohexadiene	2	Acetonitrile	0	73
Cyclohexanone	IPA	2	Acetonitrile	0	74
Bicyclohexylketone	1,3-Cylohexadiene	50	neat	100	-
Cyclohex-2-en-2-one	1,3-Cylohexadiene	2	neat	39	-
Cyclohex-2-en-2-one ^c	1,3-Cylohexadiene	10	neat	70	-
Acetophenone	1,3-Cylohexadiene	1	neat	3	-
Acetophenone	1,3-Cylohexadiene	2	neat	23	-
Acetophenone	1,3-Cylohexadiene	4	neat	20	-
Acetophenone ^d	IPA	60	neat	-	-
Propiophenone	1,3-Cylohexadiene	2	neat	65	-
Propiophenone ^e	IPA	60	neat	-	-
Acetone	1,3-Cylohexadiene	2	neat	13	-
Acetone ^{f,g}	1,3-Cylohexadiene	50	neat	-	-

^a Estimated using the integration of H¹ in the ¹H NMR spectrum

^b For reactions conducted in acetonitrile conversion from [Pt(tolpy)Cl(CO)] **4** to [Pt(tolpy)Cl(NCCH₃)] **6** occurs.

^c Headspace analysis using GC-B and GC-C: butane, cyclohexene, 1,3-cyclohexadiene and benzene were observed

^d Headspace analysis using GC-C and GC-E: benzene, carbon monoxide and methane were observed

^e Headspace analysis using GC-C: benzene was observed

^f Headspace analysis using GC-E: carbon monoxide and methane were observed

^g [Pt(tolpy)Cl(CO)] **4** used to mediate the reaction

UV-Vis Spectroscopic Analysis

Two molar equivalents of 1,3-cyclohexadiene and one molar equivalent of cyclohexanone were used with one molar equivalent of [Pt(tolpy)Cl(*S*-dmsu)] (**3**). The electronic spectrum of the reaction mixture diluted in acetonitrile was recorded before and after the reaction and the difference spectrum was deconvoluted using an 8-term Gaussian fit using custom MatLab® scripts, allowing overlapping UV-Vis peaks to be identified. Peaks at 255 and 282 nm relating to benzene and cyclohexanone, respectively, were observed.

4.3 Deuteration of Ketones at the α -Position

Potassium carbonate (0.5 g) was added to the anhydrous, outgassed substrate (7.5 ml) in deuterium oxide (25 ml, 99%) and the mixture was refluxed (100 °C) for 3 days with stirring under an atmosphere of nitrogen. The product was extracted in dichloromethane (1 x 10 ml, and washed with 2 x 5 ml), and the combined organic phase was then dried over magnesium sulfate and filtered. Dichloromethane was removed *in vacuo* to yield product. To improve the deuterium incorporation the method was repeated once.

2,2,6,6-Tetradeuterio-cyclohexanone

This reaction was conducted at twice the scale (15 ml of cyclohexanone was used).

Yield: 11.52 g, 78%

¹H-NMR δ_{H} (400 MHz, CDCl₃): 1.79 (4, m), 1.66 (2H, m).

Deuterium incorporation: 89%

²D-NMR δ_{D} (76.8 MHz, CDCl₃): 2.26 (s)

¹³C{¹H}-NMR δ_{C} (100.5 MHz, CDCl₃): 212.2, 41.35 (quintet, ¹J_{CD} = 15.8 Hz), 26.95, 24.95.

2,2,7,7-Tetradeuterio-cycloheptanone

Yield = 4.91 g, 5.17%

$^1\text{H-NMR}$ δ_{H} (400 MHz, CDCl_3): 1.62 - 1.72 (8H, m)

Deuterium incorporation: 93%.

$^2\text{H-NMR}$ δ_{D} (76.8 MHz, CDCl_3): 2.46 (s).

$^{13}\text{C}\{^1\text{H}\}$ -NMR δ_{C} (100.5 MHz, CDCl_3): 215.84, 43.43 (quintet, $^1J_{\text{DC}} = 19$ Hz), 30.51, 24.33.

2,2,8,8-Tetradeuterio-cyclooctanone

Yield = 4.52 g, 73%

$^1\text{H-NMR}$ δ_{H} (400 MHz, CDCl_3): 1.84 (4, t, $^3J_{\text{HH}} = 6.4$ Hz), 1.53 (4, m, 1.48- 1.57), 1.35 (2, m, 1.31-1.39).

Deuterium incorporation: 92%.

$^2\text{H-NMR}$ δ_{D} (76.8 MHz, CDCl_3): 2.03 (s).

$^{13}\text{C}\{^1\text{H}\}$ -NMR δ_{C} (100.5 MHz, CDCl_3): 218.7, 41.61 (q, $^1J_{\text{DC}} = 19$ Hz), 27.21, 25.61, 24.85.

4.4 Deuterium Labelling experiments**Acetone- d_6**

1,3-cyclohexadiene (0.1 ml, 1.05 mmol) and one molar equivalent of $[\text{Pt}(\text{tolpy})\text{Cl}(\text{S-dmsO})]$ (**3**, 10 mg, 0.021 mmol) were added to acetone- d_6 (1 ml) and heated to 120 °C, with stirring in a sealed constant volume reaction vessel. After 16 h the mixture was allowed to cool to 25 °C, the reaction headspace was sampled (1 ml) and analysed by GC-MS (Table 54).

GC-E: EI-MS (m/z): major isotopomer 19 ($\text{M}^{+\bullet}$, methane- d_3)

Table 54: Isotopic distribution of methane (R_T 8.8 min) formed by decarbonylation of acetone- d_8

$M^{+\bullet}$	$CH_4^{+\bullet}$	$CH_3D^{+\bullet}$	$CH_2D_2^{+\bullet}$	$CHD_3^{+\bullet}$	$CD_4^{+\bullet}$
Mass	16	17	18	19	20
Peak Area	0	19943	na	40625	0
Ratio	0	1	-	2	0

2,2',6,6'-Tetradeuterated Cyclohexanone

The general procedure for decarbonylation described above was employed and the results are summarised below.

1H -NMR δ_H (400 MHz, $CDCl_3$): 100% conversion to **4**

GC-C: EI-MS (m/z): 60 ($M^{+\bullet}$, butane- d_2) and 61 ($M^{+\bullet}$, butane- d_3), 45, 44, 43, 30, 29, 27

GC-E: EI-MS (m/z): major isotopomer 18 ($M^{+\bullet}$, methane- d_2), distribution of the isotopomers of methane summarised in Table 11.

Table 55: Isotopic distribution of methane (R_T 8.8 min) formed by decarbonylation of 2,2',6,6'-tetradeuterated cyclohexanone

$M^{+\bullet}$	$CH_4^{+\bullet}$	$CH_3D^{+\bullet}$	$CH_2D_2^{+\bullet}$	$CHD_3^{+\bullet}$	$CD_4^{+\bullet}$
Mass	16	17	18	19	20
Peak Area	6806	9284	36377	1999	306
Ratio	22	30	119	7	1

Cyclohexanone with IPA-d₈

Two hundred molar equivalents of IPA-d₈ (5 μl, 4.2 mmol) and one molar equivalent of [Pt(tolpy)Cl(S-dmsO)] (**3**) (10 mg, 0.021 mmol) were added to cyclohexanone (1 ml, 9.7 mmol) and heated to 120 °C, with stirring in a sealed constant volume reaction vessel. After 16 h the mixture was allowed to cool to 25 °C, the reaction headspace was sampled (1 ml) and analysed by GC-MS. Cyclohexanone and IPA-d₈ were removed *in vacuo* and the yellow-green residue was dissolved in CDCl₃ and analysed by NMR spectroscopy.

GC-C: EI-MS (m/z): 58 (M⁺, butane)

¹H NMR (CDCl₃): 90% conversion from [Pt(tolpy)Cl(S-dmsO)] (**3**) to [Pt(tolpy)Cl(CO)] (**4**)

[Pt(tolpy)Cl(S-dmsO)] (**3**) (10 mg, 0.021 mmol) was added to a 50:50 solution of cyclohexanone and IPA-d₈ (50 mol%, 1 ml) and heated under standard decarbonylation conditions.

GC-C: EI-MS (m/z): 58 (M⁺, butane)

¹H NMR (CDCl₃): 100% conversion from [Pt(tolpy)Cl(S-dmsO)] (**3**) to [Pt(tolpy)Cl(CO)] (**4**)

Decarbonylation of 2,2',6,6'-Tetradeuterated and Perdeuterated Cyclohexanone in the presence of 1,3-Cyclohexadiene

The general decarbonylation method described above was employed on 30% of the normal scale. The distribution of the isotopomers of methane and butane observed by GC-MS analysis using GC-E and GC-D, respectively, are summarised in Table 56.

2,2',6,6'-Tetradeuterated cyclohexanone with 1,3-cyclohexadiene:

GC-D: EI-MS (m/z): 58 (M⁺, butane)

GC-E: EI-MS (m/z): major isotopomer 18 (M⁺, methane-d₂).

Cyclohexanone-d₁₀ with 1,3-cyclohexadiene:

GC-D: EI-MS (m/z): 63 (M⁺, butane-d₅), 64 (M⁺, butane-d₆), 65 (M⁺, butane-d₇),

GC-E: EI-MS (m/z): major isotopomer 18 (M⁺, methane-d₂).

Table 56: Distribution of isotopomers observed by GC-MS analysis of the reaction headspace after the decarbonylation of 2,2',6,6'-tetradeuterated and perdeuterated cyclohexanone in the presence of 1,3-cyclohexadiene

2,2',6,6'-tetradeuterated cyclohexanone	CO at R_T 11.7 min using GC-E									
	Mass	28				Peak Area	321154			
	Methane at R_T 8.8 min using GC-E									
	Mass	16	17	18	19	20				
	Peak Area	27938	35462	180457	5468	1819				
	Ratio	15	19	100	3	1				
	Butane at R_T 15 min using GC-D									
	Mass	58	59	60	61					
	Peak Area	920761	50726	22214	50812					
	Ratio	41	2	1	2					
perdeuterated cyclohexanone	CO at R_T 11.7 min using GC-E									
	Mass	28				Peak Area	14656			
	Methane at R_T 8.8 min using GC-E									
	Mass	16	17	18	19	20				
	Peak Area	26117	41068	163237	16176	7079				
	Ratio	4	6	23	2	1				
	Butane at R_T 15 min using GC-D									
	Mass	58	59	61	62	63	64	65	66	67
	Ratio	2	2	10	35	218	218	190	7	1

2,2',7,7'-Tetradeuterated Cycloheptanone

The general procedure for decarbonylation described above was employed and the results are summarised below.

GC-C: EI-MS (m/z): 84 (M^+ , cyclohexene- d^2), 69, 68, 56, 41 and 39

^1H NMR (CDCl_3): 91% conversion from $[\text{Pt}(\text{tolpy})\text{Cl}(\text{S-dms})]$ (**3**) to $[\text{Pt}(\text{tolpy})\text{Cl}(\text{CO})]$ (**4**), 9% of **11** also observed

2,2',8,8'-Tetradeuterated Cyclooctanone

The general procedure for decarbonylation described above was employed and the results are summarised below.

GC-C: EI-MS (m/z): 98 (M^+ , cycloheptene- d^2), 69, 68, 56, 41 and 39

^1H NMR (CDCl_3): 60% conversion from $[\text{Pt}(\text{tolpy})\text{Cl}(\text{S-dms})]$ (**3**) to $[\text{Pt}(\text{tolpy})\text{Cl}(\text{CO})]$ (**4**). Residual **3** (29%) and **11** (11%) also observed in post-reaction mixture

5.0 Computational Methods

Geometry Optimisations

Density functional theory (DFT) calculations were performed using Gaussian09 at the YARCC cluster at the University of York.³³¹ A screen of combinations of different functionals and basis sets was conducted to identify a method for studying the family of compounds with the general formula, [Pt(tolpy)Cl(L)]. All combinations showed good agreement with relative bond lengths amongst the complexes and the chosen methods were the best compromise between agreement with the X-ray crystal structure data and computational cost.

The geometries of the platinum complexes, of the family [Pt(tolpy)Cl(L)], were optimised using BP86 functional. The calculations were carried out using the 6-31G(d) basis set for elements C, H, N, O, S, Cl and the LANL2DZ basis set for Pt, which includes an effective core potential (ECP). Vibrational frequencies were calculated to ensure that optimised geometries correspond to local minima on the potential energy surface. Molecular Orbitals for the optimised geometries were visualised using the cubegen utility within Gaussian09.

For the dimer complex **1**, a larger basis set was required to reproduce the geometry observed in the crystal structure and so BP86/6-311+G(d,p)/LANL2DZ was used (summary of the results of the calculations on complex **1** are given in Table 57).

Table 57: Summary of the results of the quantum mechanical calculation performed on the *cis* and *trans* isomers of [Pt(tolpy)(μ -Cl)]₂ (**1a** and **1b**)

Isomer	Functional	Basis set, H, C, N, Cl	Basis set Pt	Geometry	E, HA
<i>cis</i>	BP86	6-31G(d) ^{332,} 333 21, 22	LANL2DZ	Calculation failed to converge within 96 hours	
<i>trans</i>	BP86	6-31G(d)	LANL2DZ	bent 66.25°	-2195.37330130
<i>cis</i>	BP86	6-311+G(d,p)	LANL2DZ	planar, 0.21°	-2195.71732548
<i>trans</i>	BP86	6-311+G(d,p)	LANL2DZ	bent 62.85°	-2195.71857966
<i>cis</i>	BP86	6-31G(d)	def2TZVP	bent, 42.11°	-2195.90140379
<i>trans</i>	BP86	6-31G(d)	def2TZVP	bent 57.86°	-2195.90253878
<i>cis</i>	BP86	6-311+G(d,p)	def2TZVP	planar 4.28°	-2196.23725973
<i>trans</i>	BP86	6-311+G(d,p)	def2TZVP	bent 57.56°	-2196.23798735
<i>cis</i>	BP86	6-31G(d)	SDD	bent 52.18°	-2195.87946934
<i>trans</i>	BP86	6-31G(d)	SDD	bent 60.89°	-2195.88008775
<i>cis</i>	BP86	6-311+G(d,p)	SDD	planar, 0.57°	-2196.21177852
<i>trans</i>	BP86	6-311+G(d,p)	SDD	bent 60.95°	-2196.21309760
<i>cis</i>	BP86	6-31G(d)	LANL2TZ	bent, 51.85°	-2195.39899664

<i>trans</i>	BP86	6-31G(d)	LANL2TZ	bent	-2195.39976883
				61.98°	
<i>cis</i>	BP86	6-311+G(d,p)	LANL2TZ	planar, 0.20°	-2195.73716685
<i>trans</i>	BP86	6-311+G(d,p)	LANL2TZ	bent, 63.09°	-2195.73844721
<i>Cis</i>	B3LYP	6-31G(d)	def2TZVP	bent	-2195.63488726
				4.14°	
<i>trans</i>	B3LYP	6-31G(d)	def2TZVP	bent	-2195.63477401
				32.37°	
<i>Cis</i>	B3LYP	6-311+G(d,p)	def2TZVP	planar, 0.59°	-2195.96956228
<i>trans</i>	B3LYP	6-311+G(d,p)	def2TZVP	planar, 0.00°	-2195.96936171
<i>cis</i>	B3LYP	6-31G(d)	SDD	bent, 30.83	-2195.61201338
<i>trans</i>	B3LYP	6-31G(d)	SDD	bent	-2195.61195408
				40.71°	
<i>cis</i>	B3LYP	6-311+G(d,p)	SDD	planar	-2195.63971878
				4.29°	
<i>trans</i>	B3LYP	6-311+G(d,p)	SDD	bent, 37.77°	-2195.94358404
<i>cis</i>	B3LYP	6-31G(d)	LANL2DZ	bent	-2195.61201338
				30.83°	
<i>trans</i>	B3LYP	6-31G(d)	LanD2DZ	bent	-2195.61195408
				40.71°	
<i>cis</i>	B3LYP	6-311+G(d,p)	LanD2DZ	planar, 0.21°	-2195.49533995
<i>trans</i>	B3LYP	6-311+G(d,p)	LanD2DZ	bent, 43.68°	-2195.49482447
<i>cis</i>	B3LYP	6-31G(d)	LANL2TZ	planar	-2195.17561203
				2.24°	

<i>trans</i>	B3LYP	6-31G(d)	LANL2TZ	bent	-2195.17588503
				41.61°	
<i>trans</i>	B3LYP	6-311+G(d,p)	LANL2TZ	bent, 41.69	-2195.51320560
<i>cis</i>	B3LYP	6-311+G(d,p)	LANL2TZ	Calculation failed to converge within 96 hours	
<i>Cis</i>	M06	6-311+G(d,p)	def2TZVP	planar	-2194.88745698
				4.24°	
<i>trans</i>	M06	6-311+G(d,p)	def2TZVP	bent, 39.64°	-2194.88754499
<i>cis</i>	M06	6-311+G(d,p)	SDD	planar, 0.16°	-2194.86419775
<i>trans</i>	M06	6-311+G(d,p)	SDD	bent, 44.79°	-2194.86452204
<i>cis</i>	M06	6-311+G(d,p)	LanD2DZ	planar, 0.12	-2194.39169515
<i>trans</i>	M06	6-311+G(d,p)	LanD2DZ	bent, 49.37°	-2194.39197569
<i>cis</i>	M06	6-311+G(d,p)	LANL2TZ	planar, 0.10°	-2194.40839792
<i>trans</i>	M06	6-311+G(d,p)	LANL2TZ	bent, 48.18°	-2194.40876729

NBO Analysis

NBO analysis was carried out by Marsel Shafikov³¹¹ using Gaussian09.³¹² The geometries were optimised using the B3LYP^{262, 334, 335} functional and the def2TZVP^{336, 337} basis set which includes an effective core potential (ECP) applied to the Pt atom. This optimisation was conducted using the tight SCF convergence criterion and using a “Superfine” integration grid. A vibrational frequency analysis confirmed that the geometries achieved corresponded to minima on the potential energy surface. Natural bond orbital (NBO), natural population (NP) and Mayer-Mulliken population (MP) analyses were performed using the NBO6³³⁸⁻³⁴¹ package using the wavefunction generated by Gaussian09 and using the same level of theory described above.

Appendices

Appendix I: Details of Crystal Data and Structure Refinement

Table 58: Crystal data and structure refinement for compounds 1 - 3

	[Pt(tolpy)(Cl)] ₂	[Pt(tolpy)Cl(H-tolpy)]	[Pt(tolpy)Cl(S-dmsO)]
	(1) ^a	(2) ^a	(3) ^a
Structure solved with	Superflip	ShelXS	ShelXS
Empirical formula	C ₂₆ H ₂₂ Cl ₈ N ₂ Pt ₂	C ₂₅ H ₂₃ Cl ₃ N ₂ Pt	C ₁₄ H ₁₆ ClNOPtS
Formula weight / g mol ⁻¹	1036.23	652.89	476.88
Temperature / K	110.05(10)	110.05(10)	110.05(10)
Crystal system	monoclinic	monoclinic	monoclinic
Space group	P2 ₁ /n	C2/c	P2 ₁ /n
<i>a</i> / Å	16.7235(7)	27.6958(4)	18.3457(3)
<i>b</i> / Å	10.1620(4)	10.96209(13)	11.17028(18)
<i>c</i> / Å	19.0936(9)	15.3638(2)	20.8044(4)
<i>α</i> / °	90	90	90
<i>β</i> / °	111.419(5)	91.1995(12)	90.0094(18)
<i>γ</i> / °	90	90	90
Volume / Å ³	3020.7(2)	4663.50(11)	4263.38(13)
Z	3	8	12
ρ_{calc} / g cm ⁻³	2.279	1.860	2.229
μ / mm ⁻¹	23.758	6.377	10.198
<i>F</i> (000)	1936.0	2528.0	2712.0
Crystal size / mm ³	0.1343 × 0.0489 × 0.0237	0.3846 × 0.221 × 0.0887	0.1838 × 0.0486 × 0.0401
Radiation / nm	CuK α (λ = 0.15418)	MoK α (λ = 0.07107)	MoK α (λ = 0.07107)

	[Pt(tolpy)(Cl)] ₂	[Pt(tolpy)Cl(H-tolpy)]	[Pt(tolpy)Cl(S-dmso)]
	(1) ^a	(2) ^a	(3) ^a
2 θ range / °	8.812 to 142.43	6.618 to 64.466	6.662 to 64.266
Index ranges	-20 \leq h \leq 17, -12 \leq k \leq 10, -23 \leq l \leq 20	-41 \leq h \leq 37, -16 \leq k \leq 13, -21 \leq l \leq 23	-21 \leq h \leq 27, -16 \leq k \leq 16, -26 \leq l \leq 31
Reflections collected	11444	25941	27281
Independent reflections	5740 [R_{int} = 0.0386, R_{sigma} = 0.0526]	7579 [R_{int} = 0.0333, R_{sigma} = 0.0333]	13478 [R_{int} = 0.0407, R_{sigma} = 0.0537]
Data/Restrains/parameters	5740 / 24 / 359	7579 / 0 / 282	13478 / 0 / 524
Goodness-of-fit on F^2	1.036	1.069	1.096
Final R indexes [$I \geq 2\sigma(I)$]	R_1 = 0.0446, wR_2 = 0.1107	R_1 = 0.0224, wR_2 = 0.0454	R_1 = 0.0415, wR_2 = 0.0928
Final R indexes [all data]	R_1 = 0.0565, wR_2 = 0.1214	R_1 = 0.0307, wR_2 = 0.0490	R_1 = 0.0468, wR_2 = 0.0962
Largest diff. peak / hole / e Å ⁻³	2.80 / -2.11	0.98 / -1.31	5.42 / -4.26

The crystal structures were solved by Natalie Pridmore^a

Table 59: Crystal data and structure refinement for compounds 4-5

	[Pt(tolpy)Cl(CO)] (4) ^{b,c}	[Pt(tolpy)Cl(CO)] (4b) ^f	[Pt(tolpy)Cl(py)] (5) ^e
Structure solved with	Smtbx-flip	SheXT Direct Methods	Superflip
Empirical formula	C ₁₃ H ₁₀ CINOPt	C ₁₃ H ₁₀ CINOPt	C ₁₇ H ₁₅ CIN ₂ Pt
Formula weight / g mol ⁻¹	426.76	426.76	477.85
Temperature / K	110.05(10)	109.95(10)	110.05(10)
Crystal system	orthorhombic	monoclinic	monoclinic
Space group	Pna2 ₁	P2 ₁ /c	P2 ₁ /n
<i>a</i> / Å	7.0940(4)	9.5740(7)	10.98703(12)
<i>b</i> / Å	18.9962(10)	18.5069(11)	15.92942(17)
<i>c</i> / Å	8.6904(5)	6.6637(6)	36.2536(4)
<i>α</i> / °	90	90	90
<i>β</i> / °	90	96.512(7)	93.6202(9)
<i>γ</i> / °	90	90	90
Volume / Å ³	1171.11(12)	1173.09(15)	6332.33(12)
Z	4	4	16
ρ_{calc} / g cm ⁻³	2.420	2.416	2.005
μ / mm ⁻¹	12.189	24.309	18.072
F(000)	792	792.0	3616.0
Crystal size / mm ³	0.2847 × 0.0564 × 0.0324	0.332 × 0.077 × 0.048	0.1903 × 0.0623 × 0.0623
Radiation / nm	MoK α (λ = 0.07107)	CuK α (λ = 1.54184)	CuK α (λ = 0.15418)
2 θ range / °	6.14 to 64.2	9.298 to 134.09	7.394 to 142.322
Index ranges	-10 ≤ <i>h</i> ≤ 10, -26 ≤ <i>k</i> ≤ 26, -13 ≤ <i>l</i> ≤ 12	-10 ≤ <i>h</i> ≤ 11, -22 ≤ <i>k</i> ≤ 12, -6 ≤ <i>l</i> ≤ 7	-12 ≤ <i>h</i> ≤ 13, -19 ≤ <i>k</i> ≤ 15, -38 ≤ <i>l</i> ≤ 44

	[Pt(tolpy)Cl(CO)]	[Pt(tolpy)Cl(CO)]	[Pt(tolpy)Cl(py)]
	(4)^{b,c}	(4b)^f	(5)^e
Reflections collected	12759	3765	35763
Independent reflections	3743 [$R_{\text{int}} = 0.0446$]	2082 [$R_{\text{int}} = 0.0533$, $R_{\text{sigma}} = 0.0616$]	12086 [$R_{\text{int}} = 0.0379$, $R_{\text{sigma}} = 0.0397$]
Data / restraints / parameters	3743 / 1 / 155	2082/0/149	12086/18/761
Goodness-of-fit on F^2	1.055	1.029	1.213
Final R indexes [$I > 2\sigma(I)$]	$R_1 = 0.0342$, $wR_2 = 0.0686$	$R_1 = 0.0572$, $wR_2 = 0.1481$	$R_1 = 0.0401$, $wR_2 = 0.0957$
Final R indexes [all data]	$R_1 = 0.0416$, $wR_2 = 0.0736$	$R_1 = 0.0631$, $wR_2 = 0.1567$	$R_1 = 0.0445$, $wR_2 = 0.0978$
Largest diff. peak/hole / $e \text{ \AA}^{-3}$	1.687 / -1.701	3.60/-3.14	1.69 / -1.40

The crystal structures were solved by Adrian Whitwood^b, Sam Hart^e and Rachel Bean^f

^cThe crystal was grown by D. Dey

Table 60: Crystal data and structure refinement for compounds 7-9

	[Pt(tolpy)Cl(dms)]	[Pt(tolpy)Cl(tht)]	[Pt(tolpy)Cl(PPh₃)]
	(7)^{b,c}	(8)^d	(9)^d
Structure solved with	Direct Methods	Superflip	Superflip
Empirical formula	C ₁₄ H ₁₆ ClNPtS	C ₁₆ H ₁₈ ClNPtS	C ₃₀ H ₂₅ ClNPt
Formula weight / g mol ⁻¹	460.88	486.91	661.02
Temperature / K	110.0	110.05(10)	110.05(10)
Crystal system	monoclinic	monoclinic	triclinic
Space group	P2 ₁ /c	P2 ₁ /c	P-1
$a / \text{\AA}$	9.8518(5)	7.01161(10)	10.1683(3)
$b / \text{\AA}$	12.0882(6)	10.13625(15)	10.5639(3)
$c / \text{\AA}$	12.5268(7)	21.3664(3)	13.4192(5)

	[Pt(tolpy)Cl(dms)]	[Pt(tolpy)Cl(tht)]	[Pt(tolpy)Cl(PPh ₃)]
	(7) ^{b,c}	(8) ^d	(9) ^d
$\alpha / ^\circ$	90.00	90.00	75.668(3)
$\beta / ^\circ$	102.785(5)	93.3456(13)	68.465(4)
$\gamma / ^\circ$	90.00	90.00	65.224(3)
Volume / \AA^3	1454.84(13)	1515.96(4)	1209.90(7)
Z	4	4	2
$\rho_{\text{calc}} / \text{g cm}^{-3}$	2.104	2.133	1.814
μ / mm^{-1}	9.953	9.558	5.995
F(000)	872	928.0	644.0
Crystal size / mm^3	0.2321 × 0.1587 × 0.1408	0.2323 × 0.1276 × 0.0897	0.2872 × 0.1069 × 0.0334
Radiation / nm	MoK α ($\lambda = 0.07107$)	MoK α ($\lambda = 0.07107$)	MoK α ($\lambda = 0.07107$)
2 θ range / $^\circ$	6.68 to 64.26 $^\circ$	6.78 to 60.06	6.56 to 63.86
Index ranges	-14 ≤ h ≤ 14, -17 ≤ k ≤ 17, -18 ≤ l ≤ 18	-9 ≤ h ≤ 9, -14 ≤ k ≤ 14, -30 ≤ l ≤ 30	-14 ≤ h ≤ 14, -15 ≤ k ≤ 15, -19 ≤ l ≤ 18
Reflections collected	22770	22574	21736
Independent reflections	4762 [$R_{\text{int}} = 0.0399$]	4427 [$R_{\text{int}} = 0.0338$, $R_{\text{sigma}} = 0.0244$]	7660 [$R_{\text{int}} = 0.0334$, $R_{\text{sigma}} = 0.0395$]
Data / restraints / parameters	4762 / 0 / 166	4427/0/182	7660/0/308
Goodness-of-fit on F^2	1.101	1.061	1.070
Final R indexes [$I > 2\sigma(I)$]	$R_1 = 0.0229$, $wR_2 =$ 0.0486	$R_1 = 0.0172$, $wR_2 =$ 0.0346	$R_1 = 0.0241$, $wR_2 =$ 0.0481
Final R indexes [all data]	$R_1 = 0.0316$, $wR_2 =$ 0.0530	$R_1 = 0.0209$, $wR_2 =$ 0.0358	$R_1 = 0.0284$, $wR_2 =$ 0.0500
Largest diff. peak/hole / $e \text{\AA}^{-3}$	1.749 / -1.818	0.67 / -0.71	0.85 / -0.63

The crystal structures were solved by Adrian Whitwood^b, Jessica Milani^d and Rachel Bean^f

^cThe crystal was grown by D. Dey

Table 61: Crystal data and structure refinement for compounds **10**, **11**, **13** and **18**

	[Pt(tolpy)Cl(P(OPh)₃)] (10)^f	[Pt(tolpy)₂Cl₂] (11)^b	[Pt(tolpy)Cl(PCy₃)] (13)^f
Structure solved using	ShellXT	Superflip	ShellXT using direct methods
Empirical formula	C ₃₀ H ₂₅ ClNO ₃ PPt	C ₂₅ H ₂₁ Cl ₅ N ₂ Pt	C ₃₁ H ₄₅ Cl ₃ NPPt
Formula weight / g mol ⁻¹	709.02	721.78	764.09
Temperature / K	110.05(10)	110.05(10)	113(5)
Crystal system	monoclinic	triclinic	monoclinic
Space group	P2 ₁ /n	P-1	P2 ₁ /c
<i>a</i> / Å	10.70655(13)	9.8840(3)	17.0009(4)
<i>b</i> / Å	15.0355(2)	11.4402(4)	9.6820(2)
<i>c</i> / Å	16.56969(19)	12.4289(3)	18.9517(4)
<i>α</i> / °	90	93.065(3)	90
<i>β</i> / °	96.4464(11)	99.958(2)	102.595(2)
<i>γ</i> / °	90	115.395(3)	90
Volume / Å ³	2650.49(6)	1237.53(7)	3044.44(13)
Z	4	2	4
ρ_{calc} / g cm ⁻³	1.777	1.937	1.667
μ / mm ⁻¹	11.669	6.227	11.692
F(000)	1384.0	696.0	1528.0
Crystal size / mm ³	0.293 × 0.125 × 0.068	0.3457 × 0.1182 × 0.0329	0.221 × 0.131 × 0.044
Radiation / nm	CuK α (λ = 1.54184)	MoK α (λ = 0.07107)	CuK α (λ = 1.54184)
2 θ range / °	7.964 to 134.156	6.726 to 60.068	9.564 to 134.154
Index ranges	-12 ≤ <i>h</i> ≤ 12, -17 ≤ <i>k</i> ≤ 14, -19 ≤ <i>l</i> ≤ 19	-13 ≤ <i>h</i> ≤ 13, -16 ≤ <i>k</i> ≤ 16, -17 ≤ <i>l</i> ≤ 17	-19 ≤ <i>h</i> ≤ 20, -7 ≤ <i>k</i> ≤ 11, -22 ≤ <i>l</i> ≤ 22

	[Pt(tolpy)Cl(P(OPh) ₃)] (10) ^f	[Pt(tolpy) ₂ Cl ₂] (11) ^b	[Pt(tolpy)Cl(PCy ₃)] (13) ^f
Reflections collected	24006	13081	11063
Independent reflections	4731 [<i>R</i> _{int} = 0.0544, <i>R</i> _{sigma} = 0.0326]	7218 [<i>R</i> _{int} = 0.0216, <i>R</i> _{sigma} = 0.0376]	5446 [<i>R</i> _{int} = 0.0532, <i>R</i> _{sigma} = 0.0622]
Data / restraints / parameters	4731/0/335	7218 / 0 / 300	5446/0/335
Goodness-of-fit on <i>F</i> ²	1.042	1.061	1.040
Final <i>R</i> indexes [<i>I</i> > 2σ (<i>I</i>)]	<i>R</i> ₁ = 0.0321, <i>wR</i> ₂ = 0.0838	<i>R</i> ₁ = 0.0237, <i>wR</i> ₂ = 0.0496	<i>R</i> ₁ = 0.0497, <i>wR</i> ₂ = 0.1254
Final <i>R</i> indexes [all data]	<i>R</i> ₁ = 0.0363, <i>wR</i> ₂ = 0.0885	<i>R</i> ₁ = 0.0278, <i>wR</i> ₂ = 0.0519	<i>R</i> ₁ = 0.0580, <i>wR</i> ₂ = 0.1357
Largest diff. peak / hole / e Å ⁻³	1.35/-1.22	2.19 / -1.19	5.09/-2.60

The crystal structures were solved by Adrian Whitwood^b and Rachel Bean^f

Appendix II: Introduction to DFT and explanation of Relevant Terms

In this work DFT has been used to identify optimised geometries, compare the relative energy of different isomers and to predict IR spectra. A very brief overview of the theory that underpins the work is given here.

DFT is a method of obtaining an approximate solution to the Schrödinger equation of a many-body system.^{255, 342} A Functional, which is a function of a function, is used to describe the electron density and basis sets are functions, which are used to form molecular orbitals as linear combinations of atomic orbitals (LCAO). In this work Gaussian orbitals were used, which depend on the square of the distance between the electron and the nucleus.

The Hybrid functional, B3LYP, which includes a mixture of Hartree-Fock exchange with DFT exchange-correlation energy and the generalised gradient approximation (GGA) functionals BP86 and M06, which are hybrid functionals that also correct for rapid variation in electron density over time, were used in this study. The functionals mentioned in thesis are given in Table 62.

Table 62: Description of the functionals and methods discussed in this thesis

Functional	Description
BP86 ^{343, 344}	a hybrid functional with combines the Becke 1988 exchange functional and the Perdew 86 correlation functional.
B3LYP ^{262, 334, 335}	stands for Becke, 3-parameter, Lee-Yang-Parr, a hybrid functional, named after its inventors, used in density functional theory
M06 ³⁴⁵	Minnesota 2006 functional used in density functional theory
MP2 ³⁴⁶	Møller–Plesset perturbation theory functional and post Hartree-Fock method

There are different types of Gaussian basis sets; minimal, double-zeta, triple-zeta etc. each of which can be augmented with diffuse functions and polarisation functions. Minimal basis sets contain the minimum number of basis functions that are needed for each atom, e.g. 1s for hydrogen. Double-zeta basis sets have two functions with different exponential factors to describe each valence orbital. Similarly, triple-zeta basis use three functions for each valence orbital type. The suitability of a basis set can be improved by adding diffuse or polarisation functions. Using polarisation functions means that distortion of the atomic orbitals

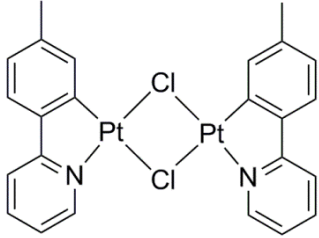
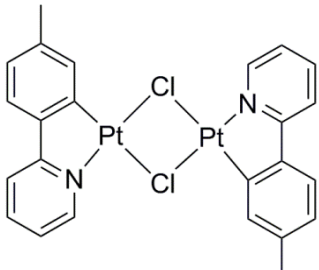
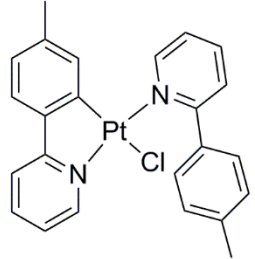
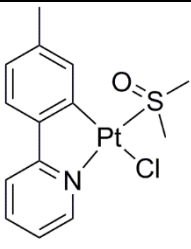
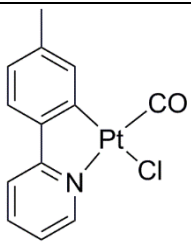
can be accounted for and using diffuse functions means that electron density further away from the atomic nuclei can be included. The basis sets mentioned in this thesis are summarised in Table 63. Effective core potentials (ECPs) were used to account for relativistic effects of the heavy element platinum for the calculations reported in this thesis for the family of complexes with the general formula, [Pt(tolpy)Cl(L)]. Using this method, the core electrons of the atom are replaced with a potential and only the valence electrons are included in the quantum chemical calculation.

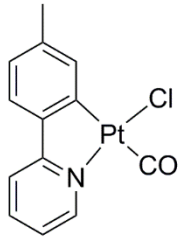
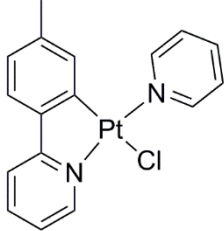
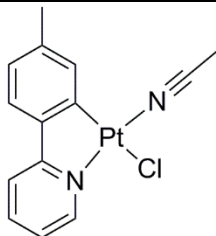
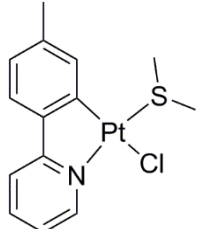
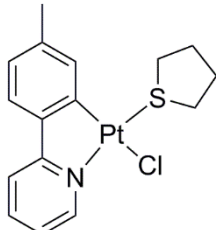
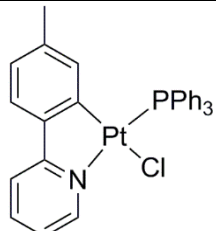
Table 63: Description of the basis sets discussed in this thesis

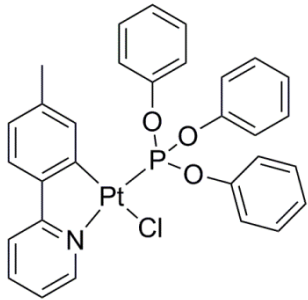
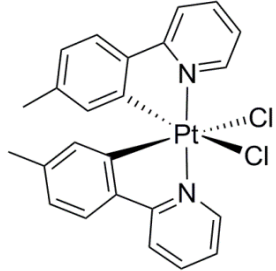
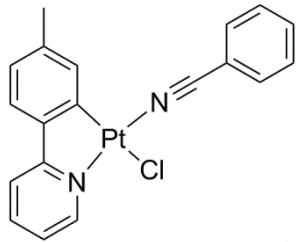
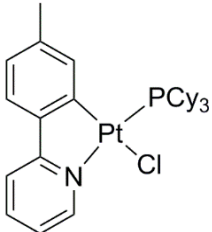
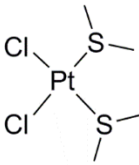
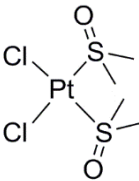
Basis Set	Description
6-31G ^{21, 22}	A split valence basis set (double-zeta) which has two sizes of basis function for each valence orbital.
6-31G(d) ^{21, 22}	6-31G with additional polarisation functions on each of the atoms
6-311+G(d,p) ³⁴⁷	A split valence basis set (triple-zeta) which has three sizes of basis function for each valence orbital with diffuse functions.
def2TZVP ³⁴⁸	A polarised triple-zeta basis
LANL2DZ ³⁴⁹	Los Alamos National Laboratory two-double-z, a basis set used in density functional theory
LANL2TZ ³⁵⁰	Los Alamos National Laboratory two-triple-z, a basis set used in density functional theory
LANL2TZ(f) ³⁵¹	With f-type polarisation functions
SDD ³⁵²	stands for Stuttgart-Dresden, the cities of the inventors of this basis set used in density functional theory

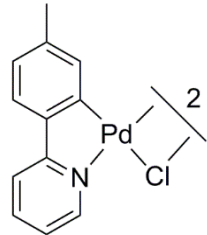
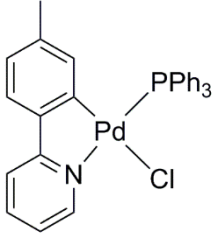
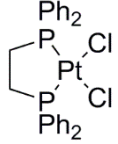
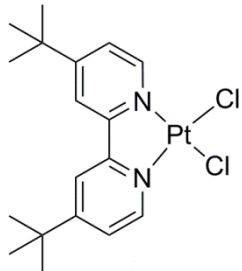
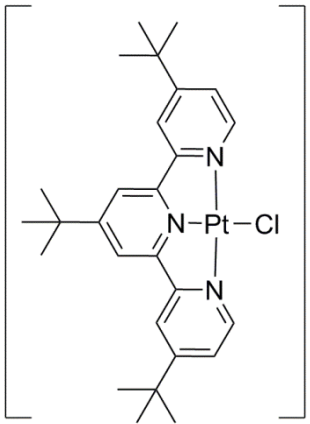
The calculations were conducted in the gas phase, but some literature references included calculations on solutions. Solvent molecules can be treated explicitly, implicitly or a mixture of the two. Models are used for implicit treatment where the solvent is replaced by an electrostatic potential. Examples include the universal solvation model based on density (SMD)³⁵³ and conductor like screening model (COSMO).³⁵⁴

Appendix III: List of Transition Metal Compounds

Compound Number	Formula	Structure
1a	$cis\text{-}[\text{Pt}(\text{tolpy})(\mu\text{-Cl})_2]$	
1b	$trans\text{-}[\text{Pt}(\text{tolpy})(\mu\text{-Cl})_2]$	
2	$[\text{Pt}(\text{tolpy})\text{Cl}(\text{H-tolpy})]$	
3	$[\text{Pt}(\text{tolpy})\text{Cl}(\text{S-dms})]$	
4	$[\text{Pt}(\text{tolpy})\text{Cl}(\text{CO})]$	

Compound Number	Formula	Structure
4b	$[\text{Pt}(\text{tolpy})\text{Cl}(\text{CO})]$	 The structure shows a platinum (Pt) center coordinated to a chlorine (Cl) atom, a carbonyl (CO) group, and the two nitrogen atoms of a 2-phenyl-1-pyridyl ligand (tolpy). The phenyl ring of the tolpy ligand has a methyl group at the para position.
5	$[\text{Pt}(\text{tolpy})\text{Cl}(\text{py})]$	 The structure shows a platinum (Pt) center coordinated to a chlorine (Cl) atom, a pyridine (py) ring, and the two nitrogen atoms of a 2-phenyl-1-pyridyl ligand (tolpy). The phenyl ring of the tolpy ligand has a methyl group at the para position.
6	$[\text{Pt}(\text{tolpy})\text{Cl}(\text{NCCH}_3)]$	 The structure shows a platinum (Pt) center coordinated to a chlorine (Cl) atom, an acetonitrile (NCCH ₃) group, and the two nitrogen atoms of a 2-phenyl-1-pyridyl ligand (tolpy). The phenyl ring of the tolpy ligand has a methyl group at the para position.
7	$[\text{Pt}(\text{tolpy})\text{Cl}(\text{dms})]$	 The structure shows a platinum (Pt) center coordinated to a chlorine (Cl) atom, a dimethyl sulfide (dms) group, and the two nitrogen atoms of a 2-phenyl-1-pyridyl ligand (tolpy). The phenyl ring of the tolpy ligand has a methyl group at the para position.
8	$[\text{Pt}(\text{tolpy})\text{Cl}(\text{tht})]$	 The structure shows a platinum (Pt) center coordinated to a chlorine (Cl) atom, a thietane (tht) ring, and the two nitrogen atoms of a 2-phenyl-1-pyridyl ligand (tolpy). The phenyl ring of the tolpy ligand has a methyl group at the para position.
9	$[\text{Pt}(\text{tolpy})\text{Cl}(\text{PPh}_3)]$	 The structure shows a platinum (Pt) center coordinated to a chlorine (Cl) atom, a triphenylphosphine (PPh ₃) group, and the two nitrogen atoms of a 2-phenyl-1-pyridyl ligand (tolpy). The phenyl ring of the tolpy ligand has a methyl group at the para position.

Compound Number	Formula	Structure
10	$[\text{Pt}(\text{tolpy})\text{Cl}(\text{P}(\text{OPh})_3)]$	 The structure shows a platinum (Pt) center coordinated to a 1-tolyl-2-pyridyl-3-pyridyl ligand (tolpy), a chloride (Cl) ligand, and a tris(phenyloxy)phosphine (P(OPh)3) ligand. The phosphorus atom is bonded to three phenoxy groups.
11	$[\text{Pt}^{\text{IV}}(\text{tolpy})_2\text{Cl}_2]$	 The structure shows a platinum (Pt) center in a +4 oxidation state coordinated to two 1-tolyl-2-pyridyl-3-pyridyl ligands (tolpy) and two chloride (Cl) ligands. The tolpy ligands are shown in a bidentate fashion, with one nitrogen atom coordinated to the platinum.
12	$[\text{Pt}(\text{tolpy})\text{Cl}(\text{PhCN})]$	 The structure shows a platinum (Pt) center coordinated to a 1-tolyl-2-pyridyl-3-pyridyl ligand (tolpy), a chloride (Cl) ligand, and a benzonitrile (PhCN) ligand. The nitrile group is coordinated to the platinum through the nitrogen atom.
13	$[\text{Pt}(\text{tolpy})\text{Cl}(\text{PCy}_3)]$	 The structure shows a platinum (Pt) center coordinated to a 1-tolyl-2-pyridyl-3-pyridyl ligand (tolpy), a chloride (Cl) ligand, and a tricyclohexylphosphine (PCy3) ligand.
14	<i>cis</i> - $[\text{PtCl}_2(\text{dms})_2]$	 The structure shows a platinum (Pt) center coordinated to two chloride (Cl) ligands and two dimethyl sulfide (dms) ligands in a cis configuration. The dms ligands are shown as sulfur atoms with two methyl groups.
15	<i>cis</i> - $[\text{PtCl}_2(\text{S-dmsO})_2]$	 The structure shows a platinum (Pt) center coordinated to two chloride (Cl) ligands and two dimethyl sulfoxide (S-dmsO) ligands in a cis configuration. The S-dmsO ligands are shown as sulfur atoms with two methyl groups and one oxygen atom.

Compound Number	Formula	Structure
16	$[\text{Pd}(\text{tolpy})(\mu\text{-Cl})_2]$	
17	$[\text{Pd}(\text{tolpy})\text{Cl}(\text{PPh}_3)]$	
18	$[\text{PtCl}_2(\kappa^2\text{-dppe})]$	
19	$[\text{PtCl}_2(4,4'\text{-di-}t\text{-Bu-2,2'\text{-bipyridine})]$	
20	$[\text{PtCl}(4,4',4''\text{-tri-tert-butyl-2,2':6',2''-terpyridine})] \text{Cl}^-$	

Abbreviations

2-MTHF	2-methyltetrahydrofuran
ATR	attenuated total reflectance
CHN	elemental analysis for carbon, hydrogen and nitrogen, %
cif	crystallographic information framework
cnst2	constant two, coupling constant used in two dimensional correlation nuclear magnetic resonance spectroscopy
cod	1,5-cyclooctadiene
COSY	correlation spectroscopy
CPME	cyclopentyl methyl ether
CSA	chemical shift anisotropy
CSD	crystallographic structural database
d	Doublet
DCB	1,2-dichlorobenzene
DCE	1,2-dichloroethane
DCM	dichloromethane
dd	doublet of doublets
DEPT	distortionless enhancement by polarisation transfer
DFT	density functional theory
DLS	dynamic light scattering
DMF	dimethylformamide
dms	dimethylsulfide
dmso	dimethylsulfoxide

dppe	1,2-bis(diphenylphosphine)ethane
dppf	1,1'-bis(diphenylphosphine)ferrocene
dppp	1,3-bis(diphenylphosphine)propane
DQF	double quantum filtered
e.e.	enantiomeric excess
ECP	electron core potential
EI	electron ionisation, also known as electron impact ionisation
ESP	electronic surface potential
FFA	furfuryl alcohol
FID	flame ionisation detector
FT-IR	Fourier transform infrared spectroscopy
GC	gas chromatography
GC-MS	gas chromatography-mass spectrometry
HETCOR	heteronuclear correlation
H-F	Hartree-Fock
HMBC	heteronuclear multiple bond correlation
HMF	5-(hydroxymethyl)furfural
HMQC	heteronuclear multiple quantum coherence
HOMO	highest occupied molecular orbital
HSAB	hard soft acids and bases
IPA	<i>iso</i> -propyl alcohol (2-propanol)
IR	infra-red

IRMS	isotope ratio mass spectrometry
LC-MS	liquid chromatography-mass spectrometry
LMO	localised molecular orbital
LUMO	lowest unoccupied molecular orbital
m	multiplet
MM	Mayer-Mullikan population
NBI	natural binding index
NBO	natural bond orbital
NLMO	natural (semi-)localised molecular orbitals
NMR	nuclear magnetic resonance
NOE	nuclear Overhauser effect
NOESY	nuclear Overhauser effect spectroscopy
OTf	Trifluoromethanesulfonate, also known as triflate
Pd/C	palladium on carbon
phen	1,10-phenanthroline
ppy	2-phenylpyridine
ppb	parts per billion
py	pyridine
PVP	polyvinylpyrrolidone
q	quartet
quin	quintet
r.t	room temperature
SAXS	small angle X-ray scattering

(S)-BINAP	(S)-(-)-(1,1'-binaphthalene-2,2'-diyl) <i>bis</i> -(diphenylphosphine)
sep	septet
t	triplet
TBP	tertiary butyl peroxide
TCD	thermal conductivity detector
TCE	tetrachloroethylene
TEM	transmission electron microscopy
TEMPO	2,2,6,6-tetramethylpiperidin-1-yl)oxyl
TFA	trifluoro acetic acid
THF	Tetrahydrofuran
THFA	tetrahydrofurfuryl alcohol
tht	tetrahydrothiophene
TIC	total ion chromatogram
tmp	5,10,15,20-tetramesitylporphyrinato
tolpy	2-(4-tolyl)pyridine
triphos	<i>bis</i> -(diphenylphosphinoethyl)phenylphosphine
ttp	tetratolylporphyrinato
UV	ultraviolet
UV-Vis	ultraviolet and visible
WI	Wiberg bond index
xantphos	4,5- <i>bis</i> -(diphenylphosphino)-9,9-dimethylxanthene
XRD	X-ray diffraction

References

1. A. Rusina and A. A. Vlcek, *Nature*, 1965, **206**, 295-296.
2. C.-H. Jun, *Chem. Soc. Rev.*, 2004, **33**, 610-618.
3. B. Rybtchinski and D. Milstein, *Angew. Chem., Int. Ed. Engl.*, 1999, **38**, 870-883.
4. A. Dermenci and G. Dong, *Sci. China Chem.*, 2013, **56**, 685-701.
5. F. Chen, T. Wang and N. Jiao, *Chem. Rev.*, 2014, **114**, 8613–8661.
6. K. Ruhland, *Eur. J. Org. Chem.*, 2012, **2012**, 2683-2706.
7. T. L. Cottrell, ed., *The Strengths of Chemical Bonds*, 2nd edn., Huheey, London, 1958.
8. J. Halpern, *Acc. Chem. Res.*, 1982, **15**, 238-244.
9. R. H. Crabtree, *J. Chem. Soc., Dalton Trans.*, 2001, 2437-2450.
10. C. F. H. Tipper, *J. Chem. Soc.*, 1955, **1**, 2045-2046.
11. D. M. Adams, J. Chatt, R. G. Guy and N. Sheppard, *J. Chem. Soc.*, 1961, 738-742.
12. M. Keeton, R. Mason and D. R. Russell, *J. Organomet. Chem.*, 1971, **33**, 259-266.
13. L. Souillart and N. Cramer, *Chem. Rev.*, 2015, **115**, 9410–9464.
14. M. Murakami, H. Amii and Y. Ito, *Nature*, 1994, **370**, 540-541.
15. M. Murakami, H. Amii, K. Shigeto and Y. Ito, *J. Am. Chem. Soc.*, 1996, **118**, 8285-8290.
16. Y. Masuda, M. Hasegawa, M. Yamashita, K. Nozaki, N. Ishida and M. Murakami, *J. Am. Chem. Soc.*, 2013, **135**, 7142-7145.
17. K. Chen, H. Li, Z. Q. Lei, Y. Li, W. H. Ye, L. S. Zhang, J. Sun and Z. J. Shi, *Angew. Chem. Int. Ed. Engl.*, 2012, **51**, 9851-9855.
18. E. Müller and A. Segnitz, *Justus Liebigs Ann. Chem.*, 1973, **1973**, 1583-1591.
19. A. L. K. Shi Shun and R. R. Tykwinski, *Angew. Chem., Int. Ed. Engl.*, 2006, **45**, 1034-1057.
20. K. Balaraman and V. Kesavan, *Synthesis*, 2010, **2010**, 3461-3466.
21. J. P. Marino and H. N. Nguyen, *J. Org. Chem.*, 2002, **67**, 6841-6844.
22. A. Dermenci, R. E. Whittaker and G. Dong, *Org. Lett.*, 2013, **15**, 2242-2245.
23. O. Daugulis and M. Brookhart, *Organometallics*, 2003, **23**, 527-534.
24. L. Zhang, X. Bi, X. Guan, X. Li, Q. Liu, B.-D. Barry and P. Liao, *Angew. Chem., Int. Ed.*, 2013, **52**, 11303-11307.
25. H. A. K. Kaneda, M. Wayaku, S. Tehanishi, *Chem. Lett.*, 1974, **3**, 215-216.

26. R. E. Whittaker and G. Dong, *Org. Lett.*, 2015, **17**, 5504-5507.
27. R. Zeng and G. Dong, *J. Am. Chem. Soc.*, 2015, **137**, 1408–1411.
28. G. Domazetis, B. Tarpey, D. Dolphin and B. R. James, *J. Chem. Soc. Chem. Comm.*, 1980, 939-940.
29. F. Abu-Hasanayn, M. E. Goldman and A. S. Goldman, *J. Am. Chem. Soc.*, 1992, **114**, 2520-2524.
30. C. M. Beck, S. E. Rathmill, Y. J. Park, J. Chen, R. H. Crabtree, L. M. Liable-Sands and A. L. Rheingold, *Organometallics*, 1999, **18**, 5311-5317.
31. M. Kreis, A. Palmelund, L. Bunch and R. Madsen, *Adv. Synth. Catal.*, 2006, **348**, 2148 – 2154.
32. T. Iwai, T. Fujihara and Y. Tsuji, *Chem. Commun.*, 2008, 6215-6217.
33. A. F. F. de Lima, R. C. Colman, F. M. Z. Zotin and L. G. Appel, *Int. J. Hydrogen Energy*, 2010, **35**, 13200-13205.
34. H. Eschinazi and H. Pines, *J. Org. Chem.*, 1959, **24**, 1369-1369.
35. J. Tsuji and K. Ohno, *Tetrahedron Lett.*, 1965, **6**, 3969-3971.
36. J. Tsuji and K. Ohno, *Tetrahedron Lett.*, 1966, **7**, 4713-4716.
37. Q. Shuai, L. Yang, X. Guo, O. Baslé and C.-J. Li, *J. Am. Chem. Soc.*, 2010, **132**, 12212-12213.
38. L. Zhao, R. Zhang, W. Guo, S. Wu and X. Lu, *Chem. Phys. Lett.*, 2005, **414**, 28-33.
39. X. Chen, W. Guo, L. Zhao, Q. Fu and Y. Ma, *J. Phys. Chem. A*, 2007, **111**, 3566-3570.
40. L. J. Gooßen and J. Paetzold, *Angew. Chem. Int. Ed. Engl.*, 2002, **41**, 1237-1241.
41. G. Wittig and U. Schöllkopf, *Chem. Ber.*, 1954, **87**, 1318-1330.
42. C. J. O'Brien, J. L. Tellez, Z. S. Nixon, L. J. Kang, A. L. Carter, S. R. Kunkel, K. C. Przeworski and G. A. Chass, *Angew. Chem., Int. Ed. Engl.*, 2009, **48**, 6836-6839.
43. R. F. Heck, in *Organic Reactions*, John Wiley & Sons, Inc., 2004.
44. Y.-C. Shih, P.-H. Tsai, C.-C. Hsu, C.-W. Chang, Y. Jhong, Y.-C. Chen and T.-C. Chien, *J. Org. Chem.*, 2015, **80**, 6669-6678.
45. A. Dermenci, R. E. Whittaker, Y. Gao, F. A. Cruz, Z.-X. Yu and G. Dong, *Chem. Sci.*, 2015, **6**, 3201-3210.
46. T. Xu, N. A. Savage and G. Dong, *Angew. Chem., Int. Ed. Engl.*, 2014, **53**, 1891 –1895.
47. P.-h. Chen, T. Xu and G. Dong, *Angew. Chem., Int. Ed. Engl.*, 2014, **53**, 1674-1678.
48. H. M. Ko and G. Dong, *Nat. Chem.*, 2014, **6**, 739-744.

49. T. Xu and G. Dong, *Angew. Chem., Int. Ed. Engl.*, 2014, **53**, 10733 – 10736.
50. T. Xu and G. Dong, *Angew. Chem., Int. Ed. Engl.*, 2012, **51**, 7567-7571.
51. L. Deng, T. Xu, H. Li and G. Dong, *J. Am. Chem. Soc.*, 2015, **138**, 369–374.
52. T. Xu, N. A. Savage and G. Dong, *Angew. Chem., Int. Ed. Engl.*, 2014, **53**, 1891-1895.
53. J. F. Hartwig, *Inorg. Chem.*, 2007, **46**, 1936-1947.
54. G. W. Huber, S. Iborra and A. Corma, *Chem. Rev.*, 2006, **106**, 4044-4098.
55. A. Corma, S. Iborra and A. Velty, *Chem. Rev.*, 2007, **107**, 2411-2502.
56. P. Azadi, O. R. Inderwildi, R. Farnood and D. A. King, *Renew. Sustainable Energy Rev.*, 2013, **21**, 506-523.
57. P. J. Deuss, K. Barta and J. G. de Vries, *Catal. Sci. Technol.*, 2014, **4**, 1174-1196.
58. M. S. Singhvi, S. Chaudhari and D. V. Gokhale, *RSC Adv.*, 2014, **4**, 8271-8277.
59. L. Yang, M. Takase, M. Zhang, T. Zhao and X. Wu, *Renew. Sustainable Energy Rev.*, 2014, **38**, 461-477.
60. C. H. Ko, S. H. Park, J.-K. Jeon, D. J. Suh, K.-E. Jeong and Y.-K. Park, *Korean J. Chem. Eng.*, 2012, **29**, 1657-1665.
61. E. Santillan-Jimenez and M. Crocker, *J. Chem. Technol. Biotechnol.*, 2012, **87**, 1041-1050.
62. G. J. S. Dawes, E. L. Scott, J. Le Notre, J. P. M. Sanders and J. H. Bitter, *Green Chem.*, 2015, **17**, 3231-3250.
63. P. T. Do, M. Chiappero, L. L. Lobban and D. E. Resasco, *Catal. Lett.*, 2009, **130**, 9-18.
64. P. Gallezot, *Chem. Soc. Rev.*, 2012, **41**, 1538-1558.
65. G. Yong, Y. Zhang and J. Y. Ying, *Angew Chem., Int. Ed. Engl.*, 2008, **47**, 9345-9348.
66. S. Yin, Y. Pan and Z. Tan, *Int. J. Green Energy*, 2011, **8**, 234-247.
67. P. K. Rout, A. D. Nannaware, O. Prakash, A. Kalra and R. Rajasekharan, *Chem. Eng. Sci.*, 2016, **142**, 318-346.
68. F. M. A. Geilen, T. vom Stein, B. Engendahl, S. Winterle, M. A. Liauw, J. Klankermayer and W. Leitner, *Angew Chem., Int. Ed. Engl.*, 2011, **50**, 6831-6834.
69. J. Mitra, X. Zhou and T. Rauchfuss, *Green Chem.*, 2014, **17**, 307-313.
70. Q. Xing, H. Lv, C. Xia and F. Li, *Chem. Commun.*, 2016, **52**, 489-492.
71. S. Y. Lee and K. S. Chan, *Organometallics*, 2013, **32**, 5391-5401.

72. P. Fristrup, M. Kreis, A. Palmelund, P.-O. Norrby and R. Madsen, *J. Am. Chem. Soc.*, 2008, **130**, 5206-5215.
73. V. Y. Kukushkin, *Coord. Chem. Rev.*, 1995, **139**, 375-407.
74. L. Alexandrova, O. G. D'Yachenko, G. M. Kazankov, V. A. Polyakov, P. V. Samuleev, E. Sansores and A. D. Ryabov, *J. Am. Chem. Soc.*, 2000, **122**, 5189-5200.
75. D. Dey, MChem Report, University of York, 2011.
76. M. Gozin, A. Weisman, Y. Ben-David and D. Milstein, *Nature*, 1993, **364**, 699.
77. J. Torroba, *Unpublished results, University of York*, 2010-2011.
78. Z. Q. Lei, H. Li, Y. Li, X. S. Zhang, K. Chen, X. Wang, J. Sun and Z. J. Shi, *Angew. Chem.-Int. Edit.*, 2012, **51**, 2690-2694.
79. R. G. W. Norrish and C. H. Bamford, *Nature*, 1937, **140**, 195 - 196.
80. S. Sakagami and M. Nakamizo, 1980, **53**, 265-266.
81. D. L. Head and C. G. McCarty, *Tetrahedron Lett.*, 1973, **14**, 1405-1408.
82. C. R. Barone, S. de Pinto, L. Maresca, G. Natile and C. Pacifico, *Inorg. Chim. Acta*, 2012, **383**, 13-19.
83. Y.-S. Lin, H. Misawa, J. Yamada and K. Matsumoto, *J. Am. Chem. Soc.*, 2001, **123**, 569-575.
84. J. Vicente, J. A. Abad, M.-T. Chicote, M.-D. Abrisqueta, J.-A. Lorca and M. C. Ramírez de Arellano, *Organometallics*, 1998, **17**, 1564-1568.
85. R. Çelenligil-Çetin, L. A. Watson, C. Guo, B. M. Foxman and O. V. Ozerov, *Organometallics*, 2004, **24**, 186-189.
86. J. F. Hartwig, R. A. Andersen and R. G. Bergman, *J. Am. Chem. Soc.*, 1989, **111**, 2717-2719.
87. K. Szőri, G. Szöllősi and M. Bartók, *J. Catal.*, 2006, **244**, 255-259.
88. G. O. Pritchard and J. P. Gute, *Int. J. Chem. Kinet.*, 1978, **10**, 759-772.
89. A. J. Gordon and R. A. Ford, *The chemist's companion: a handbook of practical data, techniques, and references*, Wiley, 1972.
90. J. M. O'Connor and J. Ma, *J. Org. Chem.*, 1992, **57**, 5075.
91. R. H. Prince and K. A. Raspin, *J. Chem. Soc. A: Inorg. Phys. Theor.*, 1969, 612-618.
92. R. H. Prince and K. A. Raspin, *Chem. Commun.*, 1966, 156-157.
93. K. Ohno and J. Tsuji, *J. Am. Chem. Soc.*, 1968, **90**, 99.
94. J. N. Coalter, J. C. Huffman and K. G. Caulton, *Organometallics*, 2000, **19**, 3569-3578.

95. D. A. Evans, L. Kværnø, T. B. Dunn, A. Beauchemin, B. Raymer, J. A. Mulder, E. J. Olhava, M. Juhl, K. Kagechika and D. A. Favor, *J. Am. Chem. Soc.*, 2008, **130**, 16295-16309.
96. X. Huang, L. Song, J. Xu, G. Zhu and B. Liu, *Angew. Chem., Int. Ed.*, 2013, **52**, 952-955.
97. J. Cornella, C. Zarate and R. Martin, *Chem. Soc. Rev.*, 2014, **43**, 8081-8097.
98. K. Alharbi, W. Alharbi, E. F. Kozhevnikova and I. V. Kozhevnikov, *ACS Catal.*, 2016, **6**, 2067-2075.
99. K. Nakamura, M. Tobisu and N. Chatani, *Org. Lett.*, 2015, **17**, 6142-6145.
100. M. Tobisu and N. Chatani, *Acc. Chem. Res.*, 2015, **48**, 1717-1726.
101. M. E. van der Boom, S.-Y. Liou, Y. Ben-David, A. Vigalok and D. Milstein, *Angew Chem., Int. Ed. Engl.*, 1997, **36**, 625-626.
102. A. Das, R. Chaudhuri and R.-S. Liu, *Chem. Commun.*, 2009, 4046-4048.
103. S. Y. Lee, T. H. Lai, K. S. Choi and K. S. Chan, *Organometallics*, 2011, **30**, 3691-3693.
104. F. Gao, J. D. Webb and J. F. Hartwig, *Angew Chem., Int. Ed. Engl.*, 2016, **55**, 1474-1478.
105. A. M. Clover, *J. Am. Chem. Soc.*, 1922, **44**, 1107-1118.
106. E. W. G. Diau, C. Kötting and A. H. Zewail, *Chem. Phys. Chem.*, 2001, **2**, 273-293.
107. R. D. Taylor, M. MacCoss and A. D. G. Lawson, *J. Med. Chem.*, 2014, **57**, 5845-5859.
108. A. Santoro, M. Wegrzyn, A. C. Whitwood, B. Donnio and D. W. Bruce, *J. Am. Chem. Soc.*, 2010, **132**, 10689-10691.
109. A. P. Pulis and D. J. Procter, *Angew Chem., Int. Ed. Engl.*, 2016, **55**, 9842-9860.
110. G. Sipos, E. E. Drinkel and R. Dorta, *Chem. Soc. Rev.*, 2015, **44**, 3834-3860.
111. C. B. Rauhut, L. Melzig and P. Knochel, *Org. Lett.*, 2008, **10**, 3891-3894.
112. M. M. Coulter, P. K. Dornan and V. M. Dong, *J. Am. Chem. Soc.*, 2009, **131**, 6932-6933.
113. R. Samanta and A. P. Antonchick, 2011, **50**, 5217-5220.
114. T. Wesch, A. Berthelot-Bréhier, F. R. Leroux and F. Colobert, *Org. Lett.*, 2013, **15**, 2490-2493.
115. J. H. Delcamp and M. C. White, *J. Am. Chem. Soc.*, 2006, **128**, 15076-15077.
116. C. Zhou and R. C. Larock, *J. Org. Chem.*, 2006, **71**, 3184.

117. G. Brasche, J. García-Fortanet and S. L. Buchwald, *Org. Lett.*, 2008, **10**, 2207-2210.
118. N. Gigant and J.-E. Bäckvall, *Chem. - Eur. J.*, 2014, **20**, 5890-5894.
119. Y. Izawa, D. Pun and S. S. Stahl, *Science*, 2011, **333**, 209-213.
120. M. M. Mdleleni, J. S. Bridgewater, R. J. Watts and P. C. Ford, *Inorg. Chem.*, 1995, **34**, 2334-2342.
121. T. J. Williams, A. J. M. Caffyn, N. Hazari, P. F. Oblad, J. A. Labinger and J. E. Bercaw, *J. Am. Chem. Soc.*, 2008, **130**, 2418-2419.
122. S. Wolfe and P. G. C. Campbell, *J. Am. Chem. Soc.*, 1971, **93**, 1497-1499.
123. B. M. Trost and P. J. Metzner, *J. Am. Chem. Soc.*, 1980, **102**, 3572-3577.
124. J. Grunes, J. Zhu, M. Yang and G. A. Somorjai, *Catal. Lett.*, 2003, **86**, 157-161.
125. R. G. W. Norrish, *Trans. Faraday Soc.*, 1937, **33**, 1521-1528.
126. F. E. Blacet and A. Miller, *J. Am. Chem. Soc.*, 1957, **79**, 4327-4329.
127. S. Y. Lee, H. S. Fung, S. Feng and K. S. Chan, *Organometallics*, 2016, **35**, 2480-2487.
128. E. A. Braude and R. P. Linstead, *J. Chem. Soc.*, 1954, 3544-3547.
129. D. Wang and D. Astruc, *Chem. Rev.*, 2015, **115**, 6621-6686.
130. S. Burling, M. K. Whittlesey and J. M. J. Williams, *Adv. Synth. Catal.*, 2005, **347**, 591-594.
131. A. Aktaş and Y. Gök, *Catal. Lett.*, 2015, **145**, 631-639.
132. A. Monney, G. Venkatachalam and M. Albrecht, *Dalton Trans.*, 2011, **40**, 2716-2719.
133. Z. Strassberger, M. Mooijman, E. Ruijter, A. H. Alberts, C. de Graaff, R. V. A. Orru and G. Rothenberg, *Appl. Organomet. Chem.*, 2010, **24**, 142-146.
134. N. Ding and T. S. A. Hor, *Dalton Trans.*, 2010, **39**, 10179-10185.
135. R. V. Jagadeesh, D. Banerjee, P. B. Arockiam, H. Junge, K. Junge, M.-M. Pohl, J. Radnik, A. Bruckner and M. Beller, *Green Chem.*, 2015, **17**, 898-902.
136. G. Zhang and S. K. Hanson, *Chem. Commun.*, 2013, **49**, 10151-10153.
137. J. Geboers, X. Wang, A. B. de Carvalho and R. Rinaldi, *J. Mol. Catal. A: Chem.*, 2014, **388**, 106-115.
138. Z. Chen, M. Zeng, Y. Zhang, Z. Zhang and F. Liang, *Appl. Organomet. Chem.*, 2010, **24**, 625-630.
139. N. Castellanos-Blanco, A. Arevalo and J. J. Garcia, *Dalton Trans.*, 2016, **45**, 13604-13614.
140. S. Mazza, R. Scopelliti and X. Hu, *Organometallics*, 2015, **34**, 1538-1545.

141. C. Bolm, *Nat Chem.*, 2009, **1**, 420-420.
142. P. J. Chirik, in *Catalysis without Precious Metals*, Wiley-VCH Verlag GmbH & Co. KGaA, 2010, pp. 83-110.
143. S. Enthaler, K. Junge and M. Beller, *Angew Chem., Int. Ed. Engl.*, 2008, **47**, 3317-3321.
144. P. Zhao, X. Feng, D. Huang, G. Yang and D. Astruc, *Coord. Chem. Rev.*, 2015, **287**, 114-136.
145. J. F. Sonnenberg, N. Coombs, P. A. Dube and R. H. Morris, *J. Am. Chem. Soc.*, 2012, **134**, 5893-5899.
146. X. Wang, J. Wang, F. Qi, L. Hu, X. Li, X. Cao and H. Gu, *Chin. J. Catal.*, 2013, **34**, 2084-2088.
147. Y. M. Y. Haddad, H. B. Henbest, J. Husbands and T. R. B. Mitchell, 1964, 361.
148. R. L. Chowdhury and J.-E. Backvall, *J. Chem. Soc., Chem. Commun.*, 1991, 1063-1064.
149. D. Morton and D. J. Cole-Hamilton, *J. Chem. Soc., Chem. Commun.*, 1988, 1154-1156.
150. J. S. M. Samec, J.-E. Backvall, P. G. Andersson and P. Brandt, *Chem. Soc. Rev.*, 2006, **35**, 237-248.
151. M. J. Gilkey and B. Xu, *ACS Catalysis*, 2016, **6**, 1420-1436.
152. K. Sawai, R. Tatumi, T. Nakahodo and H. Fujihara, *Angew Chem., Int. Ed. Engl.*, 2008, **47**, 6917-6919.
153. S. Jansat, M. Gómez, K. Philippot, G. Muller, E. Guieu, C. Claver, S. Castillón and B. Chaudret, *J. Am. Chem. Soc.*, 2004, **126**, 1592-1593.
154. V. Calò, A. Nacci, A. Monopoli and F. Montingelli, *J. Org. Chem.*, 2005, **70**, 6040-6044.
155. J. Stein, L. N. Lewis, Y. Gao and R. A. Scott, *J. Am. Chem. Soc.*, 1999, **121**, 3693-3703.
156. A. F. Schmidt and A. A. Kurokhina, *Kinet. Catal.*, 2012, **53**, 714-730.
157. M. R. Eberhard, *Org. Lett.*, 2004, **6**, 2125-2128.
158. J. G. de Vries, *Dalton Trans.*, 2006, 421-429.
159. M. Pérez-Lorenzo, *J. Phys. Chem. Lett.*, 2012, **3**, 167-174.
160. V. K. LaMer and R. H. Dinegar, *J. Am. Chem. Soc.*, 1950, **72**, 4847-4854.
161. V. K. L. Mer, *Ind. Eng. Chem.*, 1952, **44**, 1270-1277.
162. N. T. K. Thanh, N. Maclean and S. Mahiddine, *Chem. Rev.*, 2014, **114**, 7610-7630.
163. M. A. Watzky and R. G. Finke, *Chem. Mater.*, 1997, **9**, 3083-3095.

164. X. Peng, L. Manna, W. Yang, J. Wickham, E. Scher, A. Kadavanich and A. P. Alivisatos, *Nature*, 2000, **404**, 59-61.
165. Z. A. Peng and X. Peng, *J. Am. Chem. Soc.*, 2001, **123**, 1389-1395.
166. J. A. Widegren and R. G. Finke, *J. Mol. Catal. A: Chem.*, 2003, **198**, 317-341.
167. J. J. Stracke and R. G. Finke, *ACS Catal.*, 2014, **4**, 909-933.
168. Y. Lin and R. G. Finke, *Inorg. Chem.*, 1994, **33**, 4891-4910.
169. M. N. Vargaftik, I. I. Moiseev, D. I. Kochubey and K. I. Zamaraev, *Faraday Discussions*, 1991, **92**, 13-29.
170. D. R. Anton and R. H. Crabtree, *Organometallics*, 1983, **2**, 855-859.
171. G. M. Whitesides, M. Hackett, R. L. Brainard, J. P. P. M. Lavalleye, A. F. Sowinski, A. N. Izumi, S. S. Moore, D. W. Brown and E. M. Staudt, *Organometallics*, 1985, **4**, 1819-1830.
172. B. J. Hornstein, J. D. Aiken and R. G. Finke, *Inorg. Chem.*, 2002, **41**, 1625-1638.
173. K. L. Luska and A. Moores, *Adv. Synth. Catal.*, 2011, **353**, 3167-3177.
174. L. M. Baldyga, S. O. Blavo, C.-H. Kuo, C.-K. Tsung and J. N. Kuhn, *ACS Catal.*, 2012, **2**, 2626-2629.
175. V. R. Choudhary and M. G. Sane, *J. Chem. Technol. Biotechnol.*, 1998, **73**, 336-340.
176. T. C. Johnson, D. J. Morris and M. Wills, *Chem. Soc. Rev.*, 2010, **39**, 81-88.
177. E. A. Braude, L. M. Jackman and R. P. Linstead, *J. Chem. Soc.*, 1954, 3564-3568.
178. M. J. Gilkey, P. Panagiotopoulou, A. V. Mironenko, G. R. Jenness, D. G. Vlachos and B. Xu, *Catalysis*, 2015, **5**, 3988-3994.
179. D. Wang, C. Deraedt, J. Ruiz and D. Astruc, *J. Mol. Catal. A: Chem.*, 2015, **400**, 14-21.
180. *China Pat.*, CN 102453078 (A), 2012.
181. J. F. Quinn, D. A. Razzano, K. C. Golden and B. T. Gregg, *Tetrahedron Lett.*, 2008, **49**, 6137-6140.
182. L. Wolff, *Justus Liebigs Ann. Chem.*, 1912, **394**, 86-108.
183. N. J. Kishner, *Russ. Phys. Chem. Soc.*, 1911, **43**, 582.
184. E. Clemmensen, *Ber. Dtsch. Chem. Ges.*, 1914, **47**, 51-63.
185. J. E. Lyons, *J. Chem. Soc. D: Chem. Commun.*, 1969, 564-565.
186. K. Moseley and P. M. Maitlis, *J. Chem. Soc. D: Chem. Commun.*, 1969, 1156-1157.

187. L. Červený, P. Kluson and I. Paseka, *React. Kinet. Catal. L.*, 1991, **43**, 533-537.
188. H. Hintze and A. Heesing, *Chem. Ber.*, 1988, **121**, 1133-1136.
189. C. P. Newman, K. Casey-Green, G. J. Clarkson, G. W. V. Cave, W. Errington and J. P. Rourke, *Dalton Trans.*, 2007, **0**, 3170-3182.
190. L. Guzzi, F. Solymosi and P. Tétényi, *New Frontiers in Catalysis, Parts A-C*, Elsevier Science, 1993.
191. Y. Barshad, X. Zhou and E. Gulari, *J. Catal.*, 1985, **94**, 128-141.
192. A. Zecchina, S. Bordiga, G. Spoto, L. Marchese, G. Petrini, G. Leofanti and M. Padovan, *J. Phys. Chem.*, 1992, **96**, 4991-4997.
193. P. Bazin, O. Saur, J. C. Lavalley, M. Daturi and G. Blanchard, *Phys. Chem. Chem. Phys.*, 2005, **7**, 187-194.
194. J. D. Scholten, B. C. Leal and J. Dupont, *Catalysis*, 2011, **2**, 184-200.
195. J.-T. Lu, J. C. Y. Lin, M.-C. Lin, N. D. Khupse and I. J. B. Lin, *Langmuir*, 2014, **30**, 10440-10448.
196. Q. Zhou, S. Wei and W. Han, *J. Org. Chem.*, 2014, **79**, 1454-1460.
197. K. S. Weddle, J. D. Aiken and R. G. Finke, *J. Am. Chem. Soc.*, 1998, **120**, 5653-5666.
198. S. V. Jadhav, D. S. Nikam, V. M. Khot, N. D. Thorat, M. R. Phadatare, R. S. Ningthoujam, A. B. Salunkhe and S. H. Pawar, *New J. Chem.*, 2013, **37**, 3121-3130.
199. G. Lu, S. Li, Z. Guo, O. K. Farha, B. G. Hauser, X. Qi, Y. Wang, X. Wang, S. Han, X. Liu, J. S. DuChene, H. Zhang, Q. Zhang, X. Chen, J. Ma, S. C. J. Loo, W. D. Wei, Y. Yang, J. T. Hupp and F. Huo, *Nat. Chem.*, 2012, **4**, 310-316.
200. K. M. Koczkur, S. Mourdikoudis, L. Polavarapu and S. E. Skrabalak, *Dalton Trans.*, 2015, **44**, 17883-17905.
201. R. Si, Y.-W. Zhang, L.-P. You and C.-H. Yan, *J. Phys. Chem. B*, 2006, **110**, 5994-6000.
202. P. Courtot, R. Pichon and J. Y. Salaun, *J. Organomet. Chem.*, 1985, **286**, c17-c21.
203. J. Auffret, P. Courtot, R. Pichon and J.-Y. Salaun, *J. Chem. Soc., Dalton Trans.*, 1987, 1687-1692.
204. D. W. Bruce, R. F. Jones and D. J. Cole-Hamilton, *J. Chem. Soc., Dalton Trans.*, 1984, 2249-2253.
205. A. M. Thayer, *Chem. Eng. News*, 2005, **83**, 43.
206. K. S. Chan, X. Z. Li, L. Zhang and C. W. Fung, *Organometallics*, 2007, **26**, 2679-2687.

207. Y. R. Luo, *Comprehensive Handbook of Chemical Bond Energies*, 2007.
208. J. Vicente, A. Arcas, J. M. Fernandez-Hernandez, A. Sironi and N. Masciocchi, *Chem. Commun.*, 2005, 1267-1269.
209. M. Benedetti, C. R. Girelli, D. Antonucci, S. A. De Pascali and F. P. Fanizzi, *Inorg. Chim. Acta.*, 2014, **413**, 109-114.
210. T. Diao and S. S. Stahl, *J. Am. Chem. Soc.*, 2011, **133**, 14566-14569.
211. G. Ertl, *Angew Chem., Int. Ed. Engl.*, 1990, **29**, 1219-1227.
212. V. E. Henrich and P. A. Cox, *The Surface Science of Metal Oxides*, Cambridge University Press, 1996.
213. A. Pidcock, R. E. Richards and L. M. Venanzi, *J. Chem. Soc. A: Inorg. Phys. Theor.*, 1966, 1707-1710.
214. T. G. Appleton, H. C. Clark and L. E. Manzer, *Coord. Chem. Rev.*, 1973, **10**, 335-422.
215. N. K. Yurii, *Russ. Chem. Rev.*, 1974, **43**, 805-820.
216. I. I. Chernyaev, *Ann. Inst. Platine (USSR)*, 1926, **4**, 243 - 275.
217. K. M. Anderson and A. G. Orpen, *Chem. Commun.*, 2001, 2682.
218. T. Ishii, S. Tsuboi, G. Sakane, M. Yamashita and B. K. Breedlove, *Dalton Trans.*, 2009, 680-687.
219. T. G. Appleton, H. C. Clark and L. E. Manzer, *Coord. Chem. Rev.*, 1973, **10**, 335-422.
220. B. Pinter, V. Van Speybroeck, M. Waroquier, P. Geerlings and F. De Proft, *Phys. Chem. Chem. Phys.*, 2013, **15**, 17354-17365.
221. A. A. Grinberg, *Izv. Akad. Nauk SSSR, Ser. Khim.*, 1943, 350-358.
222. G. S. Manku, *Theoretical Principles of Inorganic Chemistry*, Tata McGraw-Hill, 1980.
223. A. Dedieu, *Chem. Rev.*, 2000, **100**, 543-600.
224. Y. Syrkin, *Izv. Nats. Akad. Nauk Resp. Kaz.*, 1948, 69 - 82.
225. Y.-X. Jia, B.-B. Li, Y. Li, S. A. Pullarkat, K. Xu, H. Hirao and P.-H. Leung, *Organomet.*, 2014, **33**, 6053-6058.
226. Y.-X. Jia, X.-Y. Yang, W. S. Tay, Y. Li, S. A. Pullarkat, K. Xu, H. Hirao and P.-H. Leung, *Dalton Trans.*, 2016, **45**, 2095-2101.
227. B. D. Gupta, V. Singh, R. Yamuna, T. Barclay and W. Cordes, *Organomet.*, 2003, **22**, 2670-2678.
228. H. Braunschweig, P. Brenner, A. Müller, K. Radacki, D. Rais and K. Uttinger, *Chem. - Eur. J.*, 2007, **13**, 7171-7176.
229. K. A. Netland, A. Krivokapic and M. Tilset, *J. Coord. Chem.*, 2010, **63**, 2909-2927.

230. C. B. Perry, N. Shin, M. A. Fernandes and H. M. Marques, *Dalton Trans.*, 2013, **42**, 7555-7561.
231. C. M. Donahue, S. P. McCollom, C. M. Forrest, A. V. Blake, B. J. Bellott, J. M. Keith and S. R. Daly, *Inorg. Chem.*, 2015, **54**, 5646-5659.
232. P. Kapoor, V. Y. Kukushkin, K. Löqvist and Å. Oskarsson, *J. Organomet. Chem.*, 1996, **517**, 71-79.
233. I. Nakagawa, *Coord. Chem. Rev.*, 1969, **4**, 423-462.
234. M. J. Church and M. J. Mays, *J. Chem. Soc. A: Inorg., Phys., Theor.*, 1968, 3074-3078.
235. D. M. Adams, J. Chatt, J. Gerratt and A. D. Westland, *J. Chem. Soc.*, 1964, 734-739.
236. J. R. Allkins and P. J. Hendra, *J. Chem. Soc. A: Inorg., Phys., Theor.*, 1967, 1325-1329.
237. K. Nakamoto, P. J. McCarthy, J. Fujita, R. A. Condrate and G. T. Behnke, *Inorg. Chem.*, 1965, **4**, 36-43.
238. G. W. Watt and J. E. Cuddeback, *Inorg. Chem.*, 1971, **10**, 947-950.
239. S. J. S. Kerrison and P. J. Sadler, *J. Chem. Soc., Dalton Trans.*, 1982, 2363-2369.
240. J. Powell and B. L. Shaw, *J. Chem. Soc.*, 1965, 3879-3881.
241. R. Cervantes, J. Tiburcio and H. Torrens, *New J. Chem.*, 2015, **39**, 631-638.
242. T. G. Appleton, J. R. Hall and S. F. Ralph, *Inorg. Chem.*, 1985, **24**, 4685-4693.
243. T. G. Appleton and M. A. Bennett, *Inorg. Chem.*, 1978, **17**, 738-747.
244. M. Ludwig, L. Öhrström and D. Steinborn, *Magn. Reson. Chem.*, 1995, **33**, 984-987.
245. M. A. Bennett, S. K. Bhargava, S. H. Privér and A. C. Willis, *Eur. J. Inorg. Chem.*, 2008, **2008**, 3467-3481.
246. J. Chatt and B. L. Shaw, *J. Chem. Soc.*, 1962, 5075-5084.
247. P. W. Atkins, J. C. Green and M. L. H. Green, *J. Chem. Soc. A: Inorg., Phys., Theor.*, 1968, 2275-2280.
248. B. W. Dale, R. J. Dickinson and R. V. Parish, *Chem. Phys. Lett.*, 1974, **24**, 286-288.
249. L. T. Haahr, K. P. Jensen, J. Boesen and H. E. M. Christensen, *J. Inorg. Biochem.*, 2010, **104**, 136-145.
250. E. Baba, T. R. Cundari and I. Firkin, *Inorg. Chim. Acta*, 2005, **358**, 2867-2875.
251. B. Pudasaini and B. G. Janesko, *Organomet.*, 2014, **33**, 84-93.

252. P. N. Kapoor and R. Kakkar, *J. Mol. Struct.: THEOCHEM*, 2004, **679**, 149-156.
253. K. N. Houk and P. H.-Y. Cheong, *Nature*, 2008, **455**, 309-313.
254. D. J. Tantillo, *Acc. Chem. Res.*, 2016, **49**, 1079-1079.
255. C. J. Cramer and D. G. Truhlar, *Phys. Chem. Chem. Phys.*, 2009, **11**, 10757-10816.
256. A. H. Greif, P. Hrobárik, V. Hrobáriková, A. V. Arbuznikov, J. Autschbach and M. Kaupp, *Inorg. Chem.*, 2015, **54**, 7199-7208.
257. A. J. Bridgeman, G. Cavigliasso, L. R. Ireland and J. Rothery, *J. Chem. Soc., Dalton Trans.*, 2001, 2095-2108.
258. C. A. Coulson, *Proc. R. Soc. London A: Math., Phys. Eng. Sci.*, 1939, **169**, 413-428.
259. I. Mayer, *Int. J. Quantum Chem.*, 1984, **26**, 151-154.
260. I. Mayer, *Chem. Phys. Lett.*, 1983, **97**, 270-274.
261. L. Pauling, L. O. Brockway and J. Y. Beach, *J. Am. Chem. Soc.*, 1935, **57**, 2705-2709.
262. A. D. Becke, *J. Chem. Phys.*, 1993, **98**, 5648-5652.
263. G. Aullón, G. Ujaque, A. Lledós, S. Alvarez and P. Alemany, *Inorg. Chem.*, 1998, **37**, 804-813.
264. S. Grimme, *Wiley Interdiscip. Rev. Comput. Mol. Sci.*, 2011, **1**, 211-228.
265. S. Grimme, S. Ehrlich and L. Goerigk, *J. Comput. Chem.*, 2011, **32**, 1456-1465.
266. A. Rodríguez-Castro, A. Fernández, M. López-Torres, D. Vázquez-García, L. Naya, J. M. Vila and J. J. Fernández, *Polyhedron*, 2012, **33**, 13-18.
267. S. Fuertes, A. J. Chueca and V. Sicilia, *Inorg. Chem.*, 2015, **54**, 9885-9895.
268. N. Ghavale, A. Wadawale, S. Dey and V. K. Jain, *J. Organomet. Chem.*, 2010, **695**, 1237-1245.
269. J.-Y. Lallemand, J. Soulie and J.-C. Chottard, *J. Chem. Soc., Chem. Commun.*, 1980, 436-438.
270. H. Baumgarth, G. Meier, T. Braun and B. Braun-Cula, *Eur. J. Inorg. Chem.*, 2016, Early access, DOI: 10.1002/ejic.201600682.
271. M. Chikuma and R. J. Pollock, *J. Magn. Reson.*, 1982, **47**, 324-327.
272. K. Nakamoto, *Infrared and Raman Spectra of Inorganic and Coordination Compounds: Theory and applications in inorganic chemistry*, John Wiley, 1997.
273. H. Vahrenkamp, *Angew Chem., Int. Ed. Engl.*, 1975, **14**, 322-329.
274. M. Calligaris and O. Carugo, *Coord. Chem. Rev.*, 1996, **153**, 83-154.

275. D. A. Lutterman, A. A. Rachford, J. J. Rack and C. Turro, *J. Phys. Chem. Lett.*, 2010, **1**, 3371-3375.
276. H. Li, L. Zhang, I. Zheng, X. Li, X. Fan and Y. Zhao, *Chem. - Eur. J.*, 2016, **22**, 14285-14292.
277. B. A. McClure and J. J. Rack, *Inorg. Chem.*, 2011, **50**, 7586-7590.
278. R. Thomas, C. B. Shoemaker and K. Eriks, *Acta. Crystal.*, 1966, **21**, 12-20.
279. M. Kobayashi, S. Masaoka and K. Sakai, *Acta. Crysta. Sec. E*, 2008, **64**, m1325.
280. A. Tronnier, S. Metz, G. Wagenblast, I. Muenster and T. Strassner, *Dalton Trans.*, 2014, **43**, 3297-3305.
281. B. J. Coe, T. J. Meyer and P. S. White, *Inorg. Chem.*, 1993, **32**, 4012-4020.
282. M. Y. Skripkin, P. Lindqvist-Reis, A. Abbasi, J. Mink, I. Persson and M. Sandstrom, *Dalton Trans.*, 2004, 4038-4049.
283. H. E. Gottlieb, V. Kotlyar and A. Nudelman, *J. Org. Chem.*, 1997, **62**, 7512-7515.
284. J. A. Davies, in *Advances in Inorganic Chemistry and Radiochemistry*, eds. H. J. Emeléus and A. G. Sharpe, Academic Press, 1981, vol. Volume 24, pp. 115-187.
285. M. Karplus, *J. Chem. Phys.*, 1959, **30**, 11-15.
286. M. Karplus, *J. Am. Chem. Soc.*, 1963, **85**, 2870-2871.
287. A. A. Bothner-By, in *Advances in Magnetic and Optical Resonance*, ed. S. W. John, Academic Press, 1965, vol. Volume 1, pp. 195-316.
288. S. H. Heinemann, T. Hoshi, M. Westerhausen and A. Schiller, *Chem. Commun.*, 2014, **50**, 3644-3660.
289. R. Motterlini and L. E. Otterbein, *Nat. Rev. Drug Discov.*, 2010, **9**, 728-743.
290. T. R. Johnson, B. E. Mann, J. E. Clark, R. Foresti, C. J. Green and R. Motterlini, *Angew Chem., Int. Ed. Engl.*, 2003, **42**, 3722-3729.
291. C. de la Cruz and N. Sheppard, *J. Mol. Struct.*, 1990, **224**, 141-161.
292. J. Börgel, M. G. Campbell and T. Ritter, *J. Chem. Ed.*, 2016, **93**, 118-121.
293. F. A. Cotton and C. B. Harris, *Inorg. Chem.*, 1967, **6**, 369-376.
294. D. S. Martin, *Inorg. Chim. Acta. rev.*, 1971, **5**, 107-125.
295. S. R. Desjardins, K. W. Penfield, S. L. Cohen, R. L. Musselman and E. I. Solomon, *J. Am. Chem. Soc.*, 1983, **105**, 4590-4603.
296. R. J. Deeth, *Faraday Discuss.*, 2003, **124**, 379-391.

297. C. E. Schäffer, C. Anthon and J. Bendix, *Coord. Chem. Rev.*, 2009, **253**, 575-593.
298. P. Comba and M. Kerscher, *Coord. Chem. Rev.*, 2009, **253**, 564-574.
299. K. P. Huber and G. Herzberg, eds., *Molecular Spectra and Molecular Structure IV. Constants of Diatomic Molecules*, New York,, 1979.
300. R. H. Crabtree, in *The Organometallic Chemistry of the Transition Metals*, John Wiley & Sons, Inc., 2005, pp. 87-124.
301. N. Muller, P. C. Lauterbur and J. Goldenson, *J. Am. Chem. Soc.*, 1956, **78**, 3557-3561.
302. P. G. Waddell, A. M. Z. Slawin and J. D. Woollins, *Dalton Trans.*, 2010, **39**, 8620-8625.
303. P. Pyykkö, *Theor. Chem. Acc.*, 2000, **103**, 214-216.
304. J. Mason, L. F. Larkworthy and E. A. Moore, *Chem. Rev.*, 2002, **102**, 913-934.
305. T. G. Appleton, J. R. Hall and I. J. McMahon, *Inorg. Chem.*, 1986, **25**, 726-734.
306. Y. Tanaka and A. Ono, *Dalton Trans.*, 2008, 4965-4974.
307. N. J. Farrer, P. Gierth and P. J. Sadler, *Chem. Eur. J.*, 2011, **17**, 12059-12066.
308. A. G. Algarra, V. V. Grushin and S. A. Macgregor, *Organomet.*, 2012, **31**, 1467-1476.
309. J. Zhu, Z. Lin and T. B. Marder, *Inorg. Chem.*, 2005, **44**, 9384-9390.
310. R. Salcedo, P. Sharma, A. Cabrera and S. Fomine, *J. Mol. Struct.: THEOCHEM*, 2002, **579**, 151-154.
311. M. Shafikov, 2015.
312. M. J. Frisch, G. W. Trucks, H. B. Schlegel, G. E. Scuseria, M. A. Robb, J. R. Cheeseman, G. Scalmani, V. Barone, B. Mennucci, G. A. Petersson, H. Nakatsuji, M. Caricato, X. Li, H. P. Hratchian, A. F. Izmaylov, J. Bloino, G. Zheng, J. L. Sonnenberg, M. Hada, M. Ehara, K. Toyota, R. Fukuda, J. Hasegawa, M. Ishida, T. Nakajima, Y. Honda, O. Kitao, H. Nakai, T. Vreven, J. A. Montgomery Jr., J. E. Peralta, F. Ogliaro, M. J. Bearpark, J. Heyd, E. N. Brothers, K. N. Kudin, V. N. Staroverov, R. Kobayashi, J. Normand, K. Raghavachari, A. P. Rendell, J. C. Burant, S. S. Iyengar, J. Tomasi, M. Cossi, N. Rega, N. J. Millam, M. Klene, J. E. Knox, J. B. Cross, V. Bakken, C. Adamo, J. Jaramillo, R. Gomperts, R. E. Stratmann, O. Yazyev, A. J. Austin, R. Cammi, C. Pomelli, J. W. Ochterski, R. L. Martin, K. Morokuma, V. G. Zakrzewski, G. A. Voth, P. Salvador, J. J. Dannenberg, S. Dapprich, A. D. Daniels, Ö. Farkas, J. B. Foresman, J. V.

- Ortiz, J. Cioslowski and D. J. Fox, *Gaussian 09*, (2009) Gaussian, Inc., Wallingford, CT, USA.
313. H. Kessler, H. Oschkinat, C. Griesinger and W. Bermel, *J. Magn. Reson.*, 1986, **70**, 106-133.
314. J. Stonehouse, P. Adell, J. Keeler and A. J. Shaka, *J. Am. Chem. Soc.*, 1994, **116**, 6037-6038.
315. K. Stott, J. Stonehouse, J. Keeler, T.-L. Hwang and A. J. Shaka, *J. Am. Chem. Soc.*, 1995, **117**, 4199-4200.
316. O. D. L. V. CrysAlisPro.
317. i. i. S. A. s. a. w. C. s. Empirical absorption correction using spherical harmonics, Oxford Diffraction Ltd. Version 1.171.34.40.
318. J. A. C. "Olex2" crystallography software, 2009, **42**, 339-341.
319. O. V. Dolomanov, L. J. Bourhis, R. J. Gildea, J. A. K. Howard and H. Puschmann, 2009, **42**, 339-341.
320. G. M. Sheldrick, 2008, **64**, 112.
321. U. o. G. "SHELXL-97" - program for the Refinement of Crystal Structures. G. M. Sheldrick, Göttingen, Germany, 1997.
322. A. H. Goldstein and S. L. Shaw, 2003, **103**, 5025-5048.
323. M. E. Archbold, K. R. Redeker, S. Davis, T. Elliot and R. M. Kalin, *Rapid Commun. Mass Spectrom.*, 2005, **19**, 337-342.
324. W. E. Hill, D. M. A. Minahan, J. G. Taylor and C. A. McAuliffe, 1982, **104**, 6001-6005.
325. H. Honda, T. Matsumoto, M. Sakamoto, A. Kobayashi, H.-C. Chang and M. Kato, 2013, **52**, 4324-4334.
326. F. G. Baddour, M. I. Kahn, J. A. Golen, A. L. Rheingold and L. H. Doerrer, 2010, **46**, 4968-4970.
327. I. Khazal, 2015-2016.
328. W. L. F. Armarego and C. L. L. Chai, in *Purification of Laboratory Chemicals (Sixth Edition)*, Butterworth-Heinemann, Oxford, 2009, pp. 88-444.
329. D. R. Burfield and R. H. Smithers, *J. Org. Chem.*, 1978, **43**, 3966-3968.
330. D. B. G. Williams and M. Lawton, *J. Org. Chem.*, 2010, **75**, 8351-8354.
331. R. D. Gaussian 09, M. J. Frisch, G. W. Trucks, H. B. Schlegel, G. E. Scuseria, , J. R. C. M. A. Robb, G. Scalmani, V. Barone, B. Mennucci, , H. N. G. A. Petersson, M. Caricato, X. Li, H. P. Hratchian, , J. B. A. F. Izmaylov, G. Zheng, J. L. Sonnenberg, M. Hada, , K. T. M. Ehara, R. Fukuda, J. Hasegawa, M. Ishida, T. Nakajima, , O. K. Y. Honda, H. Nakai, T. Vreven, J. A. Montgomery, Jr., , F. O. J. E. Peralta, M. Bearpark, J. J.

- Heyd, E. Brothers, , V. N. S. K. N. Kudin, T. Keith, R. Kobayashi, J. Normand, , A. R. K. Raghavachari, J. C. Burant, S. S. Iyengar, J. Tomasi, , N. R. M. Cossi, J. M. Millam, M. Klene, J. E. Knox, J. B. Cross, , C. A. V. Bakken, J. Jaramillo, R. Gomperts, R. E. Stratmann, , A. J. A. O. Yazyev, R. Cammi, C. Pomelli, J. W. Ochterski, , K. M. R. L. Martin, V. G. Zakrzewski, G. A. Voth, , J. J. D. P. Salvador, S. Dapprich, A. D. Daniels, , J. B. F. O. Farkas, J. V. Ortiz, J. Cioslowski, and G. and D. J. Fox, Inc., Wallingford CT, 2013.
332. P. C. Hariharan and J. A. Pople, *Theo. Chim. Acta.*, 1973, **28**, 213-222.
333. W. J. P. M. M. Francl, W. J. Hehre, J. S. Binkley, D. J. D. M. S. Gordon and J. A. Pople, *J. Chem. Phys.*, 1982, **77**, 3654.
334. C. Lee, W. Yang and R. G. Parr, *Phys. Rev. B*, 1988, **37**, 785-789.
335. B. Miehlich, A. Savin, H. Stoll and H. Preuss, *Chem. Phys. Lett.*, 1989, **157**, 200-206.
336. F. Weigend, *Phys. Chem. Chem. Phys.*, 2006, **8**, 1057-1065.
337. F. Weigend and R. Ahlrichs, *Phys. Chem. Chem. Phys.*, 2005, **7**, 3297-3305.
338. J. P. Foster and F. Weinhold, *J. Am. Chem. Soc.*, 1980, **102**, 7211-7218.
339. A. E. Reed and F. Weinhold, *J. Chem. Phys.*, 1983, **78**, 4066-4073.
340. A. E. Reed, R. B. Weinstock and F. Weinhold, *J. Chem. Phys.*, 1985, **83**, 735-746.
341. A. E. Reed, L. A. Curtiss and F. Weinhold, *Chem. Rev.*, 1988, **88**, 899-926.
342. W. Kohn, A. D. Becke and R. G. Parr, *J. Phys. Chem.*, 1996, **100**, 12974-12980.
343. A. D. Becke, *Phys. Rev. A.*, 1988, **38**, 3098-3100.
344. J. P. Perdew, *Phys. Rev. B*, 1986, **33**, 8822-8824.
345. Y. Zhao and D. G. Truhlar, *Theo. Chem. Acc.*, 2008, **120**, 215-241.
346. M. Head-Gordon, J. A. Pople and M. J. Frisch, *Chem. Phys. Lett.*, 1988, **153**, 503-506.
347. A. D. McLean and G. S. Chandler, *J. Phys. Chem.*, 1980, **72**, 5639-5648.
348. D. Andrae, U. Häußermann, M. Dolg, H. Stoll and H. Preuß, 1990, **77**, 123-141.
349. P. J. Hay and W. R. Wadt, *J. Phys. Chem.*, 1985, **82**, 299.
350. P. J. Hay and W. R. Wadt, *J. Phys. Chem.*, 1985, **82**, 270-283.
351. L. E. Roy, P. J. Hay and R. L. Martin, *J. Chem. Theory Comput.*, 2008, **4**, 1029.

352. K. A. Peterson, D. Figgen, M. Dolg and H. Stoll, *J. Phys. Chem.*, 2007, **126**, 124101.
353. A. V. Marenich, C. J. Cramer and D. G. Truhlar, *J. Phys. Chem. B*, 2009, **113**, 6378-6396.
354. A. Klamt and G. Schuurmann, *J. Chem. Soc., Perkin Trans. 1*, 1993, 799-805.